Coupling of Arterial Wall Cell Dynamics and Blood Flow

by

© Miharu Yamamoto

A thesis submitted to the University of Canterbury
in fulfilment of the requirement for the degree of Doctor of Philosophy
in Mechanical Engineering

Christchurch, New Zealand

January 2011

Acknowledgements

Firstly, I would like to express my gratitude to Professor Tim David, without whose knowledge, support and constructive guidance this thesis could not have been completed.

I would like to thank Dr. A. Comerford. This thesis greatly benefited from his patient and generous guidance.

Very, very special thanks go to my best friend Julian J. J. Davidson, who has the patience of a saint and is the most non-judgemental person I have met. Without his friendship, support and sense of humour, I would not be here as what I am today. I am very grateful for the chance to have met you.

Many thanks go to Tony Dale. His kind support and expertise in HPC very often prevented my research from stalling completely.

Also, very warm thanks go to Hsien Wen Chang and Foong Lian Hah, both of whom have been truly wonderful, funny, and inspiring friends. Their fair opinions, genuine support and friendship greatly helped me get through the extremely difficult times.

I would like to thank my fellow third-floor postgrads and Bioengineering colleagues for providing great office working environment and support. In particular, Dr. Samara Alzaidi, Vinod Sadashiva, Shantha Parthan, Aline Lang and Dr. Freddie Pedroso - I would like to thank you all for listening to me when I wanted to talk and making me laugh. Only with their support and sense of humour I could keep my sanity. Many thanks also go to Raj Fernandez, without whose expertise and patience my car would have been sold or even scrapped long ago. It was such a huge relief during extremely busy and stressful times. Thank you so, so much.

I would like to thank all the Bridging Programmes colleagues for providing me with the great learning opportunity and working environment. Among those, my particular thanks go to Stephanie Box for being such a wonderful, understanding

boss and also to Pamela Chivers for being such a lovely office mate and friend, who was always there to listen to me.

Finally, and most importantly, I wish to thank my father Kunimitsu Yamamoto and mother Seiko Yamamoto, for their continuous and unconditional love, support and faith in me. Without them, I would not be who, where or what I am today.

Contents

List of Figures

List of Tables

Nomenclature

List of Abbreviations

Expressions	Descriptions
ACE	Angiotensin-converting enzyme
ADP	Adenosine diphosphate
Ach	Acetylcholine
ADMA	Asymmetric dimethylarginine
AI	Angiotensin I
AII	Angiotensin II
AMP	Adenosine monophosphate
ATP	Adenosine triphosphate
ATPase	Adenosine triphosphatase
CAB	Carotid artery bifurcation
cAMP	Cyclic adenosine monophosphate
CCA	Common carotid artery
CFD	Computational fluid dynamics
cGMP	Cyclic guanosine monophosphate
CNP	C-type natriuretic peptide
COX	Cyclooxygenase
CRP	C-reactive protein
CS	Circumferential stretch
DNA	Deoxyribonucleic acid
EC	Endothelial cell
ECA	External carotid artery
ECE	Endothelin-converting enzyme
eNOS	Endothelial nitric oxide synthase

List of Abbreviations (Continued.)

Expressions	Descriptions
ET-1	Endothelin-1
FAD	Flavin adenine dinucleotide
FMD	Flow-mediated dilation
FMN	Flavin mononucleotide
FVM	Finite volume method
GTP	Guanosine triphosphate
HDL	High-density lipoprotein
HUVEC	Human umbilical vein endothelial cell
ICA	Internal carotid artery
IF	Intermediate filament
LDL	Low-density lipoprotein
MCP-1	Monocyte chemoattractant protein-1
M-CSF	Macrophage colony-stimulating factor
MMP	Matrix metalloproteinase
MRI	Magnetic resonance imaging
NADPH	Nicotinamide adenine dinucleotide phosphate
NO	Nitric oxide
ODE	Ordinary differential equation
OSI	Oscillatory shear index
oxLDL	Oxidised low-density lipoprotein
OxyHb	Oxyhaemoglobin
PDGF	Platelet-derived growth factor
PECAM	Platelet endothelium cell adhesion molecule
PKG	Protein kinase G
PS	Patient-specific
RBC	Red blood cell
RNA	Ribonucleic acid

List of Abbreviations (Continued.)

Expressions	Descriptions
SE	Strain energy
sGC	Soluble guanylate cyclase
SOD	Superoxide dismutase
SPA	Stress phase angle
TF	Tissue factor
TF-AHCB	Tuning fork-shaped average human carotid bifurcation
TNF-β	Tumour necrosis factor-β
VCAM-1	Vascular cell adhesion molecule-1
VEGF	Vascular endothelial growth factor
VLDL	Very low-density lipoprotein
vWF	von Willebrand factor
WSG	Wall shear gradient
WSR	Wall shear rate
WSS	Wall shear stress
WT	Wall thickness
Y-AHCB	Y-shaped average human carotid bifurcation

List of Symbols

Expressions	Descriptions
BH^4	Tetrahydrobiopterin
Ca^{2+}	Calcium ion
K^+	Potassium ion
Na^+	Sodium ion
O_2^-	Superoxide anion
PGI_2	Prostacyclin

Abstract

The objective of this research is to investigate both mathematically and numerically the effects of vascular geometry upon the cellular dynamics in the endothelium and its consequence in the localisation of atherosclerosis. It is widely accepted that the formation of atherosclerotic plaques preferentially occurs at specific locations in the vasculature, such as arterial branches and bends. It has also been observed that, at the sites of plaque formation, the physiological functions of the vascular endothelium are impaired due to a defect in the production mechanisms of or diminished activities of endothelial nitric oxide (NO). From these observations, a correlation between the vascular geometry, which is effected via local haemodynamic forces, and local bioavailability of endothelial NO has been postulated.

The research areas that have been involved in the investigation of atherosclerosis's localisation in the past, haemodynamics, medicine, calcium dynamics, NO kinetics and endothelial cell biology, have been studied individually, and there appears to be no integrated model to date that allows investigation of coupled haemodynamic and cellular mechanism applied in physiologically realistic model geometries. An integrated numerical model that includes these mechanisms will be developed in this research, which will lead to a further, more comprehensive understanding of the pathogenesis of atherosclerosis.

Chapter 1

Pathophysiology of Atherosclerosis, and Endothelium

1.1 Introduction

Atherosclerosis is a chronic inflammatory disease of medium to large-sized arteries characterised by the formation of plaques within the vessel wall and subsequent narrowing of the lumen. It is a primary underlying cause of many significant clinical events such as embolism and thrombosis, and in more severe cases, leads to strokes and myocardial infarction, both of which are responsible for many deaths in developed countries. Because of this, combined with the fact that its precise initiation and progression mechanisms have not yet been fully understood, atherosclerosis has been under extensive research since 1950s. This chapter describes the pathophysiology of atherosclerosis, and what is currently understood about the mechanisms of its origin and development. It also summarises the structure and physiology of arteries and in particular, the endothelium, where the initiation of plaques formation is assumed to take place.

1.2 Pathophysiology of atherosclerosis

1.2.1 Disease origin and progression

Due to the lipid degeneration often observed in autopsy, atherosclerosis has been for a long time considered as a disease of lipid accumulation within the vascular wall, caused by the high plasma concentration of cholesterol. This hypothesis remained until recently, when it started to emerge that cholesterol, along with its carrier low-density lipoprotein (LDL), represents only a part of the plaque development process, each stage of which has been discovered to be characterised by the features of the body's inflammatory responses.

The response that characterises the earliest atherosclerotic lesion is the increased expression of vascular cell adhesion molecule-1 (VCAM-1) from the endothelium. VCAM-1 mediates the adhesion of leukocytes, particularly monocytes and T cells, to the endothelial surface. Once the cells are on the EC surface, selectins facilitate their rolling, integrins the attachment and chemoattractants such as monocyte chemoattractant protein-1 (MCP-1) the subsequent transmigration into the media (Fig. 1.1(a)). Upon crossing the endothelium, monocytes differentiate to become macrophages, of which primary physiological functions are to ingest cellular debris and also to prompt immune cells' response against pathogens.

Meanwhile, at the vascular sites where plaques often develop, the permeability of endothelium is often increased (102). In normal endothelium, the ECs have an elongated shape aligned in the direction of flow, and their intercellular tight junctions do not allow the penetration of large molecules such as LDLs. However, at plaque-prone sites, where the blood flow tends to be disturbed, the ECs take more polygonal shape, exhibiting no particular preference in orientation. At these sites, the turnover of ECs is increased, which causes the tight junctions to widen and makes them more permeable (26). Under oxidative stress in the lesion, these migrated LDL molecules become modified into oxidised LDLs (oxLDLs).

Within the lesion, macrophages engulf and ingest oxidised LDLs, forming foam cells, which are to be the core of the lesion. This process is enhanced by macrophage colony-stimulating factor (MCS-F), which promotes the proliferation of macrophages and also increases the expression of scavenging receptors and thus facilitates lipid ingestion. T cells meanwhile produce inflammatory cytokines such

as γ-interferon and tumour necrosis factor-β (TNF-β), both of which can stimulate macrophages. When these processes continue, the foam cells accumulate and come to form the earliest visible form of atherosclerotic lesions termed fatty streaks (Fig. 1.1(b)). Fatty streaks, which have a yellow-white foamy appearance due to the large amount of membrane-bound cholesterol, start to appear in early adolescence, exhibiting no particular site preferences in the arteries. These are largely asymptomatic, and do not always develop into atheroma.

As the inflammatory process continues, these activated leukocytes release cytokines and fibrinogenic mediators including various growth factors, which promote the migration and proliferation of vascular smooth muscle cells (VSMCs) (78). At this point, these VSMCs and collagen synthesised from VSMCs form fibrous caps, protective layers between the intima and the lesion core. This continuing cycle of accumulation of macrophages, migration and proliferation of VSMCs and formation of fibrous tissue cause the plaque to enlarge. The lesion core is rich in lipids and necrotic due to the apoptosis of cholesterol-ingesting macrophages. Also, as these macrophages are the primary source of tissue factor (TF) (127) in the lesion, the core is extremely thrombogenic. This is a so-called stable complicated lesion, with uniform and thick fibrous caps (Fig. 1.1(c)).

The fibrous caps can become thin due to the ongoing inflammation responses. These medial VSMCs and macrophages within the lesion release matrix metalloproteinases (MMPs) (73) which are a family of extracellular matrix-degrading enzymes under inflammatory stress. It is believed that those involved in the plaque development are MMP-1 and MMP-9, the former mainly being responsible for cleaving collagen (which provides tensile strength) and the latter for degrading the basement membrane components such as collagen and elastin. Therefore these MMPs not only render fibrous caps weak and thin, but also permit the penetration of even more VSMCs through the elastic lamina. In addition, inflammatory mediators, such as interferon-γ released from activated T cells, can suppress collagen synthesis. These changes in the extracellular matrix metabolism significantly damage the integrity of the fibrous caps, and therefore make the plaque susceptible to rupture (unstable complicated lesion).

Before the lesion starts to protrude into the lumen the artery wall dilates outwards to compensate for the growing volume of the lesion, leaving the luminal volume relatively unchanged and therefore the blood flow undisrupted. This is called vascular remodelling. When the inflammatory processes and growth of

plaque volume continue, however, the dilation can no longer continue, the lesion may protrude into the lumen (stenosis). Some may rupture, which has been traditionally considered to be triggered by haemodynamic forces imposed on the lesion surface. It has been emerging that the factor that makes the lesion more vulnerable to rupture is not the extent of stenosis but the composition of plaques, i.e. those with soft lipid-rich core with thin, non-uniform fibrous caps are more susceptible to rupture even when the protrusion in to the lumen is relatively insignificant (40). Once this takes place (Fig. 1.1(d)), the thrombogenic lipid-core, which includes TF, triggers the coagulation cascade, leading to acute formation of thrombus and often occlusion of the vessel. Conditions such as strokes and myocardial infarction resulting from this are the most severe complications of atherosclerosis.

1.2.2 Risk factors

As outlined in the previous section, from the inception to rupture, every stage of lesion development is characterised by the features of inflammatory response. Risk factors on the other hand are the habits, traits or medical conditions that are not direct causative factors but may increase the risk of developing or exacerbate the progression of the disease. The main risk factors include the following (95):

- **Modifiable**: Smoking, hypertension, dyslipidemia, diabetes
- **Nonmodifiable**: Male sex, advanced age, genetic abnormalities, family history of atherosclerosis at young age
- **Uncertain**: Obesity, diet, sedentary lifestyle

Many among the above are thought to be associated with and affect the inflammatory responses seen in atherosclerosis. Abnormalities in lipid concentrations and metabolism, which were long thought to be the primary and sole causative factors of plaque initiation, are now thought to exacerbate the ongoing inflammatory response within the lesion. In addition to the known properties of oxLDLs to secrete adhesion molecules, chemokines and cytokines, lipoprotein particles can also undergo modifications in the vessel wall and stimulate T cells (78). Other forms of lipoproteins, such as very low-density lipoproteins (VLDLs) and high-density lipoproteins (HDLs) may also be involved, the former due to their going

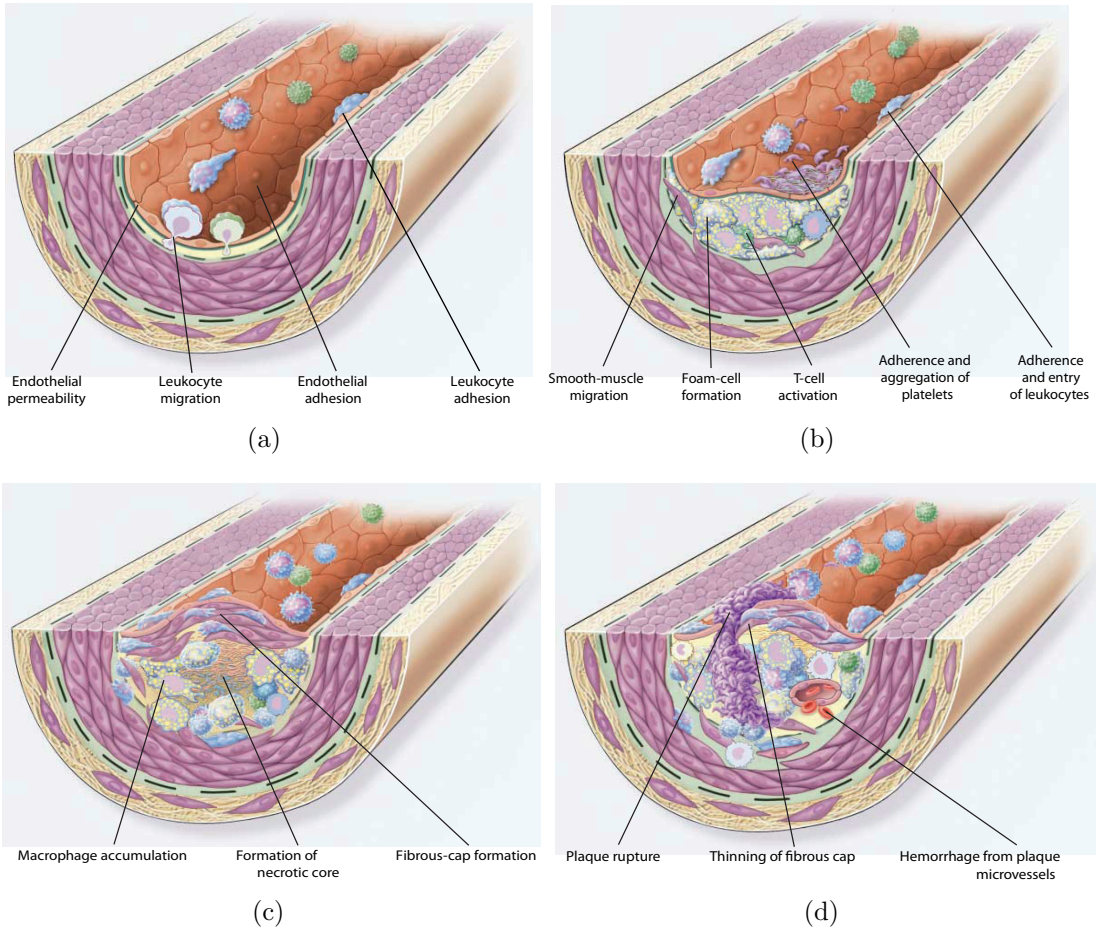

Figure 1.1: (a) Earliest changes seen in plaque initiation. Increased expression of VCAM-1 from the endothelium mediates the binding of leukocytes, particularly monocytes and T cells, onto the EC surface. Chemoattractants such as monocyte chemoattractant protein-1 (MCP-1) facilitate their transmigration into the sub-endothelial space. (b) Formation of fatty streaks. They are the earliest visible form of atherosclerotic lesions, resulting from the accumulation of lipid-rich foam cells derived from the phagocytosis (engulfing of harmful or dead cells by several kind of white blood cells termed phyagocytes) of oxLDLs by macrophages. Fatty streaks, which have a yellow-white foamy appearance due to the large amount of membrane-bound cholesterol, start to appear in early adolescence, but exhibit no particular site preferences in the arteries. These are largely asymptomatic, and do not always develop into atheroma. As the inflammatory process continues, the activated leukocytes release cytokines and various growth factors which promote the migration and proliferation of VSMCs (78). (c) Stable complicated lesion. Collagen and VSMCs form protective fibrous caps between the intima and the lesion core, walling off the lipid-rich and extremely thrombogenic necrotic centre. At this stage the fibrous caps are still dense and uniform. (d) Unstable complicated lesion. Medial VSMCs release collagen-degrading MMPs under inflammatory stress. MMPs damage the integrity of the fibrous caps, making the lesion vulnerable to rupture. Figures adapted from Ross (114).

through oxidative modifications and also inducing inflammatory responses in the endothelium, and the lack of the latter resulting in the reduced transport of LDL back into the bloodstream from the intima. Also for hypertension, another prominent risk factor, its link with inflammation via the ability of angiotensin II (AII) to induce inflammatory response has been suggested. AII, also a potent vasoconstrictor, can promote the production of superoxide anion (O_2^-) from the ECs and VSMCs, and also increase the expression of proinflammatory cytokines including MCP-1 from the VSMCs and VCAM-1 from the ECs (78). Diabetes, another well-known risk factor, can cause modification of macromolecules, which can increase the expression of inflammatory cytokines, as well as increase oxidative stress. An increase in oxidative stress, caused via the increased production of reactive oxygen species, is also caused by cigarette smoking (71).

1.2.3 Nitric oxide (NO)

Nitric oxide (NO) is a gaseous signalling molecule that has diverse biological functions in human physiology.

NO, initially known as endothelium-derived relaxing factor (EDRF), is a potent vasodilator, which counter-acts the actions of vasoconstrictors in the vessel wall and contributes to the maintenance of the basal tone. NO is synthesised constitutively in the endothelium from the substrates oxygen, L-arginine and nicotinamide adenine dinucleotide phosphate (NADPH) in the presence of the catalytic enzyme endothelial nitric oxide synthase (eNOS) and several cofactors (the details of the reactions will be discussed in Chapter 5). Once produced, NO diffuses through the endothelium into the surrounding VSMCs and activates soluble guanylate cyclase (sGC), which catalyses the production of cyclic guanosine monophosphate (cGMP) from guanosine triphosphate (GTP). This in turn activates protein kinase G (PKG), leading to the relaxation of VSMCs. This maintenance of the basal tone by NO is an important anti-atherogenic property by itself. When an artery is constricted beyond the local basal tone, a circumferential stress is generated locally and transmitted to the endothelium. Using the vessel with induced vasoconstriction, Gutstein (56) observed the endothelial cells being lifted up from the basement membrane into the lumen, which was attributed to the additional stress. They also observed the attachment of leukocytes, as well as the separation of ECs at the intercellular junctions. The inevitable consequences of this damage to the endothelium is the initiation of a coagulation cascade and

the penetration of macromolecules into the sub-endothelial space - both of which have detrimental effects on the initiation and progression of plaques.

NO has been also found to have the following anti-atherogenic properties:

- Inhibition of leukocyte recruitment, adhesion and infiltration
- Inhibition of VCAM-1 expression
- Suppression of VSMC proliferation
- Inhibition of platelet adhesion and aggregation
- Selectively depletion of macrophages in the lesions
- Scavenging of oxidative free radicals

all of which are associated with inflammatory responses observed in each developing stage of atherosclerosis (78; 88; 103).

NO's inhibitory action on platelets was one of its atheroprotective mechanisms that was known from early on. Initially, platelets had been known to be associated primarily with advanced lesions. These often contained activated and aggregated platelets, which are also the source of growth factors (113), and once the plaque ruptures, the activated platelets incite the recruitment, adhesion and aggregation of additional platelets from the circulating blood, often leading to thrombus formation and occlusion of the lumen. It was then subsequently found that platelets were involved in inflammation in all stages of plaque development. Platelets, when activated, aggregate with leukocytes, and once bound to the vascular wall, provides a "sticky surface" to facilitate recruitment and adhesion of even more leukocytes (51; 89). Also, CD40L, the ligand derived from platelets, increases the expression of MCP-1, VCAM-1 and TF in the endothelium, all of which were mentioned above as the facilitators of inflammation.

Taken together, it can be postulated that impaired NO dynamics or reduced NO concentrations would result in the increased inflammatory stress, which might potentially initiate the plaque formation or exacerbate the ongoing inflammatory processes in all stages of plaque development. Given that NO concentration in the endothelium has been observed to be low in hypertensive and hypercholesterolaemic cases (7), the implication is that the relative lack or absence of NO's anti-inflammatory actions due to reduced availability of NO in these conditions is the reason these conditions are regarded as risk factors.

1.2.4 Wall shear stress

The haemodynamic variable that reflects the features of local vascular geometry is wall shear stress (WSS), which is the tangential force exerted on the endothelial surface brought about by the flowing blood.

Since the focal nature of atherosclerosis started to emerge, numerous studies have been carried out to elucidate the roles of WSS in atherosclerosis, particularly the role of WSS as a possible causative factor in atherogenesis. The first to be proposed was that the plaque formation is initiated due to the direct mechanical damages to the endothelium (i.e. erosion) caused by high WSS (46). This was then followed the proposition by Caro et al. (22) that the plaque localisation is due to low WSS, since the low local wall shear gradient (WSG) results in the LDL particles remaining lodged in the EC wall, allowing them to accumulate. Although the focus of these earlier studies tended to be solely on WSS's influences on lipid transport, which was considered as the main culprit of atherogenesis at that time, they resulted in a shift of focus to the pathophysiological role of WSS (and therefore vascular geometry) in both the initiation and development of atherosclerosis. The numerous flow studies that followed demonstrated the involvement of WSS in the intima-media thickness. It is now widely accepted that the regions of low WSS with disturbed flow features such as flow separation, reattachment and reversal often coincide with the sites of greatest intimal thickening whereas the regions of high WSS exhibit minimum thickening (6; 52; 142), although from these results it was not possible to analyse the processes involved in-between.

Since then, many processes and mechanisms regulated by WSS that appear to fill in the gap, not only as causative factors of atherosclerosis but also as part of regulatory mechanism of vascular physiology, have been discovered (see Fig. 1.2 for summary). In arteries, the physiological range of WSS has been reported to be 1.0-7.0Pa (83), and when WSS is below this range, increases in monocyte adhesion and transmigration (133), VCAM-1 expression (134), VSMC proliferation (67) and EC turnover (76) were observed, as well as the loss of the ECs via increased apoptosis (76) and ECs' morphological change to randomly-orientated polygonal shape (133). All of which are, as outlined in Section 1.2.1, involved in the atherosclerotic lesion development, and therefore likely to be the contributing factors to exacerbating the thickening. Oscillating WSS was also observed to influence cellular processes, resulting in the failed induction of Ca^{2+}

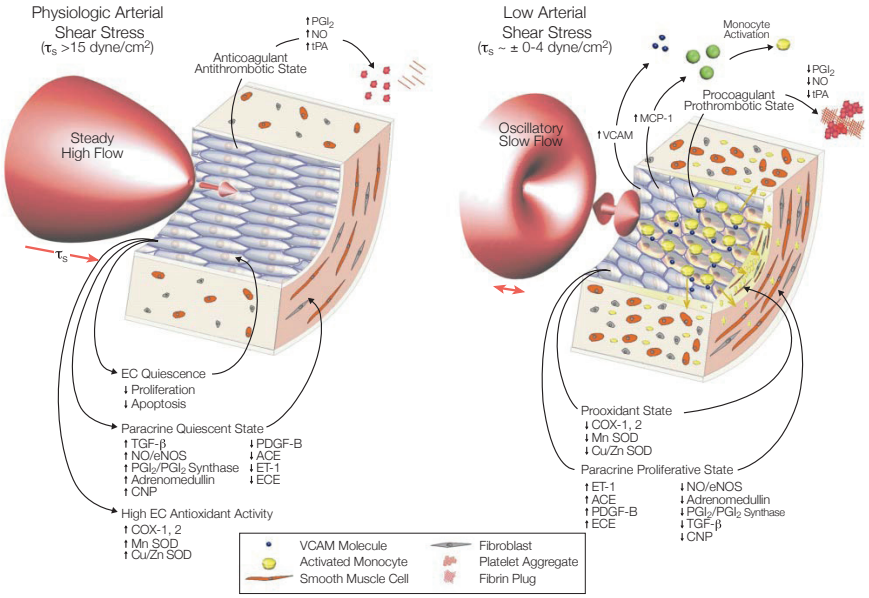

Figure 1.2: The effects of arterial physiological and low WSS on endothelial cellular responses. Elevated WSS results in the shift to anti-inflammatory, atheroprotective EC phenotype, whereas low and/or oscillating WSS leads to pro-inflammatory and pro-vasoconstriction phenotype. Acronyms not mentioned in this chapter: ACE (angiotensin-converting enzyme), CNP (C-type natriuretic peptide), COX (cyclooxygenase), ECE (endothelin-converting enzyme), ET-1 (endothelin-1), PDGF (platelet-derived growth factor). Figure taken from Malek et al. (83).

transients (59), increases in the production of O_2^- (35), monocyte adhesion (23) and EC proliferation (25).

Increased WSS, on the other hand, not only has the reverse effect but also results in an increase in cGMP in the VSMCs (and therefore inducing relaxation - likely to be due to the WSS-induced increased NO production) (8) and eNOS expression (100), and expression of prostacyclin (PGI_2) (83), which, like NO, has anti-atherogenic properties as a vasodilator and platelet activation inhibitor.

It is notable that many of the processes regulated by WSS listed here, particularly those associated with inflammation, coincide with those regulated by NO (see Section 1.2.3), implying the strong correlation between WSS (and therefore the vascular geometry) and endothelial NO.

1.2.5 Carotid artery atherosclerosis

Each of the right and left carotid artery bifurcations (CABs), located on each side of the neck, consists of the common carotid artery (CCA) and two daughter arteries, the internal and the external carotid arteries (ICA and ECA). The right CCA originates from the first branch from the aortic arch (i.e. brachiocephalic artery), and the left CCA from the second branch, both of which bifurcate into the ICA and the ECA. The former supplies the orbits and most (over 80%) (85) of the cerebrum, whereas the latter supplies most tissue of the head except for the brain and orbit.

Because of their locations, the formation of atherosclerotic plaques in these arteries often has severe clinical consequences. If the advanced plaques protrude into and occlude the lumen, it could lead to ischemia of the downstream cerebral tissues. If the plaque ruptures, it could lead to the formation of thrombus and again disrupt or block the blood flow. Another possibility is that the thrombus breaks off, which could prompt the further thrombus growth due to its thrombogenic contents within being exposed and triggering the coagulation process. Simultaneously, it also poses the risk of the broken-off thrombus segments (emboli) being carried further downstream by the circulating blood, which could become lodged in smaller arteries, causing embolism and consequently often leading to cerebral ischemia (i.e. strokes).

Atherosclerosis is a very focal disease which often develops at the bends and branches in the arterial vasculature (6; 36). The ICA, along with coronary arteries, is known to be particularly atherosclerotic lesion-prone among those sites. This is believed to be the result of the presence of the carotid sinus, the bulbous dilation of the vessel at the base of the ICA. This geometrical configuration gives rise to a unique, complex flow field that is reflected on the vessel wall surface in the form of spatially-varying low WSS. As stated in Section 1.2.4, low, disrupted WSS patterns have been observed to have various atherogenic consequences, and given that the no noticeable variation of the cellular compositions of the ICA from those of other medium-sized muscular arteries has been reported, it would be reasonable to assume that the specific geometrical difference and resulting deviation of local flow condition from that in the plaque-free regions are strongly associated with the localisation.

1.3 Arterial wall structure

The arterial system in the human vasculature is categorised into three classes: elastic (conducting) arteries, muscular (distributing/conduit) arteries, arterioles and capillaries. As stated in the previous sections, atherosclerosis is a disease of medium to large-sized arteries, and therefore the former two are of relevance here. Their structures and variations are summarised below (50; 77; 85).

All arteries consist of three layers of tissues, tunica intima, tunica media and tunica externa (Fig. 1.3). Tunica intima is the inner-most layer in the arterial vessel wall, consisting of a single layer of endothelial cells and forming an interface between the flowing blood and the vessel. In vessels having a diameter of $>1mm$, the endothelium is supported by the sub-endothelial layer of connective tissue, the basement membrane. Tunica media is the middle layer, made up mostly of layers of VSMCs which wrap around the vessel perpendicular to the vessel axis so that they can regulate the vascular tone by dilating or constricting. Tunica media, particularly in smaller arteries and arterioles, plays a significant role in regulating the flow and blood pressure, which would be greatly influenced by a small change in radius (Poiseuille's law states that the former is proportional and the latter inversely proportional to the fourth power of the radius). Tunica externa is the outermost layer, consisting mostly of connective tissue of loosely-arranged collagen fibres. Its main function is to protect and to anchor the vessel to the surrounding tissue. Also present in the tunica externa is a network of nerve fibres and lymphatic vessels, and in large arteries, also a system of small blood vessels (vasa vasorum) which transport nutrients to the outer tissue of the vessel wall.

Elastic (conducting) arteries such as the aorta, iliac and common carotid arteries have by far the largest diameters in the arterial system (1.0-2.0cm). Their primary function is to provide a low-resistance passage (which is facilitated by the large diameters) between the heart and medium-sized arteries. Since these arteries need to withstand the large pressure variations of the blood ejected from the heart, they contain a large amount (more than any in the arterial system) of connective tissue protein, elastin. Elastin is present in all of three tunica layers, among which the media (which also include the internal and external elastic laminae) contains the largest amount. This high content of elastin allows these arteries to withstand the large pressure variations due to the cardiac pulse. The elasticity and resulting distensibility also contribute to the smoothing-out of the

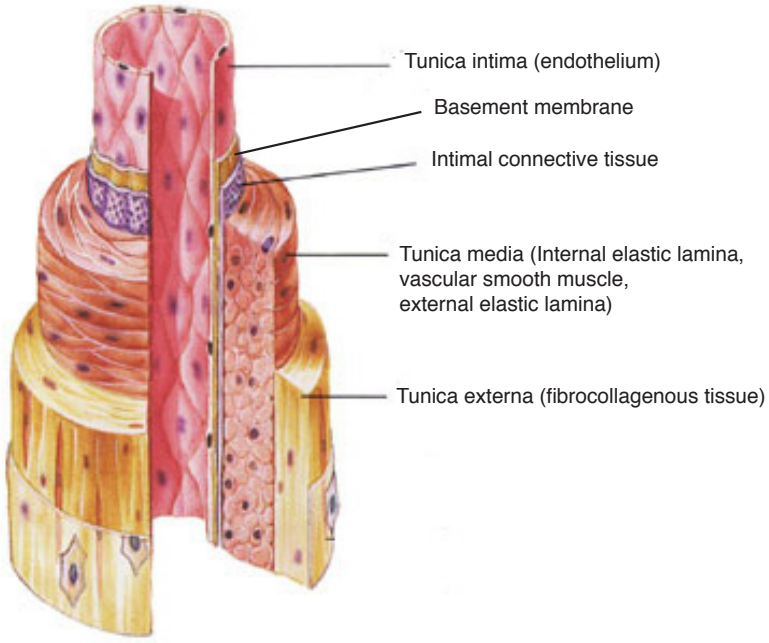

Figure 1.3: Arterial wall structure. Figure taken and modified from Human Physiology, 4th ed (45).

pressure fluctuations (due to the peripheral resistance, there is a net pressure build-up during systole, which is relieved during diastole), by dilating when the heart ejects the blood into them (systole) and then by recoiling to propel the blood forwards to the medium-sized arteries downstream. The resulting more uniform flow facilitates the maintenance of organ perfusion during diastole (Windkessel effect). The media also contains the extracellular protein, collagen, which forms a network of fibrils. Collagen is much stiffer than elastin, and thus prevents over-distention of the vessel.

Muscular (distributing/conduit) arteries are medium to small-sized vessels of diameters of 0.1-1.0cm, of which primary role is to deliver blood to specific organs. The internal carotid, external carotid, radial, cerebral and coronary arteries are examples of such vessels. The tunica media of muscular arteries is the thickest among all three tunicas, and unlike in elastic arteries, consists predominantly of vascular smooth muscle, which gives a greater wall-to-lumen ratio than that of elastic arteries. This thick media is necessary in order maintain the strength of the vessel, which is essential in preventing the collapse of the vessel at sharp bends, e.g. at the knee and elbow. Also, the greater vascular smooth muscle content in the media means that muscular vessels are more responsive than elastic arteries to vasoactive stimulations. An example is the increase in local blood flow during

exercise.

1.4 Endothelium

The endothelium had been long thought only to be a mechanical, passive barrier between the flowing blood and the vascular tissue, due largely to the lack of data available on its intracellular structure. This was challenged by Florey (43) who demonstrated that the endothelium is more than just a"nucleated cellophane" by identifying the cellular features such as caveoli, tight junctions and the basement membrane, and proposed the possible involvement of the endothelium in the initial development of atherosclerosis via altered mass transport and EC separation at the intercellular junctions. This was followed by seminal studies including those by Moncada et al. (96) and Furchgott and Zawadzki (49), the former of which demonstrated that the endogenous inhibitory effect on platelet aggregation is due to the ability of the endothlium to produce PGI_2, and the latter that the presence of the endothelium is essential in acetylcholine (Ach)-induced vascular relaxation. Since then, more of its cellular features and physiological functions have been discovered and the implications of its dysfunction proposed, which will be summarised in the following sections.

1.4.1 Structure

Endothelial cells (ECs), similarly to other eukaryotic cells, consist of the plasma membrane and its contents, cytoplasm. The plasma membrane is the lipid-bilayer membrane that encloses the cytoplasm, which is, in turn, made up of organelle, cytoskeleton, cytosol and nucleus. The relevant cellular features among these are summarised below.

The organelles contained in the ECs are largely identical to those seen in other eukaryotic cells (Fig. 1.4), except that the ECs additionally contain Weibel-Palade bodies, where von Willebrand factor (vWF) and P-selectin are stored. vWF has a role in haemostasis via its binding to sub-endothelial collagen and thus promotes platelet adhesion. P-selectin is another cell adhesion molecule, which under inflammatory stress, migrates to the EC surface and promotes leukocyte recruitment. Another important organelle in the arterial EC is the endoplasmic reticulum (ER), two types of which (rough and smooth) are present in the

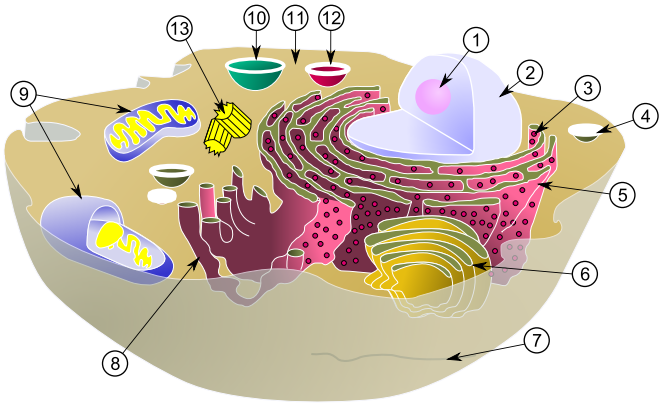

Figure 1.4: Cellular structure of eukaryotic cells. 1- nucleolus, 2- nucleous, 3- ribosome, 4- vesicle, 5- rough endoplasmic reticulum (ER), 6- Golgi apparatus, 7- cytoskeleton, 8- smooth ER, 9- mitochondria, 10- vacuole, 11- cytoplasm, 12- lysosome, 13- centrioles within centrosome. Figure taken from `http://en.wikipedia.org/wiki/Cell_biology` (2).

eukaryotic cells. While rough ER's principal function is to synthesise proteins, smooth ER is mainly involved in lipids and steroids synthesis and carbohydrates metabolism (90) as well as in the regulation of cytosolic Ca^{2+} concentration, which is a major part of endothelial cellular dynamics leading to NO production (the details will be discussed in Chapter 5). In the arterial EC, smooth ER is located within $8nm$ of the plasma membrane (77), which is likely to increase the efficiency of reactions that take place in the vicinity of the membrane, including those involving membrane-bound proteins in NO synthesis.

The endothelial cytoskeleton is the scaffolding protein made up of a large number of actin filaments (or microfilaments), microtubules and intermediate filaments (IFs). Actin filaments, distributed within the cells in bundles and networks, and proteins that connect them to the membrane define the cell shape. IFs are larger in diameter, and provide mechanical support by forming an internal criss-cross network adjacent to the plasma membrane. Microtubules radiate from the single organising centre located at the centre of the cell, and are involved in processes such as mitosis, cytokinesis and vesicular transport as well as providing structural support (80). Cytoskeleton has been observed to be involved in the cellular signalling process, as cytoskeletal elements enable the transmission of the haemodynamics force (particularly WSS) to be transmitted throughout the cell. The cellular processes that are considered to be regulated by this include EC's morphological change after exposure to flow via the re-distribution of actin filaments within the cell, and also the signal transduction of haemodynamic force

into intracellular biochemical signals, in which plasma membrane proteins are thought to be involved (32).

The plasma membrane consists of a lipid-bilayer, two layers of phospholipid molecules that surround the cell. The hydrophilic phosphate heads point outwards to the water on either side and hydrophobic tails point inwards - the presence of this central, hydrophobic layer prevents the water-soluble materials such as ions, glucose and hydrophobic amino acids from entering. What regulates the transport of these molecules and thus to maintain intracellular environment are the membrane transport proteins embedded in the bilayer, which make it selectively permeable so that only the necessary molecules and nutrients can enter. These transport proteins are transmembrane proteins (i.e. it spans the bilayer), and include ion transporters such as Na^+/K^+-ATPase and Ca^{2+}-ATPase.

The cytosol is the major site of cellular metabolism, and contains macromolecules including protein enzymes and ions such as K^+, Na^+ and Ca^{2+} that are required for intracellular signalling.

The plasma membrane encloses the components described above as well as the nucleus where genetic materials (DNA, RNA and proteins) are contained to make up an EC. These ECs are separated by intercellular junctions, of which the structure is not as well understood as for epithelial cells. In epithelial cells, the formation of tight (or occludens) junctions depends on the formation of adherens junctions, which are linked to the actin cytoskeleton in the cytoplasm. In endothelial cells, the proteins associated with tight junctions and adherens junctions have been found, such as occludin with the former and VE (vascular endothelial)-cadherin, which is a transmembrane protein that binds to the VE-cadherin of the adjacent cells, with the latter. Another component present is platelet endothelium cell adhesion molecule (PECAM), which has a role in leukocyte migration. These components form an endothelial intercellular junctional complex, which can be altered dynamically via intracellular messengers. The abluminal surface of the endothelium is tethered to the basement membrane via integrin, a transmembrane protein.

1.4.2 Endothelium in vascular homeostasis

The endothelium is now believed to participate actively in vascular homeostasis. Physiological processes that the endothelium is believed to regulate include the maintenance of vascular tone, inflammation, secretion of anti-haemostasis agents and clotting factors, regulation of blood-tissue exchange, and angiogenesis (77).

The endothelium regulates the tone of the vessel wall and maintains the basal tone (vessel walls are under partial contractile tension in the physiological state) by synthesising and secreting various vasoactive agents. Vasoconstrictors' primary physiological functions are to increase blood pressure and to reduce local blood flow (57). Endogenous vasoconstrictors synthesised in the endothelium include AII and ET-1. AII, synthesised from angiotensin I (AI) by ACE primarily in the pulmonary and renal ECs, primarily works on smaller arteries and arterioles, acting on many of them simultaneously to increase the total peripheral resistance, leading to the elevation of the arterial pressure. ET-1 on the other hand is present in the ECs of all or most blood vessels (57). Its production is stimulated by the damage to the endothelium, so that ET-1-induced local vessel constriction prevents severe blood loss. These vasoconstrictors act not only to increase the vascular tone, but also have pro-atherogenic properties: AII also acts to increase the oxidative stress, and promotes the production of ET-1, in addition to that both AII and ET-1 promote VSMC proliferation (33). Vasodilators on the other hand counteract the vasoconstrictors, and therefore decrease blood pressure and increase local blood flow. The potent endothelium-derived vasodilators include NO and PGI_2. Vasoconstriction takes place via the phosphorylation of myosin induced by the increase in the intracellular Ca^{2+} concentration, and therefore counteracting these (i.e. decrease in intracellular Ca^{2+}) will lead to the relaxation of the VSMCs. PGI_2-induced vasodilation takes place by this mechanism, which is the result of the increased uptake of intracellular Ca^{2+} by the sarcoplasmic reticulum in the VSMC, which in turn depends on the elevated cyclic adenosine monophosphate (cAMP) and protein kinase A (NO-induced pathway is described in 1.2.3).

The inflammatory processes described in Section 1.2.1 are in fact part of the body's normal inflammatory response. The main differences in physiological and atherosclerotic inflammatory processes are that it is the pathogen that activates the tissue macrophages, which subsequently start to phagocyte and recruit more leukocytes from the flowing blood, and that, after the phagocytosing of the

pathogen, the end products of the inflammation such as the necrotic core, dead macrophages and tissue fluid form the mixture called pus, which eventually autolyses over a period of days and will be absorbed into the surrounding tissue (57).

The primary function of haemostasis is to prevent blood loss after injury to the vessel, where it is achieved by vessel constriction, platelet plug formation, blood clot formation, and fibrous tissue growth within the clot to seal the injured site (57). This is an essential process of healing when vascular injury occurs, but given that the blood clot formation is not desirable or necessary in physiological conditions, this is prevented by the anti-thrombogenic (primarily the inhibition of platelet activation, adhesion and aggregation) actions of agents such as NO and PGI_2.

Blood-tissue exchange, which is involved in the majority of the physiological and pathological processes described so far, is controlled via the semi-selective nature of the EC plasma membrane, and regulated by various membrane receptors, ion transporters and intercellular junctional complexes. Finally, the endothelium releases various growth factors such as vascular endothelial growth factor (VEGF) to induce the growth of new blood vessels (angiogenesis), which is essential in processes such as tissue growth, muscle development, wound healing and tumour growth (77).

1.4.3 Endothelial dysfunction

From the descriptions in the previous sections, it is clear that the endothelium plays a vital role in the maintenance of vascular homeostasis via the regulation of the balance between vasoconstrictors and vasodilators, and also via the secretion of anti-inflammatory and anti-thrombogenic agents. Conversely, when the endothelium becomes damaged, diseased or is absent and as a result its functions become impaired, it would create a favourable environment for atherogenesis.

This was demonstrated first by Furchgott and Zawadzki (49) in their *in vitro* experiments using ECs taken from a rabbit's aorta. They observed that Ach, a powerful vasodilator, only produced the expected vasodilation in the presence of the endothelium, and that when the ECs are damaged (due to unintentional rubbing in their case) Ach stimulation resulted in vasoconstriction. The direct evidence of the involvement of endothelial dysfunction in early atherosclerosis

was demonstrated and summarised by Davignon and Ganz (33), who stated that impaired production or activity of NO leads to endothelial dysfunction which is manifested in the form of impaired endothelium-dependent vasodilation. This was demonstrated first by observing that asymmetric dimethylarginine (ADMA) inhibited NO, and that elevated concentration of ADMA has been correlated with endothelial dysfunction and atherosclerosis. The presence of endothelial dysfunction was quantified by monitoring the endothelium-derived vasodilation when stimulated by Ach and WSS. When Ach was used as a stimulant, the endothelium-dependent vasodilation would be predominant in healthy arteries while vasoconstriction predominant in the presence of endothelial damage. In the latter case the increase in flow (i.e. WSS) was used as a stimulant, observing if reactive hyperaemia (increase in blood flow in response to vessel occlusion-induced shortage of oxygen and accumulation of metabolic waste) resulted in NO synthesis and the resulting phenomenon termed flow-mediated dilation (FMD). The results showed the presence of endothelial dysfunction at pre-clinical stages of atherosclerosis.

From these observations, the implication that the endothelial dysfunction as a result of impaired local NO activity is associated with the pathogenesis of atherosclerosis is very strong. This has been further supported by the studies using other markers of future athero-thrombotic events such as C-reactive protein (42). However, the mechanisms that leads to the diminished NO activity itself has not yet been fully understood.

1.5 Concluding remarks

Contrary to the past belief that atherosclerosis is simply a disease of abnormal lipid metabolism and accumulation, it has emerged that it is a complex disease, of which initiation and development involve a combination of physiological (such as inflammation and haemostasis) and pathological (risk factors) processes. The endothelium is not only a mechanical barrier but also plays a significant role, as a host site for the synthesis and reactions of vasoactive agents, inflammation and lipid metabolism. Advances in atherosclerosis research to date point to that endothelial dysfunction caused by the impaired NO production, which is manifested by the absence of endothelium-dependent vasodilation, is involved in the early stage of clinical atherosclerosis. However, atherosclerosis is a geometrically

focal disease, and the reason behind the focal occurrence of impaired NO production has not yet been fully understood. Given that the many of the components that are considered to be involved in atherosclerosis are systemic in nature, understanding the mechanisms of this localisation would greatly contribute to the understanding of atherogenesis.

Chapter 2

Literature Review

2.1 Introduction

Atherosclerosis has been under extensive research for the past several decades, and until recently it has been considered that the principal cause of its initiation is a high plasma concentration of cholesterol LDL. Despite advances in research and medicine, the precise mechanisms of its initiation and progression have not been fully understood. However, what has been accepted is that both are the consequences of many physiological factors.

Among these physiological factors, the main components involved in this research are local blood flow, endothelial cell dynamics, EC membrane cell mechanics and nitric oxide, which are all parts of coordinated physiological phenomena *in vivo* that lead to the modelling of endothelial NO, the main parameter selected in the present research to study. This chapter analyses and summarises the previous studies of individual processes and their roles in relation to atherosclerosis. The aim of the current research is then presented based on the findings gained from the analyses.

2.2 Carotid artery haemodynamics

Haemodynamics in atherosclerosis has been studied extensively by many groups previously, both numerically and experimentally, since it had been acknowledged that haemodynamics plays an important role in atherosclerosis. There are two

primary haemodynamic parameters of interest here - wall shear stress (WSS) and stress phase angle (SPA).

2.2.1 Wall shear stress (WSS)

Wall shear stress (WSS) is one of the most significant and most studied parameters in atherosclerosis research. WSS is the tangential force that acts on the endothelial surface, induced by the blood flow. This local shearing force is determined based on the near-wall velocity gradients at that point, and therefore is the parameter that quantifies the features of the local vascular geometry. Prior to the emergence of WSS, despite that the focal nature of atherosclerosis had been noted, the primary focus of research had been on reproducing atherosclerosis in animals or observing the effects of individual risk factors, such as old age, high plasma lipid concentration, alcohol consumption or smoking on the progression of atherosclerosis, and as a result the investigation of the causes behind atherogenesis itself or plaques' preferential occurrence at particular sites had been somewhat unexplored.

One of the first groups to focus on the potential involvement of WSS in atherogenesis was Fry (46), who proposed that atherogenesis was associated with high WSS, which gives rise to increased particle (e.g. serum lipids) fluxes and increased affinity of the EC surface to blood elements due to the morphological change of EC surface and cell erosions. This observation came to form one of the major hypotheses on the roles of WSS in atherogenesis; that the formation of early plaques is the result of mechanical damage and increased lipid deposition caused by high WSS. This hypothesis, however, was dismissed by Caro et al. (22) on the grounds that the required level of WSS needed to cause the mechanical damage observed in Fry's study (46) was more than that that typically occurs *in vivo*. Additionally the sites of high WSS were not coincident with those of plaque formation. They instead proposed that, via the theoretical analysis of shear-dependent mass transport, the distribution of atheroma was associated more with low WSS, although at that time the understanding of the consequence of low WSS was still limited to the behaviour of lipids. The two studies above became cornerstones in atherosclerosis research in that they shed light on the potential roles played by WSS in the focality of atherosclerosis, and numerous, both experimental and numerical studies have been carried out in an attempt to elucidate the mechanisms of atherogenesis and its preferential occurrence.

The first of the experimental work relevant to the present research, which is primarily concerned with carotid artery atherosclerosis, was the steady-flow study by Zarins et al. (142) carried out using a Y-shaped CAB geometry. This study demonstrated that the distribution of asymptomatic plaques within the carotid sinus was thinnest on the inner wall, moderate on the side walls and thickest on the outer wall. This qualitatively coincided with local WSS distribution, which was high, moderate and low respectively at each locations. Additionally, it was quantitatively shown that WSS was low on the outer wall of the sinus, independent of the Reynolds number. They also demonstrated what are now well-acknowledged flow features, such as skewed velocity profiles, flow separation and reattachment and helicoidal flow structure in the sinus, as well as the slow clearance of dye particles in the outer region of the sinus. Similar observations had been recorded also by Bharadvaj et al. (11; 12).

Subsequent experimental studies progressed in such a way that the experimental conditions utilised became closer to those *in vivo* not only with advances in measurement and model manufacturing techniques themselves but also with introduction of additional flow haemodynamic parameters for further analysis. Ku et al. (68) conducted a pulsatile flow study using a Y-shaped CAB geometry (which had become a standard model in CAB flow studies), in order to investigate whether the transient behaviour of the flow field and WSS had major influences on the pathogenesis of atherosclerosis. The new findings in their study were the continuous variation of separation region, the possible occurrence of turbulence at the end of systole, the variation in size and energy level of vortices, and most importantly, WSS vectors' variations in both magnitude and direction. In particular, they observed that in the small region between the CCA and the distal sinus, there was a region where the flow separation line moves upstream and downstream during each cycle. From this, they deduced that, if this change in direction of WSS is what is associated with early atheroma formation, then this area over the distal CCA and proximal sinus would be where the plaque would initially develop. On the other hand, if atherogenesis is more associated with permanently low WSS magnitude or long clearance time of particles, then the initial formation would be observed in the mid- to distal part of the sinus.

Meanwhile, numerical modelling was recognised as a promising tool and has been used extensively alongside experiments in the past couple of decades. Earlier work was primarily concerned with reproducing experimental flow conditions and validating the previous observations (106). Subsequently however, it moved

relatively quickly on to modelling more complex, physiological flows thanks to progress in mesh generation techniques, increased accessibility to realistic geometries and importantly, flexibility in setting and modifying boundary conditions. In particular, the latter has not only allowed for incorporating *in vivo* conditions such as cardiac waveform at the inlet, but also made the investigation of haemodynamic behaviour in various conditions (e.g. at different Reynolds numbers representing different time-points during a cardiac cycle) considerably easier. Examples of complex flow modelling include those on carotid haemodynamics with stenosis (123), nonplanar geometry (129; 145), varying arterial geometries (141; 143) or compliant model walls (63; 105; 145).

The main relevant findings from these studies are that the resulting flow field was highly variable and depended very strongly on the individual geometry. In non-planar models, both axial and secondary flow structures (and therefore WSS) showed considerable departure from those in averaged models due to in- and out-of-plane curvatures of both CCA and ICA (129; 145). A point to note here is that the flow field observed also reflected the highly individual nature of physiological vascular geometries, which were often obtained via medical imaging techniques such as MRI and were therefore patient-specific (PS), which inevitably introduced different dimensions and shapes in all parts of the CAB. The results from compliant models on the other hand implied that the effects of wall distensibility on the haemodynamics parameters of interest was relatively minor - the maximum difference in the stress field of up to 25% was observed during systole, but only in the close proximity of the bifurcation apex. The lower WSS obtained is likely to be the result of the slight expansion of the geometry during the systolic phase, causing the flow to decelerate (141), which confirmed the previous observations (105; 145).

Although these studies have contributed greatly in promoting the understanding of physiologically-occurring flow phenomena, however, in the context of this study it is essential that the flow characteristics observed were compared concurrently against the wall thickness or plaque distribution data *in vivo* in order to gain insights into the influence of local blood flow on plaque formation. Studies of this kind had been scarce, until that carried out by Steinman et al. (122). Using phase-contrast MRI, the wall thickness (WT) of two reconstructed PS-CAB geometries was measured as representative of atherosclerotic burden and compared against WSS and OSI fields obtained in CFD simulations. One of the two subjects studied showed early atherosclerosis and the other no apparent ar-

terial disease. Qualitative relationship was observed between increased WT and both wall parameters in the sinus region, and that between elevated WSS and relatively small WT in the distal ICA. Elsewhere in the bifurcation however, low and oscillating shear were not found to have significant association with increased WT. This was also quantitatively demonstrated with scatter plots of WT, WSS and OSI from the data obtained at each node on the mesh surface of the entire geometry. They listed limitations of their method as potential error sources (e.g. precision of contour extraction and resulting uncertainties in WSS, quality of the original data set, discrepancies of CFD modelling from the conditions *in vivo*), although the velocity contours obtained from CFD and MRI showed good agreement. Despite these inconclusive results however, this point-by-point comparison of haemodynamics parameters and plaque distributions is a promising approach in elucidating atherogenesis mechanisms.

2.2.2 Pulsatile pressure

While WSS and other wall-shear parameters remain the most-studied haemodynamic factors, their precise roles in atherosclerosis have yet to be established. Although it now seems now certain that WSS is associated with plaque localisation to some extent, the correlation between the location of plaques and wall-shear parameters alone is still inconclusive when it is studied using PS geometries and the resulting data compared on point-by-point basis (122). Additionally, Joshi et al. (62) carried out another point-by-point comparison of post-mortem measurements of intimal thickness and numerically-computed WSS in four patient-specific coronary artery geometries, motivated by the lack of such studies in the past, and if the correlation should exit, it should be statistically significant. However, their results showed no consistent relationship between intimal thickness and WSS magnitude.

In an attempt to explain this departure from the conventional theory (and also to study its own potential atherogenicity), Tarbell's group proposed stress phase angle (SPA), defined as the temporal phase angle difference between pressure (which is considered to be in phase with vessel diameter for elastic vessels) and WSS (29; 30; 124; 125). SPA so far has been studied in two ways:

1. As a parameter that affects the production and attenuation of atherogenic and atheroprotective substances

2. As a novel parameter that represents the *in vivo* haemodynamic conditions more closely than wall-shear parameters alone.

The former approach demonstrated that highly negative SPA led to the reduction in atheroprotective substances (NO, prostacyclin (PGI_2)) and increase in atherogenic substance (ET-1). Ziegler et al. (146) also observed similar effects of pulsatile pressure on EC cellular processes, noting that the inclusion of the effects of pulsatile pressure altered the expression of ET-1 and eNOS messenger ribonucleic acid (mRNA).

The latter approach was used in Tada et al.'s (125) work, in which they showed that on the CAB outer wall, which is a well-establish site for plaque localisation, WSS was low, OSI high and SPA more negative, whereas in coronary arteries, another well-known site for plaque formation, WSS is not particularly low and OSI not particularly high, but SPA was highly negative. They therefore proposed that SPA was potentially a more accurate and versatile haemodynamics parameter. These findings imply that SPA is a relevant and promising haemodynamic parameter, though clearly more studies need to be carried out to establish its accuracy and usefulness in atherosclerosis research.

2.3 Endothelial cell dynamics

The numerical modelling of cellular dynamics in the ECs in relation to atherosclerosis has been a relatively recent development. As it has been observed that the binding of cytosolic Ca^{2+} to calmodulin triggers a series of reactions leading to NO production (21), the EC signalling models that have been developed are based on previous studies of endothelial Ca^{2+} dynamics. Wiesner et al. (136) developed a detailed model, in order to parametrically study the time-course of cytosolic Ca^{2+} within the cell including the influx, efflux, release, resequestration, and buffering of Ca^{2+}, which in turn depended on the input concentration and active state of the ligand thrombin (the flow-induced influx of Ca^{2+} was included in this model, but only as a lumped parameter together with the agonist-induced influx as this phenomenon was not well-understood at that time). The general finding from their "base model" was that, after a step increase in the agonist concentration, the cytosolic Ca^{2+} became depleted due to both ion exchangers on the ER whilst the EC plasma membrane was likely to compete for the cytosolic Ca^{2+}, and therefore the ER Ca^{2+}-ATPase would not be able to resequest

sufficient Ca^{2+} back into the ER. This is not surprising, however, given that this base model did not include CCE or WSS-induced Ca^{2+} influx, which are known to maintain more sustained level of cytosolic Ca^{2+}.

A more important aspect of this study, was that it provided the basis for their later study (137), in which the previous model was expanded so that the external stimuli (agonist and WSS) that had been represented with a lumped constant were now expressed by functions of position within the flow chamber. In this study, the surface concentration of the agonist was determined via the solution of the advection-diffusion equation at the endothelial surface, and WSS via the analytical steady-state representation of the velocity profile for a straight duct which is a function of position and flow rate. Due to the geometry used in their study being a 2D parallel flow chamber, and the resulting WSS being represented with a single value for all wall surface for a given flow rate however, the WSS variable in the model was used only to parametrically test the effects of different WSS values on the time-course of the cytosolic Ca^{2+} concentration.

Agonist and WSS being functions of space was to have more important implications for the future studies of EC dynamics, since the model was now capable of computing Ca^{2+} influx in each wall cell taking local, spatially varying values of agonist and WSS as inputs both in 2D and 3D, given that they are computed in advance. An additional new aspect of this particular model is the inclusion of a new Ca^{2+} influx pathway, which is dependent on the local WSS. Axial WSS stretches the EC membrane surface, and the membrane strain energy (SE) induced by the stretch then regulates the fraction of open ion channels in the membrane and subsequently the influx of extracellular Ca^{2+} into the cytosol. This is another factor that would result in the geometry-induced variations of the input parameter.

Plank et al.'s (108) numerical EC signalling model was developed taking advantage of this outcome. In addition to the single-cell analysis of endothelial Ca^{2+} dynamics, they demonstrated a coupled model of species transport and Ca^{2+} EC Ca^{2+} signalling. A backward-facing step 2D geometry was used in order to provide the model with the irregular, spatially-varying agonist (ATP) and WSS fields (which are the results of flow phenomena such as flow separation, reattachment and recirculation) as inputs. In this model, the agonist concentration was again determined via the species balance represented by the advection-diffusion equation, and WSS with the analytical solution obtained from a known velocity

field (31). The main finding from this paper was that differences in intracellular behaviour were observed between the regions of disturbed flow and those away from it. In particular, the cytosolic Ca^{2+} was observed to be low in the recirculation zones adjacent to the step, which was attributed to the reduced amount of external stimuli (WSS and ATP) in the same region. Based on these results, they proposed that the spatially differential signalling behaviour might have an implication in atherogenesis, given that eNOS activation and NO productions are the downstream consequences of EC Ca^{2+} signalling, and therefore low Ca^{2+} signalling in the ECs caused by low WSS might explain the correlation of atherosclerosis and low WSS observed previously.

Plank et al.'s model, which at this point was capable of computing the EC cytosolic Ca^{2+} based on the local values of external stimuli, was further extended by Comerford et al. (27). The first of the advancements from the previous work is that this study was conducted using 3D geometry, which made possible to obtain full, time-dependent 3D WSS and agonist maps that represent the spatial features of the geometry via the solutions of flow and species equations. Secondly, the existing EC model was further developed to include the downstream reactions of Ca^{2+} signalling relevant in atherosclerosis, i.e. eNOS activation. eNOS is an enzyme that catalyses NO synthesis, of which activation is triggered by the increased cytosolic Ca^{2+} (induced by the agonist, as modelled above (108)) binding to the protein calmodulin and this complex subsequently replacing caveolin on the eNOS molecule. The agonist-independent influx pathway of extracellular Ca^{2+}, which depends on the WSS-induced membrane stretch was also included as previously mentioned, as well as the direct activation pathway by WSS which is, unlike the previous two, independent of the increase of the cytosolic Ca^{2+}. Their results showed that the sites of low WSS and low eNOS largely coincide, implying a correlation between the two phenomena. This supports the hypothesis made above by Plank et al. (108) that low external stimuli leads to impaired EC signalling and thus to atherosclerosis, although Comerford et al.'s results imply that, of the two stimuli, WSS is the predominant factor in eNOS activation.

2.4 Nitric oxide (NO)

NO was identified in the 1980s as the primary identity or ready source of endothelium-derived relaxing factor (EDRF), which was observed to have va-

sodilatory effects and inhibit platelet adhesion and aggregation (55; 97). NO was found additionally to suppress VSMC proliferation and migration (115), and protect against the recruitment of leukocytes and their subsequent interactions with the endothelium (34; 78). As described in Chapter 1, these processes have been involved in the pathophygiology of atherosclerosis, and therefore it is easily deducible that reduced availability of NO in the vascular wall is likely to have atherogenic influence. However, despite that its importance has been well-documented in the literature, there still is much to be understood about its precise properties and functions *in vivo* due to its relatively recent discovery and difficulty in obtaining in experimental data because of its high reactivity and short half-life. Among those are NO's convective and diffusive transport mechanisms, physiological concentrations, production and degradation rate reaction constants, of which the latter two are of primary relevance here.

2.4.1 Experimental studies

Obtaining accurate direct measurements of physiological NO concentrations *in vivo* are in general extremely difficult due to NO's short half-life (the order of seconds) and high reactivity, and due additionally to the inevitably invasive nature of the procedure even when the other challenges are overcome. Therefore, most experimental studies concerning the production and/or diffusion of NO have been carried out *in situ* and/or *in silico*, consequently in simplified but more controlled conditions. One of the first seminal works was carried out by Malinski et al. (84), in which porphyrinic sensors were used to detect and measure the release of NO from the cells taken from the wall of the thoracic aorta of rabbits. They carried out the measurements of maximum NO concentrations on the EC surface as well as in the VSMC, along with the diffusion time ($1.30\pm0.05\mu M$ after $13.3\pm0.1s$ and $0.85\mu M$ after $20.2\pm0.1s$, respectively). The diffusion coefficient of NO at the physiological temperature was also measured ($3.30\times10^{-9}m^2s^{-1}$).

The important outcome of this study was that these values obtained, and the diffusion process of NO in the VSMC which they demonstrated via the solution of Fick's diffusion equation, came to provide the initial and control values for parameter estimations in later numerical studies. The maximum NO concentration on the EC surface of $1.30\mu M$ was also used in the simulations in this thesis as the representative value of physiological NO concentration while determining NO's degradation rate constant. Although the stimulus used in Malinski's (84)

study was $10nM$ of bradykinin, which differs in both kind and amount from that used in this study, this approximation was deemed necessary due to the lack of data on physiological NO concentrations at that time of modelling (details will be discussed in Chapter 5).

This experimental approach using similar sensors has been used by many others (5; 60; 101), due to that the negatively-charged Nafion coating on the sensor is highly permeable to NO but not to its degraded product NO_2^-, allowing the accurate detection only of NO on the surface of the sensors. Of particular interest is Oemar et al.'s (101) work, in which the NO release rates and its peak concentrations were measured in human specimens, healthy internal mammary artery and atherosclerotic carotid artery, after stimulation with A23187, a Ca^{2+}-mobilising ionophore. As expected, both the release rate and peak concentration were considerably lower in the diseased artery at $0.08\pm0.04\mu Ms^{-1}$ and $0.1\pm0.03\mu M$ respectively compared to $0.42\pm0.05\mu Ms^{-1}$ and $0.9\pm0.09\mu M$ in the healthy artery. They also observed that in the diseased artery the expression of eNOS was also reduced. Along with the observation that eNOS expression was increased in animal models despite impaired endothelium-dependent relaxation, they proposed that eNOS expression and NO release may be normal or increased in early lesions whereas reduced in more advanced lesions. This observation should be acknowledged with caution, however, given that the lesion in the diseased artery specimen used in their study was already in relatively advanced stage, and therefore if the phenomena observed for eNOS expression and NO release would still hold in atherogenesis is uncertain. The most recent development was Andrews et al.'s study (5), in which the measurements were carried out under shear, which showed biphasic increase in NO production rate. Overall, however, the values of rates and concentrations of NO observed in these studies varied greatly, due likely to the variations in experimental conditions, kind and extent of stimuli used and species from which the cells were obtained. Also, these observations have been possible only for a single or a small number of cells due to the nature of measurements with sensors.

The inherent disadvantages of these experimental studies are that the measurements can be recorded only at a few, discrete points where sensors are located. Also, even with the recent advances, the experimental conditions and nature of stimuli used are still not sufficient to represent physiological conditions (for example, the step increases in WSS (from 0.01 to 0.6, 1 and $2Pa$) used by Andrews et al. (5) as stimuli were sufficient to observe the NO response to the particular

values of WSS, but do not represent the flow conditions that are likely to be taking place *in vivo*).

Additionally, as stated above, the values of production rate constants or concentrations are not directly applicable to contiditions *in vivo* in humans due to the variable response to stimuli between animal models and humans. This simplification is, however, a necessary one since *in vivo* measurements in humans are not currently feasible due to their invasive nature. These experimental approaches are however essential in observing actual, overall cellular responses to specific stimuli, which is crucial in validating simulated results but cannot be observed numerically.

2.4.2 Numerical studies

In the research of physiological NO, the primary focus has been on the investigation of its production, reaction (i.e. degradation) and transport mechanisms. While the main aims and capacities of experimental studies had been to physically measure the production rate, diffusion distance and time, and therefore to determine NO's physiological properties, numerical approaches in the NO research have been primarily used for more comprehensive modelling of NO dynamics in more physiologically feasible settings, which is often not practical or currently possible to be implemented experimentally.

As stated above, one of the most significant advantages of numerical approaches are their flexibility in varying material properties or boundary conditions, enabling the behaviour of variables to be observed under different conditions. The early study by Malinski et al. (84), referred to above, involved numerically simulating the concentration profiles of NO in the VSMC after it was released from the point source on the EC surface. The concentration profiles were obtained by computationally solving the Fick's diffusion equation for different diffusion times, using the maximum NO concentration on the EC surface obtained experimentally as the initial condition. The resulting concentration profiles demonstrated the now well-accepted phenomenon of diffusion that the steeper the concentration gradient the higher the diffusion speed. What was also found from this computation was that there was a time delay for the measured NO diffusion time compared to the theoretical one, which indicated the NO in the VSMC being deactivated or reacting with other agents in the tissue. Their

calculation of NO's permeability through the membrane also showed that, due to its propagation being slower in aqueous solution inside and outside the EC, NO would tend to be concentrated in the EC membrane, which would maintain the high concentration gradient and therefore facilitate its diffusion to the VSMC.

Vaughn et al.'s (132) study is one of the more recent studies that implemented more physiological NO dynamics, in which they modelled NO's production on the EC surface and its subsequent diffusion into and reaction within the lumen and surrounding tissue (endothelium and VSMC). A mathematical model was used to estimate the NO production and degradation rates, for which the species balance equation was solved for all three regions (luminal, endothelium and abluminal) assuming different diffusion coefficients and reaction rates in each region. While in Malinski's (84) study the source of NO production was a single point, Vaughn et al. (132) assumed an ellipsoidal shape for an NO producing-source as its effects on the total production rate were deemed important in realistic prediction of NO diffusion. The simulated NO concentration in this model replicated the maximum NO concentration observed experimentally in Malinski's (84) study well, giving approximately $1.5\mu M$ in the endothelium and $0.8\mu M$ in the smooth muscle. The actual production rate obtained (which was assumed constant in their study), $6.8\times10^{-14}\mu mol \cdot \mu m^{-1}s^{-1}$, varied significantly from the values obtained numerically in the previous studies (72; 138) due to the differences in the modelling assumptions and boundary conditions (e.g. the shape of NO-producing source being a point or infinite disc, or the production of NO being catalysed by eNOS or inducible NOS (iNOS)). As for the estimated NO degradation rate constant in the tissue ($2.0\times10^{-3}\mu M^{-1}s^{-1}$, the direct comparison with the values previously obtained was even more difficult, either experimentally or numerically: the former due to reaction and diffusion in the tissue not distinguished as the cause of NO decay in experiments, and the latter due again to the geometry of the source and the time scale used. In addition, as in the production rate estimation, most experimental studies were carried out without the diffusion into, and reaction in, the lumen considered. The outcome that was likely to be considered significant is that the results supported the observation made previously by Wood and Garthwaite (138) that the reaction rate of NO is relatively insignificant near the source of the NO when the time scale is short, and therefore it was proposed that steady-state simulations are likely to be more suitable for the accurate prediction of reaction rate constants.

While Vaughn's study above shed light on NO's behaviour and properties in

physiological conditions, their computation of the NO production rate did not take into account the components of the cellular processes leading up to the NO production. In the modelling process, the involvement of eNOS was only included as the basis for approximating the NO synthesis as surface reaction, due to the majority of eNOS being membrane-bound, and therefore the eNOS's activity as a catalytic enzyme or its effects on the production rate of NO were not considered. This makes the estimation of the rate constant for eNOS-induced NO production needed in the current thesis not feasible.

This was partly addressed in the detailed, more comprehensive, biochemical modelling of endothelial NO dynamics carried out by Chen and Popel (24). *In vivo*, NO is synthesised from the substrates L-arginine, oxygen (O^2) and nicotinamide adenine dinucleotide phosphate (NADPH), catalysed by eNOS in the presence of the coenzymes flavin mononucleotide (FMN), flavin adenine dinucleotide (FAD) and tetrahydrobiopterin (BH_4). This reaction was described by a set of coupled ODEs, each of which characterised either the time-course of the substrates, intermediate reaction complexes or NO in the reaction cycle, using the experimentally-observed values for arterioles and venules as the initial conditions. All substrates and coenzymes were assumed to be available in abundance. The initial concentrations of eNOS used were taken from the previous studies (4; 58; 74), 0.015-0.045μM in arterioles and 0.008-0.097μM in venules, the ranges of which came from the variation of cell sources (human umbilical vein, dog aorta or arterioles). The results showed that, as was also the case for Vaughn et al.'s study, the values of NO production rate obtained here (0.010-0.095μM) varied considerably from those obtained previously. The likeliest source for the variation proposed by the authors was the heterogeneity of eNOS expression among the ECs taken from different vessels. It was demonstrated that increasing the concentration of the substrates did not lead to the increase in NO production rate. However, NO production was linearly dependent on the eNOS concentration in the EC, and therefore the difference in the eNOS distribution or activity could influence the NO production rate considerably.

Establishing that NO production was linearly dependent on the intracellular eNOS concentration was particularly significant in relation to the EC dynamics modelling in this research, since it would allow the derivation of the production rate constant from the NO production data obtained for different eNOS concentrations. Together with that eNOS-catalysed NO production is a first-order reaction, it enables the NO production to be estimated provided that eNOS con-

centration is known.

2.5 Summary

The major components of atherosclerosis research mentioned in the previous sections can be categorised as follows:

1. Fluid dynamics studies in which the impact of incorporating physiologically realistic flow conditions or wall properties on the flow field is investigated (105; 107)

2. Combined fluid dynamics and clinical studies, with an experimental and/or numerical focus on the distribution pattern match between intimal thickening and WSS or other wall-shear parameters (38; 69; 122; 142)

3. Biochemical studies, in which the kinetics of one particular kind of molecule or substance (such as Ca^{2+}, eNOS and NO) is studied in detail, often utilising single-cell models (24; 37; 84; 98)

4. Cellular dynamics studies, in which the behaviour of ECs themselves and related quantities is investigated in response to various haemodynamic stimuli (13; 30; 61; 75; 124; 137)

5. Integrated fluid-cellular dynamics studies, in which the activities and/or concentrations of relevant substances (e.g. Ca^{2+}, eNOS, NO) are investigated utilising mathematical models that take WSS as an input (27; 108)

Each of the first four groups is an essential part of atherosclerosis research, and the advances in experimental or numerical modelling techniques have allowed for the use, in each discipline, of increasingly physiologically accurate conditions. For example, many of the recent fluid dynamics studies were carried out using patient-specific carotid artery geometries obtained directly by MRI (81; 122) as opposed to a population-averaged model. The patient-specific approach enabled the intimal thickness and wall-shear parameters calculated based on the full 3D velocity map to be investigated. In another stream of fluid dynamics studies on the other hand, numerical studies were conducted under physiologically realistic conditions (e.g. flow pulsatility, non-Newtonian assumption and wall compliance) (105; 107). Meanwhile, Chen et al.'s (24) recent numerical model of eNOS

and NO dynamics included the kinetics of most major substrates, cofactors and intermediate products involved in the NO production reaction.

However, although atherosclerosis appears to be the consequence of inter-related biochemical and haemodynamic processes, the scope and advances of these studies so far have tended to remain within their respective disciplines, and therefore the knowledge obtained is still somewhat fragmented. For instance, the correlation between haemodynamic parameters and intimal thickness has been a strongly-supported hypothesis that has come out of fluid-dynamics studies. However, despite this approach accounting for the spatially varying characteristic of atherosclerosis by using full 3D map of the velocity field, the results obtained do not have any implications in relation to the intermediate mechanisms between flow and plaque initiation since the parameters observed in the process are flow velocities and wall thickness only. In Perktold et al's flow studies (105; 107), the results obtained from their physiologically realistic flow models were not interpreted in terms of what influences the altered flow field might have in atherosclerosis. On the other hand, ATP transport, Ca^{2+} dynamics, eNOS activation and NO production have been often studied using single-cell models, in which varying values of inputs such as WSS and substrates are used and therefore the results obtained would still be relevant. However this approach does not allow for the simultaneous observation of the large-scale cell responses that reflect the spatial variation of the vessel geometry, and therefore these results alone are neither sufficient nor suitable in observing what implications those cellular responses might have in the localisation of atherosclerotic plaques. Chen et al's eNOS-NO model mentioned above (24) did not explicitly include the pathway that represents direct activation of eNOS, although it had been observed to have a significant factor (37).

Plank et al.'s (108) comprehensive study was, to the author's best knowledge, one of the first publications in which these separate research disciplines were brought together in order to investigate the role that spatially-varying WSS plays in the localisation of atherosclerosis. In their study, using a 2D model of a backward-facing step, dynamics of the cytosolic Ca^{2+}, stored Ca^{2+} in the ER and IP_3 in the endothelium were calculated using a mathematical model that took a known profile of WSS and the agonist concentration profile determined from the solution of the advection-diffusion equation, using the biochemical reaction parameters determined in previous publications. The primary observation resulting from this study was that the ATP concentration was lowest in the region of low WSS since, in the areas of low WSS (i.e. flow velocity), the ATP release

from the endothelium tended to be diffusion-limited, and that this resulted in the endothelial Ca^{2+} signalling being low in these regions. Based on these findings, they proposed that the differential behaviour of intracellular signalling as a result of spatially varying WSS distribution might be a contributing factor to the localisation of atherosclerosis in the regions of disturbed flow. Comerford et al. (27) further advanced this model in two aspects: they introduced the activation of eNOS into the existing model, which is the downstream reaction of the IP_3 generation, and applied it to 3D geometries. Their results that the eNOS signalling was low in the regions of low WSS appeared to support the hypothesis made by Plank et al. (108) above and therefore implied that these regions would be susceptible to the endothelial dysfunction and consequently atherosclerosis.

2.6 Research aim

As stated previously, the carotid arteries (the carotid sinus in particular) are one of the sites of frequent plaque localisation. The most supported hypothesis at present to explain this phenomenon is that plaques localise as a result of the influence of the local haemodynamics, which exhibits considerable spatial variation along the vasculature reflecting the local vascular geometry.

Additionally it has been observed that a defect in the production and/or activity of nitric oxide (NO) leads to endothelial dysfunction characterised by impaired endothelium-dependent vasodilation, leading to the development of atherosclerosis (33; 82).

What could be postulated from these two observations is that the bioavailability and activity of NO was likely to be low in the carotid artery bifurcation which has been known to be particularly prone to plaque formation (36), and that there were spatial/geometrical factors involved in the process that eventually lead to low NO level. Since the spatial characteristics of local geometry are reflected on the endothelium (and underlying cellular processes) in the form of wall shear stress (WSS), WSS was postulated to play a significant role in the processes that result in the diminished local level of NO in these regions and consequent plaque initiation.

However, as it is clear from the literature reviewed and its summary above, a model that allows for the detailed investigation of such postulate is still lacking,

and therefore the aim of this research is to develop a numerical model that is capable of computing the endothelial NO concentration incorporating physiologically realistic stimuli and boundary conditions. This is to be achieved by the addition of NO dynamics modelling to the existing cell dynamics models (27; 108) then applying it to the 3D model geometry of the carotid artery bifurcation. This process is first to be carried out as a direct extension of the previous studies in which a steady-flow regime and uniaxial stress field (in the streamwise direction only) was assumed (27; 108). The model is then to be extended to include the effects of physiologically more realistic conditions on the relevant cellular processes and therefore run under pulsatile, biaxial stress field (both in streamwise and circumferential directions) assumption, which will provide the results that will be a step towards a comprehensive modelling and understanding of atherogenesis mechanisms.

2.7 Concluding remarks

Atherosclerosis is a disease that involves many factors in its pathogenesis and development, and those factors have been researched extensively in many academic disciplines. It is still true that factors such as WSS, blood cholesterol and NO are involved and play significant roles, and there has been much contribution to the understanding of atherosclerosis from fluid dynamics, medicine, biochemistry and genetics to name a few.

From haemodynamics studies, both experimental and numerical, there have been very strong implications of the correlation between low WSS and plaque localisation. There also is an emerging, additional haemodynamic mechanism which is the interaction of WSS and pulsatile pressure, that has been implicated as an influential factor. So far, studies of EC dynamics have been mostly numerical due to the complex nature of the modelling involved which is not currently feasible to be implemented in experiments. The results obtained have been implying strong influences of WSS in EC signalling and subsequent endothelial dysfunction. Experimental studies of NO have shed light on NO's functions and diffusive behaviour, while numerical studies have recently moved on to physiologically more complex, plausible modelling of NO dynamics within with the substrate and enzyme kinetics included.

However, so far these studies have tended to be carried out separately within

each discipline, particularly in biochemistry and fluid dynamics. Given that many pathophysiological processes are interrelated, what is now important is to formulate an NO dynamics model that integrates the processes involved and apply it to physiologically realistic geometries, which is the focus of the current study.

Chapter 3

Governing Equations

3.1 Introduction

As described in the previous sections, atherosclerosis develops in the environment where numerous interacting physiological processes are at work. One of the primary driving forces of these processes is the transport of blood and its component species. In this chapter, the governing equations of both fluid dynamics and mass transport are described based on the Reynolds transport theorem (derived in Appendix A.1), along with important considerations which have to be taken into account in the modelling of arterial blood flow, and important dimensionless quantities.

3.2 Fluid dynamics

Fluid dynamics plays a vital role in the physiological and pathological processes involved in atherosclerosis, many of which are regulated by haemodynamic forces exerted on the vessel wall and its influences on mass transport. It is of central importance to understand the principles of fluid dynamic phenomena and the conditions in which they are applied. This section presents the governing equations of fluid dynamics and the considerations that had to be taken into account in the modelling of arterial blood flow.

3.2.1 Assumptions in blood flow modelling

There were several assumptions that needed to be made in using fluid dynamic approach in studying blood flow.

Firstly, in the present study, blood is assumed to be an incompressible, Newtonian fluid. This assumption is deemed reasonable since, due to the high bulk modulus of water (K_{H_2O}=2.2GPa), the density change of water caused by the pressure difference typically observed in the human body is negligible. The typical net energy difference between the dorsalis pedis artery on the upper surface of the foot and the aorta (ΔP) is approximately $2mmHg$ (77), which is equivalent to 266.645Pa. Assuming the blood density of $1000kgm^{-3}$ in the dorsalis pedis artery ($\rho_{dorsalis}$) and constant body temperature, the blood density in the aorta (ρ_{aorta}) can then be determined from the following expression:

$$\rho_{aorta} = \frac{\rho_{dorsalis}}{1 - \frac{\Delta P}{K_{H_2O}}} \tag{3.1}$$

This gives the value of ρ_{aorta}=$1000.0001212kgm^{-3}$ i.e. the density variation of 0.00001212%, which was deemed sufficiently small to be considered insignificant and thus the plasma component of blood can be assumed incompressible. The rest of the whole blood is made up of the blood cells, which also have been reported to be unaffected by the pressure difference (47).

In order to discuss the assumption on the viscous properties of blood, definition of wall shear parameters should be introduced. Wall shear rate (WSR, $\dot{\gamma}$) is a spatial near-wall gradient normal to the wall of the streamwise flow velocity u, i.e.:

$$\dot{\gamma} = \left.\frac{\partial u}{\partial \eta}\right|_{\eta=0} \tag{3.2}$$

For Newtonian fluid, viscosity is the proportionality constant that characterises the fluid's resistance to flow due to friction. WSR multiplied by the dynamic viscosity μ then defines the tangential component of haemodynamic forces, wall shear stress (WSS) τ:

$$\tau = \mu\dot{\gamma} = \mu\left.\frac{\partial u}{\partial \eta}\right|_{\eta=0} \tag{3.3}$$

Normal blood plasma is a Newtonian fluid, but whole blood is non-Newtonian. What gives the blood this non-Newtonian property is the aggregates of the RBCs known as rouleaux, which form in the presence of the proteins fibrinogen and globulin under low wall shear rate (WSR, spatial near-wall gradient normal to the wall of streamwise flow velocity, i.e. $WSR = \frac{\partial u}{\partial \eta}|_{\eta=0}$). At this point, the blood viscosity is relatively high. As the shear rate is increased, the RBCs in the aggregates become separated and as a result the viscosity is reduced. The further increase in the shear rate causes the deformation of the RBCs, which become elongated and aligned with the flow, leading to the further reduction in viscosity. These effects of rouleaux on the blood viscosity values, however, stop being relevant when the blood shear rate is greater than $\approx 100 s^{-1}$ (47). Therefore, in large arteries such as the carotid arteries where WSR exceeds this value (the WSS in the CCA of approximately $0.75 Pa$ observed under the mean Re=290 (20) and the blood viscosity of $0.004 kgm^{-1}s^{-1}$ gives the WSR of $187.5 s^{-1}$), the viscosity of blood can be considered as constant, justifying the Newtonian-fluid assumption.

In addition, blood is assumed to be homogenous. Most cells suspended in the blood have diameters (RBC $7.6 \mu m$, platelet 2-$4 \mu m$, leukocytes 7-$20 \mu m$) that are at least few orders of magnitude smaller than the diameters of the large arteries relevant in atherosclerosis (the coronary arteries typically 2-$3 mm$, the carotid arteries $6 mm$), and therefore it was deemed a reasonable assumption.

3.2.2 Governing equations of fluid dynamics

Fundamental equations that characterise the blood flow, the continuity and momentum equations, are introduced in this section. Their detailed derivations can be found in Sections A.2 and A.3 respectively in Appendix A.

Continuity equation

Continuity equation represents the conservation of mass, i.e. the mass within a closed system remains constant. This can be expressed as:

$$0 = \int_{CV} (\nabla \cdot \mathbf{u}) \, dV \tag{3.4}$$

in integral form, where CV denotes the control volume. Incompressible flows are source-free (divergence-free), thus:

$$\nabla \cdot \mathbf{u} = 0 \tag{3.5}$$

Momentum equations

The momentum equations describe Newton's second law, i.e. the total force applied on a body is equal to the time rate of change of linear momentum of the body. The external forces considered here are the body and surface forces. The body forces, examples of which include gravitational and electromagnetic forces, act throughout the media within the volume element, and are normally treated as prescribed. The surface forces on the other hand, act directly on the boundary surface surrounding the volume element and are made up of normal and tangential stresses. Relating these forces to the time change of momentum within the CV and through the control surface (CS) surrounding the CV gives the momentum equation in integral form:

$$\frac{\partial}{\partial t}\int_{CV} \rho\mathbf{u}\, dV + \int_{CS} \rho\mathbf{u}\mathbf{u}\cdot d\mathbf{A} = -\int_{CS} \nabla p\dot{I}\cdot d\mathbf{A} + \int_{CS} \mu\nabla^2\mathbf{u}\cdot dA \tag{3.6}$$

where ρ is the fluid density, $\mathbf{u}$ the Cartesian velocity vector, $\mathbf{A}$ the area vector, p pressure, dV the volume of the fluid element and μ viscosity. This equation, derived from the Cauchy's momentum equations A.40 with the stress terms expressed with the viscosity and the velocity gradients, and also with the constant viscosity and density assumptions, is knows as the Navier-Stokes equation.

3.3 Mass transport

Mass transport is a very important process in human physiology, since it controls the transport of molecules of proteins or nutrients to, from and within tissue, which is inherent in many of physiological and pathological processes at all levels, from cellular to systemic. The mechanisms of mass transport relevant in the study of atherosclerosis, which are governed by the same transport properties applied to fluid, are presented in this section.

3.3.1 Governing equation of arterial mass transport

In earlier studies of mass transport in atherosclerosis (22; 46), the transport of lipoproteins, particularly LDL, to and from the vessel wall was the main focus since atherosclerosis was still considered to be a disease characterised exclusively by lipid metabolism within the vessel wall. It has since emerged that, while lipid metabolism still has a significant part in atherogenesis, it is not the sole culprit, and that it is only a part of chronic inflammatory process that is now believed to contribute to the plaque initiation and progression (78; 114). Nevertheless, mass transport in the vascular system remains relevant, since that LDL transport does have a part in the process of atherogenesis, and that there are numerous processes that depend on the transport of blood-borne molecules from the circulating blood to the vessel wall surface. Examples of this include oxygen, of which impaired transport from the blood to the vessel wall has been reported to co-localise with the sites of elevated LDL (39), and agonist adenosine triphosphate (ATP), which binds to the G protein-coupled receptors on the endothelial cell (EC) surface and triggers the reactions that lead to nitric oxide (NO) synthesis. The latter process is considered to be of vital importance in atherosclerosis, as the disease appears to manifest itself when the regulation of the vascular tone and the maintenance of vascular health normally carried out by the actions of NO is impaired (this will be discussed in detail in Chapter 5).

Mass transport in arteries is governed by convection, i.e. combined effects of two processes, diffusion and advection. Diffusion refers to the movement of individual species particles due to their random motion (Brownian motion) along the concentration gradient, whereas advection describes the transport of species in a much larger scale due to the bulk motion of the flow. The process of convective mass transport is described by the following advection-diffusion equation, derived

based on the mass balance within the flow domain:

$$\frac{\partial}{\partial t}(\rho\phi_i) + \nabla \cdot (\rho \mathbf{u}\phi_i) = -\nabla \cdot \mathbf{J_i} \tag{3.7}$$

which can be obtained from the general scalar transport equation based on the Reynolds transport theorem derived in Appendix A.1. The intensive property η in Eqn. A.17 is substituted by the mass fraction of species i, i.e. ϕ_i to describe the time rate of change of the species i within the fluid volume element and its net flux of through the control surface balanced with the rate of changes of the species i within the volume element due only to advection and diffusion (i.e. not including production or consumption due to chemical reaction). The LHS term, $-\nabla \cdot \mathbf{J_i}$, is a diffusion flux and approximated by Fick's laws of diffusion. The first law relates the diffusion flux to the concentration field by assuming that the movement of a species occurs from the regions of high concentration to those of low concentration. Its flux is proportional to the concentration gradient, with the species's diffusivity D_i as a proportionality constant:

$$\mathbf{J} = -\rho D_i \nabla \phi_i \tag{3.8}$$

Substituting this into the species mass balance equation (Eqn. 3.7) leads to:

$$\frac{\partial}{\partial t}(\rho\phi_i) + \nabla \cdot (\rho \mathbf{u}\phi_i) = -\nabla \cdot (-\rho D_i \nabla \phi_i) \tag{3.9}$$

For spherical species, the Stokes-Einstein equation states that their diffusion coefficients are a function of the solvent's viscosity and temperature. As both parameters are typically assumed to be constant for the blood flow through large arteries, D_i here can be assumed to be constant. Also, as explained in Chapter 3, blood is considered as an incompressible fluid, i.e. $\nabla \cdot \mathbf{u} = 0$. Therefore, the final form of the advection-diffusion equation for the species i becomes:

$$\frac{\partial \phi_i}{\partial t} + \mathbf{u} \cdot \nabla \phi_i = D_i \nabla^2 \phi_i \tag{3.10}$$

where the second term on the LHS represents advective mass transport and the RHS the mass transport due to diffusion.

3.3.2 Mass transfer boundary layer

When a fluid flows over a solid surface, a hydrodynamic boundary layer develops adjacent to the surface due to the difference in momentum between the bulk flow and the wall surface (on which the momentum is zero due to no-slip condition). Additionally, when the wall surface is reactive, i.e. acts as a sink, a concentration difference arises between the bulk flow and the wall surface. This leads to the development of a mass-transfer boundary layer. Its presence adjacent to the vessel wall in arteries has important implications in the maintenance of vascular wall health and therefore in the pathogenesis of atherosclerosis, since the presence of the boundary layer, which grows in the direction of flow, results in the reduced delivery of nutrients and agonists to the endothelial surface where they are needed.

3.4 Relevant dimensionless quantities

Diffusion of mass and momentum takes place simultaneously in a typical flow condition observed in arterial flow, i.e. hydrodynamic flow passing through the solid, reacting surface. There are several important dimensionless quantities that characterise the flow and mass transport processes occurring within.

Womersley number, *Wo*

Womersley number is an important parameter in the study of the blood, which characterises the relation between the pulsatile flow frequency and the viscous effects of blood, and is expressed as:

$$Wo = r\sqrt{\frac{\omega}{\nu}} \tag{3.11}$$

where r is a characteristic length scale (here it is a vessel diameter), ω the angular frequency of the oscillations and ν the kinematic viscosity.

Schmidt number, *Sc*

The Schmidt number (Sc) characterises the relative importance of momentum diffusion to that of mass diffusion, the former of which is represented by the momentum diffusion coefficient (i.e. kinematic viscosity ν) and the latter by the

mass diffusion coefficient D (both have the unit m^2s^{-1}), i.e.:

$$Sc = \frac{\nu}{D} \tag{3.12}$$

Physically, Sc relates the thickness of the hydrodynamic boundary layer relative to that of the mass transfer boundary layer. The viscosity of blood is often taken to be approx. $4 \times 10^{-6} m^2 s^{-1}$, whereas the mass diffusion coefficient of the relevant species such as oxygen, ATP and LDL are in the order of $\times 10^{-9} \sim 10^{-12}$. This gives Sc ranging from $\times 10^3$ to 10^6, which indicates that the concentration boundary layer is much thinner, and confined in much smaller region adjacent to the wall surface compared to the hydrodynamic boundary layer. Consequently, the velocity profile within the mass transfer boundary layer can be considered to be linear in form.

Péclet number, *Pe*

The Péclet number represents the relative importance of the rate of advective transport of species to the rate of diffusive transport of the same species. It is defined as:

$$Pe = \frac{UL}{D} = \frac{UL}{\nu}\frac{\nu}{D} = Re \cdot Sc \tag{3.13}$$

where U is the velocity and D the characteristic length. In the human carotid artery, the mean Reynolds number during one cardiac cycle is around 300. This, together with the Schmidt number for the relevant species in arterial blood flow mentioned above, gives that $Pe \approx \times 10^5 \sim 10^8$, implying that the transport of these species is dominated by advection.

3.5 Concluding remarks

The governing equations presented above will be the basis for studying arterial blood flow and physiological cellular processes associated with it. Due to the nonlinear and coupled nature of these equations, however, an iterative rather than an analytical approach is needed to obtain the solutions. This is achieved using computational fluid dynamics (CFD), of which descriptions and procedure are outlined in the next chapter.

Chapter 4

Theory of Computational Fluid Dynamics

4.1 Introduction

Computational fluid dynamics (CFD) is a powerful tool in analysing fluid flow and the transport phenomena associated with it, and has been used in a wide range of engineering applications. It offers many major advantages over experimental fluid dynamics, including:

- Its ability to provide complete 3D data within the flow domain
- Flexibility via the ease of changing boundary conditions and therefore suitable for testing a wide range of parameters
- Ease of post-processing
- Expandable, e.g. chemical species or heat transport processes can be coded into the fluid flow simulations and therefore can be used to model various fluid flow-related situations
- Versatility and cost-effectiveness, as one CFD platform (grid generator, solver and postprosessor) can be used to solve a wide range of problems
- Can be used in place of experiments where carrying out experiments is difficult or not practical due to cost or safety issues
- No restrictions in terms of the dimensions of the model it can handle

whereas the disadvantages include:

- Initial cost needed for extensive computational platform to solve complex, realistic problems
- Difficulties in defining and implementing boundary conditions that mimic the actual flow conditions being simulated
- Solutions need to be validated against experimental data wherever possible, which is not often possible due to the complexity of problems it is capable of modelling

A particularly important issue is that as much effort should be put into optimising the accuracy and validity of CFD solutions, given that they are approximate and prone to errors. This can be achieved by two ways. Firstly, as stated above, the numerical solutions obtained should be compared and validated against the experimental results obtained using the identical geometries and boundary conditions wherever possible. Secondly, it should be ensured that the boundary conditions prescribed to define the simulation represent the physical condition sufficiently closely.

Because of the mathematical difficulties faced in solving the Navier-Stokes equations (presented in Chapter 3), their exact solutions were found only for limited cases such as circular-pipe flows and axisymmetric flows (116). The flow environment that is often found in the human vasculature, including that relevant to atherosclerosis, is significantly more complex than these cases, incorporating the effects of geometrical deviation from those limited cases such as vessel curvature as well as those of temporal variation of boundary conditions that are inherent in blood pulsatility. As this renders obtaining analytical solutions to the Navier-Stokes equations extremely difficult or not practical, the means of obtaining the solutions numerically, computational fluid dynamics (CFD), is required.

In CFD, the common objective often is, as stated above, to obtain solutions to the problems where obtaining analytical solutions and/or carrying out experiments is not practical or currently possible, and to achieve this efficiently. Several CFD methods available at present share the following procedure:

1. Problem definition by selecting physical flow domain, governing equations and boundary conditions

2. Physical discretisation of the flow domain (Grid generation)
3. Definition of boundary and initial conditions
4. Numerical discretisation of the governing equations into the discretised spaces
5. Obtaining solutions iteratively
6. Post-processing

The well-known CFD schemes such as the finite volume method, finite element method and finite difference method all differ in how the discretisation of the governing equations into the discrete flow domain is handled.

In this chapter, the overview of solution procedure of CFD is presented through that of the finite-volume approach, which is the method adopted by the CFD solver used in this work, ANSYS FLUENT (Ansys. Inc., Lebanon, NH, USA), following closely the methodology described in the ANSYS FLUENT 12.0/12.1 Documentation (1) and (130).

4.2 Grid

Grid generation, which follows the definition and creation of a physical flow-domain model, is a crucial process during the pre-processing stage of CFD, as the accuracy and stability (and thus convergence) of the solution in subsequent simulations are greatly influenced by the final quality of the grid. Solution accuracy and stability generally improve as the grid spacing becomes finer, since, assuming the numerical process is consistent, the simulated solution should tend towards the exact solution, as smaller grid (and time-step) sizes contribute to decreased discretisation errors. Additionally, finer grid elements allows for more complete surface recovery of the geometry surface, as well as for the improved resolution of important flow features such as flow separation and reversal when placed at appropriate locations.

The important features that should be considered in grid generation are cell skewness and aspect ratio. Skewness is defined as the difference between the shape of the cell and the shape of an equilateral cell having the same volume, and so with optimal grid generation the quadrilateral/hexahedral or triangular/tetrahedral

elements have the angles close to 90° or 60°. In general, grids with highly-skewed elements should be avoided as they may cause convergence problems due to the additional terms in the discretised equations. Another parameter that should be considered carefully is the cell aspect ratio. Aspect ratio is a measure of the stretching of the cell which is computed as the ratio of the maximum to minimum distances from the cell centroid. The general guideline is that it should be kept below 5 : 1 (1; 130) as large aspect ratios again affect the solution accuracy and stability. Another important issue is that sudden large changes in the grid element size should be avoided, particularly in the regions where large solution variable gradients are expected, since it is likely to cause the accumulation of truncation errors in the critical regions, leading to solution instability.

All these factors should carefully be considered while performing grid generation in order to facilitate convergence and achieve better accuracy. However, using finer grid elements for the sake of improved accuracy comes at the cost of considerably increased computational time and resources. Therefore, it may be necessary to place coarser grid elements in the bulk flow region, and finer elements in the regions where large gradients are expected, such as at the locations of flow separation or boundary layers.

4.3 Finite volume method

The finite-volume method (FVM) is a CFD approach where the conservative form of the governing equations is discretised into a set of algebraic equations into and then solved over discrete volume spaces (termed *control volumes*) within the grid occupying the flow domain. The primary advantage of this method, as well as its ability to accommodate complex, unstructured grids, is that it is conservative. During the discretisation of the governing equations, the volume integrals (which contain a divergence term) are converted into surface integrals, which are then computed as fluxes through the faces enclosing the control volume. Since the flux leaving a cell volume is the same as that entering the neighbouring cell, and this applies to each cell within the grid, conservation is maintained for the whole system.

In FLUENT's pressure-based solver, the primary algorithm used is the projection method, in which the velocity and pressure are decoupled, and the continuity of the velocity field is maintained by solving a pressure or pressure correction

equation, which is derived from the continuity and the momentum equations in such a way that the velocity field, corrected by the pressure, satisfies the mass conservation (details described in Section 4.3.3). Since the governing equations are nonlinear and coupled, the solutions must be obtained iteratively i.e. the whole set of the governing equations is solved repeatedly until convergence is achieved. Governing equations for additional scalar quantities are next solved using the current values of the solution variables. These steps will be repeated until the pre-defined convergence criteria are met. Fig. 4.1 shows the processes described above during one iteration, using a "segregated" algorithm (where the governing equations are solved one after another, decoupled from each other). In the other, "coupled" algorithm, the second and the third steps in Fig. 4.1 are replaced by a single step in which all the equations are solved in a coupled manner. Because of this, the convergence speed improves, although at the expense of the memory requirement, which has been observed to increase by 1.5-2 times (1) due to the coupled solver having to store all the equations while they are being solved.

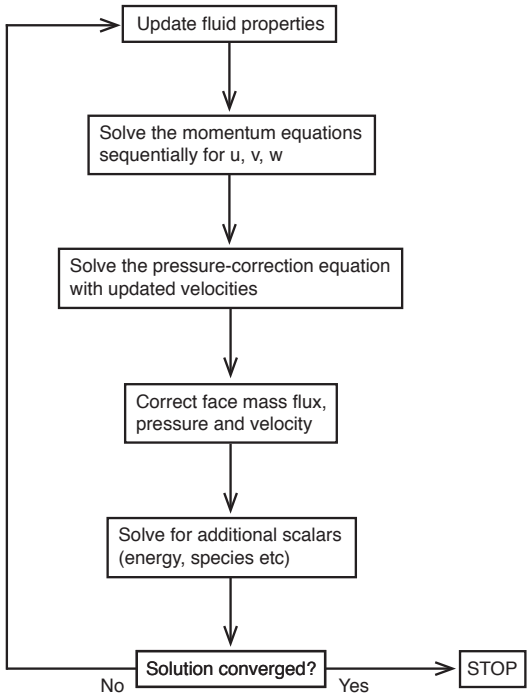

Figure 4.1: Processes involved in one iteration using FLUENT's pressure-based method.

4.3.1 Spatial discretisation of the governing equations

In order to demonstrate the FVM discretisation of the governing equations, the following, more general form of the scalar transport equation is considered:

$$\int_{CV} \frac{\partial \rho\phi}{\partial t} dv + \int_{CS} \rho\phi \mathbf{u} \cdot d\mathbf{A} = \int_{CS} \Gamma_\phi \nabla\phi \cdot d\mathbf{A} + \int_{CV} S_\phi dV \tag{4.1}$$

where Γ_ϕ is the diffusion coefficient for the quantity ϕ and S_ϕ source of ϕ per unit volume. The pressure term seen in Eqn. 3.6 is included in the source term $S_\phi V$. In FVM, the scalar transport equation is discretised into an algebraic equation for each control volume, so that the resulting equation represents the conservation law for the particular control volume. This takes the following form:

$$\frac{\partial \rho\phi}{\partial t} V + \sum_{f}^{N_{faces}} \rho_f \mathbf{u}_f \phi_f \cdot \mathbf{A_f} = \sum_{f}^{N_{faces}} \Gamma_\phi \nabla\phi_f \cdot \mathbf{A_f} + S_\phi V \tag{4.2}$$

where N_{faces} is the number of faces surrounding the control volume, ϕ_f the scalar quantity convected through face f, $\rho_f \mathbf{u_f} \cdot \mathbf{A_f}$ the mass flux through the face f, $\mathbf{A_f}$ the face area and V the cell volume. In Eqn. 4.2, the volume integrals are represented with the average value over the cell volume, and the surface integrals with the summations over all the bounding faces. The advection term on the LHS and the diffusion term on the RHS, however, still contain the value of the quantity ϕ on the face f. As FLUENT stores values at cell centres (c_0 and c_1), the value of ϕ_f needs to be evaluated in order to obtain the fully-discretised governing equation. This is achieved by interpolating the cell-centre values of two adjacent cells (ϕ_{c_0} and ϕ_{c_1}) on each side of the face. The discretisation processes of the advective and diffusive terms are described in the following sections.

Discretisation of the advection term

In order to obtain the value ϕ_f required for the discretisation of the advection term, FLUENT uses an upwind scheme, i.e. the face value of ϕ_f is derived from quantities in the cells located upstream (i.e. upwind) relative to the direction of the normal velocity $\mathbf{u_n}$. Thus the differencing used in upwind schemes takes into account the direction of the influence of the flow (termed *transportiveness*), which is an important property to be accounted for since, in arterial blood flow, the predominant transport is advection.

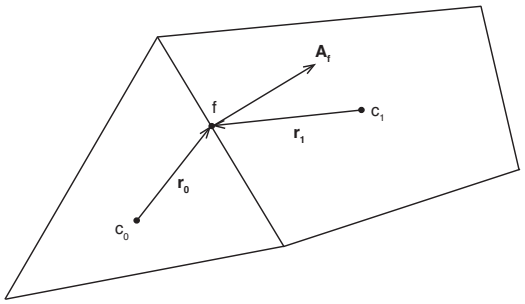

Figure 4.2: A control volume. Since FLUENT stores solution variables at cell centres, the face value of ϕ on f, which is needed for the discretisation of the advective and diffusive terms, has to be interpolated from the cell-centre values, ϕ_{c_0} and ϕ_{c_1}.

The simplest form of upwind schemes is the first-order upwind (FOU). FOU assumes that the cell-centred values of any variable represent a cell-average value which is uniform throughout the whole cell volume, and that the face values are equal to the cell-centre values. This means that ϕ_f is equal to the cell-centre value of ϕ in the upstream cell ($\phi_f = \phi_{c_0}$ in Fig. 4.2). The "upstream" direction here is determined from the direction of the velocity in the advection term in Eqn. 4.2 relative to that of the normal velocity $\mathbf{u_n}$. However, due to the numerical diffusion introduced where the gradient is large, this scheme is known to be highly inaccurate.

Second-order upwind (SOU) is one of the schemes that offer a higher-order accuracy and still maintain the transportive property. Here, the cell-centred solution is expanded via a Taylor series about the cell centroid, and the result is truncated to achieve the second-order accuracy, i.e.:

$$\phi_{f,SOU} = \phi_{c_0} + \nabla\phi_{c_0} \cdot \mathbf{r} \tag{4.3}$$

where ϕ_{c_0} and $\nabla\phi_{c_0}$ are the cell-centred value and its gradient in the cell upstream, and $\mathbf{r}$ the displacement vector from the centroid of the upstream cell to that on the face f. Now, in order to complete the discretisation of Eqn. 4.3, the gradient of ϕ must be evaluated. The Green-Gauss theorem states that the surface integral of a scalar function is equal to the volume integral of the gradient of the scalar function, so:

$$\int_{CV} \nabla\phi_{c_0} dV = \int_{CS} \phi_f dA \tag{4.4}$$

Assuming that $\nabla\phi_{c_0}$ is uniform throughout the control volume, then:

$$\int_{CV} \nabla\phi_{c_0} dV = \nabla\phi_{c_0} V = \int_{CS} \phi_f dA \tag{4.5}$$

As previously, approximating the surface integral with summations of ϕ_f at the cell face centroid of the bounding faces around the control volume, i.e.:

$$\int_{CS} \phi_f dA = \sum_{f}^{N_{faces}} \overline{\phi_f} \mathbf{A_f} \tag{4.6}$$

Combining the two equations above:

$$\nabla\phi_{c_0} = \frac{1}{V} \sum_{f}^{N_{faces}} \overline{\phi_f} \mathbf{A_f} \tag{4.7}$$

where $\overline{\phi_f}$ is the value of ϕ on the face f used in FLUENT in the computation of the gradient. It is taken to be the arithmetic average of the cell-centre values of the adjacent cells (c_0 and c_1) on either side of the face f:

$$\overline{\phi_f} = \frac{\phi_{c_0} + \phi_{c_1}}{2} \tag{4.8}$$

This, when substituted into Eqn. 4.7 gives $\nabla\phi_{c_0}$, which in turn gives the complete expression of $\phi_{f,SOU}$ when substituted into Eqn. 4.3.

The third-order MUSCL (Monotone Upstream-centred Scheme for Conservation Laws) is a blend of a central differencing (CD) and SOU schemes. ϕ_f is therefore expressed as:

$$\phi_f = \theta\phi_{f,CD} + (1-\theta)\,\phi_{f,SOU} \tag{4.9}$$

where $\phi_{f,CD}$ is defined as:

$$\phi_{f,CD} = \frac{1}{2}(\phi_0 + \phi_1) + \frac{1}{2}(\nabla\phi_0 \cdot \mathbf{r_0} + \nabla\phi_1 \cdot \mathbf{r_1}) \tag{4.10}$$

and $\phi_{f,SOU}$ as in Eqn. 4.3. The higher-order accuracy is achieved via reduced numerical diffusion compared with FOU or SOU, which makes the third-order MUSCL more suitable for complex, unstructured meshes.

Discretisation of the diffusion term

For the diffusion term in Eqn. 4.2, $\Gamma_\phi \nabla \phi_f \cdot \mathbf{A_f}$, FLUENT uses a central differencing with a second-order accuracy. For the evaluation of the gradient $\nabla \phi_f$, the same method as for the advection term described above is used.

With both advection and diffusion terms discretised, the scalar transport equation (Eqn. 4.2) can be written in the following linearised form for each cell:

$$a_{c_0} \phi_{c_0} = \sum_{nb} a_{nb} \phi_{nb} + b \tag{4.11}$$

where a_{c_0} and a_{nb} are linearised coefficients both for the advection and diffusion terms for cell c_0 and its neighbouring cells c_{nb}, and b the source and other terms. This results in a set of algebraic equations with a space coefficient matrix. FLUENT solves this system of linear equations using a point-implicit (Gauss-Seidel) solver with an algebraic multigrid (AMG) method to accelerate convergence (for details see (1)).

In addition to the general procedure of spatial discretisation outlined above, there are some considerations that have to be taken into account in the discretisation of the momentum and continuity equations.

Momentum equations

The discretisation of the momentum equations follows that described above, with special considerations for pressure. The momentum equations can be obtained by replacing ϕ with the velocity $\mathbf{u}$ in Eqn. 4.11 and expanding the source term b to separate the pressure term from other sources:

$$a_{c_0} \mathbf{u_{c_0}} = \sum_{nb} a_{nb} \mathbf{u_{nb}} + \sum p_f \mathbf{A} + S \tag{4.12}$$

The variables needed to solve the equation above, pressure and face mass fluxes, are not known *a priori*, and therefore must be obtained simultaneously during the solution process. In order to evaluate the face value of pressure p_f (which is necessary since the pressure values are stored at cell centres), FLUENT uses

interpolation based on the coefficients of the momentum equation (112):

$$p_f = \frac{\frac{p_{c_0}}{a_{c_0}} + \frac{p_{c_1}}{a_{c_1}}}{\frac{1}{a_{c_0}} + \frac{1}{a_{c_1}}} \tag{4.13}$$

which has been observed to be accurate as long as the pressure distribution between cell centres is relatively smooth, i.e. in the absence of jumps. Other (including higher-order) interpolation schemes are also available, depending on the criteria such as mesh topology and the presence of strong body forces.

Continuity equation

A more general form of continuity equation (Eqn. A.23) can be integrated over a control volume to obtain the discretised form:

$$\sum_{f}^{N_{faces}} \mathbf{J}_f \mathbf{A}_f = 0 \tag{4.14}$$

where $\mathbf{J}_f$ is the mass flux through face f, $\mathbf{J}_f = \rho \mathbf{u_n}$. As stated above, velocity values are stored at cell centres, and so the face value $\mathbf{u_n}$ needs to be related to the cell-centre values. It is well known that linear averaging of cell-centre values leads to unphysical "checker-boarding" pressure distribution (1). In order to prevent this, FLUENT uses the momentum-weighted averaging method proposed by Rhie and Chow (112), which uses weighting factors computed based on the coefficients of the momentum equation (Eqn. 4.12), a:

$$\mathbf{J_f} = \rho_f \frac{a_{c_0}\mathbf{u}_{\mathbf{n},c_0} + a_{c_1}\mathbf{u}_{\mathbf{n},c_1}}{a_{c_0} + a_{c_1}} + d_f \left(\left(p_{c_0} + (\nabla p)_{c_0} \cdot \mathbf{r_0} \right) - \left(p_{c_1} + (\nabla p)_{c_1} \cdot \mathbf{r_1} \right) \right)$$

$$= \hat{J}_f + d_f \left(p_{c_0} - p_{c_1} \right) \tag{4.15}$$

where p_{c_0} and p_{c_1}, u_{n,c_0} and u_{n,c_1} are the pressure and normal velocities respectively in the two neighbouring cells on either side of the face f. $\hat{J}_f$ therefore is the weighted mass flux, incorporating the influence of the velocities in both cells. $d_f \left(p_{c_0} - p_{c_1} \right)$ is a pressure-weighting term, where d_f is a function of momentum equation coefficients a averaged between c_0 and c_1.

4.3.2 Temporal discretisation

For the simulations of transient flows, the governing equations need to be discretised both spatially and temporally. While the spatial discretisation process is identical to that outlined in the previous section for steady flows, temporal discretisation involves the integration of every term in the governing equation (Eqn. 4.2) over a time step $\triangle t$.

The general form of the time course of a quantity ϕ is given by:

$$\frac{\partial \phi}{\partial t} V = F(\phi) \tag{4.16}$$

where the function $F(\phi)$ includes any spatial discretisation. Here, the time derivative is discretised using backward differences, which gives:

$$\frac{\phi^{n+1} - \phi^n}{\triangle t} V = F(\phi) \tag{4.17}$$

where $n+1$ and n respectively denote the value at the current time level $t + \triangle t$ and that at the previous time level t. Now, in order to evaluate the RHS of the equation, FLUENT uses a fully implicit scheme, where the computation of ϕ^{n+1} is not expressed explicitly in terms of the existing solution, but rather is a function of the values the neighbouring cells at the current time level. Therefore the above equation should be written as:

$$\frac{\phi^{n+1} - \phi^n}{\triangle t} V = F\left(\phi^{n+1}\right) \quad \Rightarrow \quad \phi^{n+1} = \phi^n + \frac{\triangle t}{V} F\left(\phi^{n+1}\right) \tag{4.18}$$

where the term $F(\phi^{n+1})$ incorporates all the spatial discretisation terms at the time level $t + \triangle t$, i.e.:

$$\begin{aligned} F\left(\phi^{n+1}\right) = &- \int_{CS} \rho^{n+1} \phi^{n+1} \mathbf{u}^{n+1} \cdot d\mathbf{A} \\ &+ \int_{CS} \Gamma_\phi^{n+1} \nabla \phi^{n+1} \cdot d\mathbf{A} + \int_{CV} S_\phi^{n+1} dV \end{aligned} \tag{4.19}$$

Since the value of ϕ at a particular point depends on those in its neighbouring cells at the same time level, the solution must be obtained by solving a set of simultaneous equations consisting of Eqn. 4.18 applied to all the cells in the

flow domain. This approach is normally computationally expensive as it involves solving a large system of algebraic equations. However, because of the stability it offers, relatively large time-step sizes are allowed and thus it often takes less computation than explicit schemes, which is easier to implement due to its solutions based only on the previous solutions but requires much smaller time steps due to its tendency towards instability (130). Eqn. 4.18 is solved iteratively at each time step before moving to the next time step, that is, when the solution converges (Fig. 4.1) the solution is advanced by $\triangle t$.

4.3.3 Pressure-velocity coupling

As described in Chapter 3 and Appendix A.3 the momentum equations describe the relationship between forces and resulting motion of flow, driven by the contribution of pressure gradients. The solutions of the momentum equations, i.e. velocity field, are constrained by the continuity equation for incompressible flows so that divergence-free condition is maintained.

There are four equations for four unknowns (u, v, w, p) in the system of equations described above, which implies that all four equations are needed to solve for both velocity and pressure fields. However, there is no independent equation for pressure, and therefore there needs to be a means of modifying the continuity equation so that pressure is coupled to velocity in the equation. This is achieved by pressure-velocity coupling, which generally involves the following steps described below.

During the solution process, the momentum equations are first solved with the prescribed pressure field p^* specified by the initial condition or obtained in the previous iteration. However, due to the pressure values used here being temporally uncoupled from velocity, the velocity field obtained as a result $\mathbf{u}^*$ is still approximate, and therefore the face mass flux calculated based on it J^* using the interpolation method in Eqn. 4.15, i.e.:

$$J^* = \hat{J}_f^* + d_f \left(p_{c_0}^* - p_{c_1}^*\right) \tag{4.20}$$

does not satisfy the continuity equation. Here, in order to enforce the conservation of mass, a correction J_f' is added to the RHS so that the corrected flux J_f satisfies the continuity equation:

$$J_f = J_f^* + J_f' = \hat{J}_f^* + d_f \left(p_{c_0}^* - p_{c_1}^*\right) + J_f' \tag{4.21}$$

The SIMPLE (Semi-Implicit Method for Pressure-Linked Equations) pressure-velocity coupling method used in FLUENT proposes that $J'_f = d_f \left(p'_{c_0} - p'_{c_1}\right)$, so that:

$$J_f = J^*_f + J'_f = \hat{J}^*_f + d_f \left(p^*_{c_0} - p^*_{c_1}\right) + d_f \left(p'_{c_0} - p'_{c_1}\right) \tag{4.22}$$

This algorithm substitutes the flux correction equation (Eqn. 4.22) into the discrete continuity equation to obtain a discrete pressure-correction (p') equation for the cell:

$$a_{c_0} p'_{c_0} = \sum_{nb} a_{nb} p'_{nb} + b \tag{4.23}$$

where b on the RHS is the net flow into the cell:

$$b = \sum_{f}^{N_{faces}} J^*_f A_f \tag{4.24}$$

Once a solution of Eqn. 4.23 is obtained, the cell pressure and the face mass flux can be corrected as:

$$p_{c_0} = p^*_{c_0} + \alpha p'_{c_0} \tag{4.25}$$

$$J_f = J^*_f + d_f \left(p'_{c_0} - p'_{c_1}\right) \tag{4.26}$$

The corrected face flux J_f now satisfies the discrete continuity equation (Eqn. 4.14) identically in each iteration. α in Eqn. 4.25 is the under-relaxation factor (URF) for pressure. The purpose of under-relaxation of a variable is to control the change of ϕ produced during each iteration, $\triangle\phi$, by reducing its change by the factor specified by URF, i.e.:

$$\phi_{new} = \phi_{old} + \alpha \triangle \phi \tag{4.27}$$

Other pressure-velocity coupling schemes available in FLUENT includes SIMPLEC (SIMPLE-Consistent) and PISO (Pressure-Implicit with Splitting Operators), both of which are variants of the original SIMPLE scheme and were developed to improve the convergence speed. In the SIMPLEC scheme, the correction

equation is the same as that in the SIMPLE, but the d_f is instead a function of $\overline{a_P - \sum_{nb} a_{nb}}$, and so less significant terms compared to those in SIMPLE are omitted. In SIMPLEC, the URF for pressure correction is set to 1.0 in FLUENT, and therefore will improve convergence speed, though often only in relatively simple flow problems (such as those for laminar flows with no other models included) in which pressure-velocity coupling is likely to be the main bottleneck to obtaining the solution. For highly skewed meshes, however, such high values of URFs can lead to instability. Thus for these cases, lowering URF (up to around 0.7), using SIMPLE or using skewness correction schemes are advised. However, convergence using these schemes can be still slow because new velocities and fluxes do not satisfy the momentum balance after the pressure-correction equation is solved, and therefore the process has to be repeated until the balance is met. The PISO scheme was developed to further aid the convergence by focusing first on this point. The repeated calculations needed in SIMPLE and SIMPLEC are moved into and performed while the pressure-correction equation is being solved, which results in the improved approximation between the pressure and velocity corrections and thus fewer iterations needed for convergence (though at a cost of slight increase in computation). This is termed momentum correction. The other correction component of PISO is skewness correction. The approximate relationship between the corrected mass flux at the cell face and the difference of the corrected pressure in the neighbouring cells is very rough for highly-skewed meshes. When this scheme is used, the pressure-correction equation is solved first, then the gradient of the corrected pressure (which is not known in advance) calculated, and then mass flux corrections are updated using the gradient. This, termed skewness correction, is often very effective in reducing convergence difficulties associated with highly skewed meshes.

4.3.4 Convergence

A numerical method is said to have converged when its solution has satisfied the two properties, consistency and stability. The former refers to a property where a numerically approximated solution approaches the exact solution when quantities such as the time step and/or grid spacing tend to zero (due to this resulting in the truncation error tending to zero), whereas the latter is concerned with the build-up or decay of numerical errors introduced at any stage of the simulation, and therefore the numerical method is considered to be stable if it does not lead

to the accumulation of errors and eventual divergence of the solution.

In CFD simulations, in which a set of algebraic equations is solved iteratively, it is often very difficult or not practical to directly establish the solution's consistency and stability simultaneously for each simulation performed. Therefore, the conditions stated above are implemented by ensuring that the solution satisfies the following conditions:

1. All the discretised equations reach their own predefined convergence criteria
2. The solution no longer changes with further iterations
3. Overall balances of mass, momentum and species are reached

The former two can be assessed by monitoring the solution residuals, which are defined as follows in FLUENT.

As introduced in the previous section, the discrete conservation equation for a general scalar quantity at cell P can be written as:

$$a_P \phi_P = \sum_{nb} a_{nb} \phi_{nb} + b \tag{4.28}$$

where a_P is the centre coefficient, a_{nb} the influence coefficients from the neighbouring cells and b the contribution from the source and other terms. The solution residual R^ϕ computed in FLUENT is the imbalance in Eqn. 4.28 summed over all the cells P in the flow domain, i.e.:

$$R^\phi = \sum_{P_{total}} \left| \sum_{nb} a_{nb} \phi_{nb} + b - a_P \phi_P \right| \tag{4.29}$$

or

$$R^\phi_{sc} = \frac{\sum_{P_{total}} \left| \sum_{nb} a_{nb} \phi_{nb} + b - a_P \phi_P \right|}{\sum_{P_{total}} \left| a_P \phi_P \right|} \tag{4.30}$$

Equation 4.30 is a scaled form of Eqn. 4.29, by a factor which is a representative of the convective flux of the quantity ϕ through the domain.

For the continuity equation, the unscaled form of the residuals is defined as:

$$R^c = \sum_{P_{total}} \left| \textit{rate of mass creation in cell } P \right| \tag{4.31}$$

and its scaled from:

$$R^c_{sc} = \frac{R^c_{iteration\ N}}{R^c_{iteration\ 5}} \tag{4.32}$$

where the denominator is the largest of the absolute value of the residual for the continuity equation in the first five iterations.

While the scaled forms of residuals are default in FLUENT and are sufficient for many problems, the unscaled forms can be more appropriate in cases such as the computation of continuity residuals, since when a good initial guess to the final solution is provided (which produces the small initial residual), the residuals computed using Eqn. 4.32 would become large, and therefore the unscaled form should be also examined.

4.4 Boundary conditions

Due to the nonlinear and coupled nature of the governing equations of fluid dynamics, the initial and boundary conditions are required to be specified at the flow domain boundaries in order to close the problem and obtain numerical solutions. At the same time it must be ensured that these boundary conditions are realistic representations of the physical flow taking place within the flow domain, as the significant deviation from it will contribute not so much to the accuracy of the solution process itself but more to the validity of the solution as a representative of the physical phenomena. Additionally, setting unrealistic initial conditions often adds to the computational time and usage of resources.

For simulations of arterial blood flow and cellular reactions taking place in the vessel wall, the domain boundaries where the conditions must be specified are the inlet, outlet and solid walls as well as the volume space occupying the flow domain via the properties of the fluid being simulated.

For the inlet boundary condition, among several available options in FLUENT the velocity-inlet condition was selected in order to make use of the inlet velocity data already available. This condition sets the values or the distribution of velocity at the inlet (Dirichlet condition), i.e.:

$$\mathbf{u} = \mathbf{u}_{inlet} \tag{4.33}$$

which FLUENT uses to calculate the mass flow rate into the flow domain and to compute the momentum and species fluxes through the inlet. The mass flow rate entering a cell adjacent to a velocity inlet is:

$$\dot{m} = \int \rho \mathbf{u}_{inlet} \cdot \mathbf{A}_{inlet} \tag{4.34}$$

where $\mathbf{A}_{inlet}$ is the face area vector at the inlet pointing normal towards the flow domain.

For steady flow simulations, the mean inlet velocity was derived from the given physiological Reynolds numbers and the diameter of the common carotid artery (CCA), and then a fully-developed parabolic velocity profile was imposed at the inlet using FLUENT's user-defined function (UDF). The reason behind using the fully-developed profile is that, by doing so, it ensured that the inlet boundary condition affecting the flow field downstream could be avoided without positioning the inlet boundary further upstream (which would have resulted in an increase in grid cells and thus computation). This rendered testing to see whether the flow is fully developed sufficiently upstream unnecessary. This principle also applies to the treatment of the velocity inlet condition in the time-dependent simulations. In this case, the physiological velocity data was first obtained from a MRI waveform taken in the CCA, which was subsequently decomposed using Fourier series and the velocity value was applied at the inlet at the beginning of each time step via a UDF. The details of inlet boundary conditions are described in the following chapters.

Other available options were pressure-inlet and mass-flow-inlet conditions. The former was ruled out due to that the physiological pressure value at the inlet was not known but the velocity was, and the latter due to that the mass flow is a derived quantity from the velocity data since the density was known and constant. Other scalar properties of the flow (mass fractions of species in the current case) are also specified here.

Outflow, the condition for the exit boundary in FLUENT, imposes at the outlet the value determined by the extrapolation from within the interior (and therefore has no impact on the flow upstream of the boundary). The prerequisite for this condition to be valid is that the convective derivative of all flow variables normal to the exit boundary plane is zero, i.e. flow is fully developed so that the gradients of each flow variable (represented with Φ) in the streamwise direction

are zero (Neumann condition):

$$\frac{\partial \Phi}{\partial n} = 0 \tag{4.35}$$

Therefore it is important to ensure that the exit boundaries were positioned sufficiently downstream. Ill-positioned outlet boundaries will cause the boundary condition to be disobeyed due to, for example, the distribution profile of Φ still changing in the flow direction, or that the quantity of flow variables are not defined due to the presence of backflow caused by flow reversal. Flow split is also specified here when there are multiple exit boundaries.

For the solid wall, boundary conditions must be specified both for flow and species transport. For the former, no-slip condition was imposed to reflect the property of fluid flowing over a solid surface where a fluid in direct contact with the solid surface sticks due to viscous effects. So:

$$\mathbf{u}_{fluid} = \mathbf{u}_{wall} = 0 \tag{4.36}$$

For the species, the concentrations of those dealt with in the current study (ATP and ADP) depend on the balance between delivery of those to the wall and reactions (or degradation) on the wall surface in which they are consumed. The former is described by the normal component of the fluid-phase transport of the species expressed based on the advection-diffusion equation for the species ψ (Eqn. 3.10) derived in the previous section, whereas the latter is approximated by the first-order Michaelis-Menten reaction. These two processes are specified via a reactive boundary condition at the wall as:

$$D_\psi \frac{\partial \phi_\psi}{\partial \eta}\bigg|_{\eta=0} = K_\psi \phi_\psi - S_\psi \tag{4.37}$$

where ϕ_ψ is the concentration of the species ψ, η the surface normal coordinate, K_ψ the reaction rate constant and S_ψ the source.

The boundary condition for the volume space is defined via the properties of the fluid occupying the flow domain. In the current study, the working fluid is that representative of human arterial blood, which has the density of $1000 kgm^{-3}$ and dynamic viscosity of $0.004 Pa \cdot s$ and is assumed to be an incompressible Newtonian fluid. The justification of this assumption is detailed in Section 3.2.1 in Chapter 3.

Lastly, another boundary condition that could be utilised was for the symmetry of the flow domain. The model geometry used i this study is planar and axisymmetric, which, combined with the absence of body forces, the flow phenomena taking place within the domain should also exhibit mirror symmetry. However, a full 3D model was adopted here due to the following reasons. Firstly, the solution results post-processed in a full 3D model are considerably easier to interpret compared to those displayed in a half-3D model. Secondly, using the full 3D model will allow the results obtained to be compared with those obtained in experimental studies where mostly full 3D models are used, and also with those from existing numerical studies using similar, complete 3D models (38; 122; 143). The details of the specific boundary conditions used in each model are described in the corresponding chapters.

4.5 User-defined functions

A user-defined function (UDF) is an external function written in C language that can be coded into the FLUENT solver during solution, and is used to enhance the standard features of the solver for customisation. Typical uses of UDFs include the definition of boundary conditions, solution initialisation and chemical reaction modelling. What adds the greater flexibility is the FLUENT' UDF macros that allow the users to access solution variables during calculation. Using this feature, various external models can be defined using the solution variables and loaded into the solver. The timing of loading and execution can also be specified using these macros. These features were used extensively in the present study in order to impose physiological boundary conditions as well as to integrate biochemical cellular processes into the solution, coupled to the fluid flow simulations. The UDF codes used in this study are included in Appendix B.

4.6 Code execution

Because of the computationally intensive nature of the numerical calculations involved in the present study, the parallel version of FLUENT was used and run on University of Canterbury's IBM Blue Fern high performance computing (HPC) facility that utilised eight IBM System power 5 575 nodes running on the AIX 5.3 operating system. Each of the multi-processing nodes consisted of 16-core processors (128 in total) and total of $256GB$ RAM.

Most simulations in the present study were carried out using 8 processors, mainly for the following two reasons. Firstly, simulations run with a greater number of nodes did not produce significant improvement in the solution speed. This was due to the increased computation capability of the larger number of processors being offset by the increased inter-processor communications. The communication channel is provided in parallel computing via the message-passing interface (MPI) protocol. Simulations utilising parallel FLUENT involve an interaction between FLUENT, a host process and a set of compute-node processes with a partition of the grid each assigned to each node. MPI facilitates the data passing and synchronisation between these compute nodes on which the actual calculations are carried out (the host process generally carries out operations such as printing messages and writing to a file after receiving required information from the compute nodes). Secondly, due to the limit on the availability of the nodes on the HPC, specifying a large number of processors (either on a single node or multiple nodes) generally delays the start of the computer job considerably since it leads to other jobs submitted with a smaller number of processors specified being started first.

In the execution of parallel FLUENT code, some considerations are required in the execution of user-defined functions (UDF). As mentioned above, a FLUENT simulation consists of the FLUENT graphical user interface (GUI/Cortex), host process and a set of compute nodes. The host process acts as an interface between the user (via the GUI) and the compute nodes, and therefore has to be excluded from the execution of UDFs that involves computation of cell values in the partitioned portions of the grid. The opposite also holds true in that the compute nodes should be excluded from the UDF operation that does not involve cell value calculation in the partitioned grid (e.g. global sums). This is achieved by UDF-parallelising macros provided in FLUENT. An example of this operation is the UDF for setting the pulsatile velocity inlet boundary condition shown in

Appendix B.3. The first part of this UDF reads an external data file and assigns memory space for the calculation of Fourier coefficients (based on which the velocity at the inlet is calculated at the start of each time step). Since it does not involve any values from the partitioned portions of the grid, it is executed on the host, which is ensured here by the macro `#if !RPNODE`.

Chapter 5

Modelling of Endothelial Cell Dynamics

5.1 Introduction

This chapter explains the physiological cellular processes that take place within the endothelium, that eventually lead to the production of endothelial nitric oxide (NO). As mentioned in Chapter 1, it is now well-accepted that the formation of atherosclerotic plaques takes place only at particular locations in the vasculature such as branchings and bends. However, the actual causative factor for the plaque localisation that reflects the geometrical variation has not been fully understood. In the current study, NO is postulated to be a key substance in investigating the relationship between the vascular geometry and atherosclerosis. First, therefore, the overall cellular processes in the endothelial cell (EC) are detailed, with a focus on the activation pathways of endothelial nitric oxide synthase (eNOS), a catalytic enzyme that is essential in NO production. Physiological functions and production mechanisms of NO are then described, and then lastly, the implementation of these processes in FLUENT is summarised.

5.2 Overall cellular processes

This section describes an overall biochemical pathway leading up to the production of NO, which links the simultaneous transport of fluid and mass in the fluid phase (outlined previously in Chapters 3 and Appendix A) and the relevant

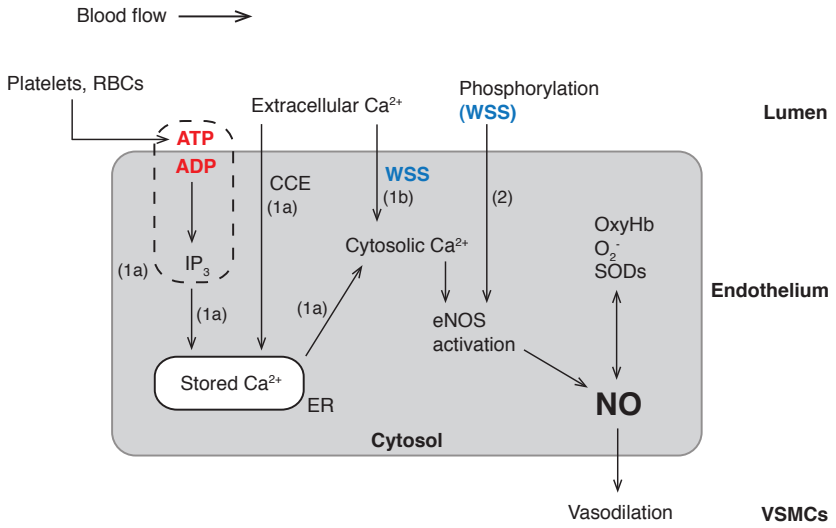

Figure 5.1: Overall cellular processes in the endothelial cell from the initiation of the process by stimulation by agonist (ATP) and WSS to the NO production. The processes denoted (1a) and (1b) make up the eNOS activation pathway that is dependent on the increase of cytosolic Ca^{2+} concentration, of which the former brings about the increase via the Ca^{2+} channel that operates depending on the store of Ca^{2+} in the endoplasmic reticulum (ER), whereas the latter describes the pathway where the Ca^{2+} increase is triggered by the WSS-induced EC membrane cell stretch. The process (2) describes the direct eNOS activation pathway, brought about by the phosphorylation of eNOS enzyme by WSS. The mechanism of IP_3 generation following the activation of G protein-coupled receptor by the ligand ATP, shown here with a dashed box, is shown expanded in Fig. 5.2.

cellular processes occurring in the endothelium.

The most important event in the NO synthesis process is the activation of endothelial nitric oxide synthase (eNOS). eNOS is a constitutive, membrane-bound enzyme that, in its activated state, catalyses the production of NO from the substrates L-arginine, oxygen and nicotinamide adenine dinucleotide phosphate (NADPH) in the presence of several cofactors such as flavin mononucleotide (FMN), flavin adedine dinecleotide (FAD) and tetrahydrobiopterin (BH_4).

The activation pathways of eNOS can be categorised into those dependent on the increase of the cytosolic calcium (Ca^{2+}) ion concentration within the endothelial cell (EC) ((1a) and (1b) in Fig. 5.1) (70; 79; 92), and that independent of it ((2) in Fig. 5.1) (37). The former can be further divided depending on the mechanism that brings about the cytosolic Ca^{2+} increase, i.e. agonist-induced (1a) or WSS-induced (1b). The following sections describe each pathway.

5.3 Activation of eNOS

5.3.1 Calcium (Ca^{2+})

Ca^{2+} is an important second messenger, and is involved in various local and global physiological phenomena ranging from intracellular energy metabolism to cardiac muscle contractions. In many of these processes the event that triggers the series of reactions is an elevation in the Ca^{2+} concentration in the cytosol (3), and thus at basal level its concentration is tightly controlled and kept low (10^{-8} to 10^{-7}M) compared to that in the elevated state (10^{-6} to 10^{-5}M) (57). Upon stimulation, the entry of Ca^{2+} takes place mainly via the opening of Ca^{2+} channels or transporters, which are located on the endoplasmic reticulum (ER, see Fig. 1.4) in the ECs, sarcoplasmic reticulum (SR) in the vascular smooth muscle cells (VSMCs) or the plasma membrane, which can be further categorised into voltage-operated, receptor-operated, mechanically (i.e. flow)-activated or store-operated channels depending on its activation mechanism. Ca^{2+} plays a vital role in the eNOS activation as a second messenger, linking the processes between agonist stimulation and the final activation, as described below.

5.3.2 Ca^{2+}-dependent eNOS activation

This pathway leads to the activation of eNOS via the increase of Ca^{2+} in the EC cytosol (summary of the pathways represented by (1a) and (1b) in Fig. 5.1), which is further divided depending on how the cytosolic Ca^{2+} increase is brought about. (1a) describes the Ca^{2+} influx pathway through the receptor-operated and store-operated Ca^{2+} channels, stimulated by agonist and ER's filling state respectively, while (1b) through the mechanically-activated Ca^{2+} channel by haemodynamic forces.

Agonist-stimulated Ca^{2+} influx

Adenosine triphosphate (ATP) is a multifunctional nucleotide which functions as a signalling molecule in the extracellular signalling. Its extracellular form is present in the circulating blood, being released primarily from platelets (121) and red blood cells (RBCs) (135). When ATP molecules are transported to the endothelial surface, they undergo dephosphorylation reaction on the EC surface by

the action of adenosine triphophatases (ATPases) and are converted to adenosine diphosphate (ADP).

On the endothelial cell (EC) surface, meanwhile, there are a family of G protein-coupled receptors (GPCRs) present. GPCRs are transmembrane receptors, which have part of the molecules protruding into the endothelial cytoplasm where it is coupled with the G protein complex consisting of subunits α, β and γ. The α subunit is bound with a unit of guanosine diphosphate (GDP) (Fig. 5.2).

When a ligand (i.e. ATP/ADP) binds to and activates the receptor (and thereby initiating Pathway (1a)), the latter undergoes a conformational change and attaches itself with the protein complex. Simultaneously, the GDP bound to the α subunit is exchanged for guanosine triphosphate (GTP). This causes the α subunit to disassociate from the protein complex, and to subsequently activate a membrane-bound enzyme phospholipase C (PLC) in the EC. This PLC cleaves phosphatidylinositol 4,5-bisphosphate (PIP_2), a phospholipid which is a component of the plasma membrane, leading to the production of diacylglycerol (DAG) and inositol trisphosphate (IP_3), a Ca^{2+}-mobilising second messenger i.e. a molecule that transmits signals from the cell membrane to the specific target molecules within the cell, that has diverse functions in human physiology. The process from the binding of ATP to the GPCR to IP_3 formation is described in Fig. 5.1 (shown with dashed box) and Fig. 5.2.

While DAG stays bound in the EC membrane, hydrophilic IP_3 diffuses into the cytosol and binds to the IP_3 receptor on the ER surface. This opens the Ca^{2+} channel on the ER surface, releasing the internally-stored Ca^{2+} into the cytosol. The increase in cytosolic Ca^{2+} following the release then leads to more Ca^{2+} channels to open and further Ca^{2+} to be released from the store in a manner of positive-feedback mechanism (termed calcium-induced calcium release, CICR (10)).

In addition to CICR, there is a separate Ca^{2+} entry mechanism into the cytosol in which the influx of Ca^{2+} takes place on a basis of the filling state of the ER store, termed capacitative calcium entry (CCE). The principle is that following the IP_3-induced depletion of the internal store, the extracellular Ca^{2+} enters the cytosol across the EC plasma membrane. However, the mechanism by which the information about the filling state of the ER is transmitted across the gap between the ER surface and the Ca^{2+} channels on the plasma membrane (8-20nm) (9; 77) is not yet fully understood, and is still somewhat disputed. Although there

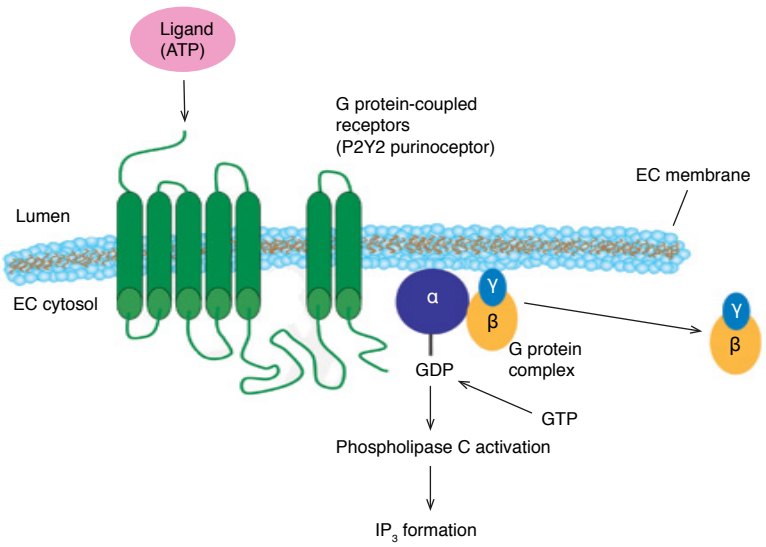

Figure 5.2: G protein-coupled receptor. Binding of a ligand (ATP here) triggers its conformational change, which results in the disassociation of the α subunit as the attached GDP is exchanged for GTP. This activates phospholipase C (PLC), which cleaves PIP_2 into IP_3 and a phosphate group. This series of reactions make up a part of agonist-induced, Ca^{2+}-dependent eNOS activation pathway shown in a dashed box in Fig. 5.1. Figure taken and modified from `http://www.sigmaaldrich.com/` (119).

have been various propositions to explain this mechanism, such as the release of diffusible factors from the ER upon depletion, vesicle fusion between the ER and the EC membrane, and direct interaction via membrane proteins (summarised in (9) and (110)) and each of these has been supported experimentally, the results are not, at this time, yet conclusive due to the difficulties in consistently reproducing the results. For example, the existence of the diffusible factor has been reported in xenopus oocytes, but its properties were observed to be markedly different from those observed endogenously in human cells (65). At present, the strongest theory among these is the protein-protein interaction called conformational coupling. It is based on the idea that the IP_3 receptor on the ER undergoes a conformational change upon the depletion of the store, resulting in a direct binding of the receptor and the Ca^{2+} channel in the EC membrane and thus allowing for the transmission of the information about ER's filling state. Nonetheless, CCE is deemed to be significant as a source of Ca^{2+} increase - it has been reported that CCE is required for sustained activation of eNOS (79).

Flow-induced Ca^{2+} influx

In addition to the influx pathways described above, there exists another route that brings extracellular Ca^{2+} into the cytosol, whereby the Ca^{2+} influx comes through flow-activated channels in the EC membrane ((1b) in Fig. 5.1). Experimental results observed that this type of Ca^{2+} channel, also called as mechanically-activated, stretch-activated or mechanosensitive channel, exists in human umbilical vein endothelial cells (HUVECs) (117) and renal tubule cells (64), and that the increase in cytosolic Ca^{2+} brought about by this channel is considerably greater than that by receptor-operated channels (137).

When flow-induced haemodynamic forces are exerted over the EC surface, these forces impose a tension gradient within the membrane and cause it to deform. The tension gradient would be uniaxial when no circumferential cell stretch is taken into account under a steady flow regime, as often assumed in the previous studies (27; 108; 137), or biaxial when the circumferential stretch due to the pressure pulse is also considered. This deformation gradient in turn induces strain energy within the membrane, which is then used as the gating energy (the difference of the energy state between open- and closed-configurations of an ion channel), leading to the opening of the Ca^{2+} channel and thus to the Ca^{2+} influx into the cytosol.

The resulting elevated cytosolic Ca^{2+} from the two influx mechanisms above results in its binding with Ca^{2+}-binding protein calmodulin, forming Ca^{2+}-calmodulin complex. This complex displaces caveolin-1, a membrane protein residing in caveolae (invagination in the EC plasma membrane), from the eNOS molecule. This removes the inhibitory effect of caveolin-1 on eNOS, and thereby activates eNOS.

5.3.3 Ca^{2+}-independent eNOS activation

This pathway represents another known eNOS activation pathway (shown as (2) in Fig. 5.1), elicited directly by WSS. The overall mechanism is that WSS exerted on the EC surface activates two kinases, phosphatidylinositol-3-OH (PI(3)K) and subsequently its downstream kinase protein kinase B (PKB), also known as Akt. Kinases are phosphotransferase, i.e. enzymes that transfer the phosphate group from high-energy donor to the target substrates within the cell (the process termed phosphorylation). In their activated state they phosphorylate specific residues of the eNOS enzyme, leading to its activation.

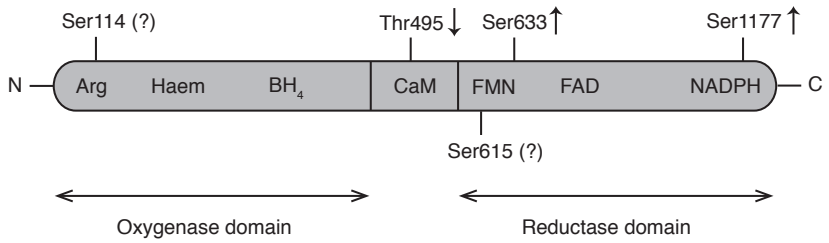

Figure 5.3: A simplified schematic of phosphorylation and substrate/cofactor binding sites of eNOS. The up/down arrows indicate the results of phosphorylation at the site on eNOS activity, i.e. phosphorylation of Ser1177 and Ser633 residues increases eNOS activity, while at Thr495 it has inhibitory effects. The effects of phosphorylation at Ser114 and Ser615 are still inconclusive (98). Based on the figure in Mount et al. (98).

A simplified schematic of eNOS enzyme and phosphorylation sites is shown in Fig. 5.3. eNOS is known to consists of C-terminal reductase and N-terminal oxygenase domains, arranged on each side of calmodulin binding site, the former of which contain binding sites for NADPH, FAD and FMN and the latter those for BH^4, haem (an iron-containing prosthetic group and a component of haemoglobin) and L-arginine.

Among the phosphorylation sites shown, Serine1177 residue (Ser1177) has been observed to be most significant. It has been associated with eNOS activation in response not only to WSS but also to humoral (e.g. bradykinin or insulin) or pharmacological (e.g statins) stimuli and subsequent increased NO synthesis, as well as enhancing eNOS activation from the Ca^{2+}-dependent pathway and increasing eNOS activation at resting level of cytosolic Ca^{2+} (98). It appears that phosphorylation at this residue causes a conformational change of eNOS enzyme, unblocking the electron transfer and thus activating eNOS (98).

Phosphorylation at residue Ser633 has also been observed to enhance eNOS activities. It has been reported to respond to similar stimuli to those listed above for Ser1177, although Ser633 phosphorylation is more implicated in the maintenance of eNOS activity following the initial activation by Ca^{2+}-dependent pathway and/or Ser1177 phosphorylation.

On the other hand, phosphorylation of eNOS at Threonine495 (Thr495) is known to reduce the eNOS activities, which appears to be due to its interference with the binding of Ca^{2+}-calmodulin complex to eNOS. It has also been reported

that phosphorylation of this site leads to the increase in production of superoxide anion O_2^- rather than that of NO.

The most significant characteristics of the direct activation of eNOS is that, unlike the agonist-stimulated pathway, it does not rely on the increase of cytosolic Ca^{2+} concentration (37; 98), and is not blocked by calmodulin antagonists, as observed by Dimmeler et al. (37). They also observed that the activation took place in the absence of extracellular Ca^{2+} and was maintained over hours. This is in contrast to the activation by agonists, where the influx of extracellular Ca^{2+} via CCE was required to maintain eNOS activities (79). This pathway is also included in the current model.

5.4 Endothelial nitric oxide (NO)

Once eNOS is activated, it catalyses the production reaction of NO from the substrates L-arginine, oxygen and NADPH in the presence of cofactors FAD, FMN and BH_4, of which reaction is expressed as:

$$\begin{aligned} &\textit{L-arginine} + 2O_2 + 1.5NADPH \\ &\xrightarrow{eNOS} \textit{L-citrulline} + NO + 1.5NADP^+ + 2H_2O \end{aligned} \tag{5.1}$$

This reaction starts with L-arginine and O_2 binding to the corresponding binding sites (*Arg* and *Haem* respectively in Fig. 5.3) of the activated eNOS. At the same time, an electron is taken from NADPH to the reductase domain and is transferred by FAD and FMN to the oxygenase domain. The electron is then further transferred to the haem group under the regulation of BH_4, where the haem iron undergoes a series of redox reactions, leading to the production of NO along with L-citrulline (the details of complete biochemical reaction pathways can be found in Chen and Popel's work (24)).

However, this is only one aspect of NO dynamics in the endothelium, the other being its scavenging by other molecules within the EC. It is a well-discussed phenomenon that the NO produced in the endothelium diffuses within the cell towards the underlying vascular smooth muscle cells (VSMCs) and causes them to relax. It is also considered important that, on the luminal side of the EC, NO

diffuses out of the EC into the lumen, and then is convected to exert its influence on the EC located downstream (109).

For the former case, NO needs to reach the VSMCs in order to exert its vasodilatory effects. However, while it travels through the cytosol in the EC, its diffusion is hindered by its interaction with other molecules within the cell, especially superoxide anion, O_2^-. O_2^- is a potent free radical (termed reactive oxygen species (ROS)), and due to having one electron missing from its valance, highly reactive. It is a byproduct of normal cell metabolism, and is mainly a part of oxygen-dependent immune activities and as a product of mitochondrial respiration. For example, in the former case, the typical reaction is that NADPH oxidase generates O_2^- by transferring electrons from NADPH (Fig. 5.3) across the membrane and couples them to molecular oxygen, leading to O_2^- formation. However, due to its toxicity, the concentration and activity of O_2^- are normally strictly controlled by enzymes such as superoxide dismutases (SODs), which neutralise O_2^- by the reaction:

$$2H^+ + 2O_2^- \xrightarrow{SOD} H_2O_2 + O_2 \tag{5.2}$$

This is a crucial process in maintaining the oxidative balance within the EC, since the excessive concentration of O_2^- or deficiency of SODs gives rise to a situation called oxidative stress in which, along with other damage, NO can be deactivated by O_2^-. In NO dynamics in the EC, this toxicity is particularly significant as not only does O_2^- react with NO more efficiently than any other molecule, but also the reaction itself is three times faster than its dismutation reaction by SODs (41). The damage caused by the deactivation of NO here is two-fold. Firstly, it directly leads to the decreased bioavailability of NO in the EC and VSMC, that is, the diminution of the anti-atherogenic properties of NO against inflammatory processes (detailed in Section 1.2.3), and an increase in the basal tone. Secondly, the reaction between O_2^- and NO leads to the formation of peroxynitrite $ONOO^-$, a reactive nitrogen species which acts together with ROSs to increase the oxidative stress further.

The reaction between NO and oxyhaemoglobin (oxyHb) is another source of NO scavenging. This mainly occurs when the NO produced within the EC diffuses out of the cell into the lumen and while being convected downstream. This part of endothelial-produced NO faces the same scavengers mentioned above during its diffusion from the production site to the EC membrane, and then once out

of the EC, is in contact with oxyHb contained in the flowing blood. Again this is a very efficient reaction, and once they are bound, NO's normal functions are irretrievable (53). The processes of the efflux and subsequent convection of NO themselves are beyond the scope of this study. However, the consequence of scavenging by oxyHb is still relevant since the overall availability of NO would also depend on the balance of the concentration gradients resulting from both the NO scavenging by oxyHb in the lumen and the NO consumption by VSMCs in the sub-endothelial space.

From the points described above, therefore, it can be summarised that the main determinants of the intracellular availability of NO in the EC are the production of NO (and therefore the concentration and activity of eNOS) and the activities of O_2^-, SODs and oxyHb.

5.5 Mathematical formulation

In this section, the cellular processes involved in the reactions from the physiological stimulations exerted by the flowing blood to NO production described in the previous sections are approximated and formulated mathematically. First, the reactions that lead to the activation of eNOS, which is the most significant process in the NO synthesis, and its triggering inputs are described. Included in this formulation is the introduction of pulsatile, biaxial approach in the computation of membrane strain energy (which governs the influx of extracellular Ca^{2+}) in addition to the conventional steady, uniaxial approach. Then the NO production and scavenging reactions is outlined along with the considerations that were made during the approximation of the reaction.

5.5.1 Model inputs

As outlined in Sections 5.3.2 and 5.3.3, there are two major pathways to achieve the activation: one dependent on and the other independent of the elevation of Ca^{2+} concentration. The former takes the concentration of agonists on the EC surface as inputs, while for the latter the process is initiated by WSS.

In the Ca^{2+}-dependent pathway, ATP is what first triggers the reaction. ATP, a blood-borne agonist that consists of a purine base adenine, a ribose sugar and three phosphate groups, is delivered to the EC surface by the flowing blood, where

it then undergoes dephosphorylation reaction by the action of the endothelial membrane ATPases:

$$ATP + H_2O \xrightarrow{ATPase} ADP + P' \tag{5.3}$$

where one of the phosphate groups ($P' = PO_4^{3-}$) is cleaved by the ATPase. The surface concentrations of ATP and ADP are both taken into account based on the finding that they both are highly effective in eliciting Ca^{2+} response (61). The products of further dephosphorylation, adenosine monophosphate (AMP) and adenosine, are not included in the modelling since they are known to have little influence on triggering the intracellular Ca^{2+} response.

As described previously, the surface concentration of the agonist is determined by the balance between its delivery to the EC surface by the flowing blood and consumption by the hydrolysis reactions. This condition is expressed with the representation of conservation of mass, in which the diffusive flux of ATP to the EC surface is balanced by the consumption due to the hydrolysis reaction and the surface source of ATP, i.e.:

$$D_{ATP} \frac{\partial \phi_{ATP}}{\partial \eta}\bigg|_{\eta=0} = K_{ATP}\phi_{ATP} - S_{ATP} \tag{5.4}$$

where D_{ATP} denotes the diffusion coefficient of ATP, ϕ_{ATP} the ATP concentration, η the surface normal coordinate (positive into the flow domain), K_{ATP} the reaction constant and S_{ATP} the ATP surface source. Here, the latter two require some clarification. Generally, the reaction rate of ATP hydrolysis k_{ATP} is governed by Michaelis-Menten kinetics, i.e.:

$$k_{ATP} = \frac{k_{ATPase \cdot max}}{\phi_{ATP} + K_{M \cdot ATP}} \cdot \phi_{ATP} \tag{5.5}$$

where $k_{ATPase \cdot max}$ is the maximum enzyme velocity for ATP hydrolysis (i.e. ATPases) and $K_{M \cdot ATP}$ the Michaelis-Menten constant for the reaction. However, it has been demonstrated that the concentration of the substrate ATP at which rate saturation is observed is very high ($> 100\mu M$) (61), and at low concentration of ATP, ϕ_{ATP} in the denominator of Eqn. 5.5 becomes insignificant. Therefore, the reaction rate formulation can be approximated with a first-order reaction with a

lumped constant $k_{ATPase \cdot max}/K_{M \cdot ATP} = K_{ATP}$, which gives the expression of the first term on the RHS of Eqn. 5.4:

$$k_{ATP} = K_{ATP}\phi_{ATP} \tag{5.6}$$

The surface source term of ATP S_{ATP} represents the phenomenon reported by several groups including Milner et al. (94), Bodin et al. (15; 16) and Yamamoto et al. (139) that ATP was released from the ECs in response to the stimulation by WSS. They observed that the release was rapid, a function of perfusion rates, the ATP level decayed to the pre-stimulation level following the release, and that ATP was repeatedly released upon re-exposure to flow although at a reduced rate.

The details of whether the release is sustainable under physiological condition has, at present, not been well documented, and is still controversial. The observed reduction in the release rate upon repeated stimulation could be argued to imply that the source could be depleting. In order to explain this diminution, the lack of adenosine (from which ATP can be synthesised by the action of ATP synthase) in the perfusion media (Krebs solution) (16), as well as the depletion of intracellular ATP store (14; 104), have been suggested, although both inconclusively. In the current study, the release term was included on the basis that the phenomenon of endothelial ATP release itself has been well-documented and observed in many studies such as those listed above, and also that it is postulated that ATP synthesis from adenosine is likely to take place to some degree under physiological conditions in which adenosine is present in the circulating blood.

ATP release rate S_{ATP} was formulated to have a sigmoidal dependence on the applied WSS based on John and Barakat's (61) model, i.e.:

$$S_{ATP} = S_{max}\left[1 - exp\left(\frac{-\tau}{\tau_0}\right)\right]^3 \tag{5.7}$$

where S_{max} is the maximum release rate and is taken to have the value of $10^{-6}\mu M m s^{-1}$ (61), τ the applied WSS and τ_0 the characteristic WSS. This choice of sigmoidal-dependence is based on that the function has been widely used to represent other physiological processes such as ion channel dynamics, and for ATP, it allows the expected behaviour of ATP, which should saturate as WSS is increased, to be represented.

The condition for ADP was defined similarly to that for ATP, which is expressed as:

$$D_{ADP}\frac{\partial \phi_{ADP}}{\partial \eta}\bigg|_{\eta=0} = K_{ADP}\phi_{ADP} - K_{ATP}\phi_{ATP} \tag{5.8}$$

where K_{ADP} is the reaction constant for ADP hydrolysis. The first term represents the hydrolysis of ADP into AMP and the second term the production of ADP from the hydrolysis of ATP.

The combined concentration of agonists $\phi = \phi_{ATP} + \phi_{ADP}$ specified by the expressions 5.4 and 5.8, along with the WSS computed in FLUENT based on Eqn. 3.3 will provide the input values to the EC dynamics model described in the next section.

5.5.2 Endothelial cell dynamics

In the endothelial cell dynamics, of which main building components are Ca^{2+} dynamics, eNOS activation and NO dynamics, key variables that characterise the processes involved are IP_3 (i), cytosolic free Ca^{2+} (C_c), Ca^{2+} stored within the ER (C_s), activated eNOS (n) and NO (N). The concentration distribution of each variable is assumed to be uniform within the ECs, and therefore a set of ordinary differential equations (ODEs) was used to express the rate of change of these variables. The descriptions and values of the model parameters used in the ODEs are summarised in Table 5.1. The formulation of i, C_c, C_s and n was partly adopted from Plank et al. (108) and Comerford et al. (27).

IP_3

The formation of IP_3 is, as described previously, the result of complex signal transduction reactions involving G protein-coupled receptor dynamics triggered by agonist binding (Fig. 5.2). The process is governed by its production represented with Michaelis-Menten functions of the agonists and the cytosolic Ca^{2+}, and by natural decay at a constant rate μ_1, thus:

$$\frac{di}{dt} = k_i \frac{\phi}{K_c + \phi}\frac{C_c}{K_1 + C_c} - \mu_1 i \tag{5.9}$$

Cytosolic Ca^{2+}

The rate change of cytosolic Ca^{2+} (C_c) depends on the balance of Ca^{2+} between its influx into and efflux out of the cytosol. So:

$$\frac{dC_c}{dt} = q_{rel} - q_{res} - q_{out} + q_{in} \tag{5.10}$$

q_{rel} represents the rate of Ca^{2+} release from the ER upon IP_3 binding. Based on the observation by Meyer and Stryer (91) that the release rate has a linear dependence on C_s and also is proportional to a cubic of a saturation function of IP_3, therefore:

$$q_{rel} = \left(\frac{i}{K_2 + i}\right)^3 C_s \tag{5.11}$$

The cubicity arises due to the IP_3 receptors on the ER surface requiring three IP_3 molecules to be opened.

The efflux of cytosolic Ca^{2+} out of the EC, q_{out}, is the result of the Ca^{2+} ATPase on the plasma membrane, which, as a regulator of cytosolic Ca^{2+}, removes Ca^{2+} ions upon the exposure to high intracellular level of Ca^{2+}. This process has been described using Michaelis-Menten kinetics by Valant et al. (131) and expressed as:

$$q_{out} = \frac{k_{out} C_c}{K_5 + C_c} \tag{5.12}$$

q_{res} describes the resequestration of Ca^{2+} back into the ER by the action of the ion transporter, Ca^{2+} ATPase, on the ER surface. It is dependent on the cytosolic Ca^{2+} and is proportional to its squared saturation function, i.e.:

$$q_{res} = k_{res} \left(\frac{C_c}{K_3 + C_c}\right)^2 \tag{5.13}$$

The power of two comes from Ca^{2+} ATPase transporting two Ca^{2+} ions in one cycle.

q_{in} represents the influx of extracellular Ca^{2+} directly into the cytosol via CCE and the flow-activated Ca^{2+} channel (1(a) and 1(b) in Fig. 5.1, respectively).

The entry via CCE depends on the depleted state of the internal store, and therefore modelled to be proportional to the decrease of Ca^{2+} below the basal level in the ER ($C_{s,0}$). The influx rate will also depend on the rate gradient between the cytosolic Ca^{2+} and the extracellular Ca^{2+} (C_{ex}), which was taken to be constant due to the latter being significantly greater than the former. So:

$$q_{in} = \frac{k_{CCE}}{K_4 + n}(C_{s,0} - C_s)(C_{ex} - C_c) + \gamma q_{max} F \tag{5.14}$$

The second term on the RHS represents the direct entry of extracellular Ca^{2+} through the Ca^{2+} channels that are activated by haemodynamic forces exerted on the ECs. γ here is the parameter that governs the degree of relative contribution of the Ca^{2+} -dependent pathway, and was taken to be 0.1 based on the experimental findings by Dimmeler et al. (37) that the flow-induced eNOS activation, compared with Ca^{2+}-dependent one, is more significant. This observation has been further, though indirectly, supported by Corson et al. (28) who observed that the ECs released NO more potently when stimulated by WSS rather than Ca^{2+}-mobilising agonists. Now, F here is the parameter that represents the fraction of the flow-activated Ca^{2+} channels that are in an open-state, which defines the rate of extracellular Ca^{2+} influx and has a Boltzmann dependence on the level of gating energy within the membrane. This gating energy of the Ca^{2+} channels, which is the energy difference between the open and closed conformations at deformation-free state, in turn is associated with the strain energy stored within the membrane, W. Taking these points into account, F is expressed as:

$$F = \frac{1}{1 + \alpha \cdot \exp\left\{\frac{-f_e \cdot W}{k_B T N}\right\}} \tag{5.15}$$

In order to compute F, therefore, the membrane strain energy W must now be formulated.

Membrane strain energy For the modelling of the strain energy, the derivation of that for the red blood cell (RBC) membrane based on the large deformation theory of elasticity was used. As briefly described previously, the EC membrane undergoes deformation due to the tension gradient induced by the haemodynamic forces applied on its surface. The tension gradient can be either

uniaxial or biaxial, depending on the assumptions made with regard to the flow regime.

The conventional approach, as adopted previously by Wiesner et al. (137), Plank et al. (108) and Comerford et al. (27), has assumed steady flow, in which the tension gradient only in the flow direction was taken into account on a basis of the *tension-field* hypothesis. This hypothesis states that the cell membrane cannot support compressive stress in its plane because the membrane thickness is far smaller than the membrane length and width, and that a situation exists where one of the principal strains in the deformed membrane is positive while the other is negative or negligible (48). Under steady flow, this can be assumed to hold since the effects of blood pulsatility, which gives rise to the transient positive membrane strain as well as the positive axial strain, are not included.

The other, biaxial approach includes the circumferential membrane stretch induced by the pressure pulse of the cardiac cycle, and is incorporated in the current study. This was motivated by the observations by Steinman et al. (122) and Joshi et al. (62) that there was no statistically significant correlation between wall-shear parameters such as WSS and OSI, both commonly used as an indicator of atherogenicity, and the intimal thickness. Concurrently, stress phase angle (SPA, described in Section 2.2.2) was emerging as a relevant parameter in atherosclerosis research. Dancu et al. (29; 30) demonstrated that negative SPA elicits vasoactive responses or change in gene patterns, whereas Tada et al.'s (125) numerical comparison of WSS, OSI and SPA distributions with clinical observation of plaque localisation demonstrated that the negative SPA was a more relevant parameter. Additionally, the results obtained with the biaxial-tension assumption undoubtedly are physiologically more realistic and reflect the environment in which plaques develop.

Endothelial NO was to be computed using both approaches for the purpose of extension and development of existing models, and therefore the expression for the membrane strain energy (where the difference in modelling approach should first become apparent) was formulated using both approaches. The details of derivation can be found in Skalak et al. (120) and Tada et al. (124).

The formulation starts with the definition of the state of deformation of the membrane. As shown in Fig. 5.4, when the initial membrane lengths in the flow and circumferential directions are defined as (x_1, x_2) and the final, post-deformation lengths (y_1, y_2), then the stretch ratios can be defined as the ratios

of final to initial lengths of the membrane in each direction. Thus:

$$\lambda_1 = \frac{\partial y_1}{\partial x_1}, \quad \lambda_2 = \frac{\partial y_2}{\partial x_2} \tag{5.16}$$

Then the Green's strain tensor components for large deformation are defined as:

$$e_{11} = \frac{1}{2}\left(\lambda_1^2 - 1\right), \quad e_{22} = \frac{1}{2}\left(\lambda_2^2 - 1\right) \tag{5.17}$$

which define the strain invariants for the cell membrane:

$$I_1 = 2\left(e_{11} + e_{22}\right), \quad I_2 = 4e_{11}e_{22} + 2\left(e_{11} + e_{22}\right) \tag{5.18}$$

In the finite deformation theory, strain energy W is assumed to be a function of e_{11} and e_{22}, and so when S_{ij} is a stress referred to the initial coordinates (Piola-Kirchoff tension) it has the following relationship with the strain energy:

$$S_{ij} = \frac{\partial W}{\partial e_{ij}} \tag{5.19}$$

A form of strain energy (W) proposed in (120) takes the form:

$$W = \frac{A}{4}\left(\frac{1}{2}I_1^2 + I_1 - I_2\right) + \frac{B}{8}I_2^2 \tag{5.20}$$

where A and B are material constants. A is defined as:

$$A = G_1 \times H_m \tag{5.21}$$

where G_1 is the shear modulus of the cell membrane and H_m the cell membrane thickness. In Skalak et al.'s (120) original study on RBC membranes, B, which is representative of the cell membrane's areal stiffness, was chosen to be much larger than A so that the areal stiffness is appropriately large, in order to incorporate the empirical observation that RBC membranes deform relatively easily but have strong resistance to any areal change. However, whether the mechanical properties of ECs are comparably similar to those of RBCs *in vivo* is not yet known. Also, it has been reported that varying the value of areal stiffness does not have

significant effects on strain energy distribution (126). For these reasons, B was selected to have the same order of magnitude as A in the present model.

S_{11} and S_{22} can be derived by evaluating Eqns. 5.19 with 5.18 and 5.20:

$$S_{11} = \frac{\partial W}{\partial e_{11}} = Ae_{11} + B\left(2e_{11}e_{22} + e_{11} + e_{22}\right)\left(2e_{22} + 1\right) \tag{5.22}$$

$$S_{22} = \frac{\partial W}{\partial e_{22}} = Ae_{22} + B\left(2e_{11}e_{22} + e_{11} + e_{22}\right)\left(2e_{11} + 1\right) \tag{5.23}$$

For small tensions, T_1 and T_2, tensions in the final position, are equal to S_{11} and S_{22}, and thus the final forms of the tensions are:

$$T_1 \cong S_{11}, \quad T_2 \cong S_{22} \tag{5.24}$$

Integrating the equation of mechanical equilibrium across the cell membrane in the flow direction gives the relationship between the tension gradient and load borne by the EC membrane:

$$\frac{\partial T_1}{\partial x_1} + (1 - \varepsilon)\,\tau = 0 \tag{5.25}$$

where ε is the fraction of WSS borne by the surface of the EC. Doing the same in the transverse direction gives

$$T_2 = const. \tag{5.26}$$

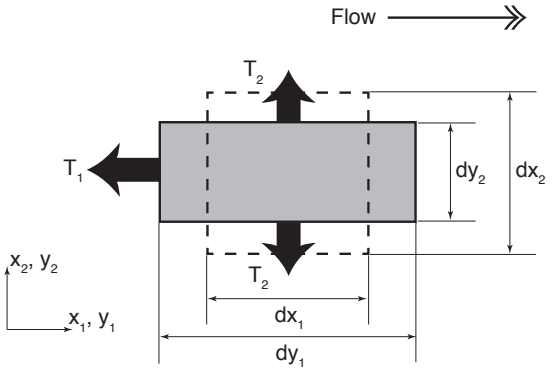

Figure 5.4: A schematic of membrane deformation under biaxial tension. dx_1 and dx_2 denote the undeformed dimensions and dy_1 and dy_2 deformed, in the flow (subscript 1) and circumferential (subscript 2) directions.

Membrane strain energy under uniaxial tension As stated above, in the absence of significant positive circumferential stretch the uniaxial tension gradient can be assumed on the basis of the *tension-field* hypothesis (48) in the derivation of the membrane strain energy. From the mechanical equilibrium of the EC membrane, T_1 and T_2 were defined as in the previous section but with $T_2 = 0$. Evaluating these with the expression for strain energy for the cell membrane (120) leads to the relationship between strain energy and WSS under uniaxial tension (137):

$$W_u = \frac{\left[(1-\varepsilon)\,\tau L + \sqrt{16A^2 + \tau^2 L^2\left(\varepsilon^2 - 2\varepsilon + 1\right)} - 4A\right]^2}{8\left[(1-\varepsilon)\,\tau L + \sqrt{16A^2 + \tau^2 L^2\left(\varepsilon^2 - 2\varepsilon + 1\right)}\right]} \tag{5.27}$$

where L is the EC length.

Membrane strain energy under biaxial tension The pulsatility of blood gives rise to the fluctuation of pressure during the cardiac cycle, and this in turn causes the vessel wall to undergo cyclic stretch and contraction. This results in not only the strain in the flow direction but also that in the circumferential direction positive, i.e. $T_2 \neq 0$. T_2 therefore must be defined as a function of time. This was formulated based on Tada et al.'s (124) single-cell model.

Equation 5.20, expressed in terms of the stretch ratios in the flow (λ_1) and circumferential (λ_2) directions is:

$$W_b = \frac{A}{8}\left[\lambda_1^4 + \lambda_2^4 - 2\left(\lambda_1^2 + \lambda_2^2\right) + 2\right] + \frac{B}{8}\left(\lambda_1^2\lambda_2^2 - 1\right)^2 \tag{5.28}$$

for which λ_1 and λ_2 are evaluated in the process of developing relationships between applied haemodynamic stresses and membrane stretches (for details, see (124)).

Defining ι as the component of displacement in the flow direction in the undeformed body and κ that in the transverse direction, Eq. 5.22 can be rewritten as:

$$T_1 = A\frac{\partial \iota}{\partial x_1} + B\left(2\frac{\partial \iota}{\partial x_1}\frac{\partial \kappa}{\partial x_2} + \frac{\partial \iota}{\partial x_1} + \frac{\partial \kappa}{\partial x_2}\right)\left(2\frac{\partial \kappa}{\partial x_2} + 1\right) \tag{5.29}$$

Differentiating both sides of Eq .5.29 and combining it with Eq .5.25 leads to a second-order differential equation for ι,

$$\left[A + B\left(2\frac{\partial \kappa}{\partial x_2} + 1\right)^2\right]\frac{\partial^2 \iota}{\partial x_1^2} + (1-\varepsilon)\,\tau = 0 \tag{5.30}$$

where τ here is the pulsatile WSS. Solving this equation with boundary conditions of $\iota|_{x_1=\delta} = \iota|_{x_1=\delta+L} = 0$ gives:

$$\iota = -\frac{(1-\varepsilon)\,\tau}{2\left[A + B\left(2\frac{\partial \kappa}{\partial x_2} + 1\right)^2\right]}\,(x_1 - \delta - L)\,(x_1 - \delta) \tag{5.31}$$

where δ is the displacement of the EC membrane under flow and expressed as:

$$\delta = \frac{H_{ec}}{G_2}\varepsilon\tau \tag{5.32}$$

From the relationship between the strain and membrane stretch ratios (Eq. 5.17):

$$\lambda_1 = \sqrt{2\frac{\partial \iota}{\partial x_1} + 1} \tag{5.33}$$

and thus using Eq. 5.31 in the expression above gives the stretch ratio in the flow direction.

Equation 5.17 also gives the circumferential strain component:

$$\frac{\partial \kappa}{\partial x_2} = \frac{1}{2}\left(\lambda_2^2 - 1\right) \tag{5.34}$$

The stretch ratio in the transverse direction, λ_2, is assumed to be a known function of time t only and takes the form defined by the oscillatory component of the Fourier series of the inlet waveform. Thus when the oscillatory component is represented by:

$$F_{osc} = \left\{\sum_{n=1}^{M} C_n \cos\left(\frac{2\pi n t}{T}\right) + \sum_{n=1}^{M} D_n \sin\left(\frac{2\pi n t}{T}\right)\right\} \tag{5.35}$$

when the diameter of the vessel changes during the cycle by 5%, λ_2 is then defined as:

$$\lambda_2 = 1.025 + 0.025\,(a \cdot F_{ocs} + b) \tag{5.36}$$

where a and b are scaling constants. Evaluating Eqn. 5.28 with the expression for stretch ratios in the flow and circumferential directions 5.33 and 5.36 gives the strain energy under biaxial tension.

W_u and W_b determined here are then substituted into the open-channel fraction function (Eqn. 5.15), which in turn completes the expression for the influx of extracellular Ca^{2+}, q_{in} (Eqn. 5.14).

Stored Ca^{2+}

The rate of change of internally-stored Ca^{2+} (C_s) is determined by the combined rate of its release (q_{rel}) from and resequestration (q_{res}) back into the ER, so:

$$\frac{dC_s}{dt} = -V_r\,(q_{rel} - q_{res}) \tag{5.37}$$

where V_r is the ratio of the volume of the cytosol to that of ER, required to impose mass balance.

Activated eNOS

The overall mechanism of eNOS activation is a combination of three processes, i.e. Ca^{2+}-dependent activation, deactivation and direct activation independent of Ca^{2+} elevation. Ca^{2+}-dependent activation is brought about by calmodulin binding to eNOS which causes the inhibitory enzyme caveolin-1 to be displaced. This reaction has a Michaelis-Menten dependence on the cytosolic Ca^{2+} concentration. The deactivation of eNOS occurs due to the enzyme becoming re-associated with caveolin-1, and is modelled to occur at a proportional rate to eNOS concentration with a rate constant μ_2. Lastly, the direct, Ca^{2+}-independent activation via WSS-induced phosphorylation of eNOS is also expressed with the weighting of $(1-\gamma)$, reflecting the previous observation that it is more dominant. Putting these three processes together, the overall rate of change of eNOS (n) is given as:

$$\frac{dn}{dt} = \frac{k_{dis}C_c}{K_6 + C_c} - \mu_2 n + (1-\gamma) g_{max} F \tag{5.38}$$

NO

The overall rate of change of NO within the EC was modelled to consist of the production term and the scavenging term and is given as:

$$\frac{dN}{dt} = k_N n - \mu_3 N \tag{5.39}$$

The NO production term, the first on the RHS, was modelled to have a linear-dependence on the eNOS concentration, based on the numerical analysis by Chen et al. (24) who calculated NO production rates in arterioles and venules with different eNOS concentrations. It was observed in their study that, after the initial transient increase in the NO production ($\sim 2s$), the reaction quickly reached a quasi-steady state regardless of eNOS concentration. Plotting the NO concentration against that of eNOS revealed a linear dependence, giving proportionality constants of 0.4 in arterioles and 0.35 in venules. The value of 0.4 is chosen in this study for the value of k_N.

The leak term, the second on the RHS, is an approximation of the deactivation and scavenging reactions of NO. As described in Section 5.4, the overall availability of NO within the endothelium is determined by the balance between its production and scavenging or deactivation, the latter of which in turn depends on the interaction between NO, O^{2-}, SODs and oxyHb. Another reaction constant is therefore needed here in order to model their combined effects on the overall NO availability. Determination of reaction constants of this kind should ideally be based on experimental results or carried out in the similar conditions or numerical results conducted based on them, but at the time of modelling, to the author's best knowledge, the value that could represent the reaction involved in the current model had not been found. It is extremely difficult to determine the rate of their combined reactions due to the complex interactions between the substrates and with other enzymes (i.e. between NO and O_2^-, O_2^- and SODs, NO and oxyHb and NO and $ONOO^-$). Therefore, the overall reaction constant for the leak term was estimated by solving Eqns. 5.9, 5.10, 5.37, 5.38 and 5.39 with various values of μ_3 under steady, mean-flow condition, and comparing the NO concentration obtained in the CCA, which is taken to be representative of the physiological NO concentration, to that experimentally observed. Among the values tested, μ_3=0.5 gave the value of 1.5μM, which was the closest to 1.3μM, the NO concentration observed experimentally by Malinski et al. (84) and numerically by Lancaster et

al. (72). While obtaining the value, the effects of NO scavenging and overlapping of NO concentration due to its being released from multiple sources are not taken into account. These should not be ignored while determining the physiological NO concentration, since it would be reasonable to assume that, at least in large arteries, all ECs are exposed to NO scavenging sources to some extent. It has been also reported that NO mainly acts in a paracrine manner (72). However, the degree of their combined effects is still uncertain, and therefore 1.3μM is taken to be the physiological concentration of NO in the present study.

Table 5.1: Simulation parameters. Values were taken from (24; 108; 137).

Expressions	Values and descriptions
α	2, a parameter that governs the open-state probability of ion channels
γ	0.1, relative contribution of the Ca^{2+}-dependent pathway
μ_1	$0.2s^{-1}$, IP_3 disassociation rate
μ_2	$0.0167s^{-1}$, eNOS-caveolin association rate
μ_3	$0.4s^{-1}$, NO disassociation rate
τ_0	$1.75Pa$, characteristic WSS
cav (subscript)	Cycle-averaged (over one cardiac cycle)
C_{ex}	$1500\mu M$, external Ca^{2+} concentration
$C_{s,0}$	$2830\mu M$, Ca^{2+} concentration in ER at resting state
D_{ADP}	$2.36 \times 10^{-10} m^2 s^{-1}$, diffusion coefficient of ADP
D_{ATP}	$2.36 \times 10^{-10} m^2 s^{-1}$, diffusion coefficient of ATP
f_e	0.013351, the fraction of the membrane strain energy used to gate WSS-activated Ca^{2+} influx channels (initial estimate)
G_1	$1000Pa$, membrane shear modulus
G_2	$10Pa$, cell body shear modulus
g_{max}	$0.06\mu M s^{-1}$, maximum WSS-induced eNOS activation rate
H_m	$10nm$, EC membrane thickness
H_{ec}	$5\mu m$, endothelial cell height
K_1	$0\mu M$, Michaelis-Menten constant
K_2	$0.2\mu M$, Michaelis-Menten constant
K_3	$0.15\mu M$, Michaelis-Menten constant
K_4	$5\mu M$, Michaelis-Menten constant
K_5	$0.32\mu M s^{-1}$, Michaelis-Menten constant
K_6	$0.45\mu M$, Michaelis-Menten constant
k_B	$1.3806504 \times 10^{-23} JK^{-1}$, Boltzmann constant
K_c	$0.026\mu M$, Michaelis-Menten constant
k_i	$5.46 \times 10^{-3} \mu M s^{-1}$, IP_3 production rate
K_{ADP}	$6.45 \times 10^{-7} m s^{-1}$, ADP reaction rate
K_{ATP}	$1.68 \times 10^{-6} m s^{-1}$, ATP reaction rate
k_{CCE}	$5.7 \times 10^{-6} s^{-1}$, Ca^{2+} influx rate via CCE
k_{dis}	$0.09\mu M s^{-1}$, eNOS-caveolin disassociation rate
k_{out}	$24.7\mu M s^{-1}$, Ca^{2+} efflux rate
k_{res}	$5\mu M$, Ca^{2+} resequestration rate
L	$35\mu m$, EC length
N	$1\mu m^{-2}$, area channel density
q_{max}	$17.6\mu M$, Max. WSS-induced Ca^{2+} influx rate
S_{max}	$1.0 \times 10^{-6} \mu M s^{-1}$, maximum ATP release rate
T	$310K$, absolute temperature
V_r	3.5, cytosol-to-ER volume ratio
W_u	Strain energy under uniaxial tension in steady flow
W_b	Strain energy under biaxial tension in pulsatile flow

5.6 Implementation in FLUENT

Equations formulated above for cellular solution variables, i.e. Eqns. 5.9, 5.10, 5.37, 5.38 and 5.39, define an initial-value problem with the initial conditions of:

$$i(0) = 0, \quad C_c(0) = C_{c,0} \quad C_s(0) = C_{s,0}, \quad n(0) = n_0, \quad N(0) = 0$$

The first four conditions were based on those used and demonstrated to be stable in previous studies (27; 108) for the given parameters and conditions. For nitric oxide, the initial condition was taken to be zero since its resting value within the EC for the given conditions of stimulants had not been found in the literature where the most values cited were recorded *in vitro* using various other stimuli. In addition, given NO's high reactivity, it would have reacted with scavengers if it was present in the EC. Therefore the assumption of NO concentration initially being zero was deemed justifiable in the absence of continuous stimulation.

This was solved using adaptive fifth-order Runge-Kutta method coded into the simulation via FLUENT's user-defined function (UDF) (the code is included in Appendix. B). The execution procedure of the UDF is as follows. Since this function is executed outside FLUENT's standard solution sequence, the domain to which the function would be applied must first be specified. In the case of EC dynamics it is relevant only in the vessel wall of the geometry (i.e. excluding the inlet and outlets). This was ensured by first identifying the particular domain ID (i.e. for the wall) that had been given by FLUENT at the problem-setup stage, and then by hard-coding it into a macro in the UDF. By passing the domain ID back into FLUENT, the cells that belong to the wall domain can be identified, which were then looped over by using a face macro to ensure that the specified calculations were carried out in the relevant cells. This UDF is executed in each wall cell after the solution converges in steady-flow calculations and at the end of each time-step in transient flows, taking the solutions of local WSS and the combined agonist concentrations ($\phi = \phi_{ATP} + \phi_{ADP}$) in each cell as inputs, returning the computed spatially-varying solution variables IP_3, cytosolic Ca^{2+}, stored Ca^{2+}, activated eNOS and NO when the convergence criteria were satisfied, that is, when the changes in solution variables have reached below 0.001 for all solution variables.

Chapter 6

Carotid Artery Haemodynamics

6.1 Introduction

This chapter presents the results obtained for the characteristics of blood flow through the carotid artery bifurcation (CAB). It has been emphasised in the previous chapters that haemodynamics plays a significant role in the maintenance of vascular homeostasis as well as the pathophysiology of atherosclerosis, and therefore it is of considerable importance that the local flow features brought about by the geometrical features of the CAB are studied and analysed carefully. Particular focus was placed on the quantitative analysis of WSS, which was carried out through the validation of numerical and experimental data obtained concurrently using the geometries derived from the identical data set and matching boundary conditions.

This validation process of numerical flow data is particularly important, not only because it ensures the credibility of the numerical data itself but also because the accuracy of flow solutions heavily influences the input values to the subsequent cellular processes (i.e. agonist concentration and WSS). Results obtained from numerical modelling should ideally be validated against experimental results obtained under the same or similar conditions wherever possible to establish the credibility of the data. However, numerical formulations of physiological processes often becomes more complex and diverse than those that could be carried out experimentally or clinically due to the inherent flexibility and versatility of the CFD approach (Section 4.1), and as a result, the validation of the results obtained is often not practical or possible, predominantly because of the diffi-

culties faced in obtaining *in vivo* data in the corresponding environment. This is also true for the cellular dynamics results obtained in the present study, and therefore it is particularly apposite here to ensure the accuracy of the solution at the flow-stage.

Despite its importance, however, detailed, quantitative validation studies of carotid artery haemodynamics have been scarce. Those who have attempted this often involved the comparison of numerical prediction with the velocity data obtained by magnetic resonance imaging (MRI) (17; 87; 144), but their analyses, particularly those of flow morphology, were very limited due mainly to the insufficient spatial resolution of MRI, and were therefore predominantly qualitative.

From the experimental point of view, the importance of data validation still holds. The technique used in this validation was particle image velocimetry (PIV), which offers superior spatial resolutions compared with other experimental techniques such as laser doppler velocimetry or *in vivo* flow visualisation technique such as MRI. However, PIV is still a developing technique, and therefore requires data validation in order to establish the validity of the technique itself. WSS is a particularly suitable parameter for this purpose as its calculation in experimental regimes requires the measurement of the velocity field and its differentiation, during which errors tend to become augmented, and therefore it is critical that the measurement errors are reduced as much as possible and that experimental results were confirmed via cross-validation with numerical results.

The details of the CAB model selection and geometry, which was also used in the cell dynamics model, and brief descriptions of PIV are first outlined in this chapter. The quantitative analysis of the axial and secondary velocities, WSS and finally error analyses, are then presented. The results presented in this chapter are based on the results presented in the previous publication by Dr. N. Buchmann (Monash University, Victoria, Australia) and the author (20). All PIV measurements were performed by Dr. Buchmann and the analysis of both PIV and CFD data sets were carried out by the author and Dr. Buchmann.

6.2 Carotid artery bifurcation model geometry

For the present study, the objective was to investigate the effects of vascular geometry on atherogenesis, so the carotid artery bifurcation (CAB) was chosen as a model geometry. The CAB is present in a pair (left and right) and consists of the common carotid artery (CCA) bifurcating into two daughter arteries, the internal (ICA) and the external (ECA) arteries (Fig. 6.1). The left CCA originates directly from the aortic arch whereas the right CCA from the brachiocephalic artery which branches off from the aortic arch. The internal carotid arteries in both CABs supply cerebral blood flow, and the ECAs the neck and face.

The selection of the geometry was primarily motivated by the frequent localisation of atherosclerotic lesions in the bifurcation and its clinical relevance of the geometry in the research of atherosclerosis.

It had been previously established that the CAB, along with coronary arteries, was one of the most atherosclerosis-prone sites in the human vasculature. DeBakey et al.'s (36) statistical study observed that the major branches of the aortic arch (which includes the CAB) was one of the predominant sites of the disease, along with the coronary arteries and branches of the abdominal aorta. This tendency for localisation is now widely believed to be due to the presence of the carotid sinus (a bulbous dilation of the vessel at the origin of the ICA shown in Fig. 6.1). The geometrically focal nature of atherosclerosis had been observed previously, and as the geometry is reflected on the endothelium in the form of WSS, numerous studies had been carried out attempting to establish the correlation between the plaque localisation and WSS(6; 69; 142). Although the results obtained from these studies pointed strongly to the correlation between intimal thickening and WSS, the degree of involvement and the role of WSS in the initiation of atherosclerosis could not be established from these results, and was still not fully understood.

Additionally, as it was described in Section 1.2.5, atherosclerotic plaques that develop in this area often have serious clinical consequences such as thrombosis and embolism. These are the result of the plaques protruding into the lumen or breaking off, obstructing or completely blocking the blood flow to the brain. In severe cases, these lead to ischemic strokes, which account for the majority (88% (128)) of all stroke cases. The mortality rate itself has been decreasing and was around 2.87% in the United States in 2003, but many patients suffer from

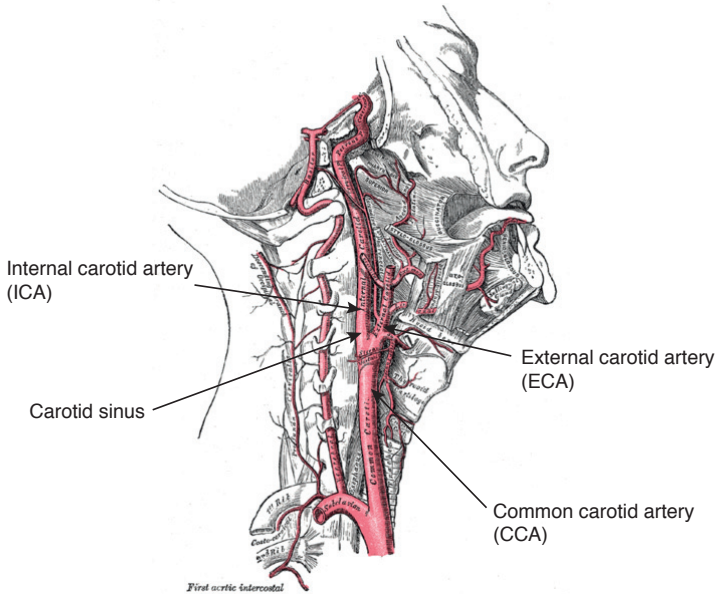

Figure 6.1: The location of carotid artery bifurcation (CAB). The common carotid arteries (CCA) branch off from the aortic arch (in the case of the right CCA show in the figure, via the brachiocephalic artery) and bifurcate into the internal (ICA) and the external (ECA) arteries. The bulbous dilation of the vessel located at the origin of the ICA is the carotid sinus. Figure taken and modified from `http://www.bartleby.com/` (54).

recurring attacks and long-term, serious disability (128). Also, the patients who originally have developed atherosclerosis in this region had greater tendency to eventually develop the disease also in the branches of the abdominal aorta, and vice versa (36).

The CAB geometry used in this study was a type termed "tuning fork-shaped average human carotid bifurcation" (TF-AHCB, shown in Fig. 6.2), adopted from that developed by Ding et al. (38).

In relation to the choice of model geometry, most initial experimental and numerical studies adopted a "Y-shaped average human carotid bifurcation" (Y-AHCB) geometry that consisted of the CCA bifurcating into the ICA and ECA, both of which were straight (11; 12; 69; 105; 142). Although the geometrical deviation of this model from that of the physiological CAB was obvious, this had become a standard model to study CAB haemodynamics primarily due to its relative ease of construction particularly for experimental studies. Also, due to the still-developing experimental techniques and the nature of flow experiments itself, it was not likely to be feasible or prioritised, at least at this stage, to obtain the full 3D flow field using a realistic flow domain and compare it with clinical

plaque distribution data. In numerical studies, on the other hand, the data obtained using this geometry was often used as control data against which that obtained under physiologically more realistic model settings (e.g. wall compliance (107)) was compared.

Recently, Ding et al. (38) focused on the correlation between an emerging wall parameter termed oscillatory shear index (OSI) and plaque localisation. OSI was originally proposed by Ku et al. in their work published in 1985 cited above (69) and is a measure of deviation of instantaneous WSS from its average direction. It had been shown to display high degree of correlation with plaque localisation on the inner and outer walls of the carotid sinus, but not at other locations. Ding et al. (38) questioned whether this weak overall correlation was due to the departure of the Y-AHCB geometry from the corresponding physiological configuration. From the CAB specimens obtained in autopsy, they found that, in many cases, the ICA was bent inwards either at the CCA-ICA intersection (spoon-shaped) and at the end of the sinus (tuning fork-shaped), and that the Y-shaped specimen with straight daughter arteries consisted only 8% of all cases compared to 51.35% of tuning fork- and 40.54% of spoon-shaped cases. Based on these statistics and the observation that the distal portion of the ICA approximately paralleled the CCA, they selected the tuning fork-shape for the model geometry and developed an average carotid bifurcation glass model (tuning fork-shaped human average carotid bifurcation, TF-AHCB) as per the description above with the bifurcation angle of 50°. The flow visualisation results obtained using this geometry and compared against those obtained using the Y-AHCB (11; 69) demonstrated significant improvement in the correlation of OSI and intimal thickness on the top and bottom walls of the bifurcation where the correlation was the weakest in the Y-AHCB models. The validity of OSI as a correlating factor between vessel geometry and plaque formation had not been fully established (122), but Ding et al's results were nonetheless encouraging, and since the TF-AHCB was derived from those that represented the largest population of specimens, the choice of TF-AHCB was deemed reasonable.

Another reason for choosing this geometry was its relative simplicity. This was a significant factor in the validation study of haemodynamics presented in the chapter since it facilitated the accurate construction of the physical experimental model.

The essential geometrical parameters were the diameters of the CCA, ICA

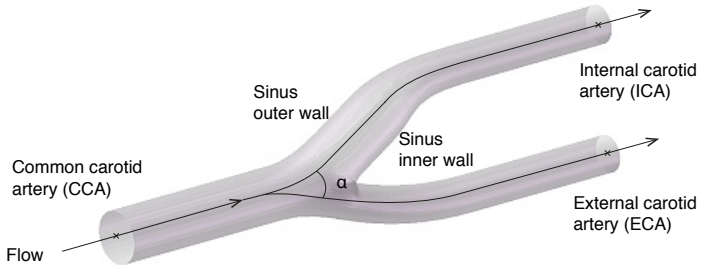

Figure 6.2: Mid-section of the tuning fork-shaped average human carotid artery bifurcation (TF-AHCB) model geometry. The common carotid artery (CCA, diameter D=20mm) branches into the internal (ICA, diameter d_{int}=0.72D) and external (ECA, d_{ext}=0.69D) carotid arteries at the bifurcation angle $\alpha = 50°$. Flow split was ICA:ECA=7:3. Carotid sinus, a bulbous dilation of the vessel, is present at the origin of the ICA. The walls in the ICA and ECA near the flow divider were defined as the inner walls of the bifurcation.

and ECA ($D = 20mm$, $d_{int} = 0.72D$ and $d_{ext} = 0.69D$ respectively) and the bifurcation angle ($\alpha = 50°$) (Fig. 6.2), which made the model dimensionally similar to that developed by Ding et al. (38). The CCA diameter value of $20mm$, which was scaled up from the typical physiological value of $\approx 6mm$ by a factor of 3.2, was for the ease of experimental model construction and in order to increase the spatial resolution in the PIV measurements.

6.3 Wall shear stress calculation

For an incompressible Newtonian fluid, WSS is proportional to the rate of deformation tensor ($\dot{\varepsilon}$ in Appendix A.3.1). When the spatial coordinates are denoted as $\mathbf{x} = (x, y, z)$, then WSS can be expressed in terms of local wall shear rate (WSR) as follows:

$$WSS = \mu \left[\left(\frac{\partial u}{\partial y} \right)^2 + \left(\frac{\partial w}{\partial y} \right)^2 \right]^{0.5} \Bigg|_{y=0} \tag{6.1}$$

where the coordinates x and z were defined as the wall-parallel directions and y as the wall-normal (see Fig. 6.3). The first term on the RHS represents the WSR in the streamwise direction and the second that in the circumferential direction. In the PIV measurements, the 3D velocity field was projected onto the x-y (i.e.

bifurcation) plane and therefore only the streamwise component in Eqn. 6.1 was included in the calculation. Numerical computation of WSS normally involves all relevant components of velocity gradients. However, in order to match the condition for comparison only the streamwise component was extracted and used.

For the comparison of errors in WSS produced in PIV and CFD, a relative (ϵ_{rel}) and normalised error (ϵ_{norm}) were defined as follows:

$$\epsilon_{rel} = \left| \frac{f_N - f_E}{f_N} \right| \tag{6.2}$$

and

$$\epsilon_{norm} = \left| \frac{f_N - f_E}{f_{C,N}} \right| \tag{6.3}$$

where f_N and f_E denote the numerical and experimental data and $f_{C,N}$ the observed numerical value in the CCA. ϵ_{rel} represents an estimate of the local error between the experimental and numerical values, and can be quite large depending on the value of f_N.

6.4 Experimental model setup

6.4.1 Principles of PIV

The experimental measurements for the validation of CFD data were carried out using PIV. A brief description of this technique is outlined first in this section. PIV is an optical flow visualisation technique used to obtain an instantaneous velocity field and other flow properties derived from it (e.g. WSS is derived from the differentiation of the velocity field) in a cross section of a flow domain. The fluid in the system (Fig. 6.4) is seeded with reflective tracer particles that were selected to match the fluid properties so that they follow the fluid motion faithfully. The motion of these tracer particles is captured in a desired cross section within the flow domain, which is illuminated with a laser light sheet. Using a CCD camera, this light pulse is captured twice at short time interval and saved in separate images. Once a series of two light pulses is recorded, the each image frame is divided into subsections (interrogation areas). The interrogation areas from each image are then cross-correlated with each other to track the motion

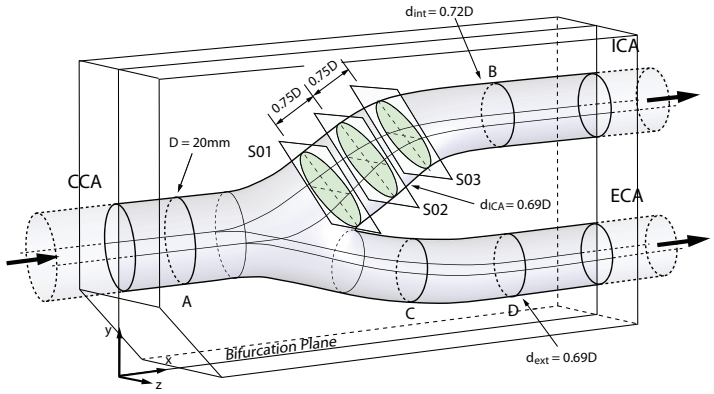

Figure 6.3: A schematic representation of carotid artery model. Data planes (A-D and S01-S03) are indicated, where cross-sectional velocity data was collected.

of tracer particles pixel by pixel. From this, the displacement of each particle can be determined. In order to achieve high accuracy, sub-pixel displacement is determined by interpolation.

6.4.2 Interfacial PIV

PIV offers several advantages over other flow visualisation techniques such as laser doppler anemometry (LDA) and medical imaging techniques such as MRI since it is also non-invasive, and can provide a highly accurate 2D velocity vector field. However, the estimation of WSR (and thus WSS) is derived via the differentiation of the velocity field, and therefore the errors produced during the measurements of the near-wall velocities (which tend to be significant due to the noise introduced during imaging and processing) tend to become further amplified.

Interfacial PIV (iPIV) was developed by Buchmann et al. (18) in order to overcome the error propagation in this estimation of WSR. The principle of iPIV is that 1D cross-correlation on a single horizontal pixel line is performed in order to obtain a wall-parallel displacement profile. The rectangular images are divided into interrogation windows of size $M \times N$ and 1D cross-correlation is performed at each horizontal line as seen in Fig. 6.5 (left). The correlation functions are stacked to produce a correlation map of horizontal displacement (wall-parallel) and vertical distance (wall-normal). The velocity gradient (i.e. WSR) at the wall is then extracted by fitting a weighted straight line through the correlation

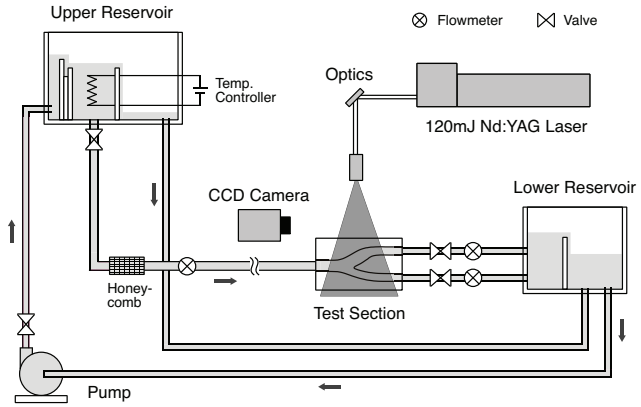

Figure 6.4: A schematic of PIV setup. Arrows indicate the flow direction. The velocity field is determined by capturing the displacement of tracer particles suspended within the fluid at short time intervals. By N. Buchmann (Monash University, Victoria, Australia).

peaks (Fig. 6.5, right). Since this is not based on the calculation of velocity field, the error propagation inherent in the conventional PIV is avoided, achieving an increased accuracy for the resulting WSS. This method is detailed in the previous publications by Buchmann et al. (18; 19).

The physical model used in the PIV measurements was created in a water soluble material by computer-controlled 3D printing and its subsequent casting into a clear silicone resin. A transparent flow phantom was obtained after curing of the resin and removal of the water-soluble prototype and then was installed in a recirculating flow system (Fig. 6.4). A steady flow was supplied by a header tank to the test section via a $1.5m$ pipe, ensuring a fully-developed flow at the entrance of the CCA. The flow split at the outlets (ICA:ECA=7:3) was controlled by a custom-made flowmeter. The working fluid was an aqueous glycerine solution which had dynamic viscosity of $11.7Pa \cdot s$ and density of $1150kgm^{-3}$.

Since the primary objective here was to quantitatively establish the validity of numerical and experimental WSS calculations, and the flow field was assumed to be steady, which also would allow for the detailed investigation of flow characteristics at physiological relevant Reynolds numbers. All experiments and CFD simulations were carried out at $Re = 290$ and $Re = 700$, which were representative of the mean and peak systolic flow calculated based on the CCA diameter.

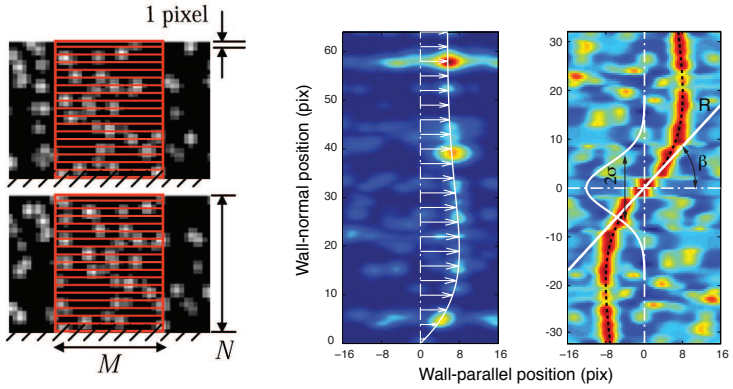

Figure 6.5: Left: principles of iPIV. Interrogation windows $M \times N$ for the first and second exposure. Centre: wall-normal correlation map constructed from instantanenous 1D correlation functions. Right: Wall shear estimation using a weighted linear fit. By N. Buchmann (Monash University, Victoria, Australia).

6.5 Numerical model setup

For the numerical model geometry, the inlet in the CCA and outlets in the ICA and ECA were positioned approximately 7 CCA diameters and 20 ICA diameters away from the bifurcation region respectively. This extension was to ensure that the flow through the regions of interest was not affected by the flow conditions at the boundaries, and also that, at the outlets, the flow was fully developed. The latter was an important consideration in the choice of boundary condition.

Based on the dimensions specified in the previous section, a CAD model was created in SolidWorks (SolidWorks, Concord, Massachusetts, USA), from which the model was subsequently discretised and saved in the STL format. In this file format, the original 3D CAD model's surface geometry was tessellated and represented with logically oriented triangles, each of which was identified by the unit outward normal vector and three sets of coordinates that represent its vertices. The tessellated model was generated at the highest accuracy setting (i.e. increased tessellation) to ensure the best surface recovery.

The discretised geometry model was then imported into the mesh generation package Harpoon (Sharc, Manchester, UK). Harpoon essentially uses the non-body-fitted Cartesian method, and therefore the structure of the volume mesh it generates is independent of discretised surface topology. In principle, the model surface geometry is first placed in a regular Cartesian grid. From the interior of

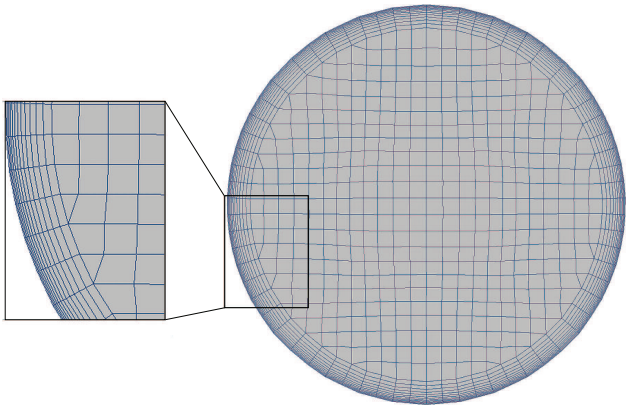

Figure 6.6: A cross section of the CFD carotid artery mesh, showing the predominantly hexahedral grid structure and the boundary layer applied adjacent to the wall surface boundary.

the surface geometry, a solid volume that can be represented by regular Cartesian cells is carved out, leaving irregular-shaped cells along the surface boundary, which are defined by the surface boundary cutting through the Cartesian cells. This means that the majority of the model volume is represented predominantly by hexahedral cells (and the rest primarily with tetrahedral elements), the result of which is a very fast and flexible grid generation. This, combined with adaptive mesh refinement, offers a considerable advantage particularly in the grid generation for complex geometries.

As it can be seen in Fig. 6.6, the actual meshes contained a structured boundary layer adjacent to the wall boundary of the geometry. This was an important step in order to ensure an accurate capture of the velocity gradients particularly as complex behaviour was expected to occur in the bifurcation region. Three meshes were generated in total in order to test the grid independence of the solution, in each of which the element size and boundary layer parameters (off-the-wall spacing, the number of layers and expansion ratio) were altered. This resulted in meshes containing 2.58-4.6 million volume cells. The results shown in Fig. 6.7 were obtained by plotting WSS along the intersecting line of the carotid sinus outer wall and the bifurcation (symmetry) plane. As the plot shows, there was not a significant variation in the solution observed for the three meshes tested. This was as the grid generated was going to be later used also for cellular dynamics, and therefore the boundary layer added alongside the wall surface was created

in such detail that it could capture the steep species gradient expected. Diffusion coefficient of the species ATP (ATP, $D_{ATP} = 2.36 \times 10^{-10} m^2 s^{-1}$), the density and dynamic viscosity of the working fluid in this study (detailed in the following sections) gave the Schmidt number of 4.31×10^6 and therefore the fluid dynamic boundary layer thickness was much greater than that of the mass transfer boundary layer. As a result the velocity profile was expected to be linear in this region, for which the boundary layers tested were observed to be more than sufficient to capture the behaviour of velocity gradients. Therefore the mesh containing the least number of elements, 2.58 million cells, was selected.

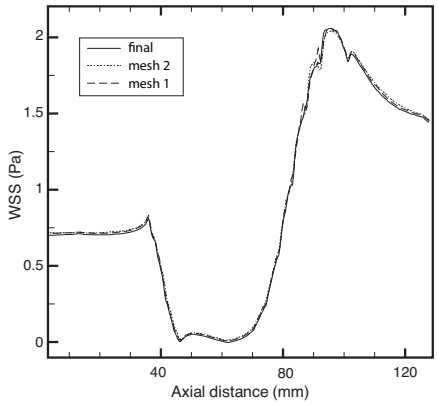

Figure 6.7: Grid sensitivity test. WSS was plotted at $Re = 290$ along the intersection of the bifurcation (symmetry) plane and the sinus outer wall.

The finite-volume solver FLUENT (Version 6.2, Ansys.Inc., Lebanon, NH, USA) was utilised in order to solve for the flow field. The blood was modelled as an incompressible, Newtonian fluid that had the identical density and viscosity to those used in the PIV experiments. The solutions of the continuity (Eqn. 3.5) and momentum (Eqn. 3.6) equations were obtained iteratively, using the SIMPLE algorithm for the pressure-velocity coupling and a second-order upwind scheme for the convective terms. All the simulations were run on the University of Canterbury IBM Blue Fern HPC, using 4 processors on IBM System power 5 575 nodes.

As in the experiments, the wall of the model geometry was assumed to be rigid and stationary, with no-slip conditions specified for all wall boundaries. A fully-developed Poiseuille flow profile expressed as follows was imposed at the

inlet:

$$u = U_{max}\left[1 - \left(\frac{r}{R}\right)^2\right] \tag{6.4}$$

where u the velocity at the radial position, U_{max} the maximum velocity across the inlet plane (which is twice the mean velocity for Poiseuille flow), r is the radial position and R the vessel diameter. The UDF code used to impose this condition is given in the Appendix B.2. At both exit boundaries in the ICA and the ECA FLUENT's outflow condition (detailed in Section 4.4) was applied. The extension of the flow domain to the position mentioned previously was in order to ensure that the convective derivative of all flow variables normal to the exit boundary plane is zero, i.e. flow was fully developed so that the gradients of each flow variable in the streamwise direction are zero, as required by FLUENT. Flow split of ICA:ECA=7:3 was also specified at the outlet. This ratio was selected based on the MRI measurements carried out using healthy volunteers by Marshall et al. (86). Density and dynamic viscosity of the fluid were matched to those used in the PIV measurements.

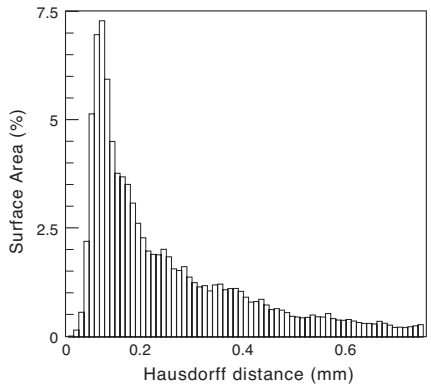

Figure 6.8: Estimated geometrical difference between the experimental and CFD carotid artery model geometries (Hausdorff distance).

6.6 Geometrical accuracy

The geometrical match of numerical and experimental models was assessed by comparing the CFD surface mesh and PIV flow phantom. The latter was obtained from a computer tomography (CT) scan of the silicone phantom and subsequent image segmentation and 3D geometry reconstruction. The difference between these two geometries was evaluated by the Hausdorff distance (Fig. 6.8). It was observed that the manufactured flow phantom was slightly larger than the CFD model, with an average variation of $0.28mm \pm 0.2mm$. This was equivalent to an error of $<1.4\%$. It was also observed that approximately 87% of the model surfaces deviated from each other by less than $0.5mm$.

6.7 Results and discussion

6.7.1 Primary velocity fields

A quantitative comparison between the experimental and numerical axial velocity profiles in the bifurcation (symmetry) plane is shown in Fig. 6.9 for $Re = 290$ and $Re = 700$. The velocity profiles were recorded at seven locations in the bifurcation plane indicated in Figs. 6.3 and 6.9.

It was observed that the axial velocity was skewed towards the sinus inner walls, both in the ICA and the ECA. This was due to the centripetal force induced due to the vessel curvature in the bifurcation region. The centripetal force

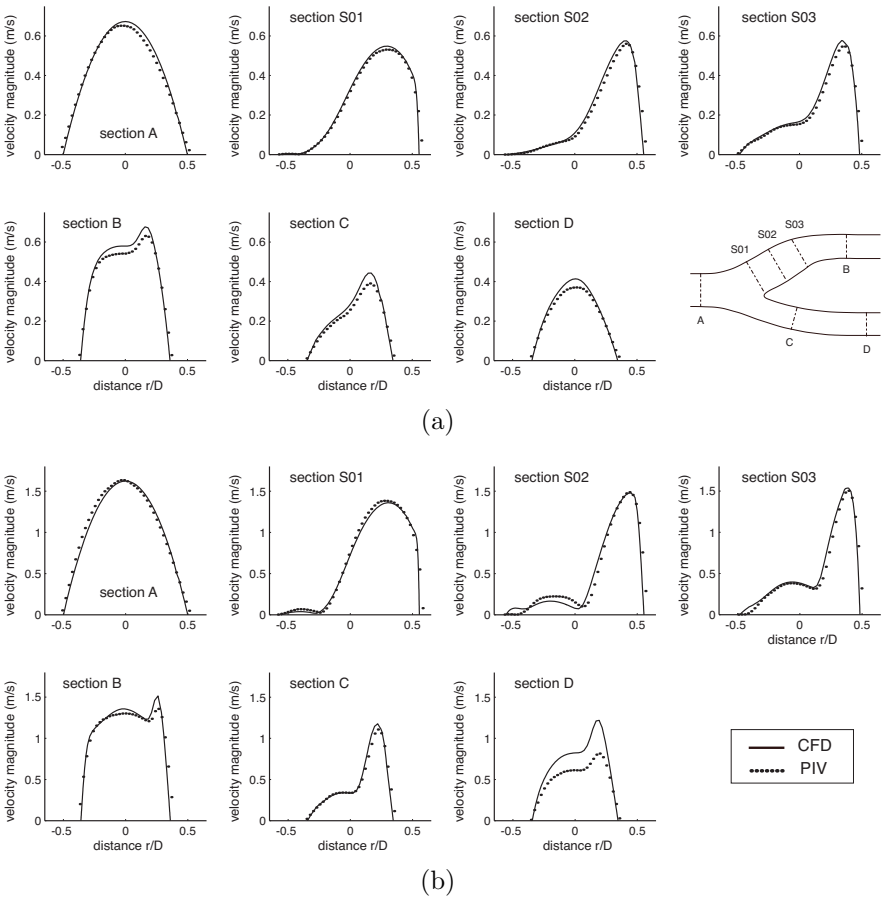

Figure 6.9: Comparison of axial velocity profile at selected data planes in the common (CCA), internal (ICA) and external (ECA) carotid arteries. Solid line indicate CFD data and points PIV measurements. (a) $Re = 290$, (b) $Re = 700$.

caused the slow-moving particles near the wall were drawn towards the outer walls, and this resulted in the fast-moving flow forced towards the inner wall near the flow divider. At $Re = 290$, CFD data was in good agreement with PIV, with the maximum ϵ_{rel} of 11.3% at location D in the ECA. The error became greater at $Re = 700$ along the ICA outer wall where larger variation occurred particularly at $s02$ leading to the maximum error of ϵ_{rel}=43%, and in the distal ECA, where a noticeable discrepancy was observed across the data plane. The average maximum relative errors for all the profiles were 6.1% for $Re = 290$ and 13.7% for $Re = 700$.

Figure 6.10 shows a 3D particle trace representation of the flow field in the bifurcation region for $Re = 290$. High-momentum flow originating from the central axis region in the CCA moves through the bifurcation region and subsequently into the ICA and ECA with little disturbance, while flow originating from the

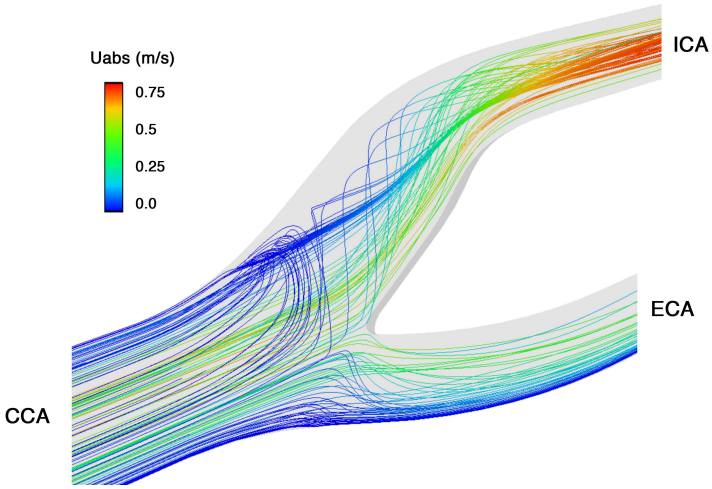

Figure 6.10: 3D particle trace representation of the flow in the bifurcation region ($Re = 290$, CFD).

near-wall region of the CCA is deflected at the flow divider and moves slowly and laterally along the top and bottom walls of the bifurcation. In the ICA, the deflected flow travels almost perpendicularly to the axial bulk flow along the top and bottom walls and impinges on the sinus outer wall in the symmetry plane. At the stagnation point, part of the flow is convected downstream, whereas the remainder travels upstream, forming a reversed axial-velocity region along the ICA outer wall. The latter portion of the flow joins the bulk flow where it separates from the wall at the CCA-ICA intersection, is restored into the bulk flow, and then convected downstream along the counter-rotating helicoidal flow through the ICA. It is important to note that this is not a recirculation region in the traditional sense where streamlines form closed loops and fluid particles become entrapped.

6.7.2 Secondary flow patterns

The secondary flow characteristics within the carotid sinus were recorded at three locations $S01$-$S03$ in Fig. 6.11(a) for $Re = 290$ and Fig. 6.11(b) for $Re = 700$. The data is presented via in-plane stream traces of secondary flow and streamwise vorticity. The curvature of the branching of the CCA introduces a radial pressure gradient, which induces a strong secondary, radial flow motion.

At $Re = 290$, the effects of centripetal force on the flow structure can clearly be seen at $S01$. The near-wall slow-moving flow moves along the top and bottom

walls towards the sinus outer wall and then is directed towards the flow divider wall along the median line. This resulted in the formation of a pair of counter-rotating vortices (Dean vortices). Downstream at the mid- and distal sinus ($S02$ and $S03$), the vortex pairs move closer to the median line and the flow enters the plane more radially, particularly at $S03$. Due to the strong circumferential velocities near the wall and the resulting radial velocity gradients, a shear layer is present in this region, which explains the elevated near-wall vorticity values. Similar vortex evolution was observed at $Re = 700$, with the secondary flow streamlines being kidney-shaped at $S01$ and $S02$, implying stronger influence from the high-momentum axial flow. Overall, the agreement observed between CFD and PIV was deemed satisfactory, with both methods reproducing very similar secondary flow structures, size and locations of the vortex cores as well as the vorticity distribution. The maximum ϵ_{rel} for vorticity was observed in the vortex centre at $S01$, giving $\epsilon_{rel} = 9.5\%$ at $Re = 290$ and $\epsilon_{rel} = 20.5\%$ at $Re = 700$.

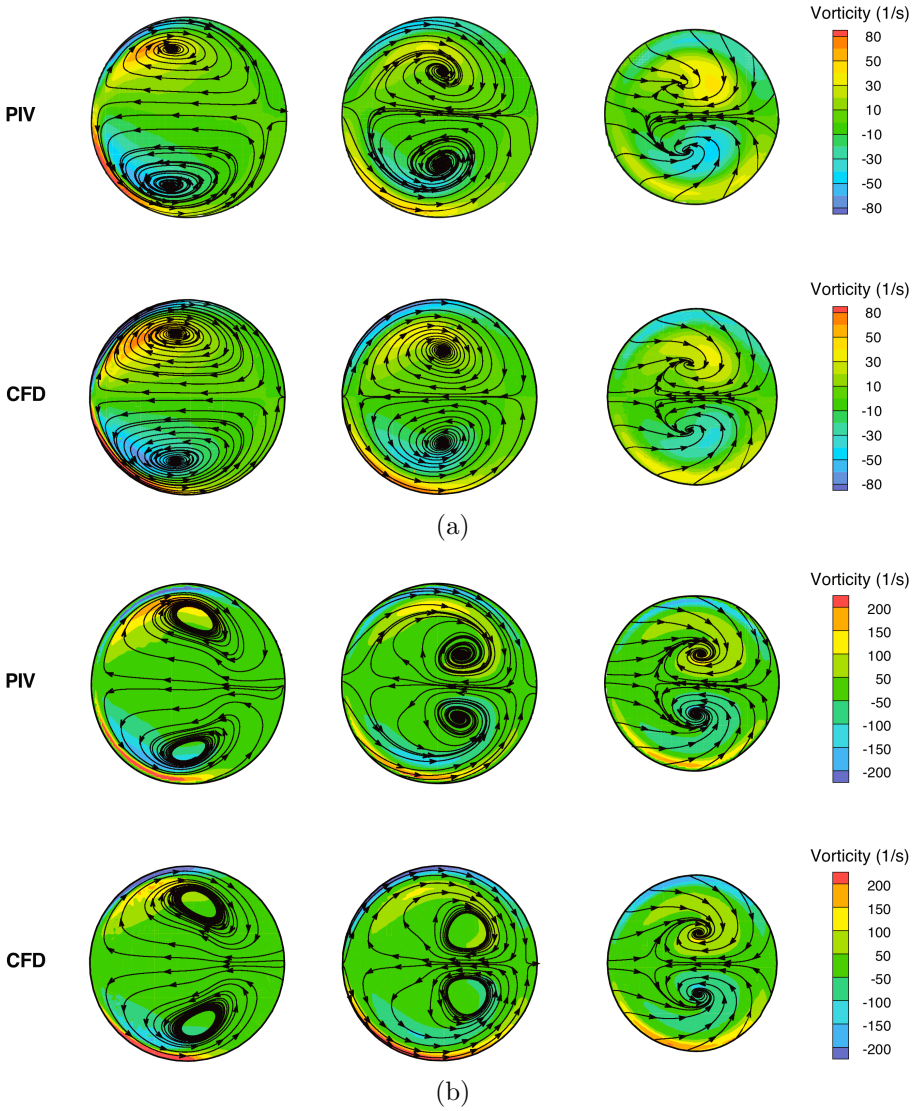

Figure 6.11: In-plane streamlines of secondary flow and streamwise vorticity for (a) $Re = 290$ and (b) $Re = 700$ at cross sections $S01$-$S03$ (from left to right). Top: PIV data, bottom, CFD data.

6.7.3 Wall shear stress

The experimental and numerical WSS, recorded on the line where the bifurcation plane intersects the sinus outer wall, were compared for the inner and outer walls of the ICA and ECA.

In the CCA, WSS is predominantly constant due a fully-developed flow imposed at the inlet being maintained. In the bifurcation region, the flow experiences an adverse pressure gradient due to the expansion of the cross sectional area and decelerates, resulting in a rapid decrease in WSS. It decreases to zero at the CCA-ICA intersection where the flow eventually separates due to the adverse pressure gradient, and then turns negative in the reversed-flow region formed between the separation point and the reattachment point. WSS then turns positive at the reattachment point and rapidly increases due to the reduction in the vessel cross section in the ICA (Fig. 6.12(a)). This trend was observed also at $Re = 700$ (Fig. 6.12(b)), except that the second reversed-flow region was present at mid-sinus ($S02$), due to another portion of fluid deflected at the apex impinging on the wall and part of it being convected upstream along the wall. This increased complexity of flow (and therefore WSS) pattern is the result of the combined effect of the higher momentum of the bulk flow reattaching further downstream and the deflected slow-moving particles at the apex being convected further downstream due to increased velocity. Flow separation was also observed in the proximal part of the ECA, and WSS exhibits a similar behaviour to that observed on the ICA outer wall but with lower peak magnitude and a smaller reversed flow region that is simpler in structure. WSS decreases steadily along the inner wall of the ECA, whereas in the ICA the second peak was observed due again to the reduction in the vessel cross-sectional area.

Regarding the comparison between the PIV and CFD data, some differences exist within the reversed, low-momentum regions along the outer ICA and ECA walls as seen in Fig. 6.12 and Fig. 6.13(a). While the size of the reversed-flow region was calculated correctly by both techniques, there were discrepancies observed for the magnitude of reversed WSS and location of the second separation and re-attachment points for $Re = 700$. This was consistent with discrepancies seen in the velocity profiles at mid-sinus, indicating slight difference in the 3D flow structure between CFD and PIV. Also, the WSS in PIV was significantly lower in the high-shear region than that computed by CFD (Fig. 6.13(b)).

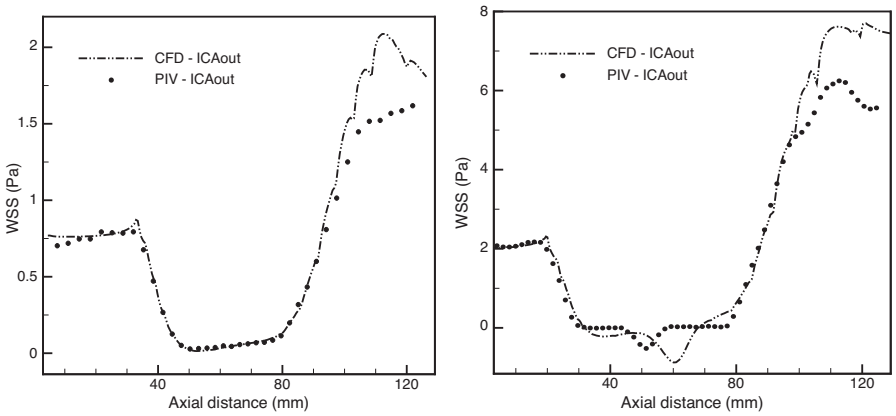

(a) (b)

Figure 6.12: WSS along the outer ICA wall for (a) $Re = 290$ and (b) $Re = 700$ (right). Dashed lines and the symbols indicate the CFD and PIV data respectively. $s/D = 0$ is located at the entrance of the daughter branches.

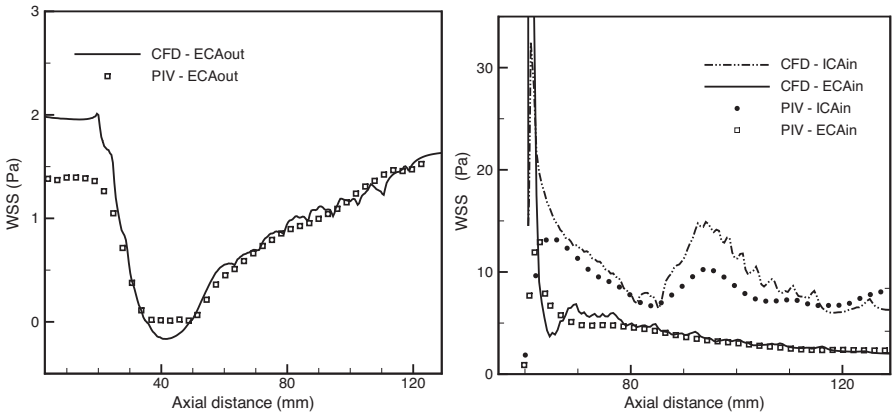

(a) (b)

Figure 6.13: WSS along the (a) outer wall of the ECA and (b) inner walls of the ICA and ECA for $Re = 700$. Solid lines and symbols indicate the CFD and PIV data respectively.

Table 6.1: Summary of percentage relative and normalised error for the comparisons of the experimental and numerical WSS at selected locations A, B and S01-S03.

Section	s/D	$Re = 290$			$Re = 700$		
		$f_N - f_E$	ϵ_{rel}	ϵ_{norm}	$f_N - f_E$	ϵ_{rel}	ϵ_{norm}
A	-1.5	0.02	1.5	1.5	0.02	1.0	1.0
S01	0	0.05	71.4	5.1	0.2	86.9	9.8
S02	0.75	0.01	95.7	1.0	0.19	42.2	9.3
S03	1.5	0.01	4.3	0.9	0.09	69.2	4.4
B	3	0.29	12.9	29.7	0.78	13.7	38.0

Absolute error in Pa.

A summary of absolute and percentage WSS errors is given in Table 6.1 for the outer wall of the CCA, sinus and ICA. An excellent agreement between CFD and PIV was achieved in the CCA with absolute errors of approx. $0.02Pa$ and ϵ_{rel} of 1.0-1.5%. In the carotid sinus, errors varied greatly (ϵ_{rel}=4.3-95.7% and ϵ_{norm}=0.9-9.8%), depending on the Reynolds number and location within the sinus. The 95.7% relative error at $S02$ was the result of extremely low near-zero WSS values observed at this location (mid-sinus) both in the numerical simulation and experiments (approx. $0.0104Pa$ and $0.0004Pa$ respectively). Absolute errors, in this area however, were observed to be low (0.01-$0.3Pa$). Downstream of the sinus, the discrepancies increased to ϵ_{rel}=12.9-13.7% and ϵ_{norm}=29.7-38.0%. Note that the ranges of ϵ_{rel} were larger for both Reynolds numbers than those of ϵ_{norm} and that the largest relative errors always occurred in the areas of low WSS (i.e. within the sinus). The corresponding normalised error is usually small in these cases (Table. 6.1). In contrast, large ϵ_{norm} occurred for higher shear rates and was of the same magnitude as the corresponding relative error.

6.7.4 Error sources

In PIV, a homogenous displacement of the tracer particles within the correlation window is assumed for the determination of the area-averaged displacement via the cross-correlation function. This however does not always apply in reality and the accuracy of the correlation function is greatly affected by spatial velocity gradients and large out-of-plane flow components. As as result, signal-to-noise ratio decreases considerably and the estimated velocity is biased towards lower values. Although precautionary measures such as increasing particle seeding density and

using iterative correlation techniques combined with interrogation window deformation had been taken at the measurement stage, these were the likely cause for the underestimation of the velocity values seen in Fig. 6.9. Therefore the experimental velocity field has greater uncertainties in the regions of strong secondary flows and steep velocity gradients such as in the carotid sinus and distal ICA as well as near the bifurcation apex. In addition, accumulation of seeding particles, predominantly in the areas of low-momentum or stagnant flow such as near the sinus outer wall, causes increased laser light reflections and locally high optical noise. A slight mismatch in refractive index between the silicone model and the blood substitute can also cause light reflections and optical distortion near the wall. These factors may have partially accounted for the discrepancies between the experimental and numerical velocity profiles in Fig. 6.9 and WSS in Fig. 6.12 and Fig. 6.13. Other factors such as deviations of the actual flow from the defined condition or the location of the laser light sheet could have also affected the accuracy of the measurements. The actual flow rate in the CCA differed slightly from that defined in the CFD simulations, resulting in differences in Reynolds number of 1.7% for $Re = 290$ and 0.7% for $Re = 700$.

One of the relevant potential error sources in CFD here is numerical errors, which are inherent in any CFD calculations and as stated in Chapter 4 primarily due to numerical diffusion. Although precautionary measures were taken to reduce the errors by selecting higher-order discretisation schemes (second-order for both pressure and momentum) and increasing the grid resolution near the wall, again it is possible that these partly contributed to the discrepancies observed.

In the validation of numerical predictions and experiments, the degree of the match of model geometry is a shared source of errors. This is inherent in both techniques. In CFD, geometrical discrepancies are inevitably introduced during the conversion process of the CAD model to the STL model. This involves discretisation of the original, smooth surface into a series of unstructured triangulated elements, and therefore the surface recovery depends directly on the resolution of the tessellation process. In PIV, manufacturing errors introduced during model construction could lead to similar deviation from the original CAD model. Although both models were created from the identical data set and generally good match had been achieved between CFD and PIV model surfaces (approximately 87% of the model surfaces deviated from each other by $0.5mm$, Fig. 6.8), it was possible that the location of relatively large errors coincided in both models, causing the flow path to change and consequently the velocity and

WSS field to be erroneously altered.

6.8 Concluding remarks

Concurrent numerical predictions and PIV measurements of axial and secondary velocity and WSS fields were carried using carotid bifurcation model geometries developed from the identical CAD model of an averaged human carotid bifurcation geometry. The primary objectives were to have the solutions of the CFD code for flow and WSS quantitatively validated by experimental data, which ensured the sufficient accuracy of model inputs to the EC dynamics cellular model (WSS and the surface concentration of ATP, Chapter 5 and Chapter 7) since they depend directly on the solution of the flow field. Reciprocally, the CFD data was used to demonstrate the validity and accuracy of iPIV, a novel method for directly estimating WSS from the recorded PIV data. Overall agreement in accuracy achieved in this chapter was deemed satisfactory for both of these purposes, and therefore the validation was deemed successful.

Additionally, the usage of an average bifurcation model allowed for detailed analyses of the flow and WSS distribution. The data obtained here therefore will provide a control case for further studies that incorporate physiologically more realistic flow conditions such as flow pulsatility, vessel stenosis and wall compliance. It will be then important that errors are reduced by addressing the avoidable sources of the errors discussed above (numerical errors and manufacturing errors being the unavoidable).

Chapter 7

Endothelial Cell Dynamics

7.1 Introduction

The carotid arteries (the carotid sinus in particular) are one of the sites of frequent plaque localisation, and the hypothesis most widely supported at present to explain this observation is that plaques localise due to the influence of the local haemodynamics, which exhibits considerable spatial variation along the vasculature reflecting the local vascular geometry. Also proposed separately is that a defect in the production and/or activity of nitric oxide (NO) leads to endothelial dysfunction characterised by impaired endothelium-dependent vasodilation, leading to the development of atherosclerosis (33; 82).

From these observations, it is postulated that the bioavailability and activity of NO was likely to be low in the carotid artery bifurcation which has been known to be particularly prone to plaque formation (36), and that there were spatial/geometrical factors involved in the processes that eventually lead to low NO level. Since the spatial characteristics of local geometry are reflected on the endothelium (and underlying cellular processes) in the form of wall shear stress (WSS), WSS was postulated to play a significant role in the processes that results in the diminished local level of NO in these regions.

The mathematical model of endothelial cellular (EC) and NO dynamics was developed in Chapter 5 in an attempt to elucidate this postulate and address the focal nature of atherosclerosis. This chapter presents the results obtained from the model, integrating the EC cellular processes and the physiological stimuli of which behaviour was governed by the local flow field (the behaviour of WSS, the

haemodynamic stimuli, was analysed and verified to be sufficiently accurate in Chapter 6).

This study aimed to integrate these fluid dynamic and biochemical aspects of atherosclerosis in order to study the influence of vascular geometry on the endothelial NO and consequently atherosclerotic plaque formation. Using a realistic geometry was an essential part of obtaining credible and useful data in order to address the spatially focal nature of atherosclerosis in a physiologically feasible environment. The integrated fluid dynamics-cellular dynamics modeling that includes NO dynamics had, to the author's best knowledge, not been carried out so far, and was a critical step in further understanding the mechanism of atherosclerotic plaque localisation.

In the following sections, the details of the grid generated for the TF-AHCB model (detailed in Sections 6.2 and 6.5), which was generated again for the model geometry of physiological size, as well as the descriptions of numerical formulation used are given. Then the mathematical model of EC and NO dynamics developed in Chapter 5 was first utilised for a single-cell model to observe the time-course behaviour of solution variables in EC dynamics after a combined flow and agonist stimulation. It was then applied to the 3D carotid bifurcation model geometry in two stages. Firstly, as it was assumed in the previous applications (27; 108; 136), the flow was steady and the tension field brought about by the flow-induced exertion of stress is in the direction of flow only (i.e. uniaxial), which allowed for the investigation of the WSS and agonist distributions at physiologically relevant Reynolds numbers, as well as for the comparison of eNOS distribution results with those obtained by Comerford et al. (27). The model was then applied with the effects of blood pulsatility incorporated, which brought about the cell membrane stretch in the circumferential direction as well as in the flow direction.

7.2 Geometry and grid

For all the EC dynamics models, the geometry of tuning-fork average carotid artery bifurcation (TF-AHCB) geometry (Fig. 6.2) described in Chapter 6 was used. While the model geometry was scaled up for the flow validation in order to allow for the ease of experimental model construction and increased measurement accuracy, the model dimensions used for the cellular dynamics model were those typically seen *in vivo* and so the CCA had the diameter of $D_{CCA} = 6mm$. The

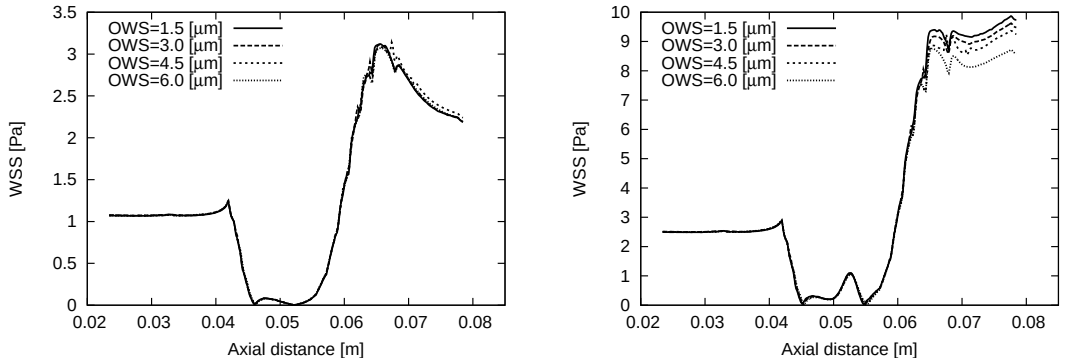

Figure 7.1: Grid dependence tests for WSS, carried out using four grids generated with different densities. Each grid was primarily characterised by boundary layer parameters, particularly off-the-wall spacing (OWS). (a) WSS at $Re = 300$, (b) WSS at $Re = 700$.

model was still dimensionally similar to that developed by Ding et al. (38), so the ICA and ECA had the diameters of $0.72 \times D_{CCA}$ and $0.69 \times D_{CCA}$ respectively. The bifurcation angle was also kept at 50°.

As in the previous case, the mesh for this model was generated using the commercial grid generation package Harpoon (Sharc, Manchester, UK) and contained a structured boundary layer alongside the wall surface. The diffusion coefficient of the species involved, ATP is extremely low ($2.36 \times 10^{-10} m^2 s^{-1}$), and this along with the density ($1000 kgm^{-3}$) and the dynamic viscosity of the model fluid ($0.004 Pa \cdot s$) gives the Schmidt number of 4×10^{-6}. This implies that the thickness of the mass transfer boundary layer is much thinner than that of the hydrodynamic boundary layer, and therefore the layer of cells adjacent to the wall must be sufficiently fine in order to achieve efficient convergence and accurately capture the behaviour of the species. In order to ensure these, preliminary solutions were carried out at four different grid densities at two physiological Reynolds numbers $Re = 300$ and $Re = 700$ (corresponding Péclet number 5.08×10^6 and 11.87×10^6 respectively), representative of the mean and peak systolic flow of the cardiac cycle. A boundary layer was defined by its off-the-wall spacing (OWS), number of layers and expansion factor. Each of the four grids was generated using varying OWS ($1.5\mu m$, $3.0\mu m$, $4.5\mu m$ and $6.0\mu m$) with the values of the number of layers and expansion ratio adjusted to give roughly the same total boundary layer thickness of less than $140\mu m$.

Due to the requirements for the small OWS, the high expansion ratio was

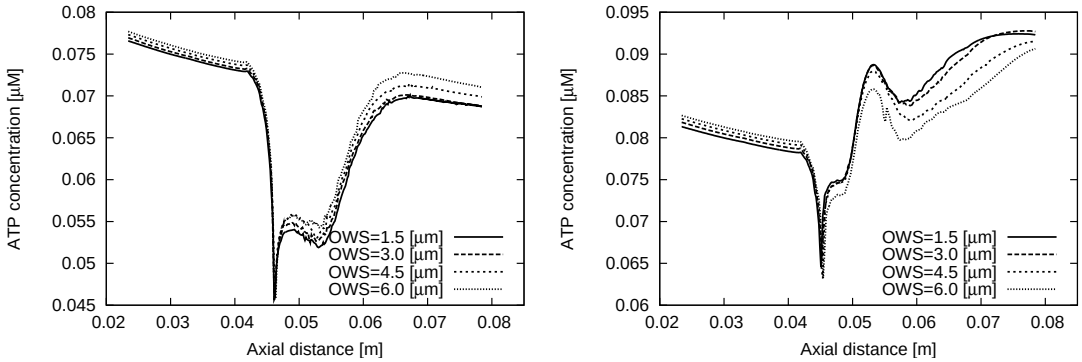

Figure 7.2: Grid dependence tests for ATP, carried out using four grids generated with different densities. Each grid was primarily characterised by boundary layer parameters, particularly off-the-wall spacing (OWS). (a) ATP at $Re = 300$, (b) ATP at $Re = 700$.

needed in order to ensure that the boundary layer cells were just sufficiently fine to achieve convergence and solution accuracy, from the perspective of computational efficiency, that is, numerical accuracy generally increases as the grid density is increased, but this also leads to the increase in the computational time and power required. This restriction on the total height of the boundary layer came from the observation made during the grid generation process in Harpoon, where a grid created with boundary layers of greater thickness resulted in producing negative minimum volumes being detected when imported into the flow solver. This was believed to be the result of the structured boundary layer being inserted into the irregularly-shaped space immediately adjacent to the wall (which had been generated by the non-body-fitted Cartesian procedure carving out the solid volume that can be represented by regular Cartesian cells from the interior of the geometry (Section 6.5)). The resulting grids consisted of 1.14-3.35 million elements. In order to check the solution independence of the grid size, WSS and ATP concentration were plotted along the intersecting line of the bifurcation plane and the sinus outer wall (termed bifurcation$-$sinus$_{out}$ line) after running simulations for the four grids.

WSS plotted along the bifurcation$-$sinus$_{out}$ line demonstrated little dependence on the element size in the boundary layer at both Reynolds numbers (Fig. 7.1(a) and Fig. 7.1(b)), except at $Re = 700$ in the distal sinus where the WSS values were considerably higher. The wall concentrations of ATP shown in Fig. 7.2(a) and Fig. 7.2(b), on the other hand, exhibited noticeable dependence on the grid size as it was progressively reduced. The grid dependence was most ap-

parent again in the distal sinus at both Reynolds numbers, and even more so at $Re = 700$. Fig. 7.2 shows that the solution was still progressively changing between the grids with OWS=3.0μm and 1.5μm. However, the rate of change slowed down considerably relative to those observed between OWS=6.0μm and 4.5μm or OWS=4.5μm and 3.0μm, and it was not considered likely that an increase in the total grid size (additional 1.12×10^6 grid cells) would justify the slight improvement in solution accuracy in the downstream reactions. Taking these points into account, the grid containing the boundary layer with OWS=3μm was deemed the most suitable in order to achieve a good balance between the solution accuracy and the computational economy. The final grid consisted 2.23×10^6 grid cells and contained the boundary layer developing over 14 layers to the total height of 135μm.

7.3 Numerical model setup

For all simulations except for the single cell model (the details of which are given in the following section), a finite-volume solver, FLUENT (Version 6.3, Ansys.Inc., Lebanon, NH, USA) was utilised to solve for the flow field and species transport. The solutions for the flow field were obtained by solving the continuity (Eqn. 3.5) and the momentum equation (Eqn. 3.6) derived previously, based on the assumption that blood is an incompressible, Newtonian fluid. For the transport of species, the species conservation equation (Eqn. 3.10) was solved simultaneously under the assumption the diffusion coefficients of all the species involved were constant. Under the assumption that blood was a dilute binary solution in terms of the species involved, the solute's diffusion coefficient could be assumed constant since the volume fraction of the solute was very low so that it could diffuse freely in the absence of intermolecular interactions. Fluid temperature was also assumed to be constant, and thus the species' diffusion coefficient was spatially independent of the solute's concentration.

As in the previous case, boundary conditions needed to be specified at the inlet (CCA), two outlets (ICA and ECA) and the wall surface for both flow and species. For steady flow simulations, fully developed velocity profiles given in Eqn. 6.4 were applied at the inlet. For transient simulations, the inlet velocity was calculated from the physiological CCA waveform obtained from a 28-year-old healthy male subject shown in Fig. 7.3, recorded using MRI.

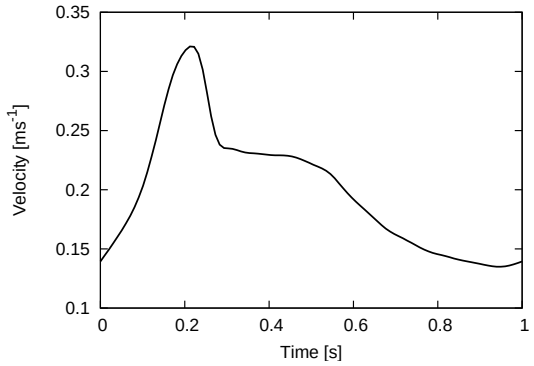

Figure 7.3: Common carotid artery velocity waveform, obtained from MRI recording of the blood velocity from a 28-year-old healthy male subject.

This waveform, which was scaled to give the mean Reynolds number of 300, was decomposed using a Fourier series in an external UDF (the code given in Appendix. B.3), in which Fourier coefficients were then calculated in order to compute the unsteady component $u(t)$ of the wave form at time t over the cardiac cycle:

$$u(t) = \frac{A_0}{2} + \sum_{n=1}^{N} \left[A_n cos\left(\frac{2\pi nt}{T}\right) + B_n sin\left(\frac{2\pi nt}{T}\right) \right] \tag{7.1}$$

where the first term on the RHS represents the mean value, n and N the indices for the number of harmonics, t the flow time, T the period of the cardiac cycle ($=1sec$) and A_n and B_n the Fourier coefficients. The unsteady components of the waveform found using the expression above were then superimposed with the steady component to obtain the inlet velocity profile. The velocity value determined was applied as a constant velocity across the inlet at the beginning of each time step. This was based on the observation made by Myers et al. (99) that the variations in the inlet velocity profile did not significantly affect the flow or WSS distributions downstream, which were more dominated by geometrical factors such as the vessel curvature. The inlet was positioned at 7 CCA diameters from the upstream end of the bifurcation region, in order to facilitate the flow development. For species modelling, a constant ATP concentration of $0.1\mu M$ was applied across the inlet in all simulations. The choice of this value was based on the experimental observation by Shen et al. (118) that it was the smallest concentration of the agonist that induced flow-dependent intracellular Ca^{2+} oscillations in the presence of ATP. The inlet upstream was also to allow the

development of the concentration boundary layer in the CCA. The Womersley number was 3.76.

At the exit boundaries in the ICA and ECA, FLUENT's Outflow condition was applied for all simulations, for which it was required that the convective derivative of all variables normal to the exit boundary plane was zero in the streamwise direction in order to extrapolate the boundary values from the interior of the flow domain. This is described in detail in Section 4.4. Flow split was ICA:ECA=7:3.

As in the previous flow case, no-slip and reactive boundary condition was applied at the wall boundaries for the flow and species transport. The general form of the reactive boundary condition is given by Eqn. 4.37. In order to specify the condition for both species involved (ATP and ADP), the source term S needed to be defined for each species in order to reflect their production mechanisms. For ATP this was its release from the endothelial surface as a function of WSS, and for ADP the hydrolisation of ATP. The expressions of the boundary conditions that incorporate these are given by Eqn. 5.4 and 5.7 for ATP and Eqn. 5.8 for ADP.

The solutions of the continuity and momentum equations were obtained iteratively, using SIMPLE algorithm for the pressure-velocity coupling and second-order upwind scheme for the convective terms. For transient simulations, a fully implicit scheme was used for temporal discretisation (detailed in Section 4.3.2). The cardiac cycle was divided into 250 time steps of $0.004 secs$. For species transport, the third-order MUSCL scheme was selected for all simulations in order to achieve higher spatial accuracy. In order to remove the influence of initial transients, the solutions were recorded after running three complete cycles at which point there were no significant changes in the solution variables.

7.4 Results

7.4.1 Single-cell model

The computations for the single-cell model was carried out on Microsoft Visual Studio 2010 Express, performed on a PC with PC Intel 3.00 GHz CPU and 4GB RAM, in order to obtain the time-course of the solution variables IP_3, cytosolic

Ca^{2+}, stored Ca^{2+}, activated eNOS and endothelial NO after a coupled flow and agonist stimulation of a step increase in ATP and WSS, to $0.09\mu M$ and $1.0Pa$ respectively. Results are shown in Fig. 7.4.

The binding of ATP to the G protein-coupled receptor and its subsequent activation leads to the formation of IP_3. As shown in Fig. 7.4(a), this reaction quickly reaches the steady state. The IP_3 binds to the IP_3 receptor on the ER surface and opens the Ca^{2+} channel, leading to the release of internally-stored Ca^{2+}. The resulting transient increase in the cytososlic Ca^{2+} and steady decrease in the stored Ca^{2+} can be seen in Fig. 7.4(b) and Fig. 7.4(c) respectively. The subsequent drop of the cytosolic Ca^{2+} to the plateau value is the combined effect of the action of the Ca^{2+} ATPase on the ER surface and that on the EC plasma membrane, the latter of which serves to remove the cytosolic Ca^{2+} to the lumen in order to regulate its concentration within the cell. The reason for its not returning to the resting level is the inclusion of CCE, which provides a sustained influx of extracellular Ca^{2+} depending on the filling state of the ER. The initial transient increase in the activated eNOS is the result of increased Ca^{2+}-calmodulin complex formation elicited by the elevation in the cytosolic Ca^{2+}, and also of its direct activation by WSS by phosphorylation. The value then gradually dropped and plateaued at a steady-state value, reflecting its decay due to the disassociation of Ca^{2+}-calmodulin complex from eNOS. Endothelial NO also followed this trend: its production was transiently elevated by the increase in eNOS activities, then decreased to a plateau value, following the drop in eNOS activities. Interactions of NO with its scavengers, primarily superoxide anion O_2^-, also contributes to the decay.

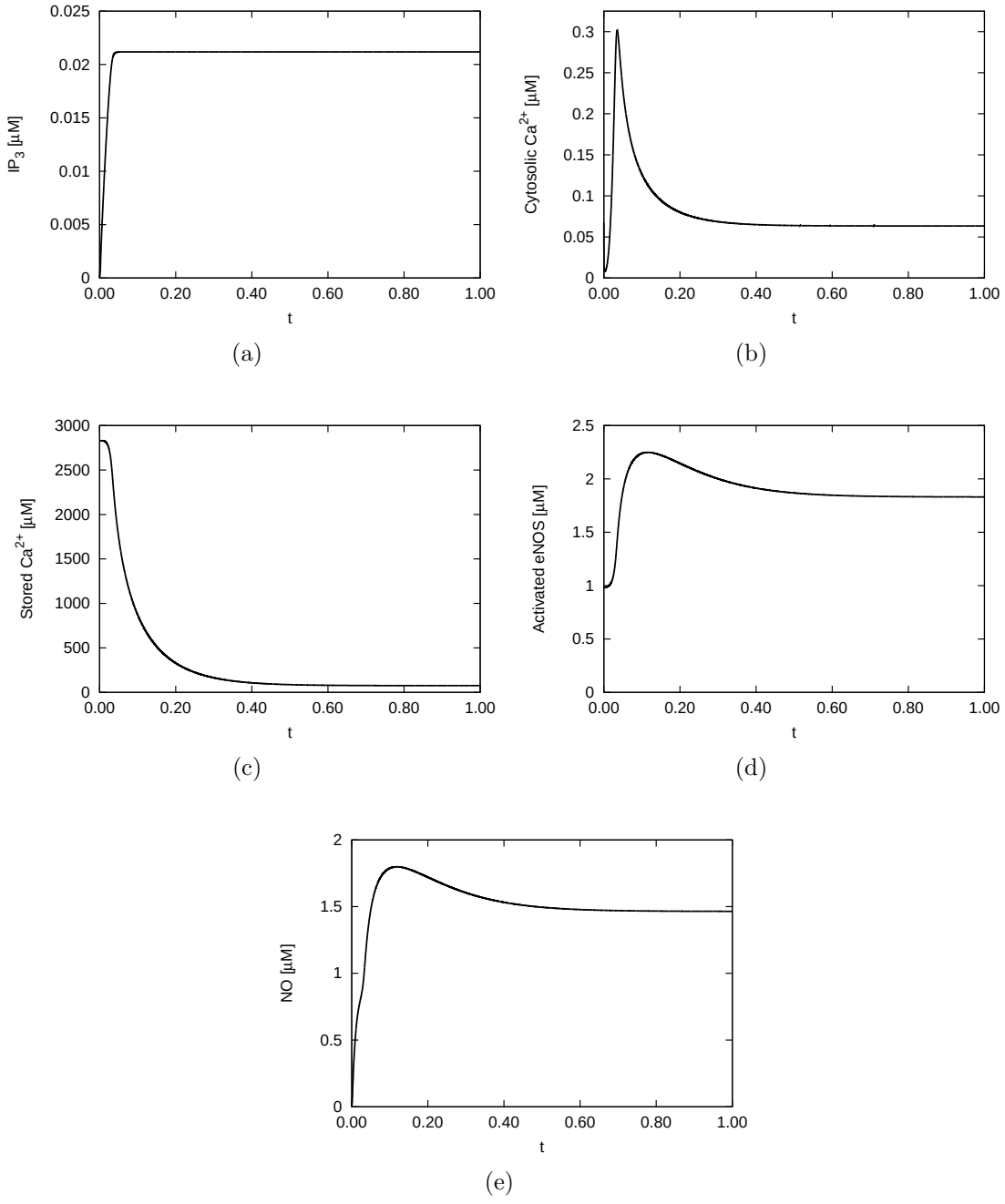

Figure 7.4: Time course of solution variable after a step increase in ATP and WSS to $0.09\mu M$ and $1.0Pa$ respectively. (a) IP_3, (b) cytosolic Ca^{2+}, (c) stored Ca^{2+}, (d) activated eNOS and (e) endothelial NO. Solutions were obtained using the fifth-order adaptive Runge-Kutta integrator until all variables reached the steady state. Note that the time t has been non-dimensionalised by the characteristic time scale T=500s (108; 136).

7.4.2 EC dynamics under uniaxial tension

The results for the mass transport and EC dynamics were first obtained under the assumption that the tension gradient experienced by the ECs when exposed to flow is uniaxial in the streamwise direction. This assumption was by the virtue of the *tension-field* hypothesis (48) (explained in Section 5.5.2), and adopted in the previous work published on EC dynamics (27; 108; 137). The results obtained here therefore would allow for a comparison with the results obtained in other studies, particularly with data obtained using spatially varying geometries.

Steady flow

Initial investigation focused on the transport properties and distributions of blood-borne agonists. It was observed by Shen et al. (118) that ADP was also effective in eliciting endothelial cell response, and therefore it also was included as a biochemical stimuli in the cellular dynamics model. However, the first part of this chapter focuses on ATP in order to understand how its distribution pattern correlates with the flow patterns. Also investigated was the influence of WSS-induced ATP release from the EC surface. The ATP release in response to flow is a well-documented phenomenon (14; 94; 139; 140). The methods used in many studies were, however, restricted to the observation of the response of single or a small cluster of cells to varying WSS. Although the values of WSS used were those observed in physiological conditions, these results did not allow for the simultaneous investigation of spatially varying, large-scale ATP distribution. The data was therefore obtained to study the larger-scale transport behaviour of ATP in the complex flow environment needed to investigate its implications in atherosclerosis.

All steady-flow simulations were performed on IBM System power 5 575 using 4 processors on a single node. The solution was considered to have converged when scaled residuals for solution variables fell below 10^{-6} and were no longer changing. Each simulation took approximately 9 hours to obtain converged solutions. The ODEs of EC dynamics (Equations 5.9, 5.10, 5.37, 5.38, 5.39) were then solved via an external UDF which took the computed WSS and agonist solution values from the solver as inputs. The computation took approximately 15 minutes.

WSS

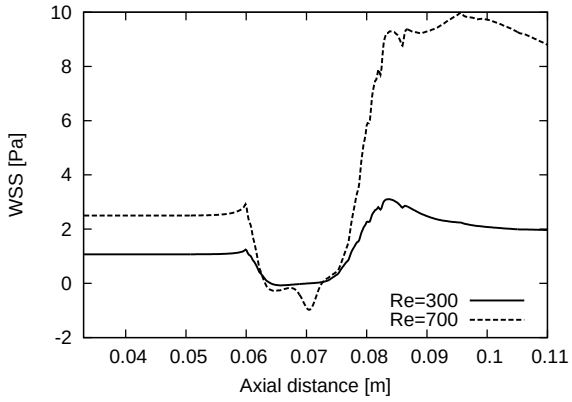

Figure 7.5: Wall shear stress along the bifurcation−sinus$_{out}$ line for Re=300 and Re=700.

Figure 7.5 shows the WSS plotted along the bifurcation−sinus$_{out}$ line for Re=300 and Re=700. The distribution patterns found here mirrored those observed in the previous chapter (Section 6.7.3), exhibiting a near-constant value in the CCA, a fall due to the cross-sectional expansion in the bifurcation region, the negative WSS region due to presence of reversed-flow regions, and a subsequent sharp rise due to the vessel cross section. The size and position of the negative WSS regions for both Reynolds numbers were approximately the same. For Re=700, the values were more negative due to the increased flow momentum towards the wall.

The local WSS value taken as an input at each cell in the EC dynamics model, however, was WSS magnitude based on the previous observation that the cellular processes involved in the EC dynamics depended more on shear stress than shear rate (140). Figure 7.6 shows the 3D distribution of WSS magnitude for Re=300.

A low WSS region was present on the outer wall of the carotid sinus, spanning the entire length of the sinus, and also on the ECA outer wall, though to a lesser extent. Also significant was the existence of low-shear regions on the top and bottom walls in the bifurcation region. This was the result of the low-momentum flow originating from the near-wall region in the CCA being deflected at the apex, then flowing circumferentially along these regions towards the outer walls of the ICA and ECA, as can be seen in the particle-trace plot in Fig. 6.10. On the other hand, WSS was observed to be generally higher on the inner walls of the bifurcation, particularly in the vicinity of the apex where the high-momentum

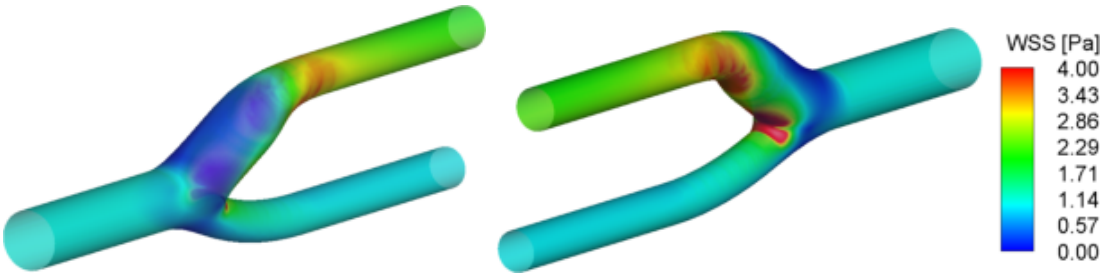

(a) (b)

Figure 7.6: 3D visualisation of wall shear stress magnitude at Re=300, observing the (a) predominantly low-WSS regions on the sinus outer wall, and (b) high-WSS regions near the bifurcation apex and the proximal ICA.

flow impinges and in the proximal ICA where the flow undergoes convective acceleration due to the reduction of the cross-sectional area (Fig. 7.6(b)).

Agonists

The transport of ATP was simulated at two Reynolds numbers of 300 and 700, representative of the mean and peak systolic flow of a cardiac cycle, in order to observe the agonist distributions at physiological flow rates, and also their implications in the downstream cellular processes in the EC dynamics.

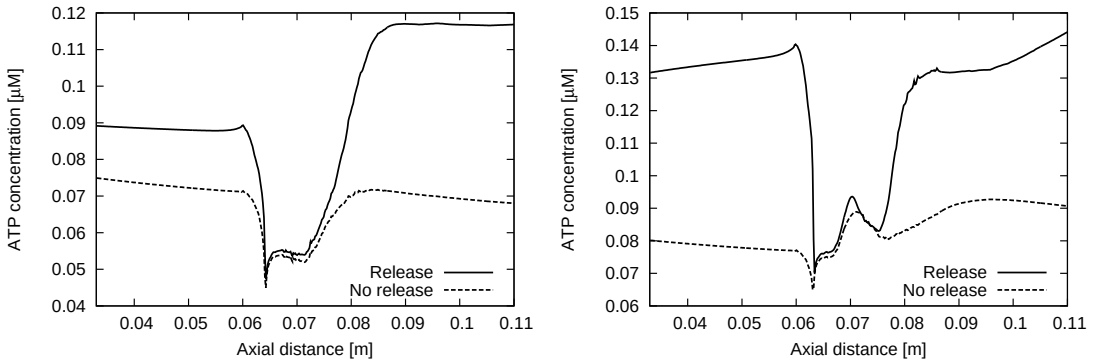

(a) (b)

Figure 7.7: ATP concentration distribution along bifurcation−sinus$_{out}$ line, for (a) Re=300 and (b) Re=700, under release and no-release conditions.

Figure 7.7 shows the concentrations of ATP plotted along the bifurcation−sinus$_{out}$ line. Under no-release condition, the common trend seen for both Reynolds numbers was that wall concentrations of ATP underwent steady decline first in the

CCA and then in the ICA due to the development of the concentration boundary layer adjacent to the wall. Within the sinus, however, marked differences in the distribution patterns were observed between Re=300 and Re=700. At Re=300, the level of ATP dropped to its minimum value where flow separated from the wall (at the axial distance of approx. $0.063m$), remained at much lower level in the reversed-flow region, rose to the pre-separation level and then started to decline as the flow re-developed and another concentration boundary layer started to form. At Re=700, however, the level of ATP was comparable to that in the CCA in the proximal sinus and noticeably higher in the distal part. The level then dropped to a local minima and then rose to the local maxima before undergoing a decline due again to the development of the concentration boundary layer. While at Re=300 ATP the concentration boundary layer started to develop at the axial distance of approximately 0.082m, at Re=700 it started well into the ICA at approximately 0.093m. This was likely to be because of the increased complexity in the flow structure due to higher flow converging into the reducing cross section and therefore resulting in strengthening of the vortical behaviour and thus delaying the re-development of the flow.

When WSS-induced ATP release was included (the release mechanism is explained in Section 5.5.1), significant changes were observed. Whereas the spatial pattern and the concentration levels did not show significant differences within the sinus (i.e. low-shear) region at both Reynolds numbers, ATP levels were considerably elevated in the CCA and the ICA, where the altered distribution patterns were also observed. At Re=300, the ATP level still showed a gradual decline despite the higher level of concentration. Then in the proximal ICA, it rapidly rose and reached a maximum value at the location at approximately $0.085m$, following the WSS distribution pattern (Fig. 7.5) closely. The value then plateaued in the ICA. At Re=700, the difference in the spatial pattern was more apparent. The ATP level was seen to gradually increase, reaching a maxima which was comparable to that in the ICA. Additionally, the ATP level was observed to increase in the ICA. This spatial pattern of ATP in the ICA, also at Re=300, showed marked departure from that of WSS, that is, ATP levels either plateaued or increased where WSS was decreasing due to the re-development of the flow.

3D representation of ATP wall concentrations are shown in Fig. 7.8. Although the 2D plot along the bifurcation$-\text{sinus}_{out}$ line shown in Fig. 7.7 showed that both ATP concentrations and WSS were relatively low for both Reynolds numbers

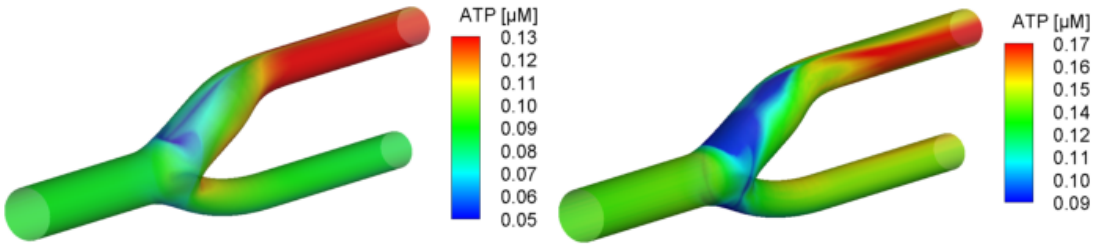

(a) (b)

Figure 7.8: 3D ATP concentration distributions for (a) Re=300 and (b) Re=700, under WSS-induced ATP release condition.

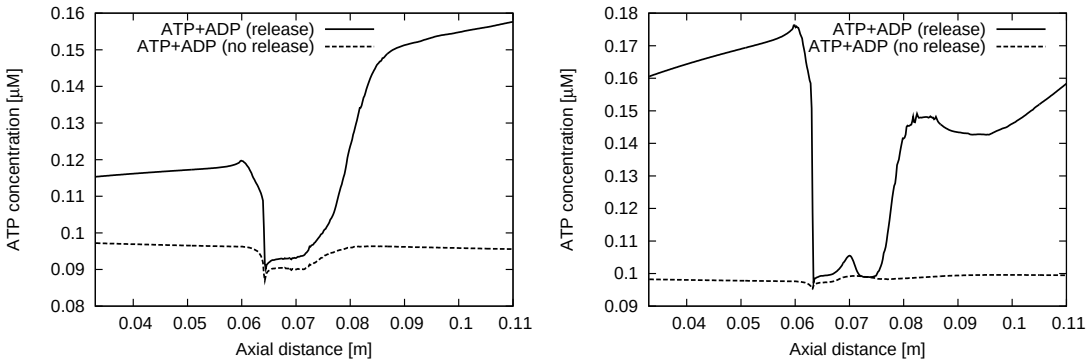

(a) (b)

Figure 7.9: Combined ATP and ADP concentration distribution along the bifurcation−sinus$_{out}$ line, for (a) Re=300 and (b) Re=700, under release- and no release-condition.

within the sinus, it could now be seen that ATP distributions do not faithfully follow those of WSS when observed in 3D. The most apparent difference is that while low WSS regions covered almost uniformly the large portion of the walls from the outer to the inner walls over the entire length of the sinus, depleted ATP regions were relatively more confined close to the the bifurcation−sinus$_{out}$ line, and its levels were predominantly low where the flow converges at the sinus outer wall. Also, by comparing Fig. 6.10 and Fig. 7.8(a) it also appeared to follow the paths of low-momentum flow that were deflected at the apex.

Figure 7.9 shows the distribution of combined concentrations of agonists ATP and ADP along the bifurcation−sinus$_{out}$ line. This was what was taken into the EC dynamics model as an input (3D representations shown in Fig. 7.10). The distribution patterns under release-conditions were observed to generally follow those observed for ATP, but the increases in the CCA and the ICA were more

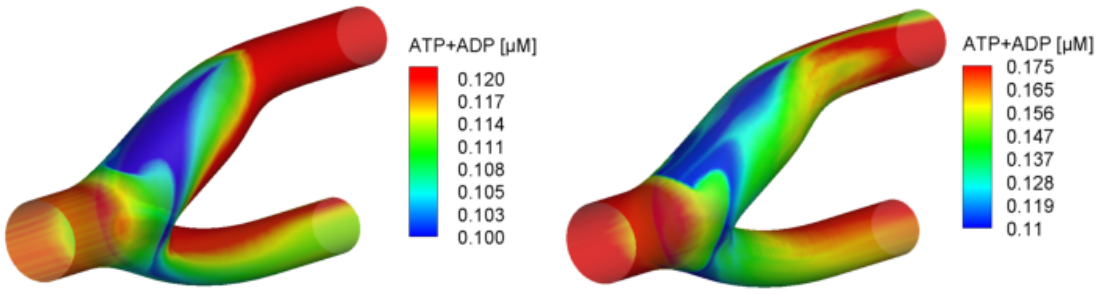

(a) (b)

Figure 7.10: 3D representations of combined ATP and ADP concentration distributions for (a) Re=300 and (b) Re=700, under ATP release-condition.

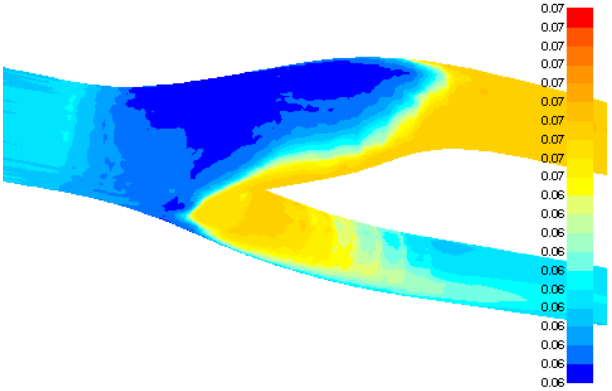

Figure 7.11: Cytosolic Ca^{2+} concentration under release-condition at Re=700, revealing the region of impaired Ca^{2+} signalling on the sinus outer wall. The unit is μM.

pronounced due to the production of ADP in these regions. The results also supported the previous observation by John and Barakat (61) that, in the absence of flow-induced ATP release, the combined concentration of ATP and ADP did not vary considerably over the range of WSS (0.01-1.0Pa in their study). This was still true in the range of WSS magnitude observed along the sinus outer wall, approximately 0.0-10.0Pa.

eNOS

The concentrations of eNOS were plotted along the bifurcation$-$sinus$_{out}$ line for Re=300 and Re=700 with flow-induced ATP release mechanisms included. The most dominant feature of the distribution pattern was that spatial variation of eNOS followed that of WSS (Fig. 7.5) very closely: at both Reynolds numbers,

eNOS level was near-constant in the CCA, dropped to and remained low in the sinus region, and rose sharply to the maximum values at the distal sinus-ICA intersection region. At Re=300, the eNOS level then gradually decreased following the WSS pattern, the latter of which was due to the flow re-development along the axial direction in the ICA. At Re=700, however, the saturation of eNOS concentration was observed in the same region. It was also noted that the eNOS level was lower at Re=700 compared to Re=300 within the sinus region, which again mirrored the feature observed for WSS. These features strongly imply that WSS is a dominant factor in eNOS signalling.

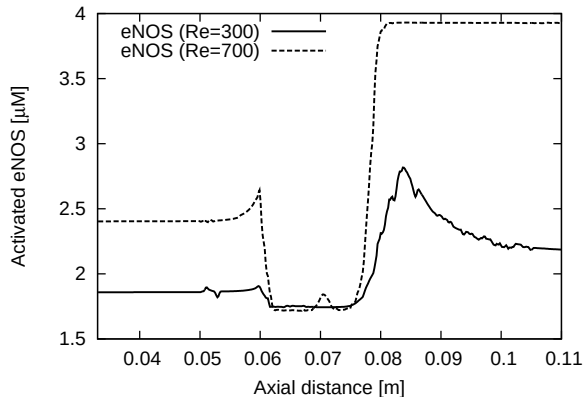

Figure 7.12: Activated eNOS concentration, plotted along the bifurcation−sinus$_{out}$ line for Re=300 and Re=700.

This overall trend of eNOS distribution following that of WSS can be confirmed by comparing Fig. 7.6 and Fig. 7.13. It could be also seen that low eNOS concentration was also present in the top and bottom walls of the bifurcation and

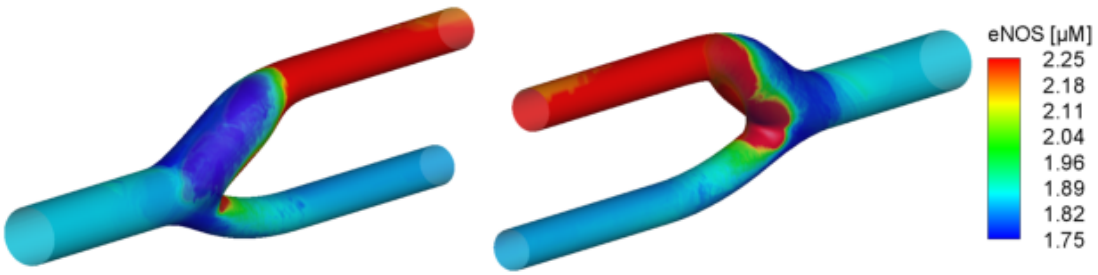

(a) (b)

Figure 7.13: 3D representations of activated eNOS concentration distributions, showing (a) predominantly low-eNOS regions on the sinus outer wall which spans the large portion of the sinus outer wall along the entire length of the sinus and (b) high-eNOS regions near the bifurcation apex and the proximal ICA.

the ECA outer wall, and high eNOS level near the apex and the entrance to the ICA.

NO

Shown in Fig. 7.14 and Fig. 7.15 are 2D plots of the endothelial NO for Re=300 and Re=700, and a 3D visualisation for Re=300 respectively. By comparing Fig. 7.12 and Fig. 7.14, it was observed that the distribution pattern of endothelial NO followed that of eNOS very closely for both Reynolds numbers. The important point observed from these results is that the endothelial NO exhibited a clear spatial variation, with its concentration being low over a wide area spanning from the sinus outer wall into the top and bottom walls of the sinus across the entire length from the distal CCA to the proximal ICA. The former in particular is known to be prone to the plaque localisation. The low NO region was also present on the top and bottom of the bifurcation region, as well as on a small part of the ECA outer wall. Meanwhile, high NO concentration region was observed in the apex region and on the inner walls of bifurcation (and further into the distal part in case of the ICA). These areas have been known to be relatively spared of plaque formation. Comparing this with Figure 7.13 shows that these spatial features of NO distribution closely mirror those observed above for eNOS, which implies that low concentration of NO is the direct result of decreased concentration/activities of eNOS.

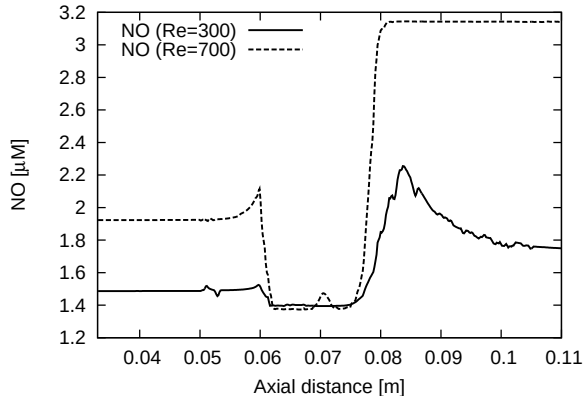

Figure 7.14: Endothelial NO concentration, plotted along the bifurcation−sinus$_{out}$ line for Re=300 and Re=700.

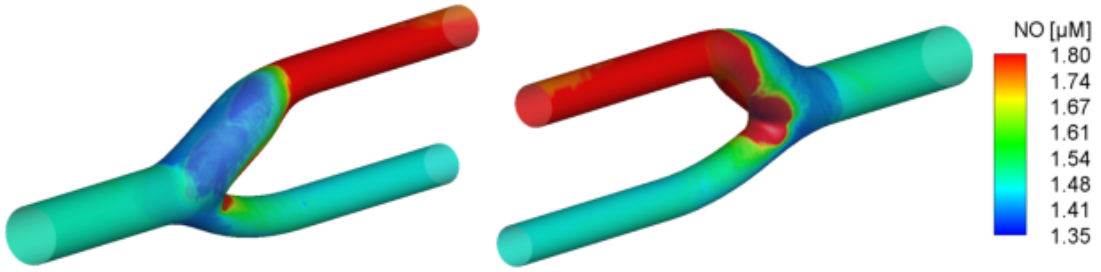

(a) (b)

Figure 7.15: 3D representations of NO concentration distributions for (a) predominantly low-NO regions on the sinus outer wall, and (b) high-NO regions near the bifurcation apex and the proximal ICA. Important point to note here is that the areas of low NO was present where atherosclerotic plaques were known to localise, whereas NO was high on the inner walls of the bifurcation and in the ICA which are known to be typically spared of plaque formation.

Pulsatile flow

Cycle-averaged values of WSS and ATP over a cardiac cycle, Fig. 7.16(a) and Fig. 7.16(b) respectively, were plotted along the bifurcation$-\text{sinus}_{out}$ line to be compared with the steady-flow results. The cycle-averaged values were calculated over a time period T using the following expression:

$$\phi_{cav} = \frac{1}{T}\int_0^T \phi \, dt \tag{7.2}$$

where *cav* denotes cycle-averaged values.

WSS was observed to show little difference between the steady-flow and pulsatile values over the entire length excect in the CCA, where the cycle-averaged values were slightly higher closer to the inlet and converged gradually to the steady-flow value towards the distal CCA. This was due to the velocity boundary condition used (which was a constant velocity profile across the inlet cross-section), which brought about higher shear gradient near the inlet. The gradual decrease reflects the development of flow towards a Poiseuille flow profile as the flow proceeds in the streamwise direction.

The plot of ATP shows that both steady-flow and cycle-averaged values exhibited an overall similar distribution patten on the sinus outer wall, although the latter values were generally slightly lower than the former. A similar phenomenon observed for WSS in the CCA was also present, which was the combined results of the elevated advection and increased ATP release due to higher WSS near the

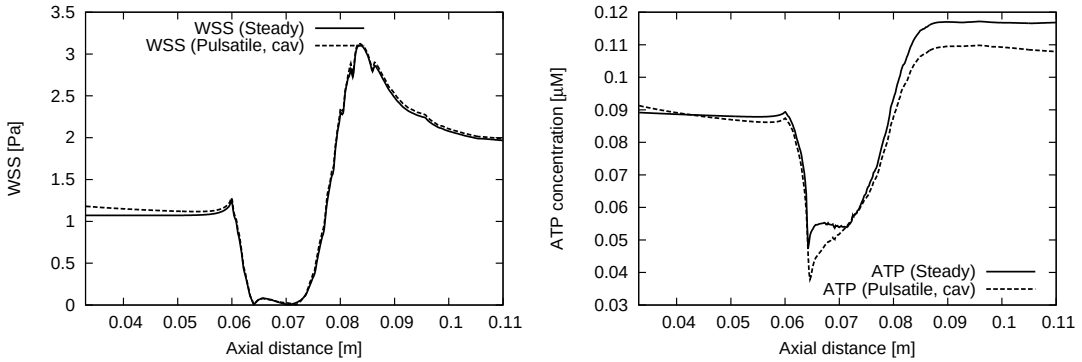

(a) (b)

Figure 7.16: Time-averaged values (a) WSS and (b) ATP over one cardiac cycle, plotted along the bifurcation−sinus$_{out}$ line.

inlet. While the steady-flow and cycle-averaged values seem to differ relatively little from each other in the CCA, there was a noticeable concentration difference observed in the sinus region and the ICA, with the maximum difference of 9% and average difference 3% between the steady-flow and the cycle-averaged model.

7.4.3 EC dynamics under biaxial tension

In the previous section, the results were obtained for the spatial distribution of agonists, eNOS and NO based on the assumption that the ECs experience uniaxial tension field in the streamwise direction when exposed to flow. This approach also allowed for the comparison of data with those obtained in the previous publications using an integrated fluid dynamics-cellular approach (27; 108) (detailed analysis and discussion are in Section 7.4.4 and Section 7.5).

The main difference of the biaxial model compared to the steady, uniaxial model presented above lies in the formulation of strain energy induction (which in turn controls the open-state of the WSS-gated Ca^{2+} channels through which the influx of extracellular Ca^{2+} takes place), which is now based on the EC membrane cell stretches in both the axial and circumferential directions, the latter of which is induced by the temporal pressure variation inherently brought about by blood pulsatility. The inclusion of this additional mechanism was motivated by its obvious outcome of making the model physiologically more realistic as well as by the report by Steinman et al. (122) and Joshi et al. (62) that disturbed local

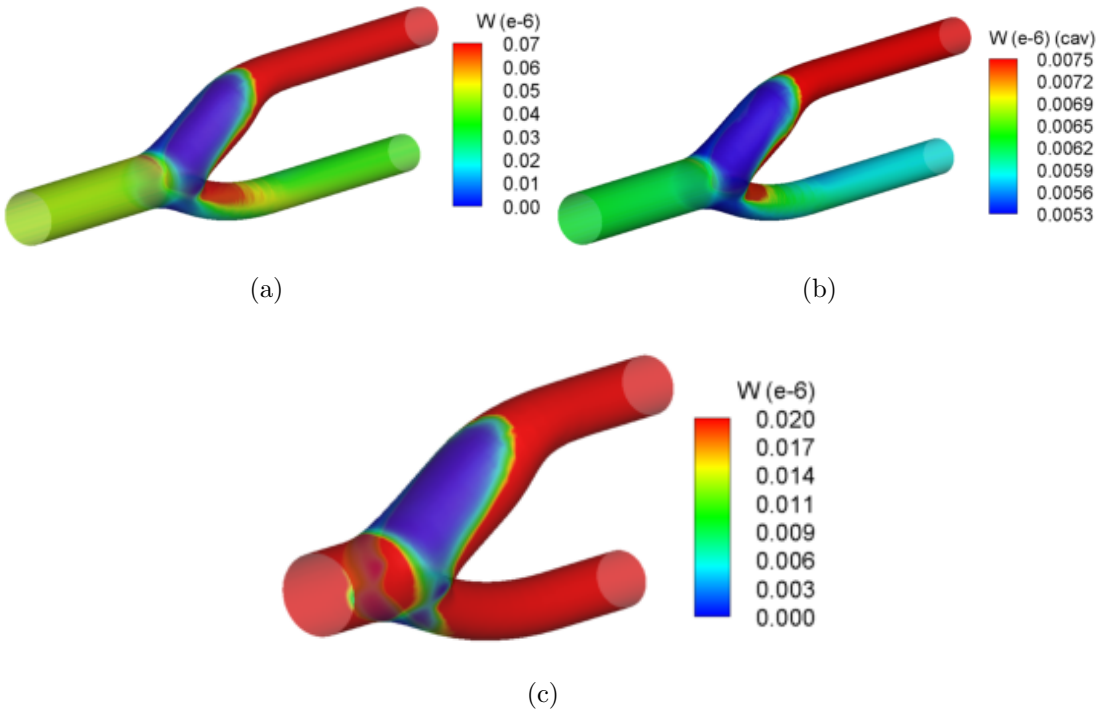

Figure 7.17: 3D contour plots of membrane strain energy for under (a) steady flow, uniaxial tension, (b) pulsatile flow, biaxial tension. (c) is an expanded view of (a) that shows detailed spatial distribution within the low W region on the sinus outer wall. The unit for W is Nm^{-1}.

WSS alone is not a sole causative or localising factor for atherosclerotic plaques.

Membrane strain energy (W)

When ECs are exposed to flow, cell membranes undergo deformation due to the tension gradients induced, one of them in the streamwise direction and the other in the circumferential direction. The deformation induces strain energy, W, within the membrane, which consequently controls the Ca^{2+}-influx pathway as a part eNOS activation mechanism that is dependent on the increase in the cytosolic Ca^{2+}.

Figure 7.17 shows the 3D contour plots of membrane strain energy when the ECs were under (a) uniaxial tension under steady flow and (b) biaxial tension under pulsatile flow. This was where the effects of the inclusion of the circumferential membrane stretch should first become apparent. Observation of the 3D strain energy field reveals similar distribution trend in both cases, where the values are near-constant in the CCA, low on the large part of the sinus outer wall,

top and bottom walls of the bifurcation and small part of the ECA outer wall while high on the ICA wall, sinus inner and proximal ECA inner walls. Comparing Fig. 7.6 and Fig. 7.17 shows that W under both uniaxial and biaxial tensions follow that of WSS very closely, implying that strain energy induction depends strongly on WSS. What should be noted here is the difference in the range of W. As it is observed in Fig. 7.17, for the pulsatile, biaxial case, strain energy values are significantly lower over the entire wall of the geometry line except the sinus region where the values are comparable. Normalised graphs in Fig. 7.18 reveal the similarity in the distribution pattern, though for the biaxial case the features (global/local maxima and minima) are less pronounced. Also, the amplitude between the maximum and minimum, which are observed within the proximal ICA and sinus respectively, is considerably smaller.

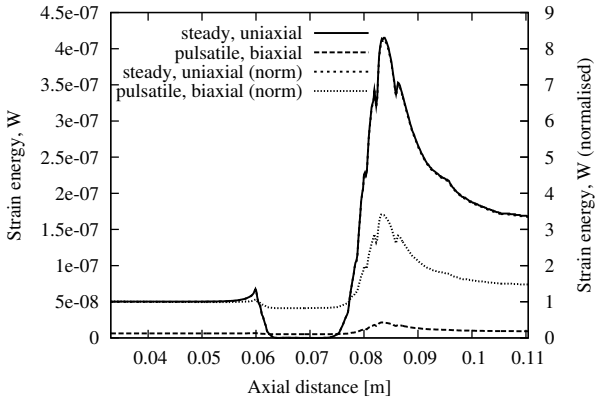

Figure 7.18: Strain energy (W) plotted for steady, uniaxial case (Re=300) and pulsatile, biaxial case (Re_{cav}=300). *norm* indicates that each data set was normalised by the corresponding CCA value. The unit for W is Nm^{-1}.

eNOS and Nitric Oxide

Figure 7.19(a) and Figure 7.20(a) show the wall distributions of eNOS and NO respectively, computed under biaxial tension in pulsatile flow, taking W obtained in the previous section as an input. What is apparent from Fig. 7.19(a) is that, with the circumferential membrane stretch included, the concentration values of eNOS were within a very narrow range and no longer exhibited clear spatial variation, except in the small vicinity of the bifurcation apex and in the sinus-ICA intersection where eNOS concentration was higher and comparable to the steady, uniaxial case. Figure 7.20(a) shows that this seems to have propagated into the calculation of endothelial NO, which also is showing near-uniform values in the

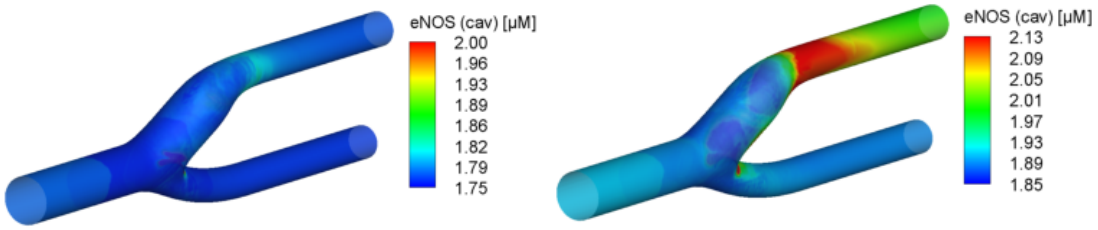

(a) (b)

Figure 7.19: 3D contour plots of activated eNOS for under (a) pulsatile flow, biaxial tension computed with all the model parameters unchanged from the steady, uniaxial case, and (b) also pulsatile flow, biaxial tension with the value of f_e increased by a factor of 10. The original value of f_e was 0.013351, as estimated and used by Wiesner et al. (137).

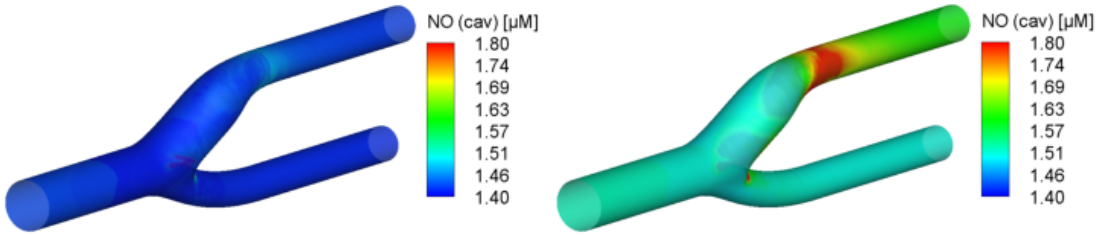

(a) (b)

Figure 7.20: 3D contour plots of endothelial NO for under (a) pulsatile flow, biaxial tension computed with all the model parameters unchanged from the steady, uniaxial case, and (b) also pulsatile flow, biaxial tension with the value of f_e increased by a factor of 10. The original value of f_e was 0.013351, as estimated and used by Wiesner et al. (137).

majority of the wall cells, again except in the very small area in the vicinity of the apex where the NO concentration was approximately $2\mu M$ and was comparable to the steady, uniaxial value.

7.4.4 Analysis

The results in the previous section (Fig. 7.19 and Fig. 7.20) show that both eNOS and NO along the bifurcation$-\text{sinus}_{out}$ line varied little and were in an extremely narrow range over the distance for pulsatile, biaxial case while those obtained for steady, uniaxial case exhibited clear, spatially-varying distribution pattern. This section looks into the validity of the model parameters and assumption used in order to examine the results.

The effects of model parameters

The model parameter that should be looked at first is the membrane strain energy density W, since it is what should first reflect the effects of the difference in input conditions.

Comparing the values of membrane strain energy W obtained for both cases (Fig. 7.17) reveals that, for the steady-uniaxial case, the spatial distribution of W reflects that of WSS strongly, i.e. constant in the CCA, low on the sinus outer, bifurcation top and bottom and proximal ECA outer walls while high on the proximal ICA and flow divider walls (Fig. 7.17(a)). This trend was also observed for the pulsatile, biaxial case. However, the strain energy induced under biaxial tension were considerably (approximately one order of magnitude) lower and in an extremely narrow range (Fig. 7.17(b) and Fig. 7.18) compared with those obtained for the steady, uniaxial case. The subsequent examination of F, which takes the strain energy W as an input, revealed that low values of W in the narrow range computed for the pulsatile, biaxial case resulted in F having a similar distribution in the range of 0.3333-0.3334 for the majority of the wall cells except those in a very small region near the apex. This was most likely to have propagated into the downstream calculations and resulted in the near-uniform concentration of eNOS and NO. However, given the widely acknowledged site specificity of atherosclerosis and NO's likely involvement in the origin and development of atherosclerosis, the results obtained here are not likely to be reflecting the physiological or pathological state *in vivo*.

Since the results obtained for the steady, uniaxial case have shown reasonable, site-specific distribution, now the pulsatile, biaxial case should be investigated in detail.

First to be examined was the behaviour of the open channel fraction function F. In Wiesner et al.'s (137) and the publications that followed (27; 108), strain energy W was one of the inputs into the function F (Eqn. 5.15) and was calculated based on the flow solution and EC membrane's material properties. Since the parameters k_B, T and N in the equation are constants, the overall behaviour of F depends on the other parameters α and f_e.

In the original formulation of F, α and f_e are estimated values, set as 3 and 0.013351 respectively (137). However, α, a parameter that governs the ion channel's open-state probability, was defined as 2 in the present study (which gives

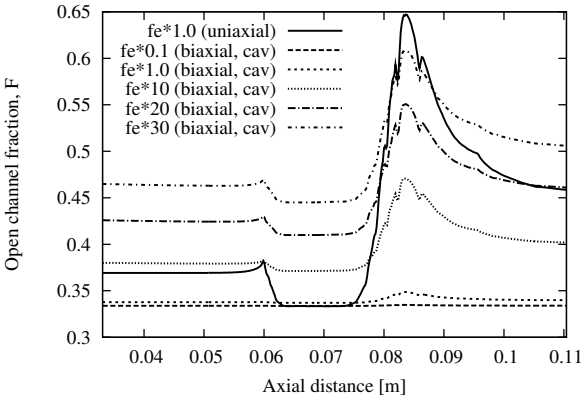

Figure 7.21: Open channel fraction F, plotted with various values of f_e (a fraction of strain energy available to gate WSS-activated Ca^{2+} channels. f_e*1.0 (=0.013351) is the initial estimate used in (137).

33% probability), based on that the original value of 3 (i.e. 25% probability) would result in non-physiological cytosolic Ca^{2+} concentration due to the imbalance between Ca^{2+} influx and efflux (108). This leaves the behaviour of Eqn. 5.15 depending on the other estimated parameter f_e. In order to test the sensitivity of F on f_e, F was computed for the pulsatile, biaxial case with various values of f_e (the original value multiplied by 0.1, 10, 20 and 30, which gives the membrane strain energy availability ranging between 0.133-40%) and plotted along the bifurcation$-\text{sinus}_{out}$ line on the sinus outer wall, along with the value obtained using the original f_e for both uniaxial and biaxial cases. This is equivalent to decreasing or increasing the amount of strain energy available to gate the Ca^{2+} channels.

The results (Fig. 7.21) show that the plot obtained for the steady, uniaxial case displayed a very clear spatial variation along the bifurcation$-\text{sinus}_{out}$, strongly mirroring those observed for W and therefore WSS. This trend was also seen for the pulsatile, biaxial case although to a much lesser degree, where it became more prominent for the higher values of f_e. As f_e became more elevated the values of F increased in all ECs along the bifurcation$-\text{sinus}_{out}$ line though with decreasing amplitudes. Also observed was that the spatial sensitivity of the function is very low with the original value of f_e (=0.013351) and $f_e * 0.1$, resulting in near-uniform values of F. This insensitivity of F for low f_e values was confirmed by plotting the maximum value of F against f_e, as shown in Fig. 7.22.

From the 2D plot of NO along the bifurcation$-\text{sinus}_{out}$ line obtained using these f_e (Fig. 7.23), it was observed that the trend seen for F had propagated

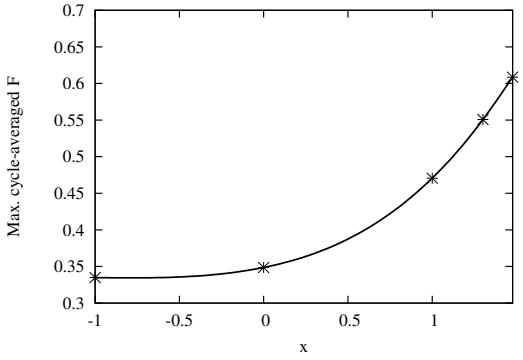

(a)

Figure 7.22: Max. F obtained for various values of f_e (the original value multiplied by 0.1, 10, 20 and 30) under biaxial tension in pulsatile flow, along with the values of F computed using the original f_e under uniaxial tension in steady flow. An exponential relationship was found between f_e and F. The values in the x-axis represent x in f_e*10^x.

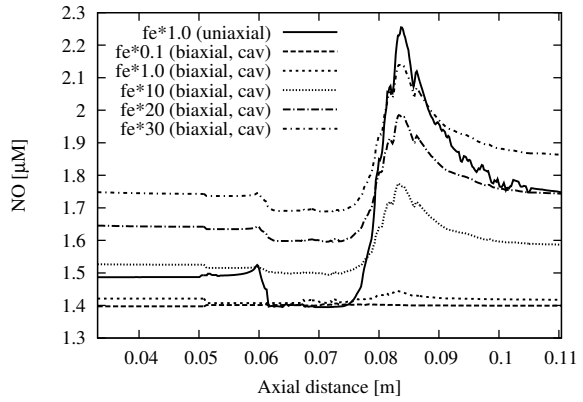

Figure 7.23: Endothelial NO, plotted with various values of f_e. f_e*1.0 (=0.013351) is the initial estimate used in (137).

into the downstream calculations, resulting in the near-uniform NO concentration seen with the original value of f_e.

It should be noted that the function behaviour testing with varying values of f_e was carried out only for the pulsatile, biaxial case. This is chiefly because, as stated above, the results obtained for the steady, uniaxial case were exhibiting reasonable, site-specific behaviour. Testing only the pulsatile, biaxial case is further justified here because the value of f_e was always an "initial estimate" without any further reference provided (137), and therefore how the value was calculated or whether f_e should vary between steady-flow and pulsatile-flow conditions has not yet been established.

Model assumption

The other approach taken to examine W was to look into the assumption used during the modelling. The models originally proposed by Wiesner et al. (137) and used in subsequent EC dynamics studies (27; 108) compute W based on the assumption that the stress field on the EC membrane is uniaxial in the direction of flow only on the grounds that the *tension-field* hypothesis holds. To reiterate, this hypothesis was originally proposed based on the assumption that (1) the cell membrane cannot support compression in its own plane due to its thinness and (2) a situation exists where one of the principal strains in the deformed membrane is positive while the other was negative or negligible (48). In Wiesner's work the principal axes were set on the EC membrane in the streamwise and circumferential directions, and the membrane deformation was assumed to take place only by WSS in the streamwise direction.

They argued that when the cell membrane undergoes stretch (i.e. positive strain) due to the streamwise WSS then the stress perpendicular to it is small and thus the simplifying assumption of the stress field being uniaxial in the direction of flow holds. However, when it is assumed that the model wall is rigid, that there are multiple cells arranged in the circumferential direction and that they remain contiguous, it will be more appropriate to assume that the strain in this direction is zero i.e. $\lambda_2 = 1$ in Eqn. 5.28. The W for the uniaxial case computed under this assumption should be more relevant to be compared with the biaxial results. Since the membrane fluctuation of 5% was assumed between the resting and dilated state, W for the biaxial case was expected to be greater for the pulsatile case due to the additional positive strain.

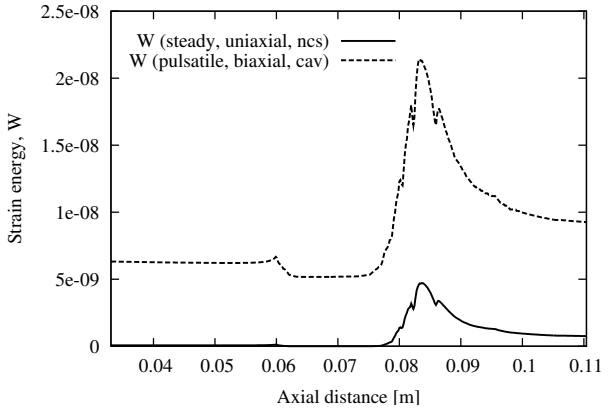

Figure 7.24: Membrane strain energy W, computed under uniaxial, no-strain assumption (i.e. $\lambda_2 = 1$ in Eqn. 5.28) and plotted on the bifurcation−sinus$_{out}$ line, shown with W computed for the biaxial case. *ncs* stands for no-circumferential strain. The unit for W is Nm^{-1}.

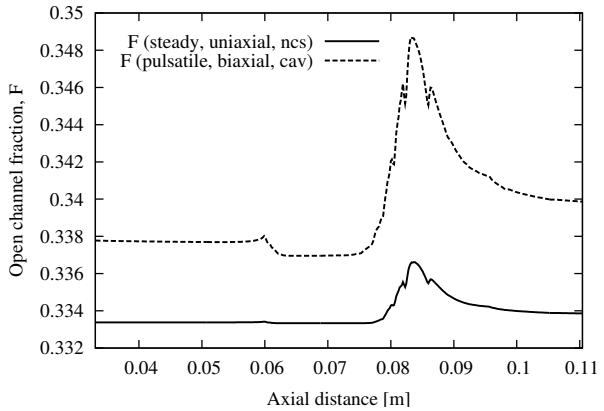

Figure 7.25: The fraction of open Ca^{2+} channels in the EC membrane, F, computed under uniaxial, no-strain assumption and plotted on the bifurcation−sinus$_{out}$ line. F computed for the biaxial case is also shown.

Figure 7.24 shows the results obtained for the steady, uniaxial case (no strain) and the pulsatile, biaxial case.

As expected, the values obtained for the biaxial case were noticeably higher than the uniaxial case. Also, although to a considerably lesser extent, those for the uniaxial show that W was still *relatively* low in the sinus region compared to the other regions in the streamwise direction.

The graphs of open Ca^{2+} channel fraction F (Fig. 7.25) are again showing the same trend. The plots of eNOS and NO obtained for the uniaxial, no-strain case reflected this (results not shown), with values in most cells being in an extremely narrow range and lower than those observed for the corresponding biaxial case.

7.5 Discussion

The focal characteristics of atherosclerosis had been a well-reported observation, and numerous studies have been carried out in an attempt to elucidate the causative factor in the initiation and progression of the disease. However, the focus of many of these studies in disciplines ranging from clinical, biochemical to fluid dynamics, was to obtain results within their respective disciplines in increasingly physiologically more realistic conditions. As a result, integrated models that incorporate these diverse factors have been scarce despite the emerging awareness that atherosclerosis is a complex disease that involves a numerous interrelated physiological processes, rather than that largely of a lipid deposition as previously considered.

The current model was developed in order to integrate these separate but interrelating phenomena, and consequently, to achieve more comprehensive understanding of atherosclerosis localisation mechanism, with a particular focus on the role the vascular geometry plays in the localisation of atherosclerotic lesions. In particular, it was essential that the model was applied to a physiologically feasible 3D model of a large scale in order to investigate the spatially varying characteristics of vascular geometry. A 3D model of an average human carotid artery bifurcation was used here for this purpose primarily because of its well-acknowledged importance in atherosclerosis research.

The focal parameter here was endothelial nitric oxide (NO), which, when not available in sufficient quantity, has been observed to lead to endothelial dysfunction and consequently to the formation of atherosclerotic lesions. The results presented in this chapter described the intermediate cellular events in the ECs involved in atherosclerosis between the physiological stimuli that reflect the spatially varying nature of vascular geometry and NO wall concentration, the latter of which is now widely believed to have direct consequences in atherosclerosis. The main components involved, and examined in the current study, were blood flow (i.e. WSS), agonist transport and distribution, Ca^{2+} dynamics, eNOS activation and subsequent endothelial NO production.

First to be investigated were WSS and agonists ATP and ADP. Obtaining 3D maps of these stimuli was one of the most important steps in this model, since these were what reflect the variation of vascular geometry, which was postulated to have a significant consequence in the localisation of atherosclerosis. The major

characteristics of WSS distribution, as detailed in Chapter 6 and Section 7.4.2 in this chapter, were that the low-WSS regions covered a very large portion of the sinus outer wall along the entire length of the sinus, as well as the top and bottom walls of the bifurcation region and a small portion of the ECA outer wall, the former of which is the region known to be prone to plaque formation. On the contrary, WSS was high near the apex and the inner walls of the bifurcation which are typically spared of the disease. Also that the increase in the flow rate resulted in the increased magnitude and complexity in the distribution pattern, but it did not affect the size of the low-WSS regions significantly. The distribution patterns, validated by experimental data in Chapter 6, also agreed well with those observed in the previous publications (66; 93).

The spatial wall distributions of the other stimuli, agonists ATP and ADP, depend on the balance between their production on or delivery to the wall surface and consumption by reaction. The production mechanisms were the flow-induced release from the EC surface for ATP and hydrolysis of ATP for ADP, whereas the sink process was hydrolysis for both agonists. The first process that initiates these reactions is the transport of ATP from the circulating blood to the wall, and therefore the distribution of ATP alone was first investigated in order to study its behaviour.

One of the critical factors that influences the transport of blood-borne substances to the vessel wall is the growth of the mass-transfer boundary layer adjacent to the wall boundary, caused by the concentration difference between the bulk flow and at the wall surface. ATP concentrations typically decrease in the streamwise direction because of the boundary-layer growth, but it fluctuates depending on the local flow conditions. These features were evident for ATP at both Reynolds numbers tested under no-release condition as shown in Fig. 7.7. ATP underwent steady decline in the CCA and ICA where flow was allowed to develop in one, streamwise direction, whereas the relative depletion of ATP observed on the outer wall within the sinus was the results of its hydrolysis to ADP, reduced advection in this region due to the low momentum of flow as well as ATP being directed away from the boundary layer adjacent to the wall due to the vortical secondary-flow. The latter feature was more evident at Re=700, where 2D plots revealed the delayed onset of flow re-development (Fig. 7.7(b)) and 3D plots the depleted-ATP region expanding from the bifurcation$-\text{sinus}_{out}$ line into the top and bottom walls of the bifurcation at the distal sinus (Fig. 7.8(b)). Both of these were due to the strengthened radial motion of the secondary flow as seen in Fig.

6.11. This also explains the sharp drop at the separation point at the CCA-ICA intersection, where reversed flow is absorbed back into the interior of the flow domain. Increased level of ATP at Re=700 indicates the effects of strengthened advective transport. With the flow-induced release included, the ATP distribution at Re=300 still maintained the similar spatial pattern though with higher levels in the CCA and ICA due to the effect of the release. At Re=700, however, it was seen that the effects of increased advection to the wall and elevated WSS were becoming more dominant in these regions, resulting in the increasing profile in the streamwise direction.

Plotting the combined concentration of ATP and ADP along the bifurcation$-$sinus$_{out}$ line under release-conditions revealed similar spatial patterns to those of ATP for both Reynolds numbers. The important implication this has is that this combined concentration was relatively low in the sinus region compared with the other locations in the domain, which would directly lead to the impaired Ca^{2+} signalling via reduced IP_3 formation in the region (Eqn. 5.9).

The 3D visualisation of the combined agonists (Fig. 7.10) revealed that its depletion was occurring not only on the bifurcation$-$sinus$_{out}$ line as described above but also in its circumferential vicinity at both Reynolds numbers. This is due to the counter-rotating near-wall flow converging and then being directed away from the region into the flow domain, resulting in the reduced advection into the boundary layer. The region of significant depletion, which is in the range of approximately 0.100-0.103μM for Re=300 and 0.11-0.119μM for Re=700, is the result of the combination of this and the reduced convection along the paths of the deflected low-momentum flow from the apex region. These are the features that were not observed in the 2D model studies by Plank et al. (108), in which the areas of depleted ATP and low WSS were observed to colocalise within the flow recirculation region, near the backward-facing step. Comparing Fig. 7.6 and Fig. 7.10 reveals that this is evidently not the case at all points in 3D. The resulting impaired Ca^{2+} signalling was confirmed by the 3D plot of cytosolic Ca^{2+} shown in Fig. 7.11.

It was observed that the cycle-averaged WSS was slightly higher in the CCA due to the constant inlet velocity profile applied at the start of each time step. At this stage this is not such a significant factor since the flow was allowed to develop before reaching the bifurcation region, which was the area of primary interest in this study. However, when more global correlation is to be sought

between WSS and plaque distributions, then it will be important to maintain physiological accuracy of WSS field throughout the flow domain, by, for example, applying a Womersley profile at the inlet.

The combined concentration of the ATP and ADP was observed to vary between the the steady and pulsatile flows, giving the maximum difference of 9% and the average 3%. The important point to note here is that, despite the difference in values, the inclusion of flow pulsatility did not significantly alter the spatial distribution pattern, which agrees with the observation made by Comerford et al. (27). Therefore the application of the EC dynamics model in steady-state conditions could be deemed reasonable. However, the aim of the present study is to investigate the correlation between vascular geometry and plaque localisation using the model that represents as close to a physiologically realistic environment as possible, as seen by the inclusion of the effect of pulsatility-induced circumferential cell stretch. The main motivation of the inclusion of the pulsatility-induced circumferential membrane stretch was that the stress phase angle (SPA), which is the phase angle difference between flow and pressure, the latter of which is represented by the circumferential stretch, correlated more accurately with plaque distribution pattern than WSS or other wall shear parameters (125). However, the overlap of the predicted plaque localisation areas was observed between WSS and SPA (125), and therefore it is deemed important to use, where possible, the pulsatile data, particularly given that the transport behaviour of low-diffusivity species such as ATP, LDL and oxygen relevant to atherosclerosis in complex 3D flow has not yet been well-documented.

One limitation of the current setting regarding the modelling of the agonist is that the depletion of ATP release source and its replenishment mechanisms are not taken into account. As stated in Section 5.5.1, the sustainability of ATP release is still not well-documented, though the phenomenon of the release itself has been well-studied (14; 94; 139; 140) and the involvement of ATP synthase on the EC surface in the WSS-induced release was observed by Yamamoto et al. (139), which makes it likely that the ATP source does get replenished from adenosine in the circulating blood. This partly justifies the assumption of continuous release in the present study, although the balance of release and replenishment should be modelled into the Eqn. 5.4 for more realistic representation of physiological agonist dynamics.

In the EC dynamics model, the factors described above (ATP, ADP and

WSS) act as external stimuli that elicit intracellular responses in the ECs that subsequently lead to NO production. These inputs, computed in FLUENT at each grid point, were taken into the EC dynamics model to produce 3D maps of cellular variables that reflect the spatially-varying nature of the stimuli.

EC membrane strain energy W, computed based on the pressure/stress-induced membrane stretch, regulates the open-state fraction of Ca^{2+} influx channels in the membrane. This is where the effects of different formulation of W between steady, uniaxial-tension and pulsatile, biaxial-tension cases should first become evident.

First the results were obtained for W for the steady, uniaxial case as a direct extension of the previous work (27; 108; 137). As expected from Eqn. 5.27, the distribution pattern of W reflects that of WSS strongly, i.e. constant in the CCA, low on the sinus outer, bifurcation top and bottom and proximal ECA outer walls while high on the ICA wall and inner walls of the sinus and proximal ECA (Fig. 7.17(a)). This trend was also observed for the pulsatile, biaxial case. However, the strain energy estimated under biaxial tension were considerably (approximately one order of magnitude) lower and in an extremely narrow range (Fig. 7.17(b) and Fig. 7.18) compared with those obtained for the steady, uniaxial case.

The near-uniform concentrations of eNOS and the endothelial NO over the entire model wall except near the bifurcation apex, observed in Fig. 7.19(a) and Fig. 7.20(a) respectively, were most likely to be the result of this. The examination of F, which takes W as an input in its exponential function (Eqn. 5.15), revealed that the W computed for the pulsatile, biaxial case led to F being in the range of 0.3333-0.3334 for the majority of the wall cells except those in the very small area around the bifurcation apex. This is due to the input into the exponential function being both very low and in a narrow range, resulting in the similarly near-uniform eNOS and NO distribution in the majority of the wall cells. However, this is unlikely to be the case in the condition *in vivo*, given that atherosclerosis is a very focal disease and that bioavailability of NO has been reported to correlate with the disease's site specificity.

Here, two approaches were taken to examine the results obtained so far focusing on the following points:

1. There were uncertainties in the validity of the model parameter, F. This was addressed and the model behaviour tested with various values of F.

2. The assumption of no-stress in the circumferential direction originally used by Wiesner et al. (137) may not have been appropriately modelled or correctly applied in the publications that followed.

1. In the original formulation of F, the parameters α and f_e were estimated values, set as 3 and 0.013351 respectively (137). However, α, a parameter that governs the ion channel's open-state probability, was defined as 2 in the present study (which gives 33% probability), based on that the original value of 3 (i.e. 25% probability) would result in non-physiological cytosolic Ca^{2+} concentration due to the imbalance between Ca^{2+} influx and efflux (108). This leaves the behaviour of Eqn. 5.15 depending on the other estimated parameter f_e. In order to test the sensitivity of F on f_e, F was computed with various values of f_e (the original value multiplied by 0.1, 10, 20 and 30, which give the membrane strain energy availability ranging between 0.133-40%) and plotted along the bifurcation$-$sinus$_{out}$ line on the sinus outer wall, along with the values obtained using the original f_e for both uniaxial and biaxial cases (Fig. 7.21). This is equivalent to decreasing or increasing the amount of strain energy available to gate the Ca^{2+} channels. Comparing F obtained for steady, uniaxial and pulsatile, biaxial cases with the original f_e reveals a similar trend to that observed for W, i.e. both share similar spatial distribution features but with smaller amplitude for the pulsatile, biaxial case. Comparing F plotted with varying values of f_e for the pulsatile, biaxial case reveals that the values of F become more elevated in all ECs along the bifurcation$-$sinus$_{out}$ line with increasing f_e, again showing the similar spatial features with decreasing amplitudes. It also reveals that the spatial sensitivity of the function is very low with the original value of f_e (=0.013351) and $f_e * 0.1$, resulting in near-uniform values of F. This insensitivity of F for low f_e value was confirmed by plotting the maximum value of F against f_e, as shown in Fig. 7.22.

The NO concentration shown in Fig. 7.20(a), however, is not considered likely to be physiologically practical for the reason mentioned previously, and therefore the computation of NO wall concentration was carried out for the pulsatile, biaxial case using f_e=0.13351, which was the minimum value of f_e with which F showed spatial sensitivity. The 3D endothelial NO distribution obtained as a result (Fig. 7.20(b)) exhibits a similar distribution trend to that observed for W, although to a smaller extent, reflecting the increase in the sensitivity of the F function. The NO plot along the bifurcation$-$sinus$_{out}$ line (Fig. 7.23) addi-

tionally shows higher concentration in the CCA and the sinus but lower in the proximal and distal ICA compared with the steady, uniaxial case. The implication of this observation is at this point uncertain, given that the physiological value of f_e and whether its value should vary between steady and pulsatile flow is currently unknown. However, what should be noted here is that the concentration of endothelial NO is still *relatively* low in the areas widely considered prone to plaque formation and that these sites colocalise with low WSS regions. This strongly implies the correlation between vascular geometry (and hence WSS) and low endothelial NO concentration, and therefore plaque localisation, under pulsatile, biaxial tension. The comparison of Fig. 7.10, Fig. 7.13, Fig. 7.15, Fig. 7.19 and Fig. 7.20 also revealed that the concentration level of agonists ATP and ADP at the wall seems to be a less significant factor in the activation of eNOS and subsequent NO production compared to WSS. The correlation had already been widely observed under steady flow by many other groups. However, to the author's knowledge, the numerical modelling of endothelial NO using physiologically realistic 3D geometry and boundary conditions has been scarce, and the author believes the current model provides a base case of integrated fluid dynamics and cellular model to which additional processes can be introduced in order to replicate the pathophysiological conditions *in vivo*.

2. The analysis and interpretation presented above are for the results obtained using the EC dynamics model developed as a direct extension of the existing models (27; 108; 137). In Section 7.4.4, further results were obtained using the model that had been modified to incorporate appropriate application of the original *tension-field* hypothesis (48).

In the original publication (137), a simplification of the stress field on the cell membrane was made by virtue of the *tension-field* hypothesis (48) so that the stress in the circumferential direction was considered negligible, resulting in the stress field that is uniaxial in the direction of flow. This assumption holds when the physical restriction by and interaction with neighbouring cells do not have to be considered (as in (137)). However, as in the current study where there are multiple cells arranged in the circumferential direction and the model wall is rigid, it would be more appropriate to assume a no-strain condition in this direction, i.e. the circumferential stretch ratio $\lambda_2 = 1$ in Eqn. 5.28 if the cells to remain contiguous. Under this assumption, a comparison of the results obtained for W and F was made between the uniaxial and biaxial cases. It was expected that the values of W for the biaxial case would be greater due to the induction

of additional positive strain field into the formulation, and that F reflected the result. The results obtained (Fig. 7.24, Fig. 7.25) confirmed these predictions. These figures show that the distribution pattern of W and F for the uniaxial, no-strain case was even more dampened out than the pulsatile, biaxial case. The plots of eNOS and NO showed the values being in a much narrower range and their spatial distribution features much less evident and almost near-uniform compared with the uniaxial, no-stress case (results not shown). It was also noted that the distribution trend of both variables still retain the features observed for WSS (i.e. constant in the CCA, low within the sinus, more elevated in the ICA), although to a much lesser extent.

The first point to be concluded from the discussion above is that more experimental work is strongly recommended to determine or facilitate the estimation of the value f_e. The second is that, more importantly, the no-strain in the circumferential direction rather than the conventional no-stress assumption should be used if further work is to be carried out using a uniaxial assumption in rigid-wall models, whether or not the results are to be compared against those from biaxial models. This is on the basis that the W values obtained for the first uniaxial case were considerably higher (approximately one order of magnitude) than the biaxial case (Fig. 7.18), which is deemed unrealistic given that higher values were expected for the biaxial case due to the inclusion of additional positive strain. However, given that the next appropriate step would be the inclusion of distensible wall properties, it is recommended that the biaxial approach be used. This, together with more accurate biochemical constants for the EC processes, would lead to physiologically more accurate estimation of variables involved in EC dynamics.

Considering all the points discussed above, the main finding here is that there still likely to be a spatial variation of endothelial NO reflecting local haemodynamic features. The primary region of low endothelial NO (and therefore at a larger risk of plaque development) was seen within the carotid sinus, which largely colocalised with the sites of low WSS. The extent of spatial variation revealed in this study with the modified (i.e. no-circumferential strain) assumption was clearly not as pronounced as it was in the results obtained with the conventional uniaxial approach with a no-circumferential stress assumption. However, considering the length of time that is needed for atherosclerosis to develop, it might be the accumulating effects of this *relatively* low concentration of endothelial NO, brought about by the low-WSS inducing vessel geometry, that turns early lesions

into clinically significant atherosclerotic lesions.

The main limitation of the present model is the assumption that the model wall is rigid and SPA is zero, i.e. the pressure and WSS are in phase. However, the SPA has been reported to be approx. -90° in straight large arteries (111), and can be more negative depending on the location of the vessel (125). It was proposed in the latter study, which was carried out using a 3D flow domain, that negative SPA correlates more precisely with plaque localisation than wall-shear parameters, observing that negative SPA values colocalised with plaque locations both in the carotid and coronary arteries whereas parameters such as low WSS and high oscillatory shear index (OSI) predicted the plaque locations only in the carotid bifurcation. In addition, the increased production of vasoconstrictors and decreased synthesis of vasodilators in the ECs under negative SPA, compared with the steady flow case, have been reported (111). While the current model should be extended to incorporate the physiological SPA and wall compliance in order to further the modelling of NO dynamics in physiologically more accurate environment, more experimental work is also strongly encouraged focusing on eNOS and NO dynamics in physiological flow and geometrical settings, which will not only allow the validation of integrated numerical models such as those used in the present study but also accelerate the understanding of atherosclerosis' localisation mechanisms.

Chapter 8

Current Findings and Recommendations for Future Work

8.1 Current findings

Chapter 6 presented detailed analyses of fluid dynamics features of flow through an average human carotid bifurcation geometry. The major outcome from the validation was that the numerical haemodynamic solutions that control the quantity of the two physiological stimuli, ATP and WSS, which were to be taken into the subsequent EC dynamics model, were quantitatively validated. Ensuring the solution accuracy in the fluid phase was an important step, since, because of the complexity of the EC dynamics model and the difficulties of obtaining *in vivo* data for each process of the EC dynamics involved in the current modelling, the numerical solutions obtained for the cellular variables are, at this stage, not able to be validated. In addition to the quantitative agreement obtained for WSS along the bifurcation−sinus$_{out}$ line (which was deemed successful), another advantage of this validation practice was the observation of the behaviour of the secondary flow. This had major implications in the transport of ATP to the wall surface as the vortical motion of the counter-rotating secondary flow, which converges at the outer wall of the bifurcation and then is directed away into the flow domain, results in the reduced delivery of ATP into the boundary layer adjacent to the wall, leading to its depletion in these regions.

The first case of the cellular model of EC dynamics modelled the production of endothelial NO via the Ca^{2+} and downstream eNOS signalling that were stimulated by ATP and WSS in steady flow, under the assumption that the cells were exposed to uniaxial, streamwise tension field. This was carried out as the direct extension of the previous publications on the relevant EC processes and their implications in atherosclerosis (27; 108; 137). The comparison of WSS distribution and eNOS concentration field revealed the latter's very strong dependence on the former. This observation agreed well with the results obtained by Comerford et al. (27) for idealised models of bifurcations and bends. In the regions of low WSS, which were observed to be present on the sinus outer wall and the top and bottom walls of the bifurcation, the eNOS signalling was found to be diminished. This was likely to be the results of the following phenomena brought about by low WSS:

- Impaired Ca^{2+} signalling (as shown in Fig. 7.11), due to reduced delivery and release of ATP and decreased WSS-induced influx of extracellular Ca^{2+}
- Reduced phosphorylation of eNOS

The numerical computation of the endothelial NO, which had not been carried out in a physiologically realistic geometry and flow environment to date, exhibited a very similar trend observed for eNOS. The bioavailability of the endothelial NO, which depends on the catalytic activity of eNOS and its removal by NO scavengers present within or in the vicinity of the ECs, was observed to be reduced at the locations of low WSS. For both eNOS and endothelial NO, the spatial distributions were not found to be significantly dependent on the concentration field of the agonists. This observation for eNOS agreed well with that previously made by Comerford et al. (27). The subsequent explicit estimation of the concentration of endothelial NO implied an even stronger influence of the vascular geometry on the localisation of atherosclerosis than previously considered.

The subsequent modelling of NO dynamics in pulsatile, biaxial tension fields included the effects of the membrane stretch in the circumferential direction as well as that in the streamwise direction. The implication of this approach was that the flow-activated influx of extracellular Ca^{2+} to the cytosol was now dependent not only on WSS but also on the pressure pulse inherent with the pulsatility of the arterial blood flow. This was motivated by the observations that WSS or other wall shear parameters alone do not correlate well with plaque localisation

when compared on a large-scale, point-by-point basis (62; 122), and that the inclusion of the effect of the other haemodynamic forces, i.e. pressure, might lead to an improved correlation (124). It was also an obvious improvement in model formulation in terms of more realistic representation of the conditions *in vivo*. As a control study, the pressure waveform brought about by the cardiac pulse was assumed to take the same form as the flow waveform and also that both forces were in phase.

The membrane strain energy was the parameter that should first reflect the difference between the uniaxial and biaxial cases. Comparison of the results obtained for both cases revealed a very similar spatial distribution pattern, which was observed to be a strong function of WSS. What was noted here, however, was the difference in the value of the strain energy: for the biaxial case the values were considerably lower than those obtained for the uniaxial case. These lower values of the strain energy resulted in the open probability of the membrane Ca^{2+} channels being near-uniform in the majority of the wall cells. This subsequently propagated into the computation of eNOS and NO and resulted in the cellular values of the variables being near-uniform in the majority of the wall cells except those near the bifurcation apex region and the proximal ICA where WSS magnitude was observed to be significantly higher than other parts within the flow domain.

Considering that the near-uniform concentration of the endothelial NO is not likely to be actually what is taking place *in vivo* given the well-documented site specificity of atherosclerosis, the validity of the model parameters and assumption used were tested and analysed at this point in order to examine the results.

The solutions for the pulsatile, biaxial case being represented with low values and in a narrow range were found to be because of the open-channel fraction function F being insensitive to the low input values of strain energy W. Since W was calculated using flow solution variables and therefore its values were unmodifiable, the model parameter f_e, which governs the energy available to gave the membrane Ca^{2+} channels, in the open Ca^{2+} channel fraction function F that was still an initial estimate in the original publication (137) was adjusted and solutions obtained in order to study how it would affect the overall spatial distribution of eNOS and NO. The results showed that the function F exhibited increased sensitivity with larger values of f_e (which would effectively increase the amount of the membrane strain energy used to gate the Ca^{2+} to 13.35-40 from the original 1.335%), and its spatial distribution patterns still displayed some

degree of similarity to those of WSS, although to a lesser extent with dampened local features and amplitudes. This trend was mirrored in the estimation of the downstream EC variables eNOS and NO. An important point to note here was that the endothelial NO was observed to be relatively diminished in the sinus region compared to the other parts of the model wall regardless of the values of f_e or the membrane stretch being modelled as uniaxial or biaxial. The sinus region is therefore still expected to be more susceptible to the upregulation of inflammatory processes, which leads to endothelial dysfunction, an early marker of atherosclerosis.

The same set of results were then obtained for the uniaxial case using a modified EC dynamics model with the assumption of zero-strain in the circumferential direction so that now it is explicitly defined that the cells remain contiguous, rather than zero-stress as it was conventionally assumed (Section 7.4.4), and were compared with those obtained for the biaxial case. The results demonstrated that the membrane strain energy for the uniaxial case was lower and its spatial features less pronounced than those for the biaxial case. However, the trend for the spatial distribution features was still present and showed that the W, F, eNOS and endothelial No were still lower in the sinus region where the localisation of plaques is often observed.

The formation of fatty plaques often starts during adolescence, but those plaques have no particular site preference, and only some develop into clinically consequential lesions which are often found in the "atherosclerosis-prone" regions three to four decades later. From this observation and the results obtained in this study, it is proposed that the development of atherosclerotic plaques is the result of chronic *relative* low availability of the endothelial NO in the vascular wall which in turn is the result of the vascular geometry that brings about low local WSS, and that the vascular geometry should be considered as an unmodifiable, anatomic risk factor.

The major limitation of the current study is that the model wall is rigid. In order to apply the NO dynamics model in physiologically more realistic environment, modification of this condition to a distensible one should be next to be incorporated. This will allow the physiological phase angle difference between WSS and the pressure pulse to be introduced to the model, and therefore to fully incorporate the effects of blood pulsatility. The comparison of the correlation between the plaque distribution and WSS or stress phase angle will then also be

possible. Further advancement can be made by applying the model to patient specific geometries and boundary conditions obtained via medical imaging techniques such as MRI, so that the results obtained from the NO dynamics model can be directly compared with the wall thickness data from MRI. This will allow the numerical cellular model to be validated, which will be a significant step given the lack of comparable experimental data available at present.

8.2 Recommendations for future work

In relation to the validation of flow solutions, further improvement can be made by measuring velocities and calculating WSS using all components in three axes. CFD is already capable of providing 3D velocity and WSS data, and therefore the improvement will depend on using a more advanced PIV technique. A suitable method currently available is the 3D stereoscopic PIV. This, unlike the current PIV method used that can capture only two velocity components, allows the third component to be captured by using two cameras positioned in a stereoscopic arrangement. Also, validation of flow solutions under pulsatile flow conditions, and ultimately in patient specific geometries, is recommended, in order to ensure the accuracy of flow solutions in an increasingly physiologically complex setting, which will be a productive and useful direction for both flow and cell dynamics studies, as well as continuing validation of developing experimental techniques.

In EC dynamics models, in addition to the suggestions made previously, future work should involve the elaboration of NO dynamics modelling. Currently, the production rate constant used is based on the numerical studies carried out for arterioles. Similar studies of NO production kinetics, particularly those involving eNOS, are encouraged for arteries, as they have been scarce thus far. For the scavenging of NO, again the data that could provide the reaction constants involving NO, its scavengers, SODs in the endothelial environment has been limited, although there had been some data available that dealt with NO and the primary scavenger superoxide anion O_2^-. Therefore experimental work is encouraged to facilitate understanding of NO kinetics involving a broader range of relevant substances in the endothelium.

In agonist modelling, experimental work will be required to establish the source and the time course of ATP release under physiological conditions. Given that the potential source of ATP, adenosine, is present in the circulating blood and

that the existence of ATP synthase on the endothelial surface has been reported, it would be reasonable to assume that ATP does become replenished. However, the combined time-dependent model of flow-induced release and replenishment is still poorly understood,

Also, there needs to be more comprehensive experimental work carried out for the investigation of EC dynamics. The application the numerical EC dynamics model to patient-specific geometries and subsequent data comparison with the wall thickness data might facilitate establishing the correlation between the geometry and NO, but the accuracy of the intermediate processes involved and simulation parameters (such as the membrane strain-energy gating fraction mentioned in the previous section) used still cannot be determined by this method.

Lastly, the addition of diffusion of NO into luminal and sub-endothelial space (and subsequent advection for the former) should be considered in order to study more global effects of NO availability on the regulation of vascular tone. The results of the endothelial NO looked at in the present study have more implication in NO's anti-atherogenic properties, and therefore this will additionally shed light on spatial variation of NO's vasodilatory properties and its implications in atherosclerosis, leading to the broader understanding of NO's role in vascular homeostasis and the pathophysiology of atherosclerosis.

Bibliography

[1] *ANSYS FLUENT 12.0/12.1 Documentation*. Lebanon, NH, USA, 2010.

[2] Cell biology, October 2010.

[3] Adams, D., Barakeh, J., Laskey, R., and Van Breemen, C. Ion channels and regulation of intracellular calcium in vascular endothelial cells. *The FASEB Journal 3*, 12 (10 1989), 2389–2400.

[4] Andersen, M. R., Walker, L. R., and Stender, S. Reduced endothelial nitric oxide synthase activity and concentration in fetal umbilical veins from maternal cigarette smokers. *American journal of obstetrics and gynecology 191*, 1 (07 2004), 346–351.

[5] Andrews, A. M., Jaron, D., Buerk, D. G., Kirby, P. L., and Barbee, K. A. Direct, real-time measurement of shear stress-induced nitric oxide produced from endothelial cells in vitro. *Nitric Oxide In Press, Corrected Proof*, –.

[6] Asakura, T., and Karino, T. Flow patterns and spatial distribution of atherosclerotic lesions in human coronary arteries. *Circulation Research 66*, 4 (4 1990), 1045–1066.

[7] Balbatun, A., Louka, F. R., and Malinski, T. Dynamics of nitric oxide release in the cardiovascular system. *Acta Biochimica Polonica 50*, 1 (2003), 61–68.

[8] Ben Driss, A., Benessiano, J., Poitevin, P., Levy, B. I., and Michel, J. B. Arterial expansive remodeling induced by high flow rates. *AJP - Heart and Circulatory Physiology 272*, 2 (2 1997), H851–858.

[9] Berridge, M. J. Capacitative calcium entry. *Biochemical Journal 312*, 1 (11 1995), 1–11.

[10] BERRIDGE, M. J. Inositol trisphosphate and calcium signaling. *Annals of the New York Academy of Sciences 766*, 1 (1995), 31–43.

[11] Bharadvaj, B. K., Mabon, R. F., and Giddens, D. P. Steady flow in a model of the human carotid bifurcation. 1 - flow visualization. *Journal of Biomechanics 15*, 5 (1982), 349 – 362.

[12] Bharadvaj, B. K., Mabon, R. F., and Giddens, D. P. Steady flow in a model of the human carotid bifurcation. 2 - laser-doppler anemometry measurements. *Journal of Biomechanics 15*, 5 (1982), 363 – 378.

[13] Blackman, B. R., Garcia-Cardena, G., and Michael A. Gimbrone, J. A new in vitro model to evaluate differential responses of endothelial cells to simulated arterial shear stress waveforms. *Journal of Biomechanical Engineering 124*, 4 (2002), 397–407.

[14] Bodin, P., Bailey, D., and Burnstock, G. Increased flow-induced atp release from isolated vascular endothelial cells but not smooth muscle cells. *British journal of pharmacology 103*, 1 (05 1991).

[15] Bodin, P., and Burnstock, G. Evidence that release of adenosine triphosphate from endothelial cells during increased shear stress is vesicular. *Journal of Cardiovascular Pharmacology 38*, 6 (2001), 900 – 908.

[16] Bodin, P., Loesch, P., Milner, P., and Burnstock, G. *Biomechanics and cells.* Society for Experimental Biology Seminar Series 54. Cambridge University Press, Cambridge, Great Britain, 1994, ch. Effect of increased flow on release of vasoactive substance from vascular endothelial cells, pp. 36–60.

[17] Botnar, R., Rappitsch, G., Scheidegger, M. B., Liepsch, D., Perktold, K., and Boesiger, P. Hemodynamics in the carotid artery bifurcation:: a comparison between numerical simulations and in vitro mri measurements. *Journal of biomechanics 33*, 2 (02 2000), 137–144.

[18] Buchmann, N. A., Jermy, M., and Nguyen, C. Experimental investigation of carotid artery haemodynamics in an anatomically realistic model. *International Journal of Experimental and Computational Biomechanics 1*, 2 (2009), 172–192.

[19] Buchmann, N. A., Nguyen, C., Wells, J. C., and Jermy, M. In-vitro wall shear stress measurements using interfacial particle image velocimetry (IPIV). In *14th International Symposium on Applications of Laser Techniques to Fluid Mechanics* (Lisbon, Portugal, 2008).

[20] Buchmann, N. A., Yamamoto, M., Jermy, M., and David, T. Particle image velocimetry (PIV) and computational fluid dynamics (CFD) modelling of carotid artery haemodynamics under steady flow- a validation study. *Journal of Biomechanical Science and Engineering 5*, 4 (2010), 421–436.

[21] Busse, R., and Mlsch, A. Calcium-dependent nitric oxide synthesis in endothelial cytosol is mediated by calmodulin. *FEBS Letters 265*, 1-2 (6 1990), 133–136.

[22] Caro, C. G., Fitz-Gerald, J. M., and Schroter, R. C. Atheroma and arterial wall shear observation, correlation and proposal of a shear dependent mass transfer mechanism for atherogenesis. *Proceedings of the Royal Society of London. Series B, Biological Sciences 177*, 1046 (Feb. 16, 1971), 109–133.

[23] Chappell, D. C., Varner, S. E., Nerem, R. M., Medford, R. M., and Alexander, R. W. Oscillatory shear stress stimulates adhesion molecule expression in cultured human endothelium. *Circulation Research 82*, 5 (3 1998), 532–539.

[24] Chen, K., and Popel, A. S. Theoretical analysis of biochemical pathways of nitric oxide release from vascular endothelial cells. *Free Radical Biology and Medicine 41*, 4 (2006), 668 – 680.

[25] Chiu, J. J., Wang, D. L., Chien, S., Skalak, R., and Usami, S. Effects of disturbed flow on endothelial cells. *Journal of Biomechanical Engineering 120*, 1 (1998), 2–8.

[26] Chuang, P. T., Cheng, H. J., Lin, S. J., Jan, K. M., Lee, M. M. L., and Chien, S. Macromolecular transport across arterial and venous endothelium in rats. studies with evans blue-albumin and horseradish peroxidase. *Arteriosclerosis 10*, 2 (1990), 188–197.

[27] Comerford, A., Plank, M. J., and David, T. Endothelial nitric oxide synthase and calcium production in arterial geometries: An integrated fluid mechanics/cell model. *Journal of Biomechanical Engineering 130*, 1 (02 2008), 011010–13.

[28] Corson, M. A., James, N. L., Latta, S. E., Nerem, R. M., Berk, B. C., and Harrison, D. G. Phosphorylation of endothelial nitric oxide synthase in response to fluid shear stress. *Circulation Research 79*, 5 (11 1996/11/1), 984–991.

[29] Dancu, M. B., Berardi, D. E., Vanden Heuvel, J. P., and Tarbell, J. M. Asynchronous shear stress and circumferential strain reduces endothelial no synthase and cyclooxygenase-2 but induces endothelin-1 gene expression in endothelial cells. *Arteriosclerosis, Thrombosis, and Vascular Biology 24*, 11 (11 2004), 2088–2094.

[30] Dancu, M. B., and Tarbell, J. M. Large negative stress phase angle (spa) attenuates nitric oxide production in bovine aortic endothelial cells. *Journal of Biomechanical Engineering 128*, 3 (2006), 329–334.

[31] David, T. Wall shear stress modulation of atp/adp concentration at the endothelium. *Annals of Biomedical Engineering 31*, 10 (11 2003/11/01/), 1231–1237.

[32] Davies, P. F., Mundel, T., and Barbee, K. A. A mechanism for heterogeneous endothelial responses to flow in vivo and in vitro. *Journal of Biomechanics 28*, 12 (1995/12), 1553–1560.

[33] Davignon, J., and Ganz, P. Role of endothelial dysfunction in atherosclerosis. *Circulation 109*, 23_suppl_1 (6 2004), III–27–32.

[34] De Caterina, R., Libby, P., Peng, H. B., Thannickal, V. J., Rajavashisth, T. B., Gimbrone, M. A., Shin, W. S., and Liao, J. K. Nitric oxide decreases cytokine-induced endothelial activation. nitric oxide selectively reduces endothelial expression of adhesion molecules and proinflammatory cytokines. *The Journal of Clinical Investigation 96*, 1 (07 1995), 60–68.

[35] De Keulenaer, G. W., Chappell, D. C., Ishizaka, N., Nerem, R. M., Alexander, R. W., and Griendling, K. K. Oscillatory and

steady laminar shear stress differentially affect human endothelial redox state : Role of a superoxide-producing nadh oxidase. *Circulation Research 82*, 10 (6 1998), 1094–1101.

[36] DeBakey, M. E., Lawrie, G. M., and Glaeser, D. H. Patterns of atherosclerosis and their surgical significance. *Annals of Surgery 201*, 2 (1985).

[37] Dimmeler, S., Fleming, I., Fisslthaler, B., Hermann, C., Busse, R., and Zeiher, A. M. Activation of nitric oxide synthase in endothelial cells by akt-dependent phosphorylation. *Nature 399*, 6736 (06 1999), 601–605.

[38] Ding, Z., Wang, K., Li, J., and Cong, X. Flow field and oscillatory shear stress in a tuning-fork-shaped model of the average human carotid bifurcation. *Journal of Biomechanics 34*, 12 (2001), 1555 – 1562.

[39] Ethier, C. R. Computational modeling of mass transfer and links to atherosclerosis. *Annals of Biomedical Engineering 30*, 4 (04 2002/04/01/), 461–471.

[40] Falk, E. Why do plaques rupture? *Circulation 86*, 6 Suppl (1992), III30–42.

[41] Faraci, F. M., and Didion, S. P. Vascular protection: Superoxide dismutase isoforms in the vessel wall. *Arteriosclerosis, Thrombosis, and Vascular Biology 24*, 8 (8 2004), 1367–1373.

[42] Fichtlscherer, S., Rosenberger, G., Walter, D. H., Breuer, S., Dimmeler, S., and Zeiher, A. M. Elevated c-reactive protein levels and impaired endothelial vasoreactivity in patients with coronary artery disease. *Circulation 102*, 9 (8 2000), 1000–1006.

[43] Florey, L. The endothelial cell. *British Medical Journal 2*, 5512 (08 1966), 487–490.

[44] Fox, R. W., and McDonald, A. T. *Introduction to Fluid Mechanics*, 4 ed. John Wiley & Sons, Inc., 1994.

[45] Fox, S. I. *Human Physiology*, 4 ed. W. C. Brown, 1993.

[46] Fry, D. L. Certain histological and chemical responses of the vascular interface to acutely induced mechanical stress in the aorta of the dog. *Circulation Research 24*, 1 (1 1969), 93–108.

[47] Fung, Y. C. *Biomechanics: Mechanical Properties of Living Tissues*, 2 ed. Springer-Verlag New York, Inc., 175 Fifth Avenue, New York, NY 10010, USA, 1993.

[48] Fung, Y. C., and Liu, S. Q. Elementary mechanics of the endothelium of blood vessels. *Journal of Biomechanical Engineering 115*, 1 (1993), 1–12.

[49] Furchgott, R. F., and Zawadzki, J. V. The obligatory role of endothelial cells in the relaxation of arterial smooth muscle by acetylcholine. *Nature 288*, 5789 (11 1980), 373–376.

[50] Ganong, M. D., and William, F. *Review of Medical Physiology*, 22 ed. The McGraw-Hill Companies, Inc., 2005.

[51] Gawaz, M., Langer, H., and May, A. E. Platelets in inflammation and atherogenesis. *The Journal of Clinical Investigation 115*, 12 (12 2005), 3378–3384.

[52] Gnasso, A., Irace, C., Carallo, C., De Franceschi, M. S., Motti, C., Mattioli, P. L., and Pujia, A. In vivo association between low wall shear stress and plaque in subjects with asymmetrical carotid atherosclerosis. *Stroke 28*, 5 (5 1997), 993–998.

[53] Gow, A. J., Luchsinger, B. P., Pawloski, J. R., Singel, D. J., and Stamler, J. S. The oxyhemoglobin reaction of nitric oxide. *Proceedings of the National Academy of Sciences of the United States of America 96*, 16 (08 1999), 9027–9032.

[54] Gray, H. Anatomy of the human body.

[55] Griffith, T. M., Lewis, M. J., Newby, A. C., and Henderson, A. H. Endothelium-derived relaxing factor. *Journal of the American College of Cardiology 12*, 3 (9 1988), 797–806.

[56] Gutstein, W. H. Vasospasm, vascular injury, and atherogenesis: A perspective. *Human pathology 30*, 4 (04 1999), 365–371.

[57] Guyton, A. C., and Hall, J. E. *Textbook of Medical Physiology*, 11 ed. Elsevier Inc., Philadelphia, Pennsylvania, 2006.

[58] Haas, T. L., and Duling, B. R. Morphology favors an endothelial cell pathway for longitudinal conduction within arterioles. *Microvascular Research 53*, 2 (3 1997), 113–120.

[59] Helmlinger, G., Berk, B. C., and Nerem, R. M. Calcium responses of endothelial cell monolayers subjected to pulsatile and steady laminar flow differ. *AJP - Cell Physiology 269*, 2 (8 1995), C367–375.

[60] Hill, N., Pierchala, B., Johns, A., Kiechle, F., Rubanyi, G. M., and Malinski, T. *In Situ* measurements of nitric oxide release from endothelial cells grown directly on a porphyrinic sensor. *Endothelium: Journal of Endothelial Cell Research 4*, 1 (1996), 63–69.

[61] John, K., and Barakat, A. Modulation of atp/adp concentration at the endothelial surface by shear stress: Effect of flow-induced atp release. *Annals of Biomedical Engineering 29*, 9 (09 2001), 740–751.

[62] Joshi, A. K., Leask, R. L., Myers, J. G., Ojha, M., Butany, J., and Ethier, C. R. Intimal thickness is not associated with wall shear stress patterns in the human right coronary artery. *Arteriosclerosis, Thrombosis, and Vascular Biology 24*, 12 (12 2004), 2408–2413.

[63] Karner, G., Perktold, K., Hofer, M., and Liepsch, D. Flow characteristics in an anatomically realistic compliant carotid artery bifurcation model. *Computer Methods in Biomechanics and Biomedical Engineering 2*, 3 (1999), 171–185.

[64] Kawahara, K., and Matsuzaki, K. Activation of calcium channel by shear-stress in cultured renal distal tubule cells. *Biochemical and Biophysical Research Communications 184*, 1 (4 1992), 198–205.

[65] Kim, H. Y., Thomas, D., and Hanley, M. R. Chromatographic resolution of an intracellular calcium influx factor from thapsigargin-activated jurkat cells. *Journal of Biological Chemistry 270*, 17 (04 1995), 9706–9708.

[66] Köhler, U., Marshall, I., Robertson, M. B., Long, Q., Xu, X. Y., and Hoskins, P. R. Mri measurement of wall shear stress vec-

tors in bifurcation models and comparison with cfd predictions. *Journal of Magnetic Resonance Imaging 14*, 5 (2001), 563–573.

[67] Kraiss, L. W., Geary, R. L., Mattsson, E. J. R., Vergel, S., Au, Y. P. T., and Clowes, A. W. Acute reductions in blood flow and shear stress induce platelet-derived growth factor-a expression in baboon prosthetic grafts. *Circulation Research 79*, 1 (7 1996), 45–53.

[68] Ku, D., and Giddens, D. Pulsatile flow in a model carotid bifurcation. *Arteriosclerosis, Thrombosis, and Vascular Biology 3*, 1 (1 1983), 31–39.

[69] Ku, D. N., Giddens, D. P., Zarins, C. K., and Glagov, S. Pulsatile flow and atherosclerosis in the human carotid bifurcation. positive correlation between plaque location and low and oscillating shear stress. *Arteriosclerosis 5*, 3 (1985), 293–302.

[70] Kuchan, M. J., and Frangos, J. A. Role of calcium and calmodulin in flow-induced nitric oxide production in endothelial cells. *AJP - Cell Physiology 266*, 3 (3 1994/3/1), C628–636.

[71] Kunitimo, M. Oxidative stress and atherosclerosis. *YAKUGAKU ZASSHI 127*, 12 (2007), 1997–2014.

[72] Lancaster, J. R. Simulation of the diffusion and reaction of endogenously produced nitric oxide. *Proceedings of the National Academy of Sciences of the United States of America 91*, 17 (08 1994), 8137–8141.

[73] Lehrke, M., Greif, M., and Broedl, U. C. e. a. Mmp-1 serum levels predict coronary atherosclerosis in humans. *Cardiovascular Diabetology 8*, 50 (2009), http://www.cardiab.com/content/8/1/50.

[74] Levesque, M., Liepsch, D., Moravec, S., and Nerem, R. Correlation of endothelial cell shape and wall shear stress in a stenosed dog aorta. *Arteriosclerosis, Thrombosis, and Vascular Biology 6*, 2 (3 1986), 220–229.

[75] Levesque, M. J., and Nerem, R. M. The elongation and orientation of cultured endothelial cells in response to shear stress. *Journal of Biomechanical Engineering 107*, 4 (1985), 341–347.

[76] Levesque, M. J., Nerem, R. M., and Sprague, E. A. Vascular endottielial cell proliferation in culture and the influence of flow. *Biomaterials 11*, 9 (11 1990), 702–707.

[77] Levick, J. R. *An Introduction to Cardiovascular Physiology*, 4 ed. Arnold, 338 Euston Road, London NW1 3BH, 2003.

[78] Libby, P., Ridker, P. M., and Maseri, A. Inflammation and atherosclerosis. *Circulation 105*, 9 (3 2002/3/5), 1135–1143.

[79] Lin, S., Fagan, K. A., Li, K.-X., Shaul, P. W., Cooper, D. M. F., and Rodman, D. M. Sustained endothelial nitric-oxide synthase activation requires capacitative ca2+ entry. *Journal of Biological Chemistry 275*, 24 (6 2000/6/9), 17979–17985.

[80] Lodish, H., Kaiser, C. A., Berk, A., Krieger, M., Matsudaira, P., Scott, M. P, L. Z. S., and Darnell, J. *Molecular Cell Biology*, 5 ed. W. H. Freeman and Company, New York.

[81] Long, Q., Xu, Y., Ariff, B., Thom, S. A., Hughes, A. D., and Stanton, A. V. Reconstruction of blood flow patterns in a human carotid bifurcation: A combined cfd and mri study. *Journal of Magnetic Resonance Imaging 11*, 3 (2000), 299–311.

[82] Ludmer, P., Selwyn, A., Shook, T., Wayne, R., Mudge, G., Alexander, R., and Ganz, P. Paradoxical vasoconstriction induced by acetylcholine in atherosclerotic coronary arteries. *The New England Journal of Medicine 315*, 17 (10 1986), 1046–1051.

[83] Malek, A. M., Alper, S. L., and Izumo, S. Hemodynamic shear stress and its role in atherosclerosis. *JAMA: The Journal of the American Medical Association 282*, 21 (12 1999), 2035–2042.

[84] Malinski, T., Taha, Z., Grunfeld, S., Patton, S., Kapturczak, M., and Tomboulian, P. Diffusion of nitric oxide in the aorta wall monitored in situ by porphyrinic microsensors. *Biochemical and Biophysical Research Communications 193*, 3 (1993), 1076 – 1082.

[85] Marieb, E. N. *Human Anatomy & Physiology*, 4 ed. Scott Foresman - Addison Wesley, Menlo Park, California, United States, 1998.

[86] Marshall, I., Papathanasopoulou, P., and K., W. Carotid flow rates and flow division at the bifurcation in healthy volunteers. *Physiological Measurement 25*, 3 (2004), 691–697.

[87] Marshall, I., Zhao, S., Papathanasopoulou, P., Hoskins, P., and Xu, X. Y. MRI and CFD studies of pulsatile flow in healthy and stenosed carotid bifurcation models. *Journal of biomechanics 37*, 5 (05 2004), 679–687.

[88] Martinet, W., Croons, V., Timmermans, J.-P., Hermna, A. G., and De Meyer, G. R. Y. Nitric oxide selectively depletes macrophages in atherosclerotic plaques via induction of endoplasmic reticulum stress. *British Journal of Pharmacology 152*, 4 (2007), 493–500.

[89] Massberg, S., Brand, K., Grüner, S., Page, S., Müller, E., Müller, I., Bergmeier, W., Richter, T., Lorenz, M., Konrad, I., Nieswandt, B., and Gawaz, M. A critical role of platelet adhesion in the initiation of atherosclerotic lesion formation. *The Journal of Experimental Medicine 196*, 7 (2002), 887–896.

[90] Maxfield, F. R., and Wüstner, D. Intracellular cholesterol transport. *The Journal of Clinical Investigation 110*, 7 (2002), 891–898.

[91] Meyer, T., and Stryer, L. Molecular model for receptor-stimulated calcium spiking. *Proceedings of the National Academy of Sciences of the United States of America 85*, 14 (07 1988), 5051–5055.

[92] Michel, J. B., Feron, O., Sacks, D., and Michel, T. Reciprocal regulation of endothelial nitric-oxide synthase by ca2+-calmodulin and caveolin. *Journal of Biological Chemistry 272*, 25 (06 1997), 15583–15586.

[93] Milner, J. S., Moore, J. A., Rutt, B. K., and Steinman, D. A. Hemodynamics of human carotid artery bifurcations: Computational studies with models reconstructed from magnetic resonance imaging of normal subjects. *Journal of vascular surgery : official publication, the Society for Vascular Surgery [and] International Society for Cardiovascular Surgery, North American Chapter 28*, 1 (07 1998), 143–156.

[94] Milner, P., Kirkpatrick, K. A., Ralevic, V., Toothill, V., Pearson, J., and Burnstock, G. Endothelial Cells Cultured from Human Umbilical Vein Release ATP, Substance P and Acetylcholine in Response to Increased Flow. *Proceedings of the Royal Society of London. Series B: Biological Sciences 241*, 1302 (1990), 245–248.

[95] Mitchell, R. S., Kumar, V., Abbas, A. K., and Fausto, N. *Robbins Basic Pathology: With STUDENT CONSULT Online Access*, 8th ed. Saunders, Philadelphia, United States, 2007.

[96] Moncada, S., Herman, A. G., Higgs, E. A., and Vane, J. R. Differential formation of prostacyclin (PGX or PGI_2) by layers of the arterial wall. an explanation for the anti-thrombotic properties of vascular endothelium. *Thrombosis Research 11*, 3 (9 1977), 323–344.

[97] Moncada, S., Palmer, R., and Higgs, E. The discovery of nitric oxide as the endogenous nitrovasodilator. *Hypertension 12*, 4 (10 1988), 365–372.

[98] Mount, P. F., Kemp, B. E., and Power, D. A. Regulation of endothelial and myocardial no synthesis by multi-site enos phosphorylation. *Journal of Molecular and Cellular Cardiology 42*, 2 (2 2007), 271–279.

[99] Myers, J. G., Moore, J. A., Ojha, M., Johnston, K. W., and Ethier, C. R. Factors influencing blood flow patterns in the human right coronary artery. *Annals of Biomedical Engineering 29*, 2 (2001-02-01), 109–120.

[100] Nadaud, S., Philippe, M., Arnal, J. F., Michel, J. B., and Soubrier, F. Sustained increase in aortic endothelial nitric oxide synthase expression in vivo in a model of chronic high blood flow. *Circulation Research 79*, 4 (10 1996), 857–863.

[101] Oemar, B. S., Tschudi, M. R., Godoy, N., Brovkovich, V., Malinski, T., and Luscher, T. F. Reduced endothelial nitric oxide synthase expression and production in human atherosclerosis. *Circulation 97*, 25 (6 1998), 2494–2498.

[102] Okano, M., and Yoshida, Y. Junction complexes of endothelial cells in atherosclerosis-prone and atherosclerosis-resistant regions on flow dividers of brachiocephalic bifurcations in the rabbit aorta. *Biorheology 31*, 2 (1994), 155–161.

[103] Panza, J. A., and Cannon, R. O., Eds. *Endothelium, nitric oxide, and atherosclerosis*. Willey-Blackwell, 1999.

[104] Pearson, J. D., Carleton, J. S., Hutchings, A., and Gordon, J. L. Uptake and metabolism of adenosine by pig aortic endo- thelial and smooth muscle cells in culture. *Biochemical Journal 170*, 2 (1978), 265–271.

[105] Perktold, K., and Rappitsch, G. Computer simulation of local blood flow and vessel mechanics in a compliant carotid artery bifurcation model. *Journal of biomechanics 28*, 7 (07 1995), 845–856.

[106] Perktold, K., Resch, M., and Peter, R. O. Three-dimensional numerical analysis of pulsatile flow and wall shear stress in the carotid artery bifurcation. *Journal of Biomechanics 24*, 6 (1991), 409–420.

[107] Perktold, K., Thurner, E., and Kenner, T. Flow and stress characteristics in rigid walled and compliant carotid artery bifurcation models. *Medical and Biological Engineering and Computing 32*, 1 (01 1994), 19–26.

[108] Plank, M. J., Wall, D. J., and David, T. Atherosclerosis and calcium signalling in endothelial cells. *Prog Biophys Mol Biol 91*, 3 (2006), 287–313.

[109] Plata, A., Sherwin, S., and Krams, R. Endothelial nitric oxide production and transport in flow chambers: The importance of convection. *Annals of Biomedical Engineering*.

[110] Putney, James W., J., Broad, L. M., Braun, F.-J., Lievremont, J.-P., and Bird, G. S. J. Mechanisms of capacitative calcium entry. *Journal of Cell Science 114*, 12 (6 2001/6/15), 2223–2229.

[111] Qiu, Y., and Tarbell, J. M. Interaction between wall shear stress and circumferential strain affects endothelial cell biochemical production. *Journal of Vascular Research 37*, 3 (2000), 147–157.

[112] Rhie, C. M., and Chow, W. L. Numerical study of the turbulent flow past an airfoil with trailing edge separation. *AIAA Journal 21*, 11 (1983), 1525–1532.

[113] Ross, R. Cell biology of atherosclerosis. *Annual Review of Physiology 57*, 1 (10 1995), 791–804.

[114] Ross, R. Atherosclerosis – an inflammatory disease. *The New England Journal of Medicine 340*, 2 (1 1999), 115–126.

[115] Sarkar, R., Meinberg, E. G., Stanley, J. C., Gordon, D., and Clinton Webb, R. Nitric oxide reversibly inhibits the migration of cultured vascular smooth muscle cells. *Circulation Research 78*, 2 (2 1996), 225–230.

[116] Schlichting, H., and Gersten, K. *Boudary-Layer Theory*, 8 ed. Springer Berlin Heidelberg, 1999.

[117] Schwarz, G., Callewaert, G., Droogmans, G., and Nilius, B. Shear stress-induced calcium transients in endothelial cells from human umbilical cord veins. *The Journal of Physiology 458*, 1 (12 1992), 527–538.

[118] Shen, J., Luscinskas, F. W., Connolly, A., Dewey, C. F., J., and Gimbrone, M. A., J. Fluid shear stress modulates cytosolic free calcium in vascular endothelial cells. *AJP - Cell Physiology 262*, 2 (2 1992), C384–390.

[119] SIGMA-ALDRICH. Diversity of G, December 2010.

[120] Skalak, R., Tozeren, A., Zarda, R. P., and Chien, S. Strain energy function of red blood cell membranes. *Biophysical Journal 13*, 3 (3 1973), 245–264.

[121] Soslau, G., McKenzie, R. J., Brodsky, I., and Devlin, T. M. Extracellular atp inhibits agonist-induced mobilization of internal calcium in human platelets. *Biochimica et Biophysica Acta (BBA) - Molecular Cell Research 1268*, 1 (7 1995), 73–80.

[122] Steinman, D. A., Thomas, J. B., Ladak, H. M., Milner, J. S., Rutt, B. K., and Spence, J. D. Reconstruction of carotid bifurcation hemodynamics and wall thickness using computational fluid dynamics and mri. *Magnetic Resonance in Medicine 47*, 1 (01 2002), 149–59.

[123] Stroud, J. S., and Berger, S. A. Numerical analysis of flow through a severely stenotic carotid artery bifurcation. *J Biomech Eng 124*, 1 (2002), 9–20.

[124] Tada, S., Dong, C., and Tarbell, J. M. Effect of the stress phase angle on the strain energy density of the endothelial plasma membrane. *Biophys J 93*, 9 (11 2007), 3026–3033.

[125] Tada, S., and Tarbell, J. M. A computational study of flow in a compliant carotid bifurcation – stress phase angle correlation with shear stress. *Annals of Biomedical Engineering 33*, 9 (09 2005), 1202–1212.

[126] Tada, S., and Yamamoto, M. Private communicaiton, January 2010.

[127] Taubman, M. B., Fallon, J. T., Schecter, A. D., Giesen, P., Mendlowitz, M., Fyfe, B. S., Marmur, J. D., and Nemerson, Y. Tissue factor in the pathogenesis of atherosclerosis. *Thrombosis and Haemostasis 78*, 1 (1997), 200–204.

[128] Thom, T., Haase, N., Rosamond, W., Howard, V. J., Rumsfeld, J., Manolio, T., Zheng, Z.-J., Flegal, K., O'Donnell, C., Kittner, S., Lloyd-Jones, D., Goff, David C., J., Hong, Y., of the Statistics Committee, M., Subcommittee, S. S., Adams, R., Friday, G., Furie, K., Gorelick, P., Kissela, B., Marler, J., Meigs, J., Roger, V., Sidney, S., Sorlie, P., Steinberger, J., Wasserthiel-Smoller, S., Wilson, M., and Wolf, P. Heart disease and stroke statistics–2006 update: A report from the american heart association statistics committee and stroke statistics subcommittee. *Circulation 113*, 6 (2 2006), e85–151.

[129] Thomas, J. B., Milner, J. S., and Steinman, D. A. On the influence of vessel planarity on local hemodynamics at the human carotid bifurcation. *Biorheology 39*, 3 (01 2002), 443–448.

[130] Tu, J., Yeoh, G. H., and Liu, C. *Computational Fluid Dynamics: A Practical Approach*. Butterworth-Heinemann, Burlington, MA, USA, 2008.

[131] Valant, P., Adjei, P., and Haynes, D. Rapid Ca^{2+} extrusion via the Na^{+}/Ca^{2+} exchanger of the human platelet. *Journal of Membrane Biology 130*, 1 (1992-10-17), 63–82.

[132] Vaughn, M. W., Kuo, L., and Liao, J. C. Estimation of nitric oxide production and reaction rates in tissue by use of a mathematical model. *AJP - Heart and Circulatory Physiology 274*, 6 (6 1998/6/1), H2163–2176.

[133] Walpola, P., Gotlieb, A., and Langille, B. Monocyte adhesion and changes in endothelial cell number, morphology, and f-actin distribution

elicited by low shear stress in vivo. *American Journal of Pathology 142*, 5 (5 1993), 1392–1400.

[134] Walpola, P. L., Gotlieb, A. I., Cybulsky, M. I., and Langille, B. L. Expression of icam-1 and vcam-1 and monocyte adherence in arteries exposed to altered shear stress. *Arteriosclerosis, Thrombosis, and Vascular Biology 15*, 1 (1 1995), 2–10.

[135] Wan, J., Ristenpart, W. D., and Stone, H. A. Dynamics of shear-induced atp release from red blood cells. *Proceedings of the National Academy of Sciences 105*, 43 (10 2008), 16432–16437.

[136] Wiesner, T. F., Berk, B. C., and Nerem, R. M. A mathematical model of cytosolic calcium dynamics in human umbilical vein endothelial cells. *AJP - Cell Physiology 270*, 5 (5 1996), C1556–1569.

[137] Wiesner, T. F., Berk, B. C., and Nerem, R. M. A mathematical model of the cytosolic-free calcium response in endothelial cells to fluid shear stress. *Proceedings of the National Academy of Sciences of the United States of America 94*, 8 (04 1997), 3726–3731.

[138] Wood, J., and Garthwaite, J. Models of the diffusional spread of nitric oxide: Implications for neural nitric oxide signalling and its pharmacological properties. *Neuropharmacology 33*, 11 (11 1994), 1235–1244.

[139] Yamamoto, K., Shimizu, N., Obi, S., Kumagaya, S., Taketani, Y., Kamiya, A., and Ando, J. Involvement of cell surface atp synthase in flow-induced atp release by vascular endothelial cells. *American Journal of Physiology - Heart and Circulatory Physiology 293*, 3 (09 2007), H1646–H1653.

[140] Yamamoto, K., Sokabe, T., Ohura, N., Nakatsuka, H., Kamiya, A., and Ando, J. Endogenously released ATP mediates shear stress-induced Ca2+ influx into pulmonary artery endothelial cells. *American Journal of Physiology - Heart and Circulatory Physiology 285*, 2 (07 2003), H793–H803.

[141] Younis, H. F., Kaazempur-Mofrad, M. R., Chan, R. C., Isasi, A. G., Hinton, D. P., Chau, A. H., Kim, L. A., and Kamm, R. D. Hemodynamics and wall mechanics in human carotid bifurcation and its

consequences for atherogenesis: investigation of inter-individual variation. *Biomechanics and Modeling in Mechanobiology 3*, 1 (2004-09-01), 17–32.

[142] Zarins, C., Giddens, D., Bharadvaj, B., Sottiurai, V., Mabon, R., and Glagov, S. Carotid bifurcation atherosclerosis. quantitative correlation of plaque localization with flow velocity profiles and wall shear stress. *Circulation Research 53*, 4 (1983), 502–514.

[143] Zhao, S. Z., Ariff, B., Long, Q., Hughes, A. D., Thom, S. A., Stanton, A. V., and Xu, X. Y. Inter-individual variations in wall shear stress and mechanical stress distributions at the carotid artery bifurcation of healthy humans. *Journal of biomechanics 35*, 10 (10 2002), 1367–1377.

[144] Zhao, S. Z., Papathanasopoulou, P., Long, Q., Marshall, I., and Xu, X. Y. Comparative study of magnetic resonance imaging and image-based computational fluid dynamics for quantification of pulsatile flow in a carotid bifurcation phantom. *Annals of Biomedical Engineering 31*, 8 (2003-09-01), 962–971.

[145] Zhao, S. Z., Xu, X. Y., Hughes, A. D., Thom, S. A., Stanton, A. V., Ariff, B., and Long, Q. Blood flow and vessel mechanics in a physiologically realistic model of a human carotid arterial bifurcation. *Journal of biomechanics 33*, 8 (08 2000), 975–984.

[146] Ziegler, T., Bouzourene, K., Harrison, V. J., Brunner, H. R., and Hayoz, D. Influence of oscillatory and unidirectional flow environments on the expression of endothelin and nitric oxide synthase in cultured endothelial cells. *Arteriosclerosis, Thrombosis, and Vascular Biology 18*, 5 (5 1998), 686–692.

Appendix A

Equations of fluid dynamics

The derivation of the equations of fluid dynamics are demonstrated in this section. First, the Reynolds transport theorem is derived as this described the transport of general scalar quantities which will be the basis of the fundamental equations in fluid dynamics, i.e. continuity and momentum equations. In order to obtain the complete expression of the latter equation, also known as the equation of motion of a control volume, the external forces acting on the control volume are analysed and formulated. The final equation is presented in the integral form, which is a suitable form in the computational fluid dynamics (CFD) approach primarily used in this thesis. The brief description of the boundary-layer equations derived from the momentum equation is then outlined. The derivations presented here are based on those by Fox and McDonald (44) and Schlichting and Gersten (116).

A.1 Reynolds transport theorem

A system, by definition, is a collection of fluid matter of fixed identity, and thus Lagrangian in nature. Because of this, system analysis can be applied directly to fluid flow, given that the basic laws of conservation of mass, momentum and energy are Lagrangian. However, because of the complex nature of flows often observed in engineering applications, it is difficult and not practical to identify and track each fluid particle, and therefore it is more convenient to analyse the flow through a fixed volume in space (control volume, CV) within the flow domain (Eulerian approach). For this, the system equations must be transformed to be related to the CV equations. This transformation is achieved by the Reynolds

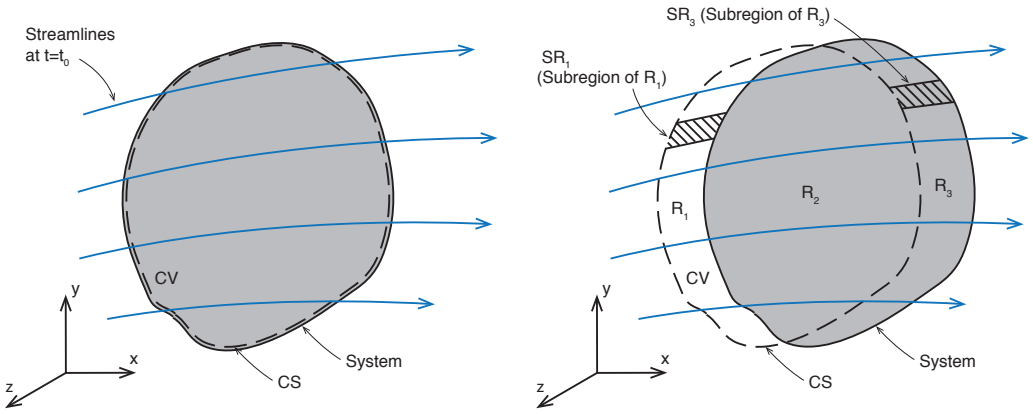

Figure A.1: System and control volume (CV) configuration, (a) at time t_0 and (b) at time $t_0 + \Delta t$.

transport theorem.

When N is any extensive property of a system (i.e. a physical quantity of a system that is directly proportional to the system size) and η its corresponding intensive property (i.e. extensive property N per unit mass), i.e.:

$$N_{system} = \int_{mass(system)} \eta dm = \int_{V(system)} \eta \rho dV \tag{A.1}$$

then the Reynolds transport theorem states that the rate of change of any arbitrary extensive property N for the system is equal to the sum of the time rate of change of N within the control volume and the net rate of flux of N through the control surface (CS). The latter is in turn associated with the mass flux and the properties convected with it through the CS.

By definition, the rate of change of N_{system} is expressed as:

$$\left.\frac{dN}{dt}\right|_{system} \equiv \lim_{x \to 0} \frac{N_{system}\big|_{t_0+\Delta t} - N_{system}\big|_{t_0}}{\Delta t} \tag{A.2}$$

At time t_0, the system and the CV coincide, so:

$$N_{system}\big|_{t_0} = N_{CV}\big|_{t_0} \tag{A.3}$$

whereas at $t_0 + \Delta t$, the system occupies the regions R_2 and R_3, thus:

$$N_{system}\big|_{t_0+\Delta t} = (N_{R_2} + N_{R_3})_{t_0+\Delta t} = (N_{CV} + N_{R_3} - N_{R_1})_{t_0+\Delta t} \tag{A.4}$$

Using Eqn. A.1 in Eqns. A.3 and A.4 gives:

$$N_{system}\big|_{t_0} = N_{CV}\big|_{t_0} = \int_{CV} \eta\rho dV\Big|_{t_0} \tag{A.5}$$

and

$$N_{system}\big|_{t_0+\Delta t} = \int_{CV} \eta\rho dV\Big|_{t_0+\Delta t} + \int_{R_3} \eta\rho dV\Big|_{t_0+\Delta t} - \int_{R_1} \eta\rho dV\Big|_{t_0+\Delta t} \tag{A.6}$$

Substituting the above into the system derivative definition (Eqn. A.2) and collecting terms using that the limits of a sum of functions is equal to the sum of the limits:

$$\frac{dN}{dt}\bigg|_{system} = \lim_{\Delta t\to 0} \frac{\int_{CV} \eta\rho dV\Big|_{t_0+\Delta t} + \int_{R_3} \eta\rho dV\Big|_{t_0+\Delta t} - \int_{R_1} \eta\rho dV\Big|_{t_0+\Delta t} - \int_{CV} \eta\rho dV\Big|_{t_0}}{\Delta t}$$

$$= \underbrace{\lim_{\Delta t\to 0} \frac{\int_{CV} \eta\rho dV\Big|_{t_0+\Delta t} - \int_{CV} \eta\rho dV\Big|_{t_0}}{\Delta t}}_{\text{(i)}} + \underbrace{\lim_{\Delta t\to 0} \frac{\int_{R_3} \eta\rho dV\Big|_{t_0+\Delta t}}{\Delta t}}_{\text{(ii)}}$$

$$\underbrace{- \lim_{\Delta t\to 0} \frac{\int_{R_1} \eta\rho dV\Big|_{t_0+\Delta t}}{\Delta t}}_{\text{(iii)}} \tag{A.7}$$

The terms (i), (ii) and (iii) simplify respectively to:

$$(i) : \lim_{\Delta t\to 0} \frac{\int_{CV} \eta\rho dV\Big|_{t_0+\Delta t} - \int_{CV} \eta\rho dV\Big|_{t_0}}{\Delta t} = \lim_{\Delta t\to 0} \frac{N_{CV}\big|_{t_0+\Delta t}}{\Delta t}$$

$$= \frac{\partial N_{CV}}{\partial t} = \frac{\partial}{\partial t}\int_{CV} \eta\rho dV \tag{A.8}$$

$$(ii) : \lim_{\Delta t\to 0} \frac{\int_{R_3} \eta\rho dV\Big|_{t_0+\Delta t}}{\Delta t} = \lim_{\Delta t\to 0} \frac{N_{R_3}\big|_{t_0+\Delta t}}{\Delta t} \tag{A.9}$$

$$(iii) : -\lim_{\Delta t \to 0} \frac{\int_{R_1} \eta \rho dV \Big|_{t_0+\Delta t}}{\Delta t} = -\lim_{\Delta t \to 0} \frac{N_{R_1}\big|_{t_0+\Delta t}}{\Delta t} \tag{A.10}$$

In order to evaluate the expressions A.9 and A.10, the expressions $N_{R_3}\big|_{t_0+\Delta t}$ and $N_{R_1}\big|_{t_0+\Delta t}$, which are the extensive property N that goes out of and comes into the CV respectively during the time interval Δt, must first be known.

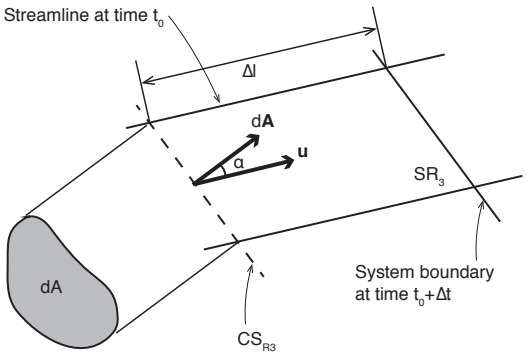

Figure A.2: A typical subregion SR_3 within the region R_3. The area vector $d\mathbf{A}$ located on the CS_{R3} has the magnitude dA and direction normal outwards from the CS_{R3}, forming an angle α with the streamline (i.e. the velocity vector $\mathbf{u}$). Since the mass within SR_3 is flowing out of the CV, α is always less than $\pi/2$. Δl is the distance travelled during the time period Δt.

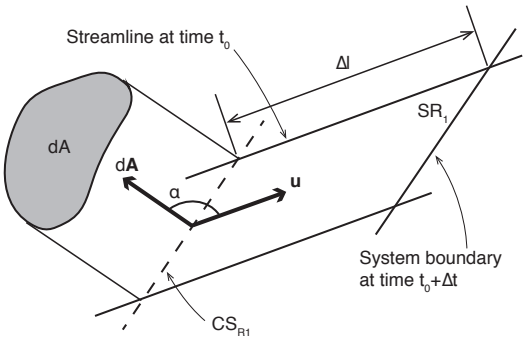

Figure A.3: A typical subregion SR_1 within the region R_1. The mass within SR_1 is flowing into the CV, and so α is always greater than $\pi/2$.

Figure A.2 shows a typical subregion of the region R_3 (SR_3). Using that $dV = \Delta l \; cos\alpha \; dA$,

$$dN_{R_3}\big|_{t_0+\Delta t} = (\eta\rho \, dV)_{t_0+\Delta t} = [\eta\rho \, (\Delta l \; cos\alpha \; dA)]_{t_0+\Delta t} \tag{A.11}$$

which is integrated over the surface shared by the CV and R_3 (CS_{R3}) to give N_{R_3} at time $t_0 + \Delta t$, i.e.:

$$N_{R_3}\Big|_{t_0+\Delta t} = \int_{CS_{R3}} \eta\rho\Delta l \; cos\alpha \; dA\Big|_{t_0+\Delta t} \tag{A.12}$$

Substituting the above into the expression A.9 for term (ii) gives:

$$(ii) : \lim_{\Delta t\to 0} \frac{\int_{R_3} \eta\rho dV\Big|_{t_0+\Delta t}}{\Delta t} = \lim_{\Delta t\to 0} \frac{N_{R_3}\Big|_{t_0+\Delta t}}{\Delta t} = \lim_{\Delta t\to 0} \frac{\int_{CS_{R3}} \eta\rho \; \Delta l \; cos\alpha \; dA}{\Delta t}$$

$$= \lim_{\Delta t\to 0} \int_{CS_{R3}} \eta\rho \; \frac{\Delta l}{\Delta t} \; cos\alpha \; dA$$

$$= \int_{CS_{R3}} \eta\rho \; |\mathbf{u}| \; cos\alpha \; |d\mathbf{A}| \tag{A.13}$$

Using a similar approach, the extensive property N that comes into the CV during the time interval Δt (Fig. A.3), $N_{R_1}\big|_{t_0+\Delta t}$ is obtained as:

$$N_{R_1}\Big|_{t_0+\Delta t} = \int_{CS_{R1}} -\eta\rho \; \Delta l \; cos\alpha \; dA\Big|_{t_0+\Delta t} \tag{A.14}$$

And therefore the expression for term (iii) (A.10) is written as:

$$(iii) : -\lim_{\Delta t\to 0} \frac{\int_{R_1} \eta\rho dV\Big|_{t_0+\Delta t}}{\Delta t} = -\lim_{\Delta t\to 0} \frac{N_{R_1}\Big|_{t_0+\Delta t}}{\Delta t} = -\lim_{\Delta t\to 0} \frac{\int_{CS_{R1}} -\eta\rho \; \Delta l \; cos\alpha \; dA}{\Delta t}$$

$$= \lim_{\Delta t\to 0} \int_{CS_{R1}} \eta\rho \; \frac{\Delta l}{\Delta t} \; cos\alpha \; dA$$

$$= \int_{CS_{R1}} \eta\rho \; |\mathbf{u}| \; cos\alpha \; |d\mathbf{A}| \tag{A.15}$$

Using the expressions formulated above for terms (i), (ii) and (iii), the system

derivative equation (Eqn. A.7) now becomes:

$$\left.\frac{dN}{dt}\right|_{system} = \frac{\partial}{\partial t}\int_{CV} \eta\rho \, dV + \int_{CS_{R3}} \eta\rho \, |\mathbf{u}| \, cos\alpha \, |d\mathbf{A}|$$

$$+ \int_{CS_{R1}} \eta\rho \, |\mathbf{u}| \, cos\alpha \, |d\mathbf{A}| \tag{A.16}$$

Since $CS = CS_{R3} + CS_{R1}$,

$$\left.\frac{dN}{dt}\right|_{system} = \frac{\partial}{\partial t}\int_{CV} \eta\rho \, dV + \int_{CS} \eta\rho \, |\mathbf{u}| \, cos\alpha \, |d\mathbf{A}|$$

$$= \frac{\partial}{\partial t}\int_{CV} \eta\rho \, dV + \int_{CS} \eta\rho \, \mathbf{u} \cdot d\mathbf{A} \tag{A.17}$$

which relates the time derivative of N for a system to the time rate of change of N associated with the control volume. This can be typically applied to the cases where N is mass, momentum, angular momentum, energy and entropy in order to transform the system formulation of continuity, Newton's second law, angular momentum principle and the first and second laws of thermodynamics, respectively. In the next section, the derivations of the former two that are most relevant in this thesis are presented.

A.2 Continuity

For the control volume formulation of mass conservation, the corresponding extensive property is the system mass M and its intensive property η unity. Substituting $N = M$ and $\eta = 1$ into Eqn. A.17 leads to:

$$\left.\frac{dM}{dt}\right|_{system} = \frac{\partial}{\partial t}\int_{CV} \rho \, dV + \int_{CS} \rho \, \mathbf{u} \cdot d\mathbf{A} \tag{A.18}$$

The system law requires that the system mass remains constant, i.e.:

$$\left.\frac{dM}{dt}\right|_{system} = 0 \tag{A.19}$$

and therefore:

$$0 = \frac{\partial}{\partial t} \int_{CV} \rho \, dV + \int_{CS} \rho \, \mathbf{u} \cdot d\mathbf{A} \tag{A.20}$$

For incompressible flow (as assumed for blood - see 3.2.1 for details):

$$0 = \rho \frac{\partial}{\partial t} \int_{CV} dV + \rho \int_{CS} \mathbf{u} \cdot d\mathbf{A}$$

$$\Rightarrow \qquad 0 = \frac{\partial}{\partial t} \int_{CV} dV + \int_{CS} \mathbf{u} \cdot d\mathbf{A} \tag{A.21}$$

The first term on the RHS (the integral of dV over the CV) is the volume of the CV itself, so:

$$0 = \frac{\partial V}{\partial t} + \int_{CS} \mathbf{u} \cdot d\mathbf{A} \tag{A.22}$$

and therefore for a non-deformable CV:

$$0 = \int_{CS} \mathbf{u} \cdot d\mathbf{A} \tag{A.23}$$

The divergence theorem relates the surface integral of a flux of a vector field through a closed surface to the volume integral of the divergence of the region within the surface, i.e.:

$$\int_{CS} \mathbf{F} \cdot \mathbf{n} \, dA = \int_{CV} (\nabla \cdot \mathbf{F}) \; dV \tag{A.24}$$

Applying this to Eqn. A.23 leads to:

$$0 = \int_{CV} (\nabla \cdot \mathbf{u}) \; dV \tag{A.25}$$

Incompressible flows are source-free (divergence-free), therefore:

$$\nabla \cdot \mathbf{u} = 0 \tag{A.26}$$

A.3 Momentum equation

The Newton's second law states that, in an inertial reference frame, the net force ($\mathbf{F}$) on a mass is equal to the time rate of change of its linear momentum ($\mathbf{P}$), i.e. for a system,

$$\sum F_{system} = \left.\frac{d\mathbf{P}}{dt}\right|_{system} \tag{A.27}$$

where the linear momentum of the system is:

$$\mathbf{P} = \int_{mass(system)} \mathbf{u}\, dm = \int_{V(system)} \mathbf{u}\, \rho\, dV \tag{A.28}$$

Setting $N = \mathbf{P}$ and $\eta = \mathbf{u}$ in Eqn. A.17 relates the system derivative to the time change of $\mathbf{P}$ within CV and the net flux through CS, i.e.:

$$\left.\frac{d\mathbf{P}}{dt}\right|_{system} = \frac{\partial}{\partial t}\int_{CV} \rho\mathbf{u}\, dV + \int_{CS} \rho\mathbf{u}\mathbf{u}\cdot d\mathbf{A} \tag{A.29}$$

At time t_0, the system and CV coincide, thus $\sum F_{system} = \sum F_{CV}$. Combining Eqns. A.27 and A.29 based on this leads to the control volume formulation of the conservation of linear momentum for an inertial control volume in integral form:

$$\sum F_{CV} = \frac{\partial}{\partial t}\int_{CV} \rho\mathbf{u}\, dV + \int_{CS} \rho\mathbf{u}\mathbf{u}\cdot d\mathbf{A} = \rho\frac{D\mathbf{u}}{Dt} \tag{A.30}$$

where $\mathbf{F}_{CV}$ consists of body forces acting on the element of CV ($\mathbf{F_B}$) and surface traction forces ($\mathbf{F_S}$) acting on CS. The equation above can therefore be written as:

$$\sum F_{CV} = \mathbf{F_B} + \mathbf{F_S} = \frac{\partial}{\partial t}\int_{CV} \rho\mathbf{u}\, dV + \int_{CS} \rho\mathbf{u}\mathbf{u}\cdot d\mathbf{A} = \rho\frac{D\mathbf{u}}{Dt} \tag{A.31}$$

Body forces are those that act throughout the medium within the CV, and normally are treated as prescribed. Examples include gravitational and electromagnetic forces. When $\mathbf{f_B}$ is the body force per unit volume, the body force acting on the whole control volume can be written as:

$$\mathbf{F_B} = \int_{CV} \rho\mathbf{f_B}\, dV \tag{A.32}$$

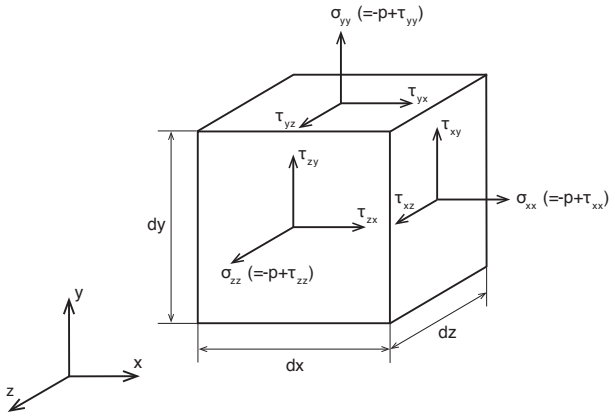

Figure A.4: Stress components on a control volume element.

Surface forces, on the other hand, are those that act directly on the boundary surfaces of a medium. When a volume element $dV = dxdydz$ is considered, then the surface forces acting on the two planes perpendicular to the x, y and z axes are respectively:

$$\begin{aligned}
&\mathbf{f_{Sx}} \quad \text{and} \quad \mathbf{f_{Sx}} + \frac{\partial \mathbf{f_{Sx}}}{\partial x} dx \quad \text{in the } x \text{ direction (surface area } dydz) \\
&\mathbf{f_{Sy}} \quad \text{and} \quad \mathbf{f_{Sy}} + \frac{\partial \mathbf{f_{Sy}}}{\partial y} dy \quad \text{in the } y \text{ direction (surface area } dxdz) \\
&\mathbf{f_{Sz}} \quad \text{and} \quad \mathbf{f_{Sz}} + \frac{\partial \mathbf{f_{Sz}}}{\partial z} dz \quad \text{in the } z \text{ direction (surface area } dxdy)
\end{aligned} \tag{A.33}$$

The total surface force F_S per unit volume is therefore:

$$\mathbf{F_S} = \frac{\partial \mathbf{f_{sx}}}{\partial x} + \frac{\partial \mathbf{f_{sy}}}{\partial y} + \frac{\partial \mathbf{f_{sz}}}{\partial z} \tag{A.34}$$

These surface forces can be decomposed into two components, the normal (σ) and tangential (τ) stresses. Both stresses are expressed using a set of two indices, the first of which denotes the axis to which the surface the force is acting on is perpendicular to, and the second the direction in which the stress is acting, as shown in Fig. A.4.

If $\mathbf{i}$, $\mathbf{j}$, $\mathbf{k}$ are the unit vectos in x, y, z directions respectively, then the surface forces in each direction can be written as:

$$\mathbf{f_{Sx}} = \sigma_{xx}\mathbf{i} + \tau_{xy}\mathbf{j} + \tau_{xz}\mathbf{k}$$

$$\mathbf{f_{Sy}} = \tau_{yx}\mathbf{i} + \sigma_{yy}\mathbf{j} + \tau_{yz}\mathbf{k} \tag{A.35}$$

$$\mathbf{f_{Sz}} = \tau_{zx}\mathbf{i} + \tau_{zy}\mathbf{j} + \sigma_{zz}\mathbf{k}$$

The *stress tensor* $\dot{\sigma}$, which defines the stress state of surface traction forces on a control volume, can be derived from these nine scalar quantities:

$$\dot{\sigma} = \begin{pmatrix} \sigma_{xx} & \tau_{xy} & \tau_{xz} \\ \tau_{yx} & \sigma_{yy} & \tau_{yz} \\ \tau_{zx} & \tau_{zy} & \sigma_{zz} \end{pmatrix} \tag{A.36}$$

Using A.34 and A.35, and given that the stress tensor A.36 is diagonally symmetric (i.e. $\tau_{xy} = \tau_{yx}$, $\tau_{xz} = \tau_{zx}$, $\tau_{yz} = \tau_{zy}$), the surface force per unit volume $\mathbf{F_S}$ is then:

$$\mathbf{F_S} = \left(\frac{\partial \sigma_{xx}}{\partial x} + \frac{\partial \tau_{xy}}{\partial y} + \frac{\partial \tau_{xz}}{\partial z}\right)\mathbf{i}$$

$$+ \left(\frac{\partial \tau_{xy}}{\partial x} + \frac{\partial \sigma_{yy}}{\partial y} + \frac{\partial \tau_{yz}}{\partial z}\right)\mathbf{j} + \left(\frac{\partial \tau_{xz}}{\partial x} + \frac{\partial \tau_{yz}}{\partial y} + \frac{\partial \sigma_{zz}}{\partial z}\right)\mathbf{k} \tag{A.37}$$

Substituting the stress terms in each direction of the Cartesian axes into the equation of motion ($\rho D\mathbf{u}/Dt = \mathbf{f_B} + \mathbf{f_S}$, Eqn. A.31) gives:

$$\rho\frac{Du}{Dt} = f_{Bx} + \left(\frac{\partial \sigma_{xx}}{\partial x} + \frac{\partial \tau_{xy}}{\partial y} + \frac{\tau_{xz}}{\partial z}\right)$$

$$\rho\frac{Dv}{Dt} = f_{By} + \left(\frac{\partial \tau_{xy}}{\partial x} + \frac{\partial \sigma_{yy}}{\partial y} + \frac{\partial \tau_{yz}}{\partial z}\right) \tag{A.38}$$

$$\rho\frac{Dw}{Dt} = f_{Bz} + \left(\frac{\partial \tau_{xz}}{\partial x} + \frac{\partial \tau_{yz}}{\partial y} + \frac{\partial \sigma_{zz}}{\partial z}\right)$$

Pressure is isotropic, and thus it is convenient to separate the pressure (p) from the normal stresses to define anisotropic normal stress components (τ_{xx}, τ_{yy}, τ_{zz}), i.e.:

$$\sigma_{xx} = -p + \tau_{xx}, \quad \sigma_{yy} = -p + \tau_{yy}, \quad \sigma_{zz} = -p + \tau_{zz} \tag{A.39}$$

The equations of motion (Eqn. A.38) then become what are knows as the Cauchy's momentum equations:

$$\begin{aligned}
\rho\frac{Du}{Dt} &= f_{Bx} - \frac{\partial p}{\partial x} + \left(\frac{\partial \tau_{xx}}{\partial x} + \frac{\partial \tau_{xy}}{\partial y} + \frac{\tau_{xz}}{\partial z}\right) \\
\rho\frac{Dv}{Dt} &= f_{By} - \frac{\partial p}{\partial y} + \left(\frac{\partial \tau_{xy}}{\partial x} + \frac{\partial \tau_{yy}}{\partial y} + \frac{\partial \tau_{yz}}{\partial z}\right) \\
\rho\frac{Dw}{Dt} &= f_{Bz} - \frac{\partial p}{\partial z} + \left(\frac{\partial \tau_{xz}}{\partial x} + \frac{\partial \tau_{yz}}{\partial y} + \frac{\partial \tau_{zz}}{\partial z}\right)
\end{aligned} \tag{A.40}$$

or in the vector form:

$$\rho\frac{D\mathbf{u}}{Dt} = \mathbf{f_B} - \nabla p + \nabla \cdot \tau \tag{A.41}$$

Note that the negative sign of the pressure terms follows the convention which defines a force or stress as positive when it is exerted by the fluid in the direction of a normal outward vector.

The separation of stresses above allows the stress tensor to be further decomposed into the isotropic and anisotropic components:

$$\dot{\sigma} = \begin{pmatrix} \sigma_{xx} & \tau_{xy} & \tau_{xz} \\ \tau_{yx} & \sigma_{yy} & \tau_{yz} \\ \tau_{zx} & \tau_{zy} & \sigma_{zz} \end{pmatrix} = \begin{pmatrix} -p & 0 & 0 \\ 0 & -p & 0 \\ 0 & 0 & -p \end{pmatrix} + \begin{pmatrix} \tau_{xx} & \tau_{xy} & \tau_{xz} \\ \tau_{yx} & \tau_{yy} & \tau_{yz} \\ \tau_{zx} & \tau_{zy} & \tau_{zz} \end{pmatrix} \tag{A.42}$$

or in tensor form:

$$\dot{\sigma} = -p\dot{I} + \dot{\tau} \tag{A.43}$$

where $\dot{\tau}$ is the *viscous stress tensor*:

$$\dot{\tau} = \begin{pmatrix} \tau_{xx} & \tau_{xy} & \tau_{xz} \\ \tau_{yx} & \tau_{yy} & \tau_{yz} \\ \tau_{zx} & \tau_{zy} & \tau_{zz} \end{pmatrix} = \tau_{ij} \tag{A.44}$$

which is also diagonally symmetrical and characterises only the anisotropic normal stresses on a control volume. Using this expression, the equation of motion of a control volume can now be written as:

$$\rho\frac{D\mathbf{u}}{Dt} = \int_{CV} \mathbf{f_B} dV - \int_{CS} \nabla p\dot{I} \cdot dA + \int_{CS} \nabla \cdot \dot{\tau} \cdot dA \tag{A.45}$$

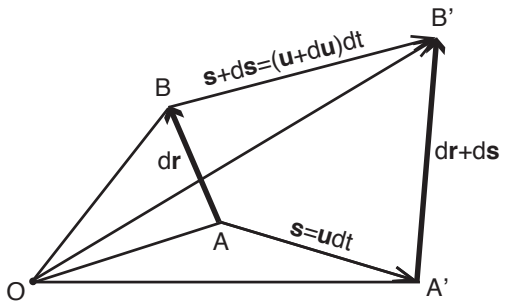

Figure A.5: Displacement of two points in the velocity field during time dt, from A and B to A' and B'.

In order to obtain the complete expression of the equation of motion above, the viscous stress terms need to be expressed using the velocity components u, v, w and their derivatives. This is achieved by relating the six components in the viscous stress tensor to the rate of deformation of the volume element.

A.3.1 State of deformation

Fluid particles experience continuous deformation in flow. Since the motion of the fluid flow can be described completely if the velocity vector is known as a function of space and time, it can be said that a relationship exists between the state of deformation and the velocity vector.

Consider the neighbouring points A and B, which moved to new positions A' and B' after some time dt (Fig. A.5):

Initially, the particle B is a distance $d\mathbf{r}$ away from A. After some time dt, A moves to A', of which location is known from a position vector $d\mathbf{s}$ as a function of the initial velocity vector $\mathbf{u}$, whereas B moves to B', $\mathbf{s} + d\mathbf{s} = (\mathbf{u} + d\mathbf{u})\, dt$ away. When the spatial velocity vector components at A are u, v, w, then those at B' can be found via Taylor series expansion, i.e.:

$$
\begin{aligned}
u + du &= u + \frac{\partial u}{\partial x}dx + \frac{\partial u}{\partial y}dy + \frac{\partial u}{\partial z}dz \\
v + dv &= v + \frac{\partial v}{\partial x}dx + \frac{\partial v}{\partial y}dy + \frac{\partial v}{\partial z}dz \\
w + dw &= w + \frac{\partial w}{\partial x}dx + \frac{\partial w}{\partial y}dy + \frac{\partial w}{\partial z}dz
\end{aligned}
\tag{A.46}
$$

neglecting the higher-order terms. The matrix of partial derivatives of local velocities, which describes the relative displacement of the particle at B to that at A:

$$\begin{pmatrix} \dfrac{\partial u}{\partial x} & \dfrac{\partial u}{\partial y} & \dfrac{\partial u}{\partial z} \\ \dfrac{\partial v}{\partial x} & \dfrac{\partial v}{\partial y} & \dfrac{\partial v}{\partial z} \\ \dfrac{\partial w}{\partial x} & \dfrac{\partial w}{\partial y} & \dfrac{\partial w}{\partial z} \end{pmatrix} \tag{A.47}$$

Arranging the components of relative velocity du, dv, dw as follows:

$$\begin{aligned} du &= (\dot{\varepsilon}_{xx}dx + \dot{\varepsilon}_{xy}dy + \dot{\varepsilon}_{xz}dz) + (\omega_y dz - \omega_z dy) \\ dv &= (\dot{\varepsilon}_{xy}dx + \dot{\varepsilon}_{yy}dy + \dot{\varepsilon}_{yz}dz) + (\omega_z dx - \omega_x dz) \\ du &= (\dot{\varepsilon}_{zx}dx + \dot{\varepsilon}_{zy}dy + \dot{\varepsilon}_{zz}dz) + (\omega_x dy - \omega_y dx) \end{aligned} \tag{A.48}$$

so that:

$$\begin{aligned} \dot{\varepsilon} &= \begin{pmatrix} \dot{\varepsilon_{xx}} & \dot{\varepsilon_{xy}} & \dot{\varepsilon_{xz}} \\ \dot{\varepsilon_{yx}} & \dot{\varepsilon_{yy}} & \dot{\varepsilon_{yz}} \\ \dot{\varepsilon_{zx}} & \dot{\varepsilon_{zy}} & \dot{\varepsilon_{zz}} \end{pmatrix} \\ &= \begin{pmatrix} \dfrac{\partial u}{\partial x} & \dfrac{1}{2}\left(\dfrac{\partial v}{\partial x} + \dfrac{\partial u}{\partial y}\right) & \dfrac{1}{2}\left(\dfrac{\partial w}{\partial x} + \dfrac{\partial u}{\partial z}\right) \\ \dfrac{1}{2}\left(\dfrac{\partial u}{\partial y} + \dfrac{\partial v}{\partial x}\right) & \dfrac{\partial v}{\partial y} & \dfrac{1}{2}\left(\dfrac{\partial w}{\partial y} + \dfrac{\partial v}{\partial z}\right) \\ \dfrac{1}{2}\left(\dfrac{\partial u}{\partial z} + \dfrac{\partial w}{\partial x}\right) & \dfrac{1}{2}\left(\dfrac{\partial v}{\partial z} + \dfrac{\partial w}{\partial y}\right) & \dfrac{\partial w}{\partial z} \end{pmatrix} \end{aligned} \tag{A.49}$$

which is diagonally symmetric, i.e. $\dot{\varepsilon_{xy}}=\dot{\varepsilon_{yx}}$, $\dot{\varepsilon_{xz}}=\dot{\varepsilon_{zx}}$, $\dot{\varepsilon_{yz}}=\dot{\varepsilon_{zy}}$. Also:

$$\omega_x = \frac{1}{2}\left(\frac{\partial w}{\partial y} - \frac{\partial v}{\partial z}\right), \quad \omega_y = \frac{1}{2}\left(\frac{\partial u}{\partial z} - \frac{\partial w}{\partial x}\right), \quad \omega_z = \frac{1}{2}\left(\frac{\partial v}{\partial x} - \frac{\partial u}{\partial y}\right) \tag{A.50}$$

which are the components of the angular velocity vector $\boldsymbol{\omega}$, which is in turn related to the vorticity vector as:

$$\boldsymbol{\omega} = \frac{1}{2}\nabla \times \mathbf{u} \tag{A.51}$$

The expression (Eqn. A.49) is called the *rate of deformation tensor* or *strain-rate tensor*. The components in the tensor $\dot{\varepsilon}$ are expressed with the spatial derivatives of the velocity vectors u, v w. As stated above, these now have to be related to the components of the stress tensor to complete the equations of motion for a control volume. This is done by considering physical interpretation of each quantity in expressions A.49 and A.50.

Fluid motions can be decomposed into the following four components: translation, rigid-body rotation, volume dilation and shear deformation, each of which will be looked at individually. For simplicity, these four motions are depicted in 2D in Fig. A.6. Also, for convenience, the coordinates of points A in Fig. A.6 are assumed to be set at the origin in the Cartesian coordinates, so that the coordinates of C can be set as (dx,dy,dz). This allows du, dv, dw in expression A.50 to be considered as the components of the relative velocity, which are linear functions of spatial coordinates.

Translation

Translation of a fluid volume (Fig. A.6(a)) is a rigid motion where the coordinates of the points A, B, C, D are moved by a constant distance in the flow field. Although the position of the fluid element changes, there is no relative displacement of the points B, C, D with respect to A and therefore the orientation is preserved and there is no deformation.

Rigid-body rotation

Rigid-body rotation (Fig. A.6(b)) involves movement of points B, C, D around a fixed reference point A, where $\partial u/\partial y = -\partial v/\partial x$ ($\because$ the right angle between the edges AB and AD is maintained) leading to $\dot{\varepsilon}_{xy} = 0$. The angular velocity is:

$$\frac{\partial v}{\partial x} dxdt \Big/ dxdt = \frac{\partial v}{\partial x} = -\frac{\partial u}{\partial y} \tag{A.52}$$

which, when substituted into the z-component of the angular velocity vector ω, leads to that $\omega_z \neq 0$. As in the case of translation, there is no displacement of points B, C, D relative to the reference point A, and therefore the fluid element does not undergo deformation.

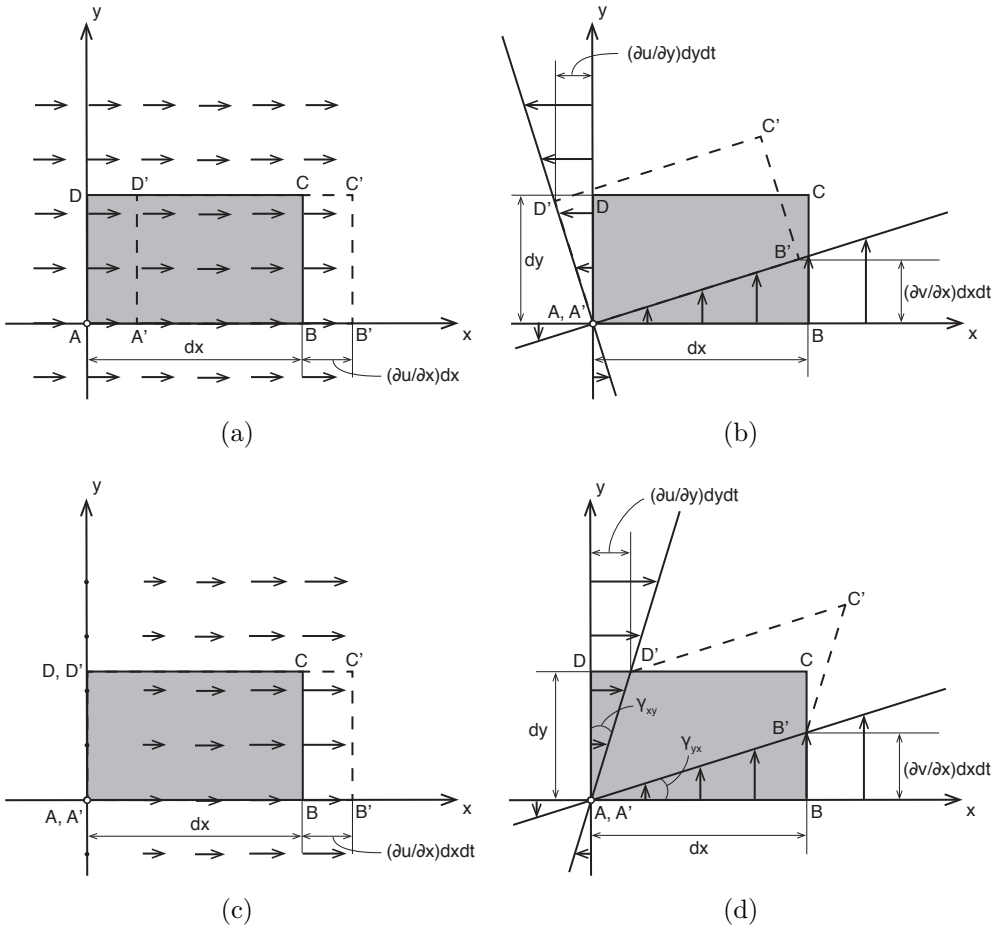

Figure A.6: Components of fluid motions. (a) Translation, (b) rigid-body rotation, (c) dilation and (d) shear deformation.

Dilation

Fig. A.6(c) shows the unidirectional, positive case of dilation of a fluid element when it is placed in a velocity field where $\partial u/\partial x > 0$ and other velocity gradients are zero in the rate of deformation tensor A.49. The edge BC is moved at velocity $du = (\partial u/\partial x)\, dx$ which increases with the distance dx from the $x = 0$ plane (similarly, in the y and z directions, the extension velocities are $dv = (\partial v/\partial y)\, dy$ and $dw = (\partial w/\partial z)\, dw$). Taking the changes in length in all three directions into

account, the relative volume change of the fluid element is then:

$$\dot{e} = \frac{\left(dx + \frac{\partial u}{\partial x}dxdt\right)\left(dy + \frac{\partial v}{\partial y}dydt\right)\left(dz + \frac{\partial w}{\partial z}dzdt\right) - dxdydz}{dxdydzdt}$$

$$\approx \frac{\frac{\partial v}{\partial y}dxdydzdt + \frac{\partial u}{\partial x}dxdydzdt + \frac{\partial w}{\partial z}dxdydzdt}{dxdydzdt}$$

$$= \frac{\partial u}{\partial x} + \frac{\partial v}{\partial y} + \frac{\partial w}{\partial z} = \nabla \cdot \mathbf{u} \tag{A.53}$$

In the 3D case, the shape of the fluid element is conserved as the right angles between the edges remain the same, and therefore $\dot{e}$ describes the local dilation of the fluid elememt. For an incompressible fluid, Eqn. A.53 above gives zero divergence, as expected.

Shear deformation

When a fluid element is placed in the vector field in which the off-the-main-diagonal shear gradients in Eqn. A.47 are not zero, it goes through shear deformation shown in Fig. A.6(d). If $\partial u/\partial y$ and $\partial v/\partial x$ are both positive, the original right angle at point A is changed by the superposition of the two motions, i.e. by $d\gamma_{yx} = (\partial v/\partial x)\, dxdt/dx$ from the edge AB and $d\gamma_{xy} = (\partial u/\partial y)\, dydt/dy$ from AD. It is observed that the right angle at A changes at a rate twice the absolute value of $\dot{\varepsilon}_{xy}$ or $\dot{\varepsilon}_{yx}$ $(= 1/2\,(\partial v/\partial x + \partial u/\partial y))$. For general 3D cases, off-the-main-diagonal elements in Eqn. A.49 (i.e. $\dot{\varepsilon_{xy}} = \dot{\varepsilon_{yx}}$, $\dot{\varepsilon_{xz}} = \dot{\varepsilon_{zx}}$, $\dot{\varepsilon_{yz}} = \dot{\varepsilon_{zy}}$) characterises the deformation of the right angle in the plane of which index does not appear. In these deformations, the volume of the fluid element is preserved and only the shape changes.

Of the four components of fluid motions outlined above, only the latter two (dilation and shear deformation) result in a deformation in reference to the point A.

A.3.2 Relationship between surface stresses and rate of deformation

Based on the details of fluid deformation described above, now the relation between the surfaces stresses and the rate of deformation is formulated.

From the descriptions of the fluid motions outlined in the previous section, it is observed that the components of the viscous stress tensor $\dot{\tau}$ (Eqn. A.44) depend only on the components of the rate of deformation tensor $\dot{\varepsilon}$ (Eqn. A.49) i.e. spatial derivatives of velocities, not directly on the velocity components u, v, w or the angular velocity components ω_x, ω_y, ω_z. From this, it can be deduced that the translation or rigid-body rotation of a fluid element does not induce any surface stresses other than the pressure forces, since the generation of tangential surface stresses takes place only when the components of the rate of deformation tensor are non-zero, which in turn is the result of the relative displacement of the points of the fluid element. From this, therefore, it can be said that the components of the viscous stress tensor $\dot{\tau}$ depend only on spatial velocity gradients.

The relationships between the components of $\dot{\tau}$ and the velocity gradients in $\dot{\varepsilon}$ must be linear, so that they remain unchanged when the coordinate system is rotated, and that the isotropy is preserved when the axes are exchanged (116). The latter condition is satisfied only when the axes of the stress tensor coincide with those of the deformation tensor. The following relations that satisfy these conditions were presented by Schlichting and Gersten (116):

$$\tau_{xx} = \lambda\left(\frac{\partial u}{\partial x} + \frac{\partial v}{\partial y} + \frac{\partial w}{\partial z}\right) + 2\mu\frac{\partial u}{\partial x} = \lambda\nabla\cdot\mathbf{u} + 2\mu\frac{\partial u}{\partial x}$$

$$\tau_{yy} = \lambda\left(\frac{\partial u}{\partial x} + \frac{\partial v}{\partial y} + \frac{\partial w}{\partial z}\right) + 2\mu\frac{\partial v}{\partial y} = \lambda\nabla\cdot\mathbf{u} + 2\mu\frac{\partial v}{\partial y}$$

$$\tau_{zz} = \lambda\left(\frac{\partial u}{\partial x} + \frac{\partial v}{\partial y} + \frac{\partial w}{\partial z}\right) + 2\mu\frac{\partial w}{\partial z} = \lambda\nabla\cdot\mathbf{u} + 2\mu\frac{\partial w}{\partial z} \tag{A.54}$$

$$\tau_{xy} = \tau_{yx} = \mu\left(\frac{\partial v}{\partial x} + \frac{\partial u}{\partial y}\right)$$

$$\tau_{yz} = \tau_{zy} = \mu\left(\frac{\partial w}{\partial y} + \frac{\partial v}{\partial z}\right)$$

$$\tau_{zx} = \tau_{xz} = \mu \left(\frac{\partial u}{\partial z} + \frac{\partial w}{\partial x} \right) \tag{A.55}$$

in which the first terms in Eqn. A.54 characterise the volume dilation and the second the linear dilation. μ is the viscosity and λ another viscosity parameter that governs the volume dilation, both of which must have the same value in all directions to preserve isotropy. It should be noted that the effects of λ can be neglected for incompressible flows, as the terms that contain λ all go to zero due to that $\nabla \cdot \mathbf{u} = 0$ for all incompressible flows. As a result Eqns. A.54 reduce to:

$$\tau_{xx} = 2\mu \frac{\partial u}{\partial x}, \quad \tau_{yy} = 2\mu \frac{\partial v}{\partial y}, \quad \tau_{zz} = 2\mu \frac{\partial w}{\partial z} \tag{A.56}$$

From Eqns. A.49, A.55 and A.56, the following relation can be formulated:

$$\dot{\tau} = \tau_{ij} = \begin{pmatrix} \tau_{xx} & \tau_{xy} & \tau_{xz} \\ \tau_{yx} & \tau_{yy} & \tau_{yz} \\ \tau_{zx} & \tau_{zy} & \tau_{zz} \end{pmatrix}$$

$$= \begin{pmatrix} 2\mu \dfrac{\partial u}{\partial x} & \mu \left(\dfrac{\partial v}{\partial x} + \dfrac{\partial u}{\partial y} \right) & \mu \left(\dfrac{\partial w}{\partial x} + \dfrac{\partial u}{\partial z} \right) \\ \mu \left(\dfrac{\partial u}{\partial y} + \dfrac{\partial v}{\partial x} \right) & 2\mu \dfrac{\partial v}{\partial y} & \mu \left(\dfrac{\partial w}{\partial y} + \dfrac{\partial v}{\partial z} \right) \\ \mu \left(\dfrac{\partial u}{\partial z} + \dfrac{\partial w}{\partial z} \right) & \mu \left(\dfrac{\partial v}{\partial z} + \dfrac{\partial w}{\partial y} \right) & 2\mu \dfrac{\partial w}{\partial z} \end{pmatrix}$$

$$= 2\mu \begin{pmatrix} \dfrac{\partial u}{\partial x} & \dfrac{1}{2} \left(\dfrac{\partial v}{\partial x} + \dfrac{\partial u}{\partial y} \right) & \dfrac{1}{2} \left(\dfrac{\partial w}{\partial x} + \dfrac{\partial u}{\partial z} \right) \\ \dfrac{1}{2} \left(\dfrac{\partial u}{\partial y} + \dfrac{\partial v}{\partial x} \right) & \dfrac{\partial v}{\partial y} & \dfrac{1}{2} \left(\dfrac{\partial w}{\partial y} + \dfrac{\partial v}{\partial z} \right) \\ \dfrac{1}{2} \left(\dfrac{\partial u}{\partial z} + \dfrac{\partial w}{\partial z} \right) & \dfrac{1}{2} \left(\dfrac{\partial v}{\partial z} + \dfrac{\partial w}{\partial y} \right) & \dfrac{\partial w}{\partial z} \end{pmatrix}$$

$$= 2\mu \dot{\varepsilon} \tag{A.57}$$

Eqn. A.57 is what we set out to obtain in order to complete the momentum equation (Eqn. A.45), i.e. the components in the viscous stress tensor $\dot{\tau}$ being expressed with the spatial derivatives of the velocity components u, v, w.

Substituting Eqn. A.57 into Eqn. A.45 gives:

$$\rho\frac{D\mathbf{u}}{Dt} = \int_{CV}\mathbf{f_B}dV - \int_{CS}\nabla p\dot{I}\cdot dA + \int_{CS}\nabla\cdot(2\mu\dot{\varepsilon})\cdot dA \tag{A.58}$$

Since that $\nabla\cdot\dot{\tau} = \nabla\cdot(2\mu\dot{\varepsilon}) = \mu\nabla^2\mathbf{u}$, Eqn. A.58 above becomes:

$$\rho\frac{D\mathbf{u}}{Dt} = \int_{CV}\mathbf{f_B}dV - \int_{CS}\nabla p\dot{I}\cdot dA + \int_{CS}\mu\nabla^2\mathbf{u}\cdot dA \tag{A.59}$$

Combining Eqns. A.31 and A.59:

$$\begin{aligned}\sum F_{CV} &= \mathbf{F_B} + \mathbf{F_S}\\ &= \frac{\partial}{\partial t}\int_{CV}\rho\mathbf{u}\,dV + \int_{CS}\rho\mathbf{u}\mathbf{u}\cdot d\mathbf{A}\\ &= \int_{CV}\mathbf{f_B}dV - \int_{CS}\nabla p\dot{I}\cdot dA + \int_{CS}\mu\nabla^2\mathbf{u}\cdot dA\end{aligned} \tag{A.60}$$

Neglecting the body force term, the final form of the momentum equation can therefore be written as:

$$\frac{\partial}{\partial t}\int_{CV}\rho\mathbf{u}\,dV + \int_{CS}\rho\mathbf{u}\mathbf{u}\cdot d\mathbf{A} = -\int_{CS}\nabla p\dot{I}\cdot dA + \int_{CS}\mu\nabla^2\mathbf{u}\cdot dA \tag{A.61}$$

This equation, derived from the Cauchy's momentum equations A.40 with the stress terms expressed with the viscosity and the velocity gradients, and also with the constant viscosity and density assumptions, is knows as the Navier-Stokes equation.

A.4 Boundary-layer equations

Boundary layer equations, which represent a reduced case of the complete Navier-Stokes equations, were developed by Prandtl in order to facilitate theoretical analyses of viscous flows, which were rendering solving of the Navier-Stokes equations mathematically difficult. The *boundary-layer* concept, proposed by Prandtl in his *On Fluid Motion with Very Small Friction* in 1904, simplifies the process

by focusing on that the effects of viscosity are significant only in the narrow region adjacent to the wall surface where the velocity gradient normal to the wall surface is large (the *boundary layer*). The resulting partial differential equations were transformed into the parabolic form, which requires simpler solution process compared to the full Navier-Stokes equations. Meanwhile, outside the boundary layer where the velocity gradient is small, the effects of viscosity become insignificant and so the flow can be treated as inviscid. Detailed derivation is outlined in (116).

For steady, incompressible fluid, the continuity and Navier-Stokes equations in the x (parallel to the surface) and y (normal to the surface) respectively take the following form:

$$\begin{aligned}
&\frac{\partial u}{\partial x} + \frac{\partial v}{\partial y} = 0 \\
&u\frac{\partial u}{\partial x} + v\frac{\partial u}{\partial y} = -\frac{1}{\rho}\frac{\partial p}{\partial x} + \nu\left(\frac{\partial^2 u}{\partial x^2} + \frac{\partial^2 u}{\partial y^2}\right) \\
&u\frac{\partial v}{\partial x} + v\frac{\partial v}{\partial y} = -\frac{1}{\rho}\frac{\partial p}{\partial y} + \nu\left(\frac{\partial^2 v}{\partial x^2} + \frac{\partial^2 v}{\partial y^2}\right)
\end{aligned} \tag{A.62}$$

where u and v are velocity components in x and y directions respectively. With order-of-magnitude analysis, these equations reduce to:

$$\begin{aligned}
&\frac{\partial u}{\partial x} + \frac{\partial v}{\partial y} = 0 \\
&u\frac{\partial u}{\partial x} + v\frac{\partial u}{\partial y} = -\frac{1}{\rho}\frac{\partial p}{\partial x} + \nu\frac{\partial^2 u}{\partial y^2}
\end{aligned} \tag{A.63}$$

with the following boundary conditions:

$$\begin{aligned}
&For \quad y = 0: \qquad u = 0, \quad v = 0 \\
&For \quad y = \infty: \qquad u = U(x)
\end{aligned} \tag{A.64}$$

where U is the velocity in the bulk-flow region, which has the following relationship:

$$U\frac{dU}{dx} = -\frac{1}{\rho}\frac{dp}{dx} \tag{A.65}$$

Appendix B

User-defined functions

B.1 Agonists wall reaction rates

This UDF defines the reaction rates for the hydrolysis reactions of ATP to ADP and of ADP to AMP. This code includes the release of ATP from the endothelial cell surface in response to WSS. The reaction rates are computed using the values of WSS computed in and obtained from the solver, FLUENT, and then applied at the wall boundary.

```
#include "udf.h"
#include "math.h"
#include "stdio.h"
#include "string.h"

#define Katp 1.68e-6
#define Kadp 6.45e-7
#define Smax 1e-12
#define WSSref 1.75

DEFINE_SR_RATE(ATPreleaseRR,f,fthread,r,mw,yi,rr)
{
double WSS,A[ND_ND],area,Satp;

F_AREA(A,f,fthread);
area=NV_MAG(A);
WSS=NV_MAG(F_STORAGE_R_N3V(f,fthread,SV_WALL_SHEAR))/area;
```

```
Satp=Smax*pow((1-exp(-WSS/WSSref)),3);

if(STREQ(r->name,"reaction-1)){
*rr=Satp;}

if(STREQ(r->name,"reaction-2)){
*rr=Katp*C_R(F_C0(f,fthread),F_C0_THREAD(f,fthread))*yi[0]/mw[0];}

if(STREQ(r->name,"reaction-3)){
*rr=Kadp*C_R(F_C0(f,fthread),F_C0_THREAD(f,fthread))*yi[1]/mw[1];}
}
```

B.2 Steady flow velocity inlet

This code imposes the fully-developed velocity boundary condition at the inlet, calculated from the desired Reynolds number and fluid properties of the model. Adjustments have been made to match the centre of the flow domain and that of the inlet cross section.

```
#include "udf.h"
#include "math.h"
#include "string.h"
#include "stdio.h"

double tot_x1,tot_x2,Uav,Rcca;
void centroid(int inlet_zID);

DEFINE_ON_DEMAND(correctcentroid)
{
int inlet_zID = 15;
centroid(inlet_zID);
}

DEFINE_PROFILE(Uin_re300,thread,position)
{
double x[ND_ND];
double r;
```

```
face_t f;

begin_f_loop(f,thread)
{
F_CENTROID(x,f,thread);
r=sqrt(pow((x[1]-(tot_x1)),2.0)+pow((x[2]-(tot_x2)),2.0));
F_PROFILE(f,thread,position)=2.0*Uav*(1.0-r*r/(Rcca*Rcca));
}
end_f_loop(f,thread)
}

void centroid(int inlet_zID)
{
double A[ND_ND],x[ND_ND];
double tot_area=0.0, ArCe_x1=0.0, ArCe_x2=0.0, Atmp=0.0;
double Re=300 ,rho=1000, mu=0.004, nu=0.0, Qm=0.0, Qv=0.0, d=0.0;
Domain *domain;
face_t face;
Thread *face_thread;
domain = Get_Domain(1);
face_thread = Lookup_Thread(domain,inlet_zID);

begin_f_loop(face,face_thread)
{
F_AREA(A,face,face_thread);
Atmp=NV_MAG(A);
tot_area+=Atmp;
F_CENTROID(x,face,face_thread);
ArCe_x1+=NV_MAG(A)*x[1];
ArCe_x2+=NV_MAG(A)*x[2];
}
end_f_loop(face,face_thread)

tot_x1=ArCe_x1/tot_area;
tot_x2=ArCe_x2/tot_area;

d=sqrt((4*tot_area)/M_PI);
Rcca=d/2;
nu=mu/rho;
```

```
Uav=(Re*nu)/d;
Qm=rho*Uav*tot_area;
Qv=Uav*tot_area;

if (tot_area!= 0){
Message("\n\nInlet data on node %d;\n",myid);
Message("\nDynamic viscosity: %.3f Pa.s",mu);
Message("\nMean inlet velocity: %.13f m/s",Uav);
Message("\nTotal inlet area: %.13f m^2",tot_area);
Message("\nCCA radius: %.13f m",Rcca);
Message("\nMean y-coordinate of centroid: %.13f",tot_x1);
Message("\nMean z-coordinate of centroid: %.13f\n\n",tot_x2);}

return;
}
```

B.3 Pulsatile flow velocity inlet

This code reads in discrete values that define a common carotid artery waveform stored in an external file, decomposes the waveform using Fourier series, and then calculates Fourier coefficients at each time step. The velocity value is computed based on the coefficients at the beginning of each time step, and was imposed as a constant value across the inlet.

```
#include "udf.h"
#include "stdio.h"
#include "string.h"
#include "stdlib.h"
#include "math.h"
#include "para.h"

#define  pi 3.14159

double D[16]={0};
double B[16]={0};
double U;
```

```
double lambda2;
static int last_time=-1;
int number_items;
int z=0;

DEFINE_ON_DEMAND(Fourier)
{
#if !RPNODE
char Buffer[1000];
int size,n,N,p;
int allocation;
double C,*Y;
FILE *wave_data;

allocation=10;
Y=malloc(allocation*sizeof(double));
Message0("\nAllocating memory space for the waveform array...\n");
number_items=0;

if ((wave_data= open("CABif6mm_waveform.txt", "r"))==NULL)
Message0("\n Warning: Unable to open %s for reading\n","CABif6mm_waveform.txt");
else
Message0("\nReading waveform data from %s... ","CABif6mm_waveform.txt");
Message0("Done.\n");

while (fgets(Buffer,100,wave_data) !=NULL){

if(number_items>=allocation){
double *np;
allocation+=100;
np=realloc(Y,allocation*sizeof(double));

if(np == NULL){
printf("Memory allocation failed. Exiting.\n");
free(np);
exit(1);}

Y=np;
Message0("\nAllocated more memory.\n");}
```

```
Y[number_items++]=atof(strtok(Buffer,"\n"));}

Message("\nContents of array Y:");
for(z=0;z<number_items;z++){
Message0("\nElement %2d: \t%.9f",z,Y[z]);}

fclose(wave_data);

N=number_items;
C=(double)number_items;

Message0("\n\nCalculating Fourier coefficients...\n\n");
for (p=0;p<=N/2;p++){
D[p]=0;
B[p]=0;

for (n=0;n<=N-1;n++){
D[p]=D[p]+2/C*Y[n]*cos(2*pi*p*(n+1)/C);
B[p]=B[p]+2/C*Y[n]*sin(2*pi*p*(n+1)/C);}

Message0("%2d : % f  % f\n",p,D[p],B[p]);
}

D[N/2]=D[N/2]/2;
B[N/2]=0;

Message0("\nThe size of array is: %d\n",N);

free(Y);
#endif
}

DEFINE_PROFILE(CABif6mm_Uin_pulsatile,thread,index)
{
int hmax=16,h;
double x[ND_ND],Ut,T=1.0;
double t;
double Fosc;
```

```
int ts;
t=RP_Get_Real("flow-time");
ts=RP_Get_Integer("time-step");
face_t f;

Ut=D[0]/2;

for (h=1;h<=hmax;h++){
Fosc=D[h]*cos(2*pi*h*t/T)+B[h]*sin(2*pi*h*t/T);
lambda2=1.025+0.025*((10.88634403*Fosc)-0.313659905);
Ut=Ut+D[h]*cos(2*pi*h*t/T)+B[h]*sin(2*pi*h*t/T);}

Message0("\nCurrent time step: %d",ts);
Message0("\nCurrent time: %f\n",t);

if (last_time != t){
last_time=t;
Message0("\nPulsatile velocity: %f\n",Ut);}

begin_f_loop(f,thread)
{
F_CENTROID(x,f,thread);
F_PROFILE(f,thread,index)=Ut;
}
end_f_loop(f,thread)
}
```

B.4 Pulsatile flow EC dynamics

This UDF calculates the concentrations of the EC dynamics cellular variables by solving Eqns. 5.9, 5.10, 5.37, 5.38, 5.39 using the fifth-order Runge-Kutta integrator.

```
#include "udf.h"
#include <stdio.h>
#include <string.h>
#include <stdlib.h>
#include <math.h>
```

```
static double maxarg1,maxarg2;
#define FMAX(a,b) (maxarg1=(a),maxarg2=(b),(maxarg1) > (maxarg2) ?\
(maxarg1) : (maxarg2))

static double minarg1,minarg2;
#define FMIN(a,b) (minarg1=(a),minarg2=(b),(minarg1) < (minarg2) ?\
(minarg1) : (minarg2))

/* Adaptive step parameters */
#define SAFETY 0.8
#define PGROW -0.2
#define PSHRNK -0.25
#define ERRCON 1.89e-4
#define TINY 1e-30

/* Model parameters */
#define ki 5.46e-3
#define mu1 0.2
#define krel 6.64
#define kres 5
#define kout 24.7
#define kdis 0.09
#define mu2 0.0167
#define gmax 0.06
#define qmax 17.6
#define kcce 5.7e-6
#define Cs0 2830
#define Cex 1500
#define Kc 0.026
#define K1 0
#define K2 0.2
#define K3 0.15
#define K4 5
#define K5 0.32
#define K6 0.45
#define Vr 3.5
#define Cc0 0.1
#define Te 310
```

```
#define l 3.7491e-5
#define s 1e-5
#define N 1e12
#define vareps 0.9
#define fe 0.0134
#define k 1.3807e-23
#define alpha 2
#define gamma 0.1
#define gamma2 0.9            /* gamma2=(1.0-gamma) */

/* Model parameters (sed)*/
#define Hec 5.0e-6
#define Hm 1.0e-8
#define G2 10.0
#define Am 0.00001
#define Bm 0.00001

/* Other parameters */
#define Kcicr 0
#define n 5
#define agonistREF 1.80152e-8

/* NO synthesis and leak parameters */
#define kNO 0.4
#define mu3 0.5

/* Global variables */
double WSS;
double agonist;
double F;
double y[5]=0,Cc0,Cs0,(kdis*Cc0)/(mu2*(K6+Cc0)),0};
double yscal[5]={0};
double dydx[5]={0};
double yout[5]={0};
double yerr[5]={0};
double ytemp[5]={0};
double hdid=0.001;
double hnext=0;
double h=0.01;
```

```
double x=0;

/* Global variables (strain energy)*/
extern double lambda2;
double WB;

/* Function prototype definitions */
void SED();
void derivs(double x,double y[],double dydx[],double agonist);
void rk4();
void rkadap();
void odeprog();
void odeoutput(int zID);

DEFINE_EXECUTE_AT_END(celldynamics_bi)
{
int wall=12;
odeoutput(wall);
}

void SED()
{
double zeta;
double omega;
double lambda1;

omega=(1.0-vareps)*WSS/(2*(Am+Bm*pow(lambda2,4)));

zeta=Hec*vareps*WSS/G2;

lambda1=sqrt(4.0*omega*zeta+1.0);

WB=(Am/8)*(pow(lambda1,4)+pow(lambda2,4)-2*(pow(lambda1,2)+pow(lambda2,2))+2)
+(Bm/8)*pow((pow(lambda1,2)*pow(lambda2,2)-1),2);
}

void derivs(double x,double y[],double dydx[],double agonist)
{
SED();
```

```
F=1/(1+alpha*exp((-fe*WB)/(k*Te*N)));

dydx[0]=ki*(agonist/(Kc+agonist))*(y[1]/(K1+y[1]))-mu1*y[0];

dydx[1]=krel*y[2]*pow(y[0]/(K2+y[0]),3)-kres*pow(y[1]/(K3+y[1]),2)
+(kcce*(Cs0-y[2])*(Cex-y[1]))/(K4+y[3])+gamma*F*qmax-(kout*y[1])/(K5+y[1]);

dydx[2]=-Vr*(krel*y[2]*pow(y[0]/(K2+y[0]),3)-kres*pow(y[1]/(K3+y[1]),2));

dydx[3]=(kdis*y[1])/(K6+y[1])-mu2*y[3]+gamma2*F*gmax;

dydx[4]=kNO*y[3]-mu3*y[4];
}

void rk4()
{
int i;
double ak2[n], ak3[n], ak4[n], ak5[n], ak6[n];
static double a2=0.2,a3=0.3,a4=0.6,a5=1.0,a6=0.875,b21=0.2,
b31=3.0/40.0,b32=9.0/40.0,b41=0.3,b42 = -0.9,b43=1.2,
b51 = -11.0/54.0, b52=2.5,b53 = -70.0/27.0,b54=35.0/27.0,
b61=1631.0/55296.0,b62=175.0/512.0,b63=575.0/13824.0,
b64=44275.0/110592.0,b65=253.0/4096.0,c1=37.0/378.0,
c3=250.0/621.0,c4=125.0/594.0,c6=512.0/1771.0,
dc5 = -277.0/14336.0;
double dc1=c1-2825.0/27648.0,dc3=c3-18575.0/48384.0,
dc4=c4-13525.0/55296.0,dc6=c6-0.25;

for (i=0;i<n;i++){
ytemp[i]=y[i]+b21*h*dydx[i];}

derivs(x+a2*h,ytemp,ak2,agonist);

for (i=0;i<n;i++){
ytemp[i]=y[i]+h*(b31*dydx[i]+b32*ak2[i]);}

derivs(x+a3*h,ytemp,ak3,agonist);
```

```
for (i=0;i<n;i++){
ytemp[i]=y[i]+h*(b41*dydx[i]+b42*ak2[i]+b43*ak3[i]);}

derivs(x+a4*h,ytemp,ak4,agonist);

for (i=0;i<n;i++){
ytemp[i]=y[i]+h*(b51*dydx[i]+b52*ak2[i]+b53*ak3[i]+b54*ak4[i]);}

derivs(x+a5*h,ytemp,ak5,agonist);

for (i=0;i<n;i++){
ytemp[i]=y[i]+h*(b61*dydx[i]+b62*ak2[i]+b63*ak3[i]+b64*ak4[i]+b65*ak5[i]);}

derivs(x+a6*h,ytemp,ak6,agonist);

for (i=0;i<n;i++){
yout[i]=y[i]+h*(c1*dydx[i]+c3*ak3[i]+c4*ak4[i]+c6*ak6[i]);}

for (i=0;i<n;i++){
yerr[i]=h*(dc1*dydx[i]+dc3*ak3[i]+dc4*ak4[i]+dc5*ak5[i]+dc6*ak6[i]);}
}

void rkadap()
{
int i;
double errmax,htemp;
double eps=1e-5;

for(;;){

rk4();

errmax=0.0;

for (i=0;i<n;i++){errmax=FMAX(errmax,fabs(yerr[i]/yscal[i]));}

errmax=errmax/eps;

if (errmax <= 1.0) break;
```

```
htemp=SAFETY*h*pow(errmax,PSHRNK);
h=(h >= 0.0 ? FMAX(htemp,0.1*(h)) : FMIN(htemp,0.1*(h)));
}

h=((errmax > ERRCON) ? (SAFETY*h*pow(errmax,PGROW)) : (5.0*h));
x+=h;
}

void odeprog()
{
int i;

for(;;){
derivs(x,y,dydx,agonist);

for(i=0;i<n;i++){yscal[i]=fabs(y[i])+fabs(dydx[i]*(h))+TINY;}

rkadap();

if (fabs(dydx[0])<0.001 && fabs(dydx[1])<0.001 && fabs(dydx[2])<0.001
&& fabs(dydx[3])<0.001 && fabs(dydx[4])<0.001) break;

for (i=0;i<n;i++){y[i]=yout[i];}
}
}

void odeoutput(int zID)
{
double A[ND_ND],area;
Domain *domain;
domain=Get_Domain(1);
face_t f;
Thread *fthread;
fthread=Lookup_Thread(domain,zID);

begin_f_loop(f,fthread)
{
F_AREA(A,f,fthread);
```

```
area=NV_MAG(A);

WSS=NV_MAG(F_STORAGE_R_N3V(f,fthread,SV_WALL_SHEAR))/(area);

agonist=(F_YI(F_C0(f,fthread),THREAD_T0(fthread),0)+F_YI(F_C0(f,fthread),
THREAD_T0(fthread),1))/agonistREF;

odeprog();

C_UDMI(F_C0(f,fthread),THREAD_T0(fthread),0)=yout[0];
C_UDMI(F_C0(f,fthread),THREAD_T0(fthread),1)=yout[1];
C_UDMI(F_C0(f,fthread),THREAD_T0(fthread),2)=yout[2];
C_UDMI(F_C0(f,fthread),THREAD_T0(fthread),3)=yout[3];
C_UDMI(F_C0(f,fthread),THREAD_T0(fthread),4)=WSS;
C_UDMI(F_C0(f,fthread),THREAD_T0(fthread),5)=yout[4];
C_UDMI(F_C0(f,fthread),THREAD_T0(fthread),6)=WB;
C_UDMI(F_C0(f,fthread),THREAD_T0(fthread),7)=F;

}
end_f_loop(f,fthread)
}
```